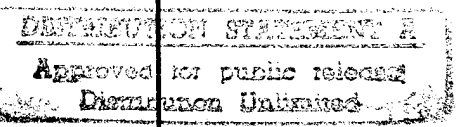
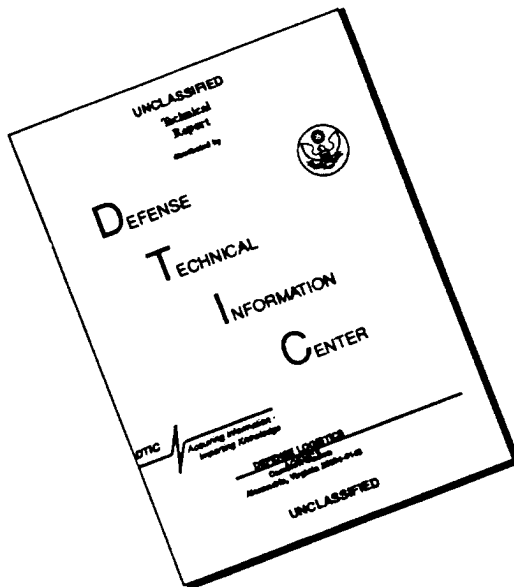


19960415041
REPORT DOCUMENTATION PAGE**Form Approved
OMB No. 0704-0188**

Public reporting burden for this collection of information is estimated to average 1 hour per response, including the time for reviewing instructions, searching existing data sources, gathering and maintaining the data needed, and completing and reviewing the collection of information. Send comments regarding this burden estimate or any other aspect of this collection of information, including suggestions of reducing this burden, to Washington Headquarters Services, Directorate for Information Operations and reports, 1215 Jefferson Davis Highway, Suite 1204, Arlington, VA 22202-4302, and to the Office of Management and Budget, Paperwork Reduction Project (0704-0188), Washington, DC 20503.

1. AGENCY USE ONLY (Leave blank)	2. REPORT DATE	3. REPORT TYPE AND DATES COVERED	
	5/25/95	Final report, 1JAN93 - 18MAY95	
4. TITLE AND SUBTITLE A Wind Tunnel Investigation of a Wing-tip Trailing Vortex			5. FUNDING NUMBERS G N00014-94-1-0744
6. AUTHOR(S) Engel, M.A. and Devenport, W.J.			
7. PERFORMING ORGANIZATION NAME(S) AND ADDRESS(ES) Department of Aerospace and Ocean Engineering Virginia Polytechnic Institute and State University Blacksburg, VA 24061			8. PERFORMING ORGANIZATION REPORT NUMBER VPI-AOE-218
9. SPONSORING / MONITORING AGENCY NAME(S) AND ADDRESS(ES) Office of Naval Research Ballston Tower One 800 North Quincy Street Arlington, VA 22217-5660			10. SPONSORING / MONITORING AGENCY REPORT NUMBER
11. SUPPLEMENTARY NOTES			
12a. DISTRIBUTION / AVAILABILITY STATEMENT UNCLASSIFIED Unlimited		12b. DISTRIBUTION CODE  Approved for public release Distribution Unlimited	
13. ABSTRACT (Maximum 200 words) The 3'x2' Subsonic Wind Tunnel was used to study a wing-tip trailing vortex during its development at the wingtip and at 10 chordlengths downstream. The vortex was found to be well developed by 10 chordlengths. Helium bubble flow-visualization was used to study the development of the vortex in the near-tip regions. Hot wire anemometry was used to study the vortex at 10 chordlengths. Two vortices were found in the tip-flow studies, a primary vortex formed on the suction side surface of the wingtip and a weaker secondary vortex formed on the endcap. The primary vortex lifts from the surface of the wingtip as it proceeds along the chord. The vertical displacement is a strong function of angle of attack. The primary vortex is displaced from the endcap towards the wing root at the trailing edge. The spanwise displacement is a strong function of chord Reynolds number. The primary and secondary vortices co-rotate after leaving the wingtip trailing edge. The primary vortex core follows a steady helical path. The radius of the helical path quickly diminishes with downstream distance.			
14. SUBJECT TERMS Trailing Vortices, Wing-tip Aerodynamics			15. NUMBER OF PAGES 258
			16. PRICE CODE
17. SECURITY CLASSIFICATION OF REPORT UNCLASSIFIED	18. SECURITY CLASSIFICATION OF THIS PAGE UNCLASSIFIED	19. SECURITY CLASSIFICATION OF ABSTRACT UNCLASSIFIED	20. LIMITATION OF ABSTRACT

DISCLAIMER NOTICE



THIS DOCUMENT IS BEST
QUALITY AVAILABLE. THE COPY
FURNISHED TO DTIC CONTAINED
A SIGNIFICANT NUMBER OF
PAGES WHICH DO NOT
REPRODUCE LEGIBLY.

The vortex core was extensively analyzed with a four-sensor quad-hot-wire probe at 10 chordlengths behind the model. Flow visualization showed clearly no visible probe interference with the probe stationed inside, outside, and traversing through the vortex core.

The vortex core radius, peak tangential velocity, and core circulation increase with increasing angle of attack. The tangential velocity profiles and axial vorticity profiles indicate the development of inner and outer core regions by 5.0 degrees angle of attack. The regions become increasingly differentiated with increasing angle of attack. The inner and outer core regions appear to be associated with the primary and secondary tip vortices, respectively. An heuristic model of the differentiated vortex core regions has been developed.

**A Wind Tunnel Investigation
of a Wing-tip Trailing Vortex**

by

Mark A. Engel and William J. Devenport

Abstract

A 3'x2' subsonic wind tunnel has been constructed and calibrated. The flow in the wind tunnel accelerates 6.1% along the test section due to boundary layer growth. The potential core flow at both the entrance and exit locations is strongly uniform. The mean velocity varies .4% across the entrance and exit planes. The turbulence level at the entrance and exit locations is approximately .2%.

The tunnel was used to study a trailing vortex during its development at the wingtip and at 10 chordlengths downstream. The vortex was found to be well developed by 10 chordlengths. Helium bubble flow visualization was used to study the development of the vortex in the near-tip regions. Hot-wire anemometry was used to study the vortex at 10 chordlengths.

Two vortices were found in the tip-flow studies, a primary vortex core formed on the suction side surface of the wingtip and a weaker secondary vortex formed on the endcap. The primary vortex core lifts from the surface of the wingtip as it proceeds along the chord. The vertical displacement is a strong function of angle of attack. The primary vortex is displaced from the endcap towards the wing root at the trailing edge. The spanwise displacement is a strong function of chord Reynolds number.

The primary and secondary vortices co-rotate after leaving the wing, and the primary vortex core follows a steady helical path. The radius of the helical path quickly diminishes with downstream distance.

The vortex was extensively analyzed with a four-sensor quad-hot-wire probe at 10 chordlengths behind the model. Flow visualization showed clearly no visible probe interference with the probe stationed inside, outside, and traversing through the vortex core.

The vortex core radius, peak tangential velocity, and core circulation increase with increasing angle of attack. The tangential velocity profiles and axial vorticity profiles indicate the development of inner and outer core regions by 5.0° angle of attack. The regions become increasingly differentiated with increasing angle of attack. The inner and outer regions appear to be associated with the primary and secondary tip vortices, respectively. An heuristic model of the differentiated vortex core regions has been developed.

Acknowledgements

I need to acknowledge first the help and guidance of the Lord above. Without His intervention, none of this could have ever been. I also wish to thank my Mom for her support and for lending an ear when I had no one else to whom to complain. And, as always, thanks to my fiance', Pamela Jean, for all of her support and caring. I could have done none of this without the help of these people.

I need to give a special thanks to my principal advisor, Dr. William J. Devenport. For some unknown reason, he decided to take a chance with me and give me a research position when no one else even considered it. I only hope that given a similar chance someday, I will be as generous.

The number of people involved in with the current study, to varying degrees, is quite large. Thanks to Mike Rife for showing me how to conduct meaningful research and still make it out to the range every now and then. Thanks to Matt Sextone for his extensive help in the tunnel improvements. Many thanks to my good friend Ken Wittmer for his insightful help with the wing mount, the traverse modifications, and the many evenings spent discussing the fundamentals of life and everything else. Thanks also to my good friend George Anderson, without whose help I would probably still be cutting and pasting. And many thanks to the fellas without whom none of the contraptions "designed" could have been made: Frank "what do you want now" Shelor, Bruce "Red Dog" Stanger, Kent

"don't mess with sweetpea" Morris, and Greg "Turkey Caller" Dudding, the good bunch of people from the machine shop. Thanks to all who helped with the work.

A special thanks goes to Dr. Ed Hampton. He is not a karate guru, nor a karate dispenser, nor a sensei. He is not a lot of things, to listen to him speak. But he is an amazing individual who has taught me a lot about life, living, and myself. His help goes far beyond anything I can list. I just hope that I can do justice to his teachings. May God bless him and his family.

I would like to thank the Office of Naval Research, in particular Dr. L. Patrick Purtell, for their support under grant number N00014-92-J4087 and ASERT grant N00014-94-1-0744.

Table of Contents

List of Tables

List of Figures

List of Symbols

1. Genesis	1
1.1 Introduction	1
1.2.1 General Structure of Trailing Vortices	2
1.2.2 Tip Vortex Formation	5
1.2.3 Instantaneous Structure/Core Waves	9
1.3 Objectives	11
2. Wind Tunnel Fabrication and Calibration	12
2.1 Settling Chamber and Contraction	12
2.2 Test Section	15
2.3 Diffuser	16
2.4 Fan/Motor	17
2.5 Flow Characteristics	17
2.5.1 Pitot-Static Instrumentation	18
2.5.2 Hot-Wire Instrumentation	18
2.5.3 Traversing Equipment	20
2.5.4 Coordinate System and Measurement Locations	21

2.5.5 Longitudinal Tunnel Traverse	22
2.5.6 Entrance and Exit Locations	24
3. Trailing Vortex Visualization	27
3.1 Apparatus	27
3.2 Results	30
3.2.1 Discussion	31
3.2.2 Modeling	34
3.2.3 Other Cases	37
3.2.4 Ratio of Vortex Strengths	38
3.2.5 Primary Vortex Circulation	41
3.2.6 Secondary Vortex Circulation	42
3.2.7 Maximum Vertical Separation	43
3.2.8 Primary Vortex Position	43
3.2.8.1 Vertical Position	44
3.2.8.2 Spanwise Displacement	44
3.2.9 Flow Angularity	46
3.2.10 Probe Interference Studies	47
3.2.11 Particle Image Velocimetry	49
4. Hot-Wire Measurements	51
4.1 General	51
4.2 Apparatus	51

4.3 Results	53
4.3.1 Grid Measurements	54
4.3.2 Correction of Quad-Hot-Wire Results for the effects of Wandering	55
4.3.3 Axial Velocity Results	57
4.3.4 Tangential Velocity Results	58
4.3.4.1 Maximum Tangential Velocity	59
4.3.4.2 Core Radius	60
4.3.4.3 Core Circulation	60
4.4 Axial Vorticity	61
4.5 Vortex Core Model	62
5. Conclusions and Future Work	66
References	70
Appendix 1. Operation Procedures	75
Appendix 2. Schlieren Flow-Visualization	76
Tables	93
Figures	97
Vita	258

List of Tables

Table 1. Measurements from Tip Flow Visualizations	94
Table 2. Errors and Uncertainties Associated with the Tip Flow Analysis	95
Table 3. Vortex Core Parameters	96

List of Figures

Figure 1. Coalescence of a General System of Wingtip Vortices	98
Figure 2. Experimental Model of Bandyopadhyay, et.al. ²²	99
Figure 3. Experimental Setup of Devenport, et.al. ^{10,37}	100
Figure 4. Vortex/Free-Surface Interaction (Sarpkaya ¹⁸)	101
Figure 5. Experimental Setup of Sarpkaya ²⁴	102
Figure 6. Complex Wingtip Vortex System about a Blunt Tip Hydrofoil (Francis and Katz ²⁷)	103
Figure 7. Schematic of Shear Layer System about a Blunt Tip Airfoil (Hoffman and Velkoff ²⁶)	104
Figure 8. Coherent Structure Organization of Fine Scale Turbulence (Melander and Hussain ¹⁹)	105
Figure 9. “Slow” Time Dependent Axial Velocities of a Trailing Vortex Core (Green and Acosta ²³)	106
Figure 10. 3’x2’ Subsonic Wind Tunnel Profile Sketch	107
Figure 11. Contraction Sideview	108
Figure 12. Contraction Topview	109
Figure 13. Inlet Proximity to Laboratory Walls	110
Figure 14. Settling Chamber with Bellmouth	111
Figure 15. Flow Angularity	112
Figure 16. Test Section, Right Side	113
Figure 17. Test Section, Left Side	114

Figure 18. Test Section, Top View	115
Figure 19. Wall, Ceiling, and Floor Compression	116
Figure 20. Inside and Outside Seam Sealant	117
Figure 21. Blower and Diffuser Sections, Front View	118
Figure 22. Test Section Coordinate System and Pitot-Static Locations	119
Figure 23. VA Tech Stability Tunnel 2-Axis Traverse	120
Figure 24. Probe Support	121
Figure 25. Hot-Wire Probe Offset	122
Figure 26. Streamlined Longitudinal Traverse	123
Figure 27. U/U_{ref} Variations along Tunnel Centerline, $Re_x=1.6 \times 10^6$	124
Figure 28. u^2 / U_{ref}^2 Variations along the Tunnel Centerline, $Re_x=1.6 \times 10^6$	125
Figure 29. G_{uu} Power Spectrum at $X=0''$	126
Figure 30. G_{uu} Power Spectrum at $X=114''$	127
Figure 31. G_{uu} Power Spectrum at $X=216''$	128
Figure 32. U/U_{ref} Variations across the Test Section Entrance	129
Figure 33. U/U_{ref} Variations across the Test Section Exit	130
Figure 34. u^2 / U_{ref}^2 , Block Averaged, Variations across the Test Section Entrance	131
Figure 35. u^2 / U_{ref}^2 , Time Averaged, Variations across the Test Section Entrance	132
Figure 36. u^2 / U_{ref}^2 , Block Averaged, Variations across the Test Section Exit	133

Figure 37. u^2 / U_{ref}^2 , Time Averaged, Variations across the Test Section Exit	134
Figure 38. Over-Designed Wing Mount	135
Figure 39. Coordinate System	136
Figure 40. Flow Visualization Layout	137
Figure 41. Tip Flow Visualizations, Endcap View Aspect Ratio=3.0, Angle of Attack=2.5°, $Re_c=130000$	138
Figure 41. Tip Flow Visualizations, Endcap View Aspect Ratio=3.0, Angle of Attack=2.5°, $Re_c=130000$	139
Figure 41. Tip Flow Visualizations, Suction Surface View Aspect Ratio=3.0, Angle of Attack=2.5°, $Re_c=130000$	140
Figure 41. Tip Flow Visualizations, Suction Surface View Aspect Ratio=3.0, Angle of Attack=2.5°, $Re_c=130000$	141
Figure 42. Tip Flow Visualizations, Endcap View Aspect Ratio=3.0, Angle of Attack=2.5°, $Re_c=260000$	142
Figure 42. Tip Flow Visualizations, Endcap View Aspect Ratio=3.0, Angle of Attack=2.5°, $Re_c=260000$	143
Figure 42. Tip Flow Visualizations, Suction Surface View Aspect Ratio=3.0, Angle of Attack=2.5°, $Re_c=260000$	144
Figure 42. Tip Flow Visualizations, Suction Surface View Aspect Ratio=3.0, Angle of Attack=2.5°, $Re_c=260000$	145
Figure 43. Tip Flow Visualizations, Endcap View Aspect Ratio=3.0, Angle of Attack=2.5°, $Re_c=335000$	146
Figure 43. Tip Flow Visualizations, Endcap View Aspect Ratio=3.0, Angle of Attack=2.5°, $Re_c=335000$	147
Figure 43. Tip Flow Visualizations, Suction Surface View Aspect Ratio=3.0, Angle of Attack=2.5°, $Re_c=335000$	148
Figure 43. Tip Flow Visualizations, Suction Surface View	

Aspect Ratio=3.0, Angle of Attack=2.5°, Re_c =335000	149
Figure 44. Tip Flow Visualizations, Endcap View	
Aspect Ratio=3.0, Angle of Attack=5.0°, Re_c =130000	150
Figure 44. Tip Flow Visualizations, Endcap View	
Aspect Ratio=3.0, Angle of Attack=5.0°, Re_c =130000	151
Figure 44. Tip Flow Visualizations, Suction Surface View	
Aspect Ratio=3.0, Angle of Attack=5.0°, Re_c =130000	152
Figure 44. Tip Flow Visualizations, Suction Surface View	
Aspect Ratio=3.0, Angle of Attack=5.0°, Re_c =130000	153
Figure 45. Tip Flow Visualizations, Endcap View	
Aspect Ratio=3.0, Angle of Attack=5.0°, Re_c =260000	154
Figure 45. Tip Flow Visualizations, Endcap View	
Aspect Ratio=3.0, Angle of Attack=5.0°, Re_c =260000	155
Figure 45. Tip Flow Visualizations, Suction Surface View	
Aspect Ratio=3.0, Angle of Attack=5.0°, Re_c =260000	156
Figure 45. Tip Flow Visualizations, Suction Surface View	
Aspect Ratio=3.0, Angle of Attack=5.0°, Re_c =260000	157
Figure 46. Tip Flow Visualizations, Endcap View	
Aspect Ratio=3.0, Angle of Attack=5.0°, Re_c =335000	158
Figure 46. Tip Flow Visualizations, Endcap View	
Aspect Ratio=3.0, Angle of Attack=5.0°, Re_c =335000	159
Figure 46. Tip Flow Visualizations, Suction Surface View	
Aspect Ratio=3.0, Angle of Attack=5.0°, Re_c =335000	160
Figure 46. Tip Flow Visualizations, Suction Surface View	
Aspect Ratio=3.0, Angle of Attack=5.0°, Re_c =335000	161
Figure 47. Tip Flow Visualizations, Endcap View	
Aspect Ratio=3.0, Angle of Attack=7.5°, Re_c =130000	162
Figure 47. Tip Flow Visualizations, Endcap View	
Aspect Ratio=3.0, Angle of Attack=7.5°, Re_c =130000	163

Figure 47. Tip Flow Visualizations, Suction Surface View Aspect Ratio=3.0, Angle of Attack=7.5°, $Re_c=130000$	164
Figure 47. Tip Flow Visualizations, Suction Surface View Aspect Ratio=3.0, Angle of Attack=7.5°, $Re_c=130000$	165
Figure 48. Tip Flow Visualizations, Endcap View Aspect Ratio=3.0, Angle of Attack=7.5°, $Re_c=260000$	166
Figure 48. Tip Flow Visualizations, Endcap View Aspect Ratio=3.0, Angle of Attack=7.5°, $Re_c=260000$	167
Figure 48. Tip Flow Visualizations, Suction Surface View Aspect Ratio=3.0, Angle of Attack=7.5°, $Re_c=260000$	168
Figure 48. Tip Flow Visualizations, Suction Surface View Aspect Ratio=3.0, Angle of Attack=7.5°, $Re_c=260000$	169
Figure 49. Tip Flow Visualizations, Endcap View Aspect Ratio=3.0, Angle of Attack=7.5°, $Re_c=335000$	170
Figure 49. Tip Flow Visualizations, Endcap View Aspect Ratio=3.0, Angle of Attack=7.5°, $Re_c=335000$	171
Figure 49. Tip Flow Visualizations, Suction Surface View Aspect Ratio=3.0, Angle of Attack=7.5°, $Re_c=335000$	172
Figure 49. Tip Flow Visualizations, Suction Surface View Aspect Ratio=3.0, Angle of Attack=7.5°, $Re_c=335000$	173
Figure 50. Tip Flow Visualizations, Endcap View Aspect Ratio=2.5, Angle of Attack=2.5°, $Re_c=130000$	174
Figure 50. Tip Flow Visualizations, Endcap View Aspect Ratio=2.5, Angle of Attack=2.5°, $Re_c=130000$	175
Figure 50. Tip Flow Visualizations, Suction Surface View Aspect Ratio=2.5, Angle of Attack=2.5°, $Re_c=130000$	176
Figure 51. Tip Flow Visualizations, Endcap View Aspect Ratio=2.5, Angle of Attack=2.5°, $Re_c=260000$	177

Figure 51. Tip Flow Visualizations, Endcap View Aspect Ratio=2.5, Angle of Attack=2.5°, $Re_c=260000$	178
Figure 51. Tip Flow Visualizations, Suction Surface View Aspect Ratio=2.5, Angle of Attack=2.5°, $Re_c=260000$	179
Figure 51. Tip Flow Visualizations, Suction Surface View Aspect Ratio=2.5, Angle of Attack=2.5°, $Re_c=260000$	180
Figure 52. Tip Flow Visualizations, Endcap View Aspect Ratio=2.5, Angle of Attack=2.5°, $Re_c=335000$	181
Figure 52. Tip Flow Visualizations, Endcap View Aspect Ratio=2.5, Angle of Attack=2.5°, $Re_c=335000$	182
Figure 52. Tip Flow Visualizations, Suction Surface View Aspect Ratio=2.5, Angle of Attack=2.5°, $Re_c=335000$	183
Figure 53. Tip Flow Visualizations, Endcap View Aspect Ratio=2.5, Angle of Attack=5.0°, $Re_c=130000$	184
Figure 53. Tip Flow Visualizations, Endcap View Aspect Ratio=2.5, Angle of Attack=5.0°, $Re_c=130000$	185
Figure 53. Tip Flow Visualizations, Suction Surface View Aspect Ratio=2.5, Angle of Attack=5.0°, $Re_c=130000$	186
Figure 54. Tip Flow Visualizations, Endcap View Aspect Ratio=2.5, Angle of Attack=5.0°, $Re_c=260000$	187
Figure 54. Tip Flow Visualizations, Endcap View Aspect Ratio=2.5, Angle of Attack=5.0°, $Re_c=260000$	188
Figure 54. Tip Flow Visualizations, Suction Surface View Aspect Ratio=2.5, Angle of Attack=5.0°, $Re_c=260000$	189
Figure 54. Tip Flow Visualizations, Suction Surface View Aspect Ratio=2.5, Angle of Attack=5.0°, $Re_c=260000$	190
Figure 55. Tip Flow Visualizations, Endcap View Aspect Ratio=2.5, Angle of Attack=5.0°, $Re_c=335000$	191
Figure 55. Tip Flow Visualizations, Endcap View	

Aspect Ratio=2.5, Angle of Attack=5.0°, Re_c =335000	192
Figure 56. Tip Flow Visualizations, Endcap View Aspect Ratio=2.5, Angle of Attack=7.5°, Re_c =130000	193
Figure 56. Tip Flow Visualizations, Endcap View Aspect Ratio=2.5, Angle of Attack=7.5°, Re_c =130000	194
Figure 56. Tip Flow Visualizations, Suction Surface View Aspect Ratio=2.5, Angle of Attack=7.5°, Re_c =130000	195
Figure 57. Tip Flow Visualizations, Endcap View Aspect Ratio=2.5, Angle of Attack=7.5°, Re_c =260000	196
Figure 57. Tip Flow Visualizations, Endcap View Aspect Ratio=2.5, Angle of Attack=7.5°, Re_c =260000	197
Figure 58. Tip Flow Visualizations, Endcap View Aspect Ratio=2.5, Angle of Attack=7.5°, Re_c =335000	198
Figure 58. Tip Flow Visualizations, Endcap View Aspect Ratio=2.5, Angle of Attack=7.5°, Re_c =335000	199
Figure 59. Co-Rotating Vortices Aspect Ratio=3.0, Angle of Attack=5.0°, Re_c =130000	200
Figure 60. Diminishing Trailing Vortex Core Spiral Path Aspect Ratio=3.0, Angle of Attack=5.0°, Re_c =130000	201
Figure 61. Co-Rotating Ideal Point Vortices in a Uniform Freestream	202
Figure 62. Model of Co-Rotating Non-Ideal Vortices	203
Figure 63. Ratio of Primary to Secondary Vortex Strengths as a Function of Angle of Attack	204
Figure 64. Ratio of Primary to Secondary Vortex Strengths as a Function of Chord Reynolds Number	205
Figure 65. Normalized Primary Vortex Strength as a Function of Angle of Attack	206
Figure 66. Normalized Secondary Vortex Strength as a Function of Angle of	

Attack	207
Figure 67. Normalized Primary Vortex Strength as a Function of Chord Reynolds Number	208
Figure 68. Normalized Secondary Vortex Strength as a Function of Chord Reynolds Number	209
Figure 69. Data of Devenport, et.al. ³⁷ Showing Development of Inner and Outer Core Regions and a Simplistic Model of the Inner Region as a Batchelor ⁵ q-vortex	210
Figure 70. Separation of the Primary and Secondary Tip Vortices as a Function of Angle of Attack	211

Figure 71. Separation of the Primary and Secondary Tip Vortices as a Function of Chord Reynolds Number	212
Figure 72. Test Section Wall Proximity Effects	213
Figure 73. Height of the Primary Vortex Core above the Suction Surface at the Wing Trailing Edge as a Function of Angle of Attack	214
Figure 74. Height of the Primary Vortex Core above the Suction Surface at the Wing Trailing Edge as a Function of Chord Reynolds Number	215
Figure 75. Spanwise Movement of the Primary Vortex Core Relative to the Endcap at the Wing Trailing Edge as a Function of Angle of Attack	216
Figure 76. Spanwise Movement of the Primary Vortex Core Relative to the Endcap at the Wing Trailing Edge as a Function of Chord Reynolds Number	217
Figure 77. Quad-Hot-Wire Probe Configuration, as Used by Devenport, et.al ^{10,37}	218
Figure 78. Quad-Hot-Wire Probe 1/8" below the Vortex Core Centerline X/C=10, $Re_c=130000$, Exposure Time=1/15 second	219
Figure 79. Quad-Hot-Wire Probe Centered in the Vortex Core X/C=10, $Re_c=130000$, Exposure Time=1/15 second	220
Figure 80. Quad-Hot-Wire Probe Centered in the Vortex Core, Viewed from below and behind the Probe. Flow is from the bottom of the Photograph to the Top. X/C=10, $Re_c=130000$, Exposure Time=1/15 second	221
Figure 81. Quad-Hot-Wire Probe Traversing Through the Vortex Core X/C=10, $Re_c=130000$, Exposure Time=4 seconds	222
Figure 82. PIV Analysis	223
Figure 83. PIV Analysis of Figure 44a	224
Figure 84. PIV Analysis of Figure 47a	225
Figure 85. PIV Analysis of Figure 53a	226

Figure 86. Quad-Hot-Wire Probe Holder	227
Figure 87. Location of Vortex with Respect to Test Section Walls Single Sensor Hot-Wire Measurements of u^2 / U_{ref}^2 X/C=12, Aspect Ratio=3.0, Angle of Attack=5.0°, $Re_c=330000$	228
Figure 88. Contours of U/U_{ref} in Trailing Vortex Single Sensor Hot-Wire Measurements X/C=12, Aspect Ratio=3.0, Angle of Attack=5.0°, $Re_c=330000$	229
Figure 89. Contours of u^2 / U_{ref}^2 in Trailing Vortex Single Sensor Hot-Wire Measurements X/C=12, Aspect Ratio=3.0, Angle of Attack=5.0°, $Re_c=330000$	230
Figure 90. Contours of U/U_{ref} Showing no Evidence of an Organized Vortex Single Sensor Hot-Wire Measurements X/C=25, Aspect Ratio=3.0, Angle of Attack=5.0°, $Re_c=330000$	231
Figure 91. Contours of u^2 / U_{ref}^2 Showing no Evidence of an Organized Vortex. Single Sensor Hot-Wire Measurements X/C=25, Aspect Ratio=3.0, Angle of Attack=5.0°, $Re_c=330000$	232
Figure 92. Contours of U/U_{ref} Showing a Well Organized Trailing Vortex Quad-Hot-Wire Measurements X/C=10, Aspect Ratio=2.5, Angle of Attack=5.0°, $Re_c=330000$	233
Figure 93. Color Contours of U/U_{ref} Showing Strong Axial Velocity Deficit at the Core Center. Quad-Hot-Wire Measurements X/C=10, Aspect Ratio=2.5, Angle of Attack=5.0°, $Re_c=330000$	234
Figure 94. Contours of u^2 / U_{ref}^2 Showing a Well Organized Trailing Vortex Quad-Hot-Wire Measurements X/C=10, Aspect Ratio=2.5, Angle of Attack=5.0°, $Re_c=330000$	235
Figure 95. Contours of Turbulent Kinetic Energy (TKE) X/C=10, Aspect Ratio=2.5, Angle of Attack=5.0°, $Re_c=330000$	236
Figure 96. Contours of $\sqrt{(vw^2 + uw^2)}$ X/C=10, Aspect Ratio=2.5, Angle of Attack=5.0°, $Re_c=330000$	237

Figure 97. Contours of $(v^2 + w^2)$ X/C=10, Aspect Ratio=2.5, Angle of Attack=5.0°, $Re_c=330000$	238
Figure 98. A Typical Curve Fit to the Data X/C=10, Aspect Ratio=2.5, Angle of Attack=5.0°, $Re_c=330000$	239
Figure 99. Curve Fits to Measured Data and Data Corrected for Wandering. Tangential Velocity. X/C=10, Aspect Ratio=2.5, Angle of Attack=5.0°, $Re_c=330000$	240
Figure 100. Curve Fits to Measured Data and Data Corrected for Wandering. Axial Velocity. X/C=10, Aspect Ratio=2.5, Angle of Attack=5.0°, $Re_c=330000$	241
Figure 101. Maximum Tangential Velocity as a Function of Angle of Attack for the Current Data Set and that of Devenport, et.al. ³⁷ X/C=10, Aspect Ratio=2.5, Angle of Attack=5.0°, $Re_c=330000$	242
Figure 102. Core Radius as a Function of Angle of Attack for the Current Data Set and that of Devenport, et.al. ³⁷ X/C=10, Aspect Ratio=2.5, Angle of Attack=5.0°, $Re_c=330000$	243
Figure 103. Normalized Core Circulation as a Function of Angle of Attack for the Current Data Set and that of Devenport, et.al. ³⁷ X/C=10, Aspect Ratio=2.5, Angle of Attack=5.0°, $Re_c=330000$	244
Figure 104. $\frac{\omega_x C}{U_{ref}}$ Profiles X/C=10, Aspect Ratio=2.5, Angle of Attack=5.0°, $Re_c=330000$	245
Figure 105. $\frac{\omega_{xm} C}{U_{ref}}$ as a Function of Angle of Attack X/C=10, Aspect Ratio=2.5, Angle of Attack=5.0°, $Re_c=330000$	246
Figure 106. A Possible Model for the Cause of the Differentiated Core Regions	247
Figure 107. A Typical Toepler Schlieren System	248
Figure 108. A Toepler Schlieren Knife Edge	249
Figure 109. A Focusing Schlieren System	250

Figure 110. Geometric Image Separation at the Image Plane	251
Figure 111. Definitions of Depth of Focus	252
Figure 112. The Laser Table with Adjustable Beam Height	253
Figure 113. The Initial Focusing Schlieren Optical Layout	254
Figure 114. The Second Focusing Schlieren Optical Layout	255
Figure 115. Heater Element in the Optical Path of a Focusing Schlieren System	256
Figure 116. The Toepler Schlieren Optical Layout	257

List of Symbols

A, B, n	empirical constants in King's law
C	wing chord
d_m	radial scale of the axial velocity profile
e	correlation coefficient for wandering corrections
E	mean voltage output from hot-wire
E_c, E_m	unlinearized corrected and measured hot-wire voltages
G_{uu}	power spectrum for streamwise velocity fluctuations
H_{te}	vertical displacement of the primary vortex core above the suction side surface
r_{1m}	core radius
Re_c	Reynolds number based on chordlength
Re_D	Reynolds number based on diameter
Re_x	Reynolds number based on length
S_{te}	spanwise displacement of the primary vortex core from the endcap towards the wing root at the trailing edge
T_c, T_m	measured and corrected temperatures
u'^2, v'^2, w'^2	turbulence normal stresses in the x,y,z directions
uv, vw, uw	Reynolds shear stresses in the x,y,z coordinate system
U, V, W	mean velocity components in the x,y,z directions
U_{dm}	centerline axial velocity relative to the freestream

U_{ref}	reference velocity
X	streamwise direction
Y	vertical direction
Z	spanwise direction
v_θ	angular velocity in the r, θ, z coordinate system
$V_{\theta m}$	measured angular velocity in the r, θ, z coordinate system
$V_{\theta 1m}$	measured peak tangential velocity

Greek Symbols

δ	uncertainties
δ^*	boundary layer displacement thickness
γ	overheat ratio
Γ_1	core circulation
λ	pitch of the primary vortex core spiral path
ω_x	axial vorticity
σ_y, σ_z	r.m.s. wandering amplitudes in the y and z directions
θ	angular direction about the x -axis

1. Genesis

1.1. Introduction

All lifting surfaces generate trailing vortices due to the inherent roll-up of shed vorticity¹. The trailing vortices behind aircraft wings and behind lifting surfaces on submarines are particular examples where such phenomenon are important.

Trailing vortices are long-lived. Such longevity can be a problem for following aircraft on which the vortex can cause control failures and possibly flip the aircraft. Because of such inherent dangers, aircraft are required to land at particular intervals at airports, intervals which reduce the number of possible landings in a day with subsequent loss of revenues. The longevity is also a problem for submarines: as the vortices rise to the surface, the submarine's path becomes apparent to others.

Trailing vortices also generate drag. The drag on aircraft limits their range and payload, with subsequent financial impact. Similarly, the drag on submarines caused by the vortices may hinder the range and speed of such craft. The possible noise production of trailing vortices is also of great importance in submarine applications where stealthiness is critical.

Accurate modeling of trailing vortices could allow improvements in all of these problematic areas. However, not much is known about the fluid dynamics of trailing

vortices; and consequently improvement in designs due to accurate computer modeling of these phenomenon has been hampered to date.

1.2.1. General Structure of Trailing Vortices

As fluid sweeps around a lift producing wing, chordwise and spanwise pressure gradients form. The chordwise pressure gradients serve to slow the fluid on the pressure side surface and accelerate the fluid on the suction side surface, thus giving rise to the lift. The spanwise pressure gradients develop out of the necessity to equalize the pressure at the wing tip. As the pressure gradients force fluid around the wingtip endcap, shear layers develop. Out of these shear layers may develop coherent vortical structures. Consisting of a primary vortex and one or more secondary vortices, the system of vortices in the region of a wing-tip coalesces into a single trailing vortex. The trailing vortex evolves, becoming fully developed some distance downstream (Figure 1).

Many models have been proposed for the mean structure of trailing vortices (Moore and Saffman⁶, Phillips⁷, Owen⁸, Saffman²⁵) for both laminar and turbulent vortices. All of the models have as the core of the vortex a viscous region exhibiting solid body rotation such that as $r \rightarrow 0$,

$$v_r = 0$$
$$v_\theta \propto r$$

Disagreement exists as to the nature of the surrounding regions: the degree to which the regions immediately surrounding the core and further out to the wake exhibit a turbulent or inviscid nature differentiates the models.

Recent experimental work has brought into question the nature of the vortex core. Bandyopadhyay, et.al.²² studied a low Reynolds number vortex flow ($15 \times 10^3 < Re_\Gamma < 25 \times 10^3$) produced by a split-wing configuration joined on a flow aligned body (Figure 2). The airfoil sections were NACA 0012. The measurements were conducted using 7-hole yaw probes, single and cross hot-wires, and smoke flow visualization. The measurements indicated a periodic relaminarizing of the vortex core, associated with puffs of smoke being thrown out of the core. However, the applicability of their results to an isolated wingtip trailing vortex is questionable, as the complex 3-dimensional flowfield about split-wing/body configuration employed is certainly different from the 3-dimensional flowfield about an isolated wingtip. The issue of vortex wandering was not addressed by Bandyopadhyay, et.al., and significant wandering could result in an unsteady signal similar to the evidence suggesting a relaminarizing signal.

Devenport, et.al.^{10,37} have investigated the trailing vortex downstream of a NACA 0012 half-wing at $Re_c \leq 530000$ (Figure 3). They employed 4-sensor quad-hot-wires to investigate the turbulence structure of a trailing vortex up to 30 chordlengths downstream. The researchers address vortex wandering explicitly, developing theoretical models to subtract the results of wandering from their data and then employing the models to do so. Devenport, et.al.¹⁰ report the vortex core exhibits a laminar nature. Any apparent

turbulence in the core is attributed to buffeting of the core by surrounding turbulent wake structures.

Sarpkaya¹⁸ has studied the interactions of vortices with a free-surface at chord Reynolds numbers up to 400000. His flow visualizations show the core throwing off vortex sheets and being replenished by freestream fluid (Figure 4). Because the study necessarily involved a vortex in close proximity to a free-surface, the applicability of his results to a wingtip trailing vortex far from any boundaries is uncertain. Proximity to a boundary is certain to affect the growth of a vortex, necessarily concentrating vorticity between the core and the surface differently than would be found far from any boundaries.

Sarpkaya²⁴ has also studied vortex core breakdowns. The vortical flow was of low Reynolds number ($Re_D < 10000$). He reported tentacles of vorticity peeling off of the vortex core. The apparatus (Figure 5) was an intrinsically internal flow device with the vortical flow generated by 32 streamlined foils. Certainly the close boundaries to the large vortical flow influenced the development of the flow. Whether these results can be applied to a trailing vortex generated by a single airfoil far from any boundaries is again not clear.

Clear and concise flow visualization of the wingtip trailing vortex showing the interaction of spiral wake structures and the vortex core has apparently not been done to date. Such visualization of this general flow would define convincingly the role wake structures play in the instantaneous structure of a trailing vortex. Such would also suggest

the role that the wake structures serve in the development of a trailing vortex core. Clear flow visualization of the wingtip trailing vortex core is needed.

1.2.2 Tip Vortex Formation

Wing-tip trailing vortices form when the pressure side fluid rolls around the airfoil tip towards the suction side fluid. The roll-up around the tip of a low aspect ratio wing is a complex process; and the flowfield in the vicinity of the tip may consist of the primary vortex, one or more secondary vortices, and various shear layer structures (Figures 6 and 7)^{26-34, 38, 42}.

Many researchers have investigated the near tip regions of a variety of airfoils and hydrofoils. Francis and Kennedy²⁸ studied a NACA 64009 hydrofoil. The researchers employed helium bubble flow visualization in the near tip region. Francis and Katz²⁷ and Katz and Bueno Galdo²⁹ studied the near tip flowfield of a NACA-66 hydrofoil for chord Reynolds numbers from $.9 \times 10^5$ to 9.5×10^5 . They employed laser light sheet illumination of the dye injected flow about the blunt tipped hydrofoil. Katz and Bueno Galdo²⁹ also employed surface pressure measurements. Hoffmann and Velkoff²⁶ studied the wingtip flowfield of a blunt tipped helicopter rotor. The tip Reynolds number was 8×10^5 . The flow visualization employed was diazonium salt reacting with ammonia vapor. Chow, et.al.^{31,32,38} studied the flowfield about a NACA 0012 half-wing, aspect ratio of .75, with a rounded tip. The chord Reynolds number of their study was 4.6×10^6 . Chigier and

Corsiglia³³ studied the wingtip flowfield about a blunt tipped NACA 0015 airfoil, half aspect ratio 5.33. The chord Reynolds number of the flow was 9.53×10^5 . Spivey³⁴ studied a helicopter rotor tip flowfield at tip Reynolds numbers from 2.4×10^6 to 5.6×10^6 . Measurements were made using balances and wake pressure wakes. Surface pressure measurements on a blunt tipped model were taken. Stinebring, et.al.⁴¹ studied a hydrofoil, aspect ratio 1.28, at tip chord Reynolds numbers of 8.5×10^5 . Surface oil flow visualization, air bubble ejection, and cavitation flow visualizations were conducted. Laser velocimeter measurements were also taken. Winkelmann⁴² studied the wingtip flowfield of a NACA 0012 half-wing. Two different aspect ratio models were used, a large 137.2 cm model, with an aspect ratio of .26, and a smaller model, aspect ratio 3. Both models had blunt tips. Oil flow and smoke flow visualizations were conducted. Fluorescent oil flow tests were conducted with the larger model at chord Reynolds numbers from 1.1×10^6 to 3.32×10^6 . The smaller model was oil flow tested at 1.1×10^6 . Smoke flow tests were conducted at much slower speeds, maximum freestream velocity up to 11 m/s.

The primary vortex forms on the suction side of the airfoil tip for blunt and rounded tip configurations^{26-29,31-34,38,41,42}. Hoffman and Velkoff²⁶ report the point of vortex inception varied from .3C to .7C, where C is the chordlength, for their blunt tipped helicopter rotor, decreasing with increasing angle of attack. The primary vortex then tends to migrate towards the wing root as it progresses down the chord^{27-29, 33}, shifting more with increasing angle of attack and decreasing Reynolds number. The universality of primary vortex spanwise migration is questionable. Chow, et.al.^{31,32}, studying the flow around a

low aspect ratio, high chord Reynolds number NACA 0012, report no evidence of any tendency of the primary vortex to migrate towards the wing root.

The primary vortex increases in size²⁷ and lifts further from the airfoil surface^{27,29,31,32} as it progresses along the chord. Chordwise growth rate increases with increasing angle of attack and decreasing Reynolds number²⁷. Continued entrainment of vorticity by the primary vortex occurs along the airfoil chordlength^{26,29}.

Secondary vortical structures develop on the endcap^{27,28,31,32,34,42} for both blunt^{27,28,34,42} and rounded^{31,32} wingtips. The secondary vortex appears as early as .05C, where C is the model chordlength, on the blunt tipped NACA 64009 hydrofoil studied by Francis and Kennedy²⁸. Chigier and Corsiglia³³, Winkelmann⁴², and Spivey³⁴ studied blunt tipped planforms; and all of the researchers reported evidence of a secondary structure developing on the suction side surface. Arndt, et.al.³⁰ studied a vortex generated by a NACA 66-445 hydrofoil. The base chord length Reynolds numbers varied from 3×10^5 to 11.5×10^5 . The elliptical planform hydrofoil had an aspect ratio 3. They also report evidence of a secondary vortex on the suction surface of the hydrofoil.

The secondary endcap vortex can be relatively large. Francis and Katz²⁷ report the vortex is “larger than the main tip vortex at upstream regions and low incidence angles.” Migration of the endcap secondary vortex occurs at a location dependent upon angle of attack²⁸.

Francis and Katz²⁷ and Spivey³⁴ report secondary vortices counter-rotating with the primary vortex. Chow, et.al.^{31,32,38} report a co-rotating tertiary vortex on the endcap.

Chigier and Corsiglia³³ report a counter-rotating secondary vortex on the suction side surface. The differences in flow characteristics strongly indicates that the tip region flow structure is highly planform dependent.

The primary and secondary vortices are not isolated flow structures. The secondary vortex wraps around the primary vortex as they proceed along the airfoil chordlength^{27,29,30}. The primary vortex has been seen to kink as it leaves the trailing edge of the airfoil^{23,41,42}, the effect conjectured to be due to the interaction of the primary and secondary structures⁴². Measured asymmetrical axial velocity profiles are speculated to be due to the entrainment of the secondary vortex by the primary vortex³⁰. Clear visualization of the kinking would illuminate the role the secondary vortex plays in the process of primary vortex kinking, though such has apparently yet to be successfully done.

At first glance, differences appear to exist in the results reported for axial velocity measurements in the primary tip vortex. Core centerline axial velocity surpluses from as high as $1.77U_{\infty}$ ^{31,32,38} down to $1.4 U_{\infty}$ ³³ have been reported. Evidence indicates that these excesses increase linearly with increasing angle of attack⁴⁷. However, axial velocity deficits of as much as 40% U_{∞} on the core centerline have been reported and also stated to vary linearly with angle of attack⁴⁰. Thompson³⁹ concludes that the tip shape is “particularly important,” and comparison of results from different studies with different planforms and airfoil shapes is, at the very least, difficult.

The nature of the tip region vortical structures appears to be dependent upon Reynolds number and angle of attack. Researchers have found that changes in angle of attack affect

the size and displacement of the tip flow structures more than variations in Reynolds number^{27,28}. But working with a NACA 66-445 hydrofoil of elliptical planform, Arndt, et.al.³⁰ proclaim a “surprising non-dependence” of the tip vortex downstream trajectory on angle of attack or Reynolds number variations. The incongruity of results is attributable to differences in planforms³⁹.

The tip region flowfield is highly planform dependent. Little is known about how the tip flow details influence the resulting wing-tip trailing vortex form. To link the downstream form of the trailing vortex to the initial wingtip flowfield conditions, a comprehensive understanding of the near-tip flowfield is required.

1.2.3 Instantaneous Structure/Core Waves

Little is known about the instantaneous structure of trailing vortices. Analogies have been made to simplify calculation schemes in an attempt to shed light on this complex problem. Melander and Hussain¹⁹ conducted a direct numerical simulation of a very low Reynolds number, axisymmetric vortex flow of variable diameter. The vortex was embedded in homogeneous turbulence. The vortex generates into a laminar core vortex with spiral ring-like structures organized about it (Figure 8). The resulting organization of the small scales in the flow was comprised of three parts including alignment of the incoherent vorticity by the columnar vortex shearing, conglomeration by pairing and/or by transport, and a feedback/excitation of bending waves on the vortices¹⁹.

Numerical studies have been conducted on vortex core waves and instabilities.

Maxworthy²¹ describes three forms of solitary waves on vortex cores: varicose, helicoidal, and fluted waves, representing “a periodic swelling and contraction, a bending, and a ‘krinkling’ of the core, respectively.” Thus, the existence of core waves has been numerically established.

Experimental work has been aimed at proving the existence of such waves. Through the utilization of quantitative hot-wire measurements and qualitative smoke flow visualization, Bandyopadhyay, et.al.²² identified three core wavelengths associated with “shear-stress-rich low-momentum core fluid” ejection. Green and Acosta²³ have identified two wavelengths of disturbances corresponding to “fast” and “slow” disturbances (Figure 9).

Flow visualization has been conducted in an attempt to properly assess the processes occurring instantaneously in the core of a vortex. The exchange of momentum between the vortex core and the outer regions may lead to vortex core oscillation²⁴, with subsequent effects on the measured velocity components. The fluid material being thrown out of the vortex core region is contained in “tentacle-like” sheets of vorticity of finite extent, caused by helical instabilities²⁴. Sarpkaya²⁴ contends the instabilities require a turbulent momentum exchange between the core fluid and the surrounding regions.

The instantaneous processes occurring in the core region of a wing-tip trailing vortex are not well understood. The nature of any waves upon the vortex core, as well as the

interaction of the vortex core with surrounding spiral wake structures, needs to be examined. Clear flow visualization of the instantaneous core structure is needed.

1.3. Objectives

The objectives of the following work are seven-fold:

1. To set-up, improve, and calibrate a boundary layer type wind tunnel.
2. To evaluate the feasibility of studying trailing vortices in this facility.
3. To ensure that the turbulence results for the trailing vortex flow are similar to those obtained in a larger facility, i.e., the Stability Wind Tunnel, VA Tech, over a range of flow conditions.
4. To visualize the vortex core to reveal the process of core formation in the wing-tip region
5. To employ hot-wire anemometry techniques to examine the properties of the rolled-up vortex core.
6. To visualize the instantaneous core structure to reveal any instantaneous structures on or encircling the vortex core.
7. To systematically link the downstream structure of the trailing vortex to the initial, complex wing-tip flowfield.

2. Wind Tunnel Fabrication and Calibration

The 3'x2' subsonic wind tunnel (Figure 10) was originally designed by Dr. Pierce of the Department of Mechanical Engineering, Virginia Tech. Air enters the tunnel through a bellmouth, passes through a settling chamber and a contraction, passes into the test section and thence into a diffuser, ultimately being pulled through and exhausted by a blower.

The original wind tunnel design of Dr. Pierce required improvements. The flow conditioning included only three seamed nylon screens and a cardboard tube honeycomb. The honeycomb did not provide adequate flow angularity restriction, and three screens were insufficient to provide adequate flow quality. Thus, improvements in the tunnel design have centered around improving the flow conditioning.

2.1 Settling Chamber and Contraction

The settling chamber and contraction section have a super-structure of welded 2" angle iron supported on casters (Figures 11 and 12). The settling chamber is internally 3'3" long by 12 feet wide by 8 feet tall. It is constructed of 1/2" plywood bolted to the section's super-structure. The 16:1 contraction chamber is constructed of heavy gauge sheet steel bolted to the angle iron super-structure at the beginning and end of the contraction

chamber and is supported in the middle by hanging 1/4-20 all-thread rods attached to the section's super-structure.

The contraction section was placed in the laboratory such that the effects of wall proximity on the incoming flow would be minimized (Figure 13). Also, a bellmouth constructed of thin gauge rolled sheet steel (Figure 14) is attached to the outer periphery of the settling chamber. The bellmouth prevents separation of the flow entering the tunnel. The bellmouth sections on the two sidewalls and the top have the same shape, but proximity to the floor resulted in a truncated shape for the bottom section of the bell-mouth (Figure 11).

Flow conditioning elements included an aluminum honeycomb and a series of seamless and seamed screens placed inside the settling chamber (Figure 14). These are used to reduce free-stream turbulence and flow angularity. The first 5 screens are all supported on frames of 1/2" by 6" fir shelving boards, 12 feet inside width by 8 feet inside height. The honeycomb and the outermost protective screen are supported on frames made of 1/2" by 5" pine shelving boards of the same nominal dimensions as the other frames. The screens were placed in the settling chamber with the frames flush together, resulting in a nominal separation between successive screens of 6". The protective screen was placed in the settling chamber such that it is flush with the outside edge of the settling chamber walls, resulting in a mean separation of 5" between the screen and the honeycomb (Figure 14).

The seamless screen, purchased from TSI, Appleton, WI, was placed so that it would be the last screen encountered by the flow. Constructed of steel wire mesh, wire diameter

.010", the screen has a porosity ratio of 64% closed area/open area. The five seamed screens are constructed of standard nylon window screening of porosity ratio 31% closed area/open area. They were inserted in the flow conditioning section immediately behind the seamless screen.

The honeycomb is constructed of aluminum foil hexagonal honeycombs, measured material thickness .0007". It was purchased in three 8'x4'x3" sections from the Hexcel Corporation of Arlington, TX. The honeycomb rests inside the outermost seamed screen frame. The honeycomb was attached to the frame, and small diameter string was woven along two 2' sections of the honeycomb-to-honeycomb seams to prevent slipping of one section relative to another.

The size of the honeycombs was chosen so as to provide the best possible flow angularity improvements with the least possible blockage (Figure 15). The original honeycomb consisted of 2" diameter cardboard tubes 4" long, allowing maximum flow angularity of 26.6 degrees. The hexagonal aluminum honeycomb allows a maximum flow angularity of 4.95 degrees, with a closed area to open area ratio of only .54%.

Another seamed screen was made of standard aluminum window screen cloth. This screen was placed over the settling chamber entrance to prevent incidental damage to the honeycomb.

2.2 Test Section

The wind tunnel test section is 3 feet wide by 2 feet high by 20'11" long and is depicted in figures 16, 17, and 18. The test section is bolted to the contraction chamber exit and is supported on a super-structure of 2" angle iron frame bolted to 3" C-channel iron support legs that are firmly bolted to the floor. The test section is comprised of wood and Plexiglas. The wooden walls, ceiling, and floor are constructed of 3/4" plywood covered on the inside surface by a 1/4" thick hardboard. The Plexiglas sections are composed of 3/4" non-economy grade clear Plexiglas. The walls fit into grooves milled in the floor and ceiling panels, with the entire unit being compressed by bolts from above (Figure 19).

Access to the test section is provided by several means. There are two small access doors on the left side (looking downstream) of the tunnel test section, each measuring nominally 22" wide by 20.5" tall (Figure 17). Further access is provided by removable ceiling panels along the test section (Figure 18). Visual access to the front of the test section is provided by two 5" x 5" square Plexiglas viewports constructed from 1/4" clear Plexiglas mounted flush to the inside walls.

The tunnel test section was leveled in both spanwise and streamwise directions on vibration isolation rubber pads. The contraction chamber was aligned with the test section entrance and bolted to the test section super-structure. Maximum step size due to misalignment of the sections is approximately 3/16", along the floor seam.

The diffuser section was aligned with the test section exit but was not physically attached to the test section, thus isolating the test section from the mechanical vibration transmitted by the diffuser section from the blower section. The gap between the sections was filled with silicone rubber sealant. Maximum step size due to misalignment of the sections and diffuser section warpage is approximately 7/16".

Due to its operation as a "suckdown" tunnel, the static pressure inside the test section is lower than the ambient static pressure. As a consequence, any leaks around the seams of the tunnel result in thickening and possible separation of the wall boundary layers with a consequent degradation of flow quality. Leaks were detected by application of soapy water along the tunnel seams and were sealed with silicone sealant (Figure 20).

2.3 Diffuser

The diffuser has an expansion ratio of 1:1.6, connecting the rectangular test section exit to the circular fan entrance. It is constructed of sheet metal and angle iron and is 6'2" in length (Figure 21). The diffuser is bolted to the floor to prevent any movement due to vibration.

Inside the exit of the diffuser is a honeycomb constructed of 1.5" diameter cardboard tubes, 6" long, epoxied together. Designed to prevent upstream propagation of fan induced swirl, the honeycomb rests against a large grid screen that is intended to prevent passage of large objects into the fan.

2.4 Fan/Motor

The fan/motor section was constructed by Twin City Fan & Blower Co., Minneapolis, Minn. (Figure 21). It consists of a 12 flat bladed fan powered by a Lincoln Electric Company 480V, 30 hp. 3-phase AC motor operating at 1765 rpm. The section body is constructed of thick gauge sheet steel welded at the seams and welded to an angle iron super-structure. The section is bolted to the floor at all four corners to prevent movement due to vibration.

A 3-phase, 480V disconnect box and motor starter are mounted on the wall near the motor. Flow speed is continuously variable from near 0 to a top speed of 84.5 ft/sec by variation of blower exit vanes (Figure 21). Maximum flow speed can be increased to almost 30 m/s by removal of the vane box, though no flow speed control is then available.

2.5 Flow Characteristics

Measurements were made 23" from the test section entrance and 39" from the test section exit in the 3'x2' Subsonic Wind Tunnel to determine the flow quality.

Measurements were made using pitot-static probes and single hot-wire anemometry.

2.5.1 Pitot-Static Instrumentation

Pitot-static measurements were made using 4 mm diameter pitot-static probes purchased from Davis Instruments, inc. A reference pitot-static was mounted 3" downstream of the tunnel test section entrance, 6" from the left wall (looking downstream) and 6" from the ceiling (Figure 22). A second pitot-static, of the same design, was mounted 17'8" from the test section entrance, 5.5" from the ceiling and 10.25" from the right wall (looking downstream). Velocities were determined from these pitot-static probes using two Setra pressure transducers, one having a 0-5V output range and the other having an output range of +/- 2.5 V. Reference pressure measurements were made by connecting the pressure transducer output to an A/D board and a computer. Measurements from the second pitot-static were made by connecting its output to a Fluke 8050A digital multimeter.

2.5.2 Hot-Wire Instrumentation

Velocity measurements along the tunnel length and in the entrance and exit cross section planes were made using a single hot-wire anemometer. The anemometer consisted of a TSI model 1210T.5 probe connected to a Dantec 56C17 bridge and a Dantec 56C01 constant temperature unit.

The voltages output from the system were sent to a x10 buck-and-gain amplifier system built in-house with Burr-Brown integrated circuits, with a flat frequency response out to approximately 50 kHz (Zsoldos, 1991). Voltages were then passed to an Analogic 12 bit HSDAS-12 A/D converter with a voltage range of 0-5.0 V. This A/D converter is capable of sampling four simultaneous channels up to a maximum sampling frequency of 100 kHz, though only one channel was used for hot-wire data acquisition. One other channel acquired the freestream dynamic pressure from the reference pitot-static tube.

All of the digitized signals were processed by an IBM AT computer. Linearization and computation of the streamwise velocity fluctuations and mean velocities was accomplished by an 18-8 Laboratories PL2510 array processor. Data was ultimately stored on optical disk.

The single hot-wire was calibrated before and after each traverse in the freestream at a given calibration location. The output voltage from the hot-wire was related to the effective velocity by King's law,

$$E^2 = A + BU_{\text{eff}}^n$$

with $n=45$. The empirically determined constants A and B were determined via a least squares fit of 9 to 10 points for each calibration measurement. Velocity errors were required to be less than 1% for each point.

Though the laboratory is climate controlled, some temperature drift, typically $+\/- .5^\circ$ Fahrenheit, did occur during the measurements. Thus, the hot-wire results were temperature corrected following the method of Bearman (1970),

$$E_c = E_m \sqrt{\frac{\gamma - 1}{\gamma - T_m / T_c}}$$

with γ as the overheat ratio (1.7) and E and T the unlinearized voltage and temperature, subscripts (m) and (c) standing for measured and corrected, respectively.

2.5.3 Traversing Equipment

The 2 axis computer driven traverse from the Virginia Tech Stability Wind Tunnel facility was modified for use in the 3'x2' subsonic wind tunnel (Figure 23). To prevent lateral vibration of the traverse (which is provided by pinning the top and bottom during use in the Stability Tunnel), additional structural support was added to the traverse superstructure, thus allowing reliable stand-alone operation of the traverse. Also needed was a probe support extension from the traverse gantry down into the tunnel to allow traversing across the majority of the tunnel test section. The probe support consisted of two parallel pieces of flat steel, nominally separated by 3/8", bolted to both the gantry and the streamlined probe holder (Figure 24).

The hot-wire was offset laterally from the traverse streamlined probe holder stem by two 3/16" diameter rods approximately 1 3/4" long supporting the single hot-wire probe holder. The hot-wire was offset longitudinally from the streamlined probe holder by approximately 5 3/8" (Figure 25). Selection of the probe support design was based upon minimizing flow disruption, probe vibration, and required slot size. The probe holder was

designed to allow 90 degree rotation of the probe (Figure 25), thus facilitating near wall measurements. Traverse accuracy was estimated to be 0.001" in both horizontal and vertical positioning.

The longitudinal traverse is shown in Figure 26. The aerodynamic traverse is designed to be longitudinally mobile while remaining laterally stable. The device is moved by first loosening on the outside of the tunnel the fishing line attached to the front of the traverse and then pulling on the trailing edge tape measure while maintaining tension on the fishing line. Relative displacement of the traverse is determined by the tape measure. The longitudinal traverse accuracy was estimated to be +/- 1/16", owing to tensile stretching of the fishing line and the tape measure.

2.5.4 Coordinate System and Measurement Locations

The right-hand coordinate system in Figure 22 is used. X is defined positive in the streamwise direction from the test section entrance; Y is measured vertically upwards from the bottom right corner of the test section at that location (looking downstream); and Z is measured horizontally from the bottom right corner (looking downstream).

Measurements were made in Y-Z planes at the test section entrance and exit and in a streamwise traverse along the tunnel centerline (Figure 22). The entrance measurements were made at $X=23"$. The exit measurements were made at $X=212", 39"$ from the test section exit.

Uncertainties associated with hot-wire measurements and Reynolds number are

$$\begin{aligned}\delta \left(\frac{\bar{U}}{U_{ref}} \right) &\equiv 0.01 \\ \delta \left(\frac{u^2}{U_{ref}^2} \right) &\equiv 1.8 \times 10^{-6} \\ \delta (Re_c) &\equiv 1460\end{aligned}$$

These uncertainties were calculated based upon 95% confidence limits and using the most pessimistic estimates of uncertainties in the primary measurements.

2.5.5 Longitudinal Tunnel Traverse

A streamwise mean velocity profile in the potential core along the tunnel centerline is presented in Figure 27. The measurements were made at a freestream velocity, U_{ref} , based upon the entrance location reference pitot-static, of 27.5 m/s, resulting in a Reynolds number per meter of approximately 1.6×10^6 .

The acceleration shown is primarily due to the growth of boundary layers within the test section. The results are consistent with power-law calculations for a zero-pressure gradient flat plate boundary layer. That is, assuming for the boundary layer displacement thickness on all four walls of the test section the relationship

$$\delta^* = 0.046 x Re_x^{-1/5},$$

and assuming an initially negligible boundary layer thickness at the test section entrance, the acceleration of the flow along the test section should be approximately 6.15%.

Measurements from the reference pitot-static probe and a similar probe located near the X=212" location indicate a 6.2% increase of potential core velocity, consistent with the power law calculations and the longitudinal single-hot-wire measurement indications of an increase of approximately 6.0%. This is further confirmation that all leaks have been eliminated from the tunnel test section.

Measurements were made over 100 blocks of 1000 samples at a sampling frequency of 30,000 Hz. Thus the time averaged results, averaged over the measurement interval of approximately 25 seconds, represent the true time-averaged mean-square velocity fluctuations. The block averaged results are averages of the statistics computed over each of the 1/30th second blocks and are, thus, high-pass filtered results. Electrical noise has been subtracted from the measurements. Figure 28 shows streamwise mean-square velocity fluctuation variations measured from the longitudinal traverse, including the block averaged and time averaged results.

A large proportion of the mean-square velocity fluctuation is due to low-frequency unsteadiness. This can be seen as the decreased levels of mean-square velocity fluctuations of the block averaged results, where low-frequency unsteadiness is not taken into account. The unsteadiness may be partly fan induced. Air currents in the laboratory may also contribute to the unsteadiness.

The power spectrum for streamwise velocity fluctuations, G_{uu} , was measured at three tunnel streamwise locations: at $X=0''$ (the inlet to the test section), $X=114''$, and $X=216''$. The results are plotted as G_{uu}/U_{ref}^2 vs. fC/U_{ref} , where f is the frequency in Hz, in Figures 29,30, and 31, respectively. Figures 30 and 31 are practically identical, showing clearly that no large differences in the flow turbulence and unsteadiness structure exist between those two stations. However, Figure 29 shows levels of G_{uu} at low frequencies that are about 27% higher than downstream.

The scatter in the results presented in Figure 28 may be due in part to the vibration of the probe holder. While not quantified, the vibration was seen to be of low-frequency and intermittent in nature, with a magnitude of less than 6mm. The large spike in the spectrum exists at all locations. The spike may be due to electrical noise.

2.5.6 Entrance and Exit Locations

Data was taken in grids at both entrance and exit locations. Figures 32 and 33 show the variations of the mean velocity across the entrance and exit planes, respectively. The mean flow is largely uniform in the test section freestream at both the entrance and exit locations (Figures 32 and 33). The mean flow variation across the potential core at both the entrance and exit test section locations is .4%.

Defining the edge of the boundary layers to be at $U/U_{ref}=.99$, the boundary layer thicknesses on all surfaces at the exit location are approximately $3\frac{1}{2}''$ to $4''$, in

agreement with the longitudinal measurements and calculations previously discussed. However, in Figure 32, the entrance location floor boundary layer is approximately 1.8" thick, in contrast to the boundary layers on all of the other walls which are all on the order of 1.0". In an attempt to explain this thick initial boundary layer, small tufts of string were applied along the floor centerline from the beginning of the test section 25" to the entrance test location and in a series across the span of the test section entrance to test for possible flow separation. No signs of flow separation were found. A large area of silicon sealant along the bottom of the contraction section and test section seam, which was not present on the sidewalls or the ceiling, may have tripped and thickened the boundary layer. Or this thick initial boundary layer may be a remnant of the settling chamber flow or may be an artifact of the asymmetric bellmouth. The exact cause of the structure has not been positively determined.

Several other regions of flow disturbances are visible in the figures. The somewhat circular region in the upper left of Figure 32 is the wake of the reference pitot-static probe. Another peculiarity of the test section flow is visible on the sidewalls as an acceleration of fluid in those areas (Figures 32 and 33). These may be due to probe blockage near the walls. The waviness apparent in the contours figures near the walls is due to the interpolation scheme used by the graphics software and does not represent any significant physical feature of the flow.

Contours of u'^2/U_{ref}^2 are shown in Figures 34, 35, 36, and 37 for block averaged and time averaged results at the entrance and exit test locations, respectively. Electrical noise

was subtracted from the results. The same definitions for block averaged and time averaged results, described in conjunction with the centerline traverse, apply.

The flow is strongly uniform across the potential core, with a turbulence level of approximately .2% to .3% for both the block averaged and time averaged data. The plots show again the strong influence of low-frequency unsteadiness on the flow quality. Careful visual observation determined that probe vibration was negligible. Thus, most of the unsteadiness seems to be due to a combination of unsteadiness induced by fan blade passage and laboratory air currents and motions.

Low-frequency disturbances can be seen in the regions of the two sidewalls in both the entrance and exit surveys (Figures 35 and 37). These appear to be associated with the aforementioned accelerations visible in the mean flow (Figures 32 and 33), conjectured to be due to probe interference.

3. Trailing Vortex Visualization

Two means of vortex core flow visualization were attempted. The first, which involved heating the core and using schlieren visualization, met with limited success and is described in Appendix 2. The second method involved visualizing the flow in the tip region of a rectangular wing using laser light illumination of helium-filled soap bubbles. This method and its results are described here. A secondary vortex on the outermost extremity of the wingtip was observed. The effects of varying aspect ratio, angle of attack, and chord Reynolds number upon the relative strengths of the primary and secondary vortices were investigated, along with the associated effects upon the path of the primary vortex, and the chordwise development of the primary and secondary vortices.

3.1 Apparatus

A rectangular, unswept NACA 0012 half-wing with a chordlength, C , of 8 inches was used. The wing was mounted horizontally in the 3' x 2' subsonic wind tunnel test section described in Chapter 2 with its quarter chord location was 110 inches downstream of the test section entrance.

The wing mount (Figure 38) allowed the wing to pivot to angle of attack about its quarter chord location. Zero angle of attack was determined by sighting the wing trailing edge from downstream with a leveled cathetometer set to the height of the wing's quarter

chord: when equal amounts of the wing were above and below the cross hairs of the cathetometer, the wing was assumed to be at zero angle of attack. Other angles of attack were measured relative to this position with an electronic inclinometer.

The wing boundary layer was tripped using .5 mm diameter glass beads glued to the model surface between 20% and 40% chord locations. The average bead density was approximately 200 beads/cm². The trip fixes the location of transition of the boundary layer from laminar to turbulent.

The right-handed coordinate system employed for this study (Figure 39) has its origin at the wingtip 1/4-chord. X is measured downstream; and Y is positive up, with positive Z following the right handed rule (Figure 39).

Helium-filled soap bubbles were produced by a Sage Action, inc. Model 5 helium bubble generator. The generator required helium, compressed air, and Sage Action bubble solution. Adjustment of the generator controls affects the rate of production of bubbles and their nominal sizes. The generator was adjusted to produce bubbles of approximately 1 to 2 mm diameter. The helium-filled soap bubbles leave the bubble generator through 12.7 mm diameter plastic tubing connected to a streamlined bubble injector. The bubble probe was placed at a spanwise location to optimize the number of bubbles encircling the wingtip. This placement was typically directly upstream of the wingtip. The injector was a 3/4" wide streamlined hollow tube (Figure 40). The lighter than air bubbles centrifuged into the low pressure vortex cores, showing distinctly the locations of any vortices present in the flow. In neither this study nor former, similar studies (Zsoldos⁴⁸) were there any

visible bubble probe interferences. For the present study, a variety of spanwise and vertical placements of the probe were tested. Though the capability of the flow visualization scheme to identify the vortical structures changed, the paths and the overall structure of the tip flow did not change.

The light source used to illuminate the light stream was an Oxford Lasers model ACL 45 pulsed copper vapor laser operating at 45 Watts. The laser operated at a nominal pulse frequency of 6.05 kHz. The 40 mm diameter beam was expanded through a 1000 mm focal length achromatic lens. The expanded beam was redirected along the length of the tunnel by a flat mirror 15 chordlengths downstream of the model (Figure 40). Because the 2"x3.5" flat mirror was considerably smaller than the beam at that point, the excess beam was stopped on the outside of the tunnel (Figure 40). The angle of projection of the laser light was varied to provide a light sheet tangential to the wingtip endcap and top surfaces, though double reflection from the front and back surfaces of the mirror reduced the effectiveness of this light sheet alignment procedure.

Still and motion pictures were taken of the flowfield from $X/C=0$ to $X/C=10$. Still photographs were taken over a range of exposure times, from 30 seconds to .001 seconds, with a Nikon N6006 camera utilizing Kodak Gold ASA 1000 film. Motion pictures were taken with a handheld JVC GRAX-7 video camera with a 30 Hz framing rate. Photographs were taken through the sidewall Plexiglas panels and through a small Plexiglas window installed in the roof of the test section near the wingtip. The procedure allowed for a perpendicular view of the wing suction side from the top of the tunnel for all

of the aspect ratio of 3 cases and for near perpendicular viewing for aspect ratio 2.5 cases. End views of the wingtip were possible for all conditions. Viewing of the vortex core from beneath the tunnel at $X/C=10$ was possible.

3.2 Results

The NACA 0012 half-wing model was installed in the wind tunnel at half-aspect ratios of 2.5 and 3.0. At each aspect ratio, the Reynolds number and the angle of attack of the wing were varied. The angles of attack were 2.5° , 5.0° , and 7.5° about the quarter chord. The tunnel speed was varied to provide Reynolds numbers of 130000, 260000, and 335000, based on the chordlength of 8 inches.

The results of this study are depicted in Figures 41 through 58. The figures are grouped according to conditions, with the views of the endcap and suction side being presented conjointly. The endcap views are lettered (a) through (d) with the suction side surface views following for each figure. Suction side views are presented only where the results are illuminating. In all of the photographs, the flow is from left to right.

A variety of exposure times is presented in the results, ranging from as much as 15 seconds to as little as 1/125 second. In the longer exposure photographs, the bubble paths appear as streaks; but as the exposure time is reduced, the bubble paths appear more as a string of bubble images. The spacing between successive bubble images is directly proportional to the velocity of the flow, which may be calculated using the pulse frequency

of the laser. This led to attempts to analyze the flow via particle image velocimetry techniques, the results of which will be discussed later.

The bubble paths represent particle paths coincident with streamlines where the flow is steady. The lighter than air bubbles tend to centrifuge to the vortex core centers which therefore appear as bright streaks in the photographs.

In the following discussion, the term endcap stands for the outermost surface of the blunt ended wingtip. The terms pressure side and suction side stand for the bottom surface and the top surface of the wingtip, respectively.

3.2.1 Discussion

Figures 47 a-h show the results for the aspect ratio 3, angle of attack 7.5° , and chord Reynolds number 130000 case. There is a strong upwash of low-momentum fluid, as indicated by the decreased bubble spacing of that fluid with respect to the bubble spacing of the freestream fluid, from the pressure-side of the airfoil to the suction side around the endcap. The angle the upwash makes with the horizontal appears to increase with increasing distance along the chord. An apparently strong spanwise pressure gradient exists near the leading edge of the wingtip which pushes fluid outboard of the endcap. The outboard fluid curves back to a nominally streamwise direction near $X/C=2$. The fluid then commences to curve back over the suction side surface. The strong flow curvature suggests a high-shear environment in the near tip regions.

The flow appears steady away from the surfaces of the model. The flow appears unsteady or turbulent near the surface of the endcap ($Z/C \leq .1$) along the entire length of the chord. The flow appears steady before the suction-side surface trip, though it is certainly turbulent after the trip. The flow is likewise unsteady or turbulent near the large coherent structures formed on the endcap and the suction-side surface.

The large, bright coherent structure formed on the suction side of the airfoil is the primary vortex core. It is formed near the surface of the airfoil and appears to be formed soon after the boundary layer trip ($X/C \approx .4$). The primary vortex forms out of the streamwise-aligned vorticity field created when low-momentum pressure side fluid upwashes and rolls over the suction side fluid. The primary vortex forms near the suction side airfoil surface and progressively lifts from the surface along the chordlength. The vortex core center is thus displaced a vertical distance, H_{te} , from the suction side surface at the trailing edge

$$H_{te}/C = .0614$$

The primary vortex is also laterally displaced from the endcap towards the wing root a distance S_{te} ,

$$S_{te}/C = .0463$$

These characteristics have been investigated by other researchers. Francis and Katz²⁷ and Francis and Kennedy²⁸ investigated the flow around a NACA 66-445 hydrofoil. They found that angle of attack affects the spanwise displacement of the primary vortex more than chord Reynolds number. Arndt, et.al.³⁰, however, found a "surprising non-

dependence" of the tip vortex downstream trajectory on angle of attack or chord Reynolds number. Thompson³⁹ attributes the differences in results to differences in planforms.

As the primary vortex passes from the wingtip trailing edge, the path becomes helical. The path appears in the end-views (Figures 47a-d) and the top surface views (Figures 47e-h) to be sinusoidal in nature. The amplitude of the sinuous path decreases rapidly (Figure 60). Careful measurements of the pitch, λ , and the maximum radius, a , of the helical path result in

$$\lambda/C = .600$$

$$a/C = .0135$$

Many researchers have seen similar vortex core paths (Winkelmann⁴², Stinebring, et.al.⁴¹, Green and Acosta²³). Such results from other studies have led to speculations about the nature of the vortex kinks. Green and Acosta²³ employed double-pulsed holographic techniques to a trailing vortex from a hydrofoil and found a similar kinking of the vortex core. Their findings suggested that the vortex kink could be similar in nature to a free helical wave disturbance on a line vortex. Other researchers have suggested that the phenomenon may be due to the interaction of the primary and secondary vortical structures (Winkelmann⁴²). The current results strongly suggest that the primary vortex core spiraling is caused by the interaction and merging of the primary and the secondary vortices as they travel downstream (Figure 59).

Perhaps one of the most interesting features of the flow is the secondary vortex, indicated by the brightly illuminated coherent structure near the endcap. The structure

appears to be formed by $X/C \approx .08$. The secondary vortex crosses to the suction side of the airfoil near $X/C \approx .7$, thenceforth crossing over the primary vortex. The two vortices appear to entwine as they follow helical paths downstream of the trailing edge. The maximum separation, r , of the two vortices appears to be about

$$r/C = .0497$$

3.2.2 Modeling

Consider an ideal three-dimensional flow consisting of two unequal strength point vortices in a uniform freestream, U_∞ , far from any boundaries. The vortices have strengths Γ_1 and Γ_2 and are initially separated by a distance r (Figure 61a). As the vortices travel downstream, they rotate about a common center, defined as the center of momentum and denoted in Figure 61a as X . Define the distances from Γ_1 and Γ_2 to the center of momentum as a and b , respectively, such that

$$a+b = r \quad (3.1)$$

A simple relation can be derived for the ratio of the strengths of the two vortices in terms of the distances of each from the center of momentum. The tangential velocity at a distance r from a vortex with circulation strength Γ is defined as

$$v_\theta = \Gamma/2\pi r \quad (3.2)$$

Substituting values for the current problem, the ratio of the strengths of the vortices becomes, from geometry,

$$v_{\theta 1} / v_{\theta 2} = \Gamma_1 / \Gamma_2 = b/a \quad (3.3)$$

where $v_{\theta 1}$ and $v_{\theta 2}$ are the induced velocities of the two vortices. As the two vortices proceed in time, they rotate about a common center of momentum.

The interaction of the primary and secondary vortices in the wingtip region is not an ideal situation. The primary and secondary vortices would co-rotate about a center of momentum, but the interaction would not be the ideal situation previously outlined. The flowfield is highly non-uniform in the region of the wingtip. Most importantly, the primary and secondary vortices are not point vortices. The secondary vortex will deform in the straining field of the primary vortex as they interact. The secondary vortex would thus become weaker, being continuously blended into a region about the primary vortex core. As this happens, the spiral path of the vortices would rapidly approach a straight line, with the center of momentum approaching the center of the primary vortex core (Figure 62).

The ratio of the circulations of two co-rotating vortices can be determined by measuring the separation of the vortices, r , and the maximum peak-to-peak amplitude, $2a$, of the strong vortex, Γ_1 . Employing relationships already developed, the ratio becomes,

$$\Gamma_1 / \Gamma_2 = (2 \times b) / (2 \times a) \quad (3.4a)$$

$$= ((2 \times r) - (2 \times a)) / (2 \times a) \quad (3.4b)$$

where Γ_2 is the circulation of the secondary vortex.

Similarly, estimates of the individual circulations of the two vortices may be attained. Measuring the half-wavelength of the co-rotating pair, $\lambda/2$ (Figure 61), and assuming the

vortex is convected at a characteristic velocity U_∞ , the distance traveled in 1/2 period of rotation is related to the tangential velocity of the primary and secondary vortices, $v_{\theta 1}$ and $v_{\theta 2}$, respectively, by

$$\lambda/2 = \pi a U_\infty / v_{\theta 2} = \pi b U_\infty / v_{\theta 1} \quad (3.5)$$

Now, substituting equation (3.2),

$$\lambda/2 = (2a) \pi^2 r U_\infty / \Gamma_2 = (2b) \pi^2 r U_\infty / \Gamma_1 \quad (3.6)$$

which leads to

$$\Gamma_1 / U_\infty C = (2b) \pi^2 (r/C) / (\lambda/2) \quad (3.7)$$

$$\Gamma_2 / U_\infty C = (2a) \pi^2 (r/C) / (\lambda/2) \quad (3.8)$$

Calculated as root sum square uncertainties, the uncertainties associated with each of the values are compiled in Table 2. Note that the uncertainties associated with fundamental measurements from the photographs were estimated at +/- .002 C, based upon repeated measurements. Also, the uncertainties do not include errors due to the model limitations.

The maximum amplitude, b, of the secondary vortex was calculated as

$$b/C = .0361$$

The normalized circulations of the primary and secondary vortices shown in Figures 10a-h are, respectively,

$$\Gamma_1 / U_\infty C = .1180$$

$$\Gamma_2 / U_\infty C = .0442$$

thus supporting the conjecture that the primary vortex is stronger than the secondary vortex.

3.2.3 Other Cases

Other cases show some interesting differences. The primary vortex appears to be formed by $X/C=.4$ for 5.0° and 7.5° angle of attack; but the formation appears to be delayed, until as late as $X/C=.6$ (Figure 41b), for the 2.5° angle of attack cases.

No sinuous path of the primary vortex was apparent during observation nor in the photographs for any of the 2.5° angle of attack cases viewed from the endcap (Figures 41a,b, 42a,b, 43a,b, 50a,b, 51a,b, 52a,b). However, evidence of a slightly sinuous path in the spanwise direction is evident in the top views (Figures 41e,f, 42e, 43e,f). This suggests an absence of the secondary vortex at 2.5° angle of attack.

Strong upsurges of pressure-side fluid are visible in all 5.0° and 7.5° angle of attack cases at all chord Reynolds numbers and aspect ratios (Figures 44, 45, 46, 47, 48, 49). The upwashes appear stronger than those at 2.5° angle of attack cases. No clear conclusions can be made regarding the effects of aspect ratio. Any apparent aspect ratio effects may be due to differences in bubble probe positioning relative to the end of the wing, bubble flow rates, bubble sizes, or light positioning.

The secondary vortex always forms very near the endcap surface ($Z/C<.08$) (Figure 41f,g, 44e-g, 47e-h). Chordwise location of formation appears to be from $.05C$ (Figures

47a,b) to .1C (Figures 41f,g, 50a,b, 53a-d, 54a-c, 55a-c), though lack of formation until .4C was also seen (Figures 44a-d, 45b). The vortex appears to form near the chordline at higher angles of attack (Figures 44a-d, 45b, 47a,b, 48a,b, 49b,d, 53a-d, 54a-c, 55a-c, 56b-d, 57a-c, 58a,b), though at 2.5° angle of attack, aspect ratio of 2.5, for all Reynolds numbers the swirling flow seems to form near the pressure side on the endcap (Figures 50a,b, 51a,c, 52a-c). The secondary vortex crosses to the suction side of the airfoil between X/C=.6 and .8 and co-rotates with the primary vortex as they proceed downstream (see for example Figure 59). The downstream interaction of the two vortices is visible in the photographs to greater than X/C=1.5 (Figure 47b), beyond which the secondary vortex is not discernible.

The existence of such a secondary structure has been deduced by other researchers from various measurement techniques and some smoke flow visualization results^{23, 27-29, 38}. Those studies, however, do not define the role of the secondary vortex in the flowfield. The results of the current study clearly depict the secondary vortex and allow a determination of the structure's role in the wingtip flowfield.

3.2.4 Ratio of Vortex Strengths

The dependencies of the ratio of primary to secondary vortex strength on angle of attack and chord Reynolds number are shown in Figures 63 and 64. A typical value for this ratio is $\Gamma_1 / \Gamma_2 = 2.83$, for $Re_c=260000$, 7.5° angle of attack, and aspect ratio 3.0. The

maximum and minimum values are both for aspect ratio of 2.5 cases, the minimum being 1.26 for $Re_c=130000$, angle of attack equal to 5.0° . The maximum value is 5.21 for $Re_c=260000$ and angle of attack equal to 7.5° .

The ratio of primary vortex strength to secondary vortex strength increases with angle of attack. However, the aspect ratio appears to have a strong influence: the ratio Γ_1 / Γ_2 increases with angle of attack considerably less for the higher aspect ratio cases. Furthermore, the ratio Γ_1 / Γ_2 is higher for the aspect ratio 3.0 cases than for the aspect ratio 2.5 cases at 5.0° angle of attack; but at 7.5° angle of attack, the trends are reversed. This may be a sign of blockage effects in the wind tunnel test. The proximity of the primary and secondary vortices to the tunnel walls may alter their paths in contrast to the paths they would take far from any boundaries. Because the relative strengths herein calculated are functions of the flow pattern, wall blockage effects would show up in the results as aspect ratio effects. The ratio Γ_1 / Γ_2 shows no particular dependence on chord Reynolds number (Figure 64).

The variations of primary vortex strength with increasing angle of attack are consistent with the findings of Francis and Katz²⁷. Though the existence of secondary vortices on the endcap has been inferred by other researchers^{27, 28, 31, 32, 34, 42}, no studies appear to have been attempted to date that examine the strengths of the secondary vortex as flow parameters are changed. Thus, comparison of the current secondary vortex results with other studies appears to be somewhat difficult. However, comparisons of the primary vortex core path, in particular H_{te} and S_{te} , with the results of others is possible.

An interesting conjecture can be developed by examining the quantitative results of other researchers. Devenport, et.al.³⁷ studied the downstream development of the trailing vortex behind a NACA 0012 half-wing at angles of attack from 2.5° to 7.5°, for Reynolds numbers based on an 8" chordlength from 130000 to 530000. The aspect ratio in their study was fixed at 4.33. Their results show some evidence of a double core 5 chordlengths downstream from the wing which smoothes out to a single core at further downstream locations. Corsiglia, et.al.⁴³ and Steger, et.al.⁴⁴ have previously described such results associated with co-rotating vortices of different strengths: as the weaker vortex wraps around and is assimilated by the stronger vortex, an apparent "annulus" of vorticity, associated with the minor vortex, is formed around the core of the stronger vortex.

The data of Devenport, et.al.³⁷ is represented in Figure 69a. By modeling the primary vortex as having a peak tangential velocity at the first "bump" on the v_θ curve, the secondary vortex adds its circulation, raising the overall v_θ level to the peak v_θ presented (Figure 69b). More explicitly, assume the primary vortex has peak tangential velocity $v_{\theta 1}$ / U_∞ ,

$$v_{\theta 1} / U_\infty = \Gamma_1 / 2\pi r U_\infty \quad (3.9)$$

Assume the secondary vortex adds its circulation to the primary vortex, taking the total tangential velocity to the peak velocity on the graphs,

$$v_{\theta 1}' / U_\infty = (\Gamma_1 + \Gamma_2) / 2\pi r U_\infty \quad (3.10)$$

Thus, the ratio of primary to secondary vortex strength becomes, approximately,

$$\Gamma_1 / \Gamma_2 = (v_{\theta 1} / U_{\infty}) / \{ (v_{\theta 1}' / U_{\infty}) - (v_{\theta 1} / U_{\infty}) \} \quad (3.11)$$

This analysis was applied to the data of Devenport, et.al.³⁷. Their data indicates a decrease of Γ_1 / Γ_2 with angle of attack, from approximately 18 at 5.0° angle of attack to approximately 5.0 at 7.5° angle of attack, at 10 chordlengths downstream from the wingtip, AR=4.33, and $Re_c=530000$. The value from the data of Devenport, et.al.³⁷ of Γ_1 / Γ_2 at 7.5° angle of attack, $\Gamma_1 / \Gamma_2 = 5.0$, is in rough agreement with the current flow visualization results. However, the trends are opposite to those found in the current study. This may be due to the simplicity of the current model. A more rigorous analysis is presented in Chapter 4.

3.2.5 Primary Vortex Circulation

Figures 65 and 67 show the variation of the primary vortex circulation, normalized on freestream velocity and measured chordlength, with angle of attack and chord Reynolds number. The primary vortex circulation was calculated as $\Gamma_1 / U_{\infty} C$,

$$\Gamma_1 / U_{\infty} C = (2b) \pi^2 (r/C) / (X'/2) \quad (3.7)$$

where the terms are as previously defined. The normalized primary vortex circulation increases with angle of attack, increasing more from 5.0° to 7.5° for the lower aspect ratio cases than for the higher aspect ratio cases. Increasing primary vortex circulation with

increasing angle of attack is in agreement with the findings of Devenport, et.al.³⁷.

Devenport, et.al.³⁷ also report an increase of primary vortex core circulation with increasing chord Reynolds number. The current results support those trends too.

3.2.6 Secondary Vortex Circulation

Figures 66 and 68 show the variation of the secondary vortex circulation, normalized on freestream velocity and measured chordlength, with angle of attack and Reynolds number. The secondary vortex circulation was determined similarly to that of the primary vortex,

$$\Gamma_2/U_\infty C_{\text{meas}} = (2a)\pi^2 (r/C_{\text{meas}}) / (X'/2) \quad (3.8)$$

with the terms as previously defined. The normalized secondary vortex circulation tends to decrease slightly from 5.0° to 7.5° angle of attack, with a perceptibly stronger decrease for the higher aspect ratio cases. The normalized circulation of the secondary vortex shows a slight tendency to decrease with increasing chord Reynolds number, though no particular dependence on aspect ratio is apparent in Figure 31. The apparent decrease of circulation with increasing chord Reynolds number may be due to wall interference.

3.2.7 Maximum Vertical Separation

Figures 70 and 71 depict the variations of the maximum vertical separation, r/C , of the primary and secondary vortices, again normalized on chordlength, with angle of attack and chord Reynolds number. At low aspect ratio, the separation increases with increasing angle of attack. However, for the higher aspect ratio cases the maximum separation decreases with increasing angle of attack. The proximity of the vortices to the tunnel sidewall may have been a strong factor. This is depicted in Figure 72. The images of the primary and secondary vortices in the tunnel walls would tend to push the vortices up and towards the right in the figure.

3.2.8 Primary Vortex Position

Further analysis of the pictures was conducted to determine the effects of varying angle of attack, aspect ratio, and chord Reynolds number on the position of the primary vortex core as it leaves the airfoil trailing edge. Similar studies were conducted by Francis and Katz²⁷ and Katz and Bueno Galdo²⁹. Measurements were made of the height of the core center from the suction side surface at the trailing edge. The symbols denoting these positions are H_{te} and S_{te} , for vertical and spanwise position, respectively. The current results were normalized on chordlength and compiled in Figures 73, 74, 75, and 76.

3.2.8.1 Vertical Position

Figures 73 and 74 show that the angle of attack affects the vertical position of the vortex above the suction side surface of the airfoil more dramatically than the chord Reynolds number for a given aspect ratio. This is in agreement with the results of Francis and Katz²⁷. H_{te}/C increases with increasing angle of attack, increasing more significantly from 5.0° to 7.5° angle of attack than from 2.5° to 5.0°. Francis and Katz²⁷ reported a square root variation of H_{te} with angle of attack. The trends in the current results are in disagreement with theirs, perhaps due to significant differences between the NACA-66 hydrofoil employed in their study and the NACA 0012 herein employed. In addition, their test facility geometry, 11'x5' cross section, was different from the current 3'x2' test section cross section. All of these differences could affect the results²⁷.

For a given angle of attack, H_{te}/C increases with increasing aspect ratio. This could be due to the increasing influence of the images of the vortices in the test section walls at higher aspect ratios. Further testing with wings of different aspect ratios needs to be conducted to definitively state any dependence of H_{te}/C on aspect ratio.

3.2.8.2 Spanwise Displacement

Figures 75 and 76 show the effects of varying the angle of attack, chord Reynolds number, and aspect ratio on the spanwise displacement from the wingtip of the primary vortex. S_{te}/C appears to be only mildly dependent on angle of attack, increasing slowly with increasing angle of attack. And though the data is limited, the spanwise movement

appears to decrease with increasing aspect ratio. In contrast to many of the other flow features studied, the spanwise movement seems to show a strong increase with chord Reynolds number. Any blockage effects would be evident with these particular results, as would any effects due to tunnel wall proximity. Nonetheless, the strong dependence upon chord Reynolds number of S_{te}/C present in the current results is consistent with the results of Francis and Katz²⁷.

The spanwise displacement of the primary vortex appears to be moderated by the secondary vortex. A strong secondary vortex would moderate the primary vortex location through mutual induction. The estimated circulation of the secondary vortex core decreases with increasing chord Reynolds number and decreasing aspect ratio. The spanwise displacement of the primary vortex from the endcap increases with increasing chord Reynolds number and with decreasing aspect ratio. Further testing is needed to examine the nature of this influence, but the current results indicate that the secondary vortex does influence the spanwise movement of the primary vortex core in the region of the wingtip.

3.2.9 Flow Angularity

The flow visualization scheme employed allowed for a determination of maximum flow angles involved in this and similar tip flow studies. These findings are important for any

researchers attempting to use yaw probes or any of the myriad of hot-wire anemometry configurations to analyze the flowfield in the near-tip regions.

Short time exposure photographs were used. Measurements were made assuming a typical direction for the flow at that location (determined by analyzing the long time averaged photographs). While inaccuracies are certain to have been introduced, the trends are believed to be accurate.

The results are presented in Table 1. The photographs revealed the strongest flow angularity to be in the immediate vicinity of the wingtip endcap and in the region of the vortex kink, with particularly high values for angles of attack of 5° and 7.5° . Flow angles of approximately 25° relative to the assumed direction (for example Figure 44d, 49d) appeared to be common. Several photographs revealed flow angles in excess of 30° (Figures 48d, 53d), and in at least one case flow angles were measured to be approximately 42° to the assumed direction (Figure 58d). Such high flow angles place significant restrictions upon the types of measurement apparatus employed in any near-tip region experiments, and careful consideration will have to be given to determine proper alignment for the probe.

3.2.10 Probe Interference Studies

The sensitivity of the trailing vortex to probe introduction has been of concern from the beginnings of trailing vortex research, and the issue is addressed at length in Devenport,

et.al.³⁷. Previous flow visualization work by Devenport and Sharma⁵⁰ and Zsoldos and Devenport⁴⁹, along with the simple potential flow modeling of Devenport, et.al.³⁷, showed no significant probe interference due to a hot wire probe traversing through a trailing vortex core. However, the clarity possible with the current flow visualization scheme warranted further investigation of the probe interference issue.

Helium-filled soap bubble flow visualization of the vortex core was performed, and the experimental setup was exactly as described for the tip-flow studies. The wing model was set to 5.0° angle of attack with an aspect ratio of 3.0. The chord Reynolds number was approximately 260000.

The region of interest was 10 chordlengths downstream of the NACA 0012 model. An Auspex Corporation type AVOP-4-100 sub-miniature four sensor hot wire probe was used. The probe consists of two orthogonal X-wire arrays on 8 independent prongs, total measurement volume approximately 0.4 mm³ (Figure 77). The quad-hot-wire was mounted on the y-z traverse used in tunnel flow quality measurements (see Chapter 2). The configuration was similar to the hot-wire setup employed by Devenport, et.al.^{10,37} in their trailing vortex studies (Figure 3).

The quad-hot-wire probe was stationed inside of the vortex core, just outside of the vortex core, and traversed through the core. The vortex core center location was estimated by visually inspecting the flow and attributing the brightest region, which appears as a streak in the photographs, to the core. Thus, the probe was placed approximately 1/8" outside of the edge of the streak, was placed in the center of the

streak, and was traversed through the entire region. Observation of the probe and vortex was possible from the tunnel sidewall and from a window in the floor of the tunnel just downstream from the probe location. Long and short time exposure photographs were taken of the flowfield about the probe from both the sidewall and the floor viewports.

The results are depicted in Figures 78 to 81. In the photographs, the probe extends horizontally from the white Delrin block. The measurement volume is labelled in the figures. The probe shadow covers part of the vortex core as the probe measurement volume is approached, not to be confused with a departure of the core path. Figure 78 depicts side views of the vortex probe as it rests $1/8"$ below the core center. Figure 79 depicts side views of the vortex probe located in the center of the vortex, with Figure 80 showing a view from below the tunnel of the same flow. Figure 81 is a 4 second time exposures of the probe traversing through the vortex core $+\text{-} .5715"$.

In the photographs, the core of the vortex is seen to diverge from its original path as it approaches the thick metallic stem from which the prongs extend, though that is approximately $1.5"$ downstream of the measurement volume. Further disturbances are seen as the vortex core passes by the white Delrin block, with the vortex core practically indiscernible further downstream from the Delrin block. This region is greater than $3.5"$ downstream of the measurement volume. No disturbances of any kind are seen to propagate upstream of the measurement volume. Also, no discernible vortex wandering was visible during the experiment nor in the photographs for either a stationary or

traversing probe. Thus, the current results indicate that any probe interference is at least visually negligible.

3.2.11 Particle Image Velocimetry

The current flow visualization scheme allowed for employment of particle image velocimetry techniques for the determination of flow angularity and velocity. For demonstration purposes, Insight PIV Analysis Software, developed by TSI, Inc., was used by TSI to analyze some of the current results. The PIV system scans the photographic image into a PC computer. The flow image is divided into grids consisting of small regions, and an autocorrelation algorithm is conducted on the particle images within each grid region to determine the particle displacement. Knowing the time between laser pulses and the particle displacements, the particle velocity representing each grid is thus computed.

The current results were processed for Figures 44a, 47a, 53a, and a 1/4 second exposure photograph not herein depicted, assuming a nominal pulse repetition rate of 6.05kHz. Analysis was not attempted for particles originally in the image of the airfoil. The results are presented in Figures 82 to 85.

The results give an idea of the general flow characteristics in the region of the wingtip. The fluid on the pressure side of the airfoil is considerably slower than the fluid on the suction side of the airfoil (Figures 82-85). The flow accelerates around the endcap in

going from the pressure side surface towards the suction side (Figures 83 and 84). Figure 82 clearly shows an acceleration of the fluid around the endcap associated with the secondary vortex as it crosses to the suction side surface. A glaring deficiency of this PIV examination is the inability of the system to analyze the primary vortex core flow: no evidence is visible to suggest either an excess or deficit of axial velocity on the vortex core. The closest any of the figures approaches the subject is in Figure 82, where flow near the primary vortex accelerates in the streamwise direction as the trailing edge is approached. Unfortunately, it is not clear if the fluid is associated with the vortex core.

Significant flow angularity is also visible in the results (Figures 82-85). The strongest flow angularity is visible in Figure 84 near mid-chord towards the suction side surface. The highest flow angles are approximately 20° . These results are associated with long time average flow features, greater than 1/4 second in duration, whereas the previously reported flow angularity results were associated with considerably shorter time period flow characteristics, typically 1/125 second in duration.

4. Hot-Wire Measurements

4.1 General

Hot wire measurements of the trailing vortex flowfield downstream of the NACA 0012 airfoil have been conducted. Measurements were made with both a single and a sub-miniature four sensor hot-wire. The measurements were to validate the vortex flow in this facility and to investigate any effects of the secondary vortex on the endcap (see Chapter 3) on the primary vortex core at a fixed downstream location.

4.2 Apparatus

The experiments were performed in the 3'x2' subsonic wind tunnel previously described in Chapter 2. The NACA 0012 half-wing employed for these experiments was similar to the NACA 0012 half-wing employed for the flow visualization experiments discussed in Chapter 3. It consisted of a .203m chord with a blunt tip. It was mounted in the same wing mount at the same test section location as the model in Chapter 3. The boundary layer of the wing was tripped using .5mm diameter glass beads glued to the surface of the wing model between the 20% and 40% chord locations, with an average bead density of approximately 200 beads/cm². These parameters were consistent with those employed in the flow visualizations discussed in Chapter 3 and with the quantitative experiments of Devenport, et.al.^{10,37}.

The single hot-wire setup employed was exactly the same as that described in Chapter 2 for the tunnel flow quality determinations. For the quad-hot wire measurements, a miniature 4-sensor hot-wire probe (Auspex Corporation type AVOP-4-100) was used for the velocity measurements in the vortex. The probe provides simultaneous three component velocity measurements. The probes consist of 2 orthogonal X-wire arrays on 8 independent prongs with a total measurement volume of approximately 1.1 mm^3 . The tungsten wires were operated simultaneously by 4 Dantec 56C17/56C01 constant temperature anemometer units. Anemometer outputs were read through an Analogic 12 bit HSDAS-12 A/D converter operated by an IBM AT compatible computer. Each signal passed through a 10x buck-and-gain amplifier before being passed to the A/D board. The magnitude and phase response of each of the four channels was optimized using the square wave response. All four sensors of the quad-wire probe were calibrated in the freestream, employing King's law to correlate the output voltages of the sensors with the cooling velocities. The absolute flow direction at the calibration location was determined in advance using a 7-hole yaw probe. Temperature drift during measurements was minimal, and drift corrections were performed using the method of Bearman⁵¹.

The same traverse as employed for the tunnel test section flow quality determinations was employed for the hot-wire experiments. The traverse allowed for extensive horizontal and vertical traversing of the quad-wire and was controllable by the computer. The probe holder, a 12.7 mm diameter steel rod aligned with the freestream, positioned the tip of the probe well upstream of the probe holder vertical stem (Figure 86). The probe was held

parallel to the freestream for the entire experiment. Direct calibration of the probe before the experiment, by pitching and yawing the probe through a series of known angles in a jet of known direction, enabled the true relationship between the outputs from the probe sensors and the instantaneous flow direction to be accurately determined. The relationships are then employed during post-processing of the data.

4.3 Results

Experiments were conducted over a range of angle of attacks and aspect ratios and are tabulated in Table 3. Grid measurements were made with both the single hot-wire and the quad-hot-wire, and profile measurements through the vortex core were conducted using the quad-hot-wire. The single hot-wire measurements were made at $X/C=12$ and 25. The quad-hot-wire measurements were made at $X/C=10$. All quad-hot-wire measurements and single hot-wire measurements were conducted at Reynolds number based on chordlength of 330000. The rectangular and cylindrical coordinate system shown in Figure 22 will be employed in presenting the data. Distance x is measured from the wing leading edge at 0° angle of attack. Distances y , z , and r are measured from the vortex center. Velocity components U , V , and W are defined in the directions x , y , and z , respectively.

4.3.1 Grid Measurements

Single sensor and 4-sensor hot-wires were employed to evaluate the trailing vortex flowfield in the 3'x2' Subsonic Wind Tunnel. The quad-hot-wire was traversed in a 17 point by 17 point grid. The wing was set at 5.0° angle of attack and aspect ratio 2.5. The single hot-wire was traversed in a 10 point by 10 point grid. The wing was set at 5.0° angle of attack and aspect ratio 3.0.

The wing model was initially mounted with the quarter-chord 23" from the test section entrance. Measurements were made at $X/C=25$ with the single sensor hot-wire. The results are shown in Figures 90 and 91. No definable vortex is visible. The wing model was then moved 13 chordlengths downstream, and measurements were taken at the same location (now only 12 chordlengths downstream of the model). The first thing to note is the existence of a well defined vortex at $X/C=12$, as measured by the single sensor hot-wire (Figure 87). The exact cause of the disappearance of the vortex by $X/C=25$ when the model is placed near the entrance is unknown. Flow angularity near the test section entrance is insignificant. Leaking at the wing root had no effect on the vortex at $X/C=12$ and was assumed to have no effect upon the vortex with the wing mounted near the entrance. The vortex may have wandered sufficiently to interact with the thickening test section boundary layers by $X/C=25$, thus causing rapid diffusion of the vortex. The wing model may have interfered with the contraction flow, thus altering the test section inlet flow significantly.

The wrapping of the spiral wake about the core is visible in the figures (Figures 87-89, 92-97). In both the single-sensor and four-sensor hot-wire results, the levels of turbulent kinetic energy and axial normal stresses decrease as the core is approached along the spiral wake. These trends are similar to those reported by Devenport, et.al.³⁷ who attribute the trends to the rates of strain and lateral curvature suffered by the wake turbulence. Interestingly, the magnitudes of the turbulent kinetic energy and axial stresses are quite comparable to those reported by Devenport, et.al.³⁷, further confirming the viability of the 3'x2' Subsonic Wind Tunnel for the investigation of trailing vortices.

4.3.2 Correction of Quad-Hot Wire Results for the Effects of Wandering

Vortex measurements by fixed probes are subject to the effects of vortex core wandering. Core wandering results in overestimates of turbulence levels in the vortex core and of the core radius. The method for removal of wandering effects, developed by Devenport, et.al.³⁷, consists of modeling the vortex core by a series of Q-vortices of the form (Batchelor⁵),

$$V_{\theta m} = V_{\theta 1m} (1 + 0.5/\alpha) (r_{1m}/r_p) \{ 1 - \exp[-\alpha(r_p^2 / r_{1m}^2)] \} \quad (4.1)$$

and

$$U_m = U_{Dm} \exp[-\alpha(r_p^2 / d_m^2)] \quad (4.2)$$

where $r_p^2 = y^2 + z^2$, $\alpha = 1.25643$ and $V_{\theta 1m}$, U_{Dm} , r_{1m} , and d_m are the measured peak tangential velocity, centerline axial velocity relative to the freestream, core radius, and radial scale of the axial velocity profile. To find the true velocity field of the trailing vortex core, the method assumes that the vortex core is axisymmetric and that the wandering position of the vortex core can be described by the general correlated Gaussian function. Though the details of the method need not be extensively discussed here (see rather Devenport, et.al.^{10,37}), the deconvolution method yields the true unwandered mean velocity field of the trailing vortex and the apparent stress field imposed by wandering.

The current quad-hot-wire vortex core profile measurements were processed to remove the effects of wandering. Pursuant to the deconvolution method of Devenport, et.al.³⁷, each profile was curve fit to a 20 term exponential series.

The measured tangential and axial velocity data and the corresponding curve fits for a representative case are shown in Figure 98. The curve fits describe the data within the core very well and closely approximate the data outside of the core. Wandered and corrected for wandering curve fits are shown for all of the cases in Figures 99 and 100. The r.m.s. amplitudes of wandering, σ_y and σ_z , and the correlation coefficient, e , developed in the deconvolution process are presented in Table 3.

Vortex core wandering in the current experiment is significantly less than that reported by Devenport, et.al.³⁷ for their similar experiments in the Virginia Tech Stability Wind Tunnel facility. For 5.0° angle of attack, aspect ratio 2.5, chord Reynolds number 330000, the current results indicate a vortex core wandering, σ_y/C and σ_z/C , of .003 and .004,

respectively. For their baseline case $X/C=10$, aspect ratio 4.33, angle of attack 5.0° , and chord Reynolds number 530000, Devenport, et.al.³⁷ report vortex core wandering, σ_y and σ_z , of .007 and .005, respectively. Interestingly, the maximum dimension of the test section employed in the current study is approximately 1/2 that of the test section employed by Devenport, et.al.³⁷ in their experiments. Further, the primary axis of wandering corresponds to that of the maximum width of the test section. Thus, the overall magnitude of wandering appears proportional to the geometric distance from the core to the boundaries of the test section.

Wandering amplitude in the y-direction decreases from .007 to .003, for an increase of angle of attack from 2.5° to 7.5° . A similar decrease is seen in the z-axis direction. This implies that strengthening of the vortex stabilizes the vortex core against buffeting by surrounding wake structures. Increasing aspect ratio appears to have no effect.

4.3.3 Axial Velocity Results

Figure 100 shows the axial velocity results. Because of the slight amount of wandering in the current results, the corrected for wandering profiles do not differ greatly from the wandered profiles. The axial velocity deficit appears to be relatively unaffected by variations of aspect ratio. The magnitude of the axial velocity deficit decreases with increasing angle of attack. This trend is in agreement with that reported by Devenport, et.al.³⁷. The axial velocity profiles show some evidence of an outer region which becomes

more noticeable with increasing angle of attack and moves further outboard. The deficit of the outer region appears to increase with increasing angle of attack. The influences of the region are visible above 3.75° angle of attack.

4.3.4 Tangential Velocity Results

The wandered and corrected for wandering results are presented in Figure 99. An inflection in the tangential velocity within the vortex core is visible, appearing at 5.0° and increasing in severity with increasing angle of attack. The inflection is seen at all aspect ratios. Importantly, the inflection is also visible in the wandered results, ensuring that the inflection is not a result of the correction for wandering process. The correction process merely emphasizes the severity of the inflection.

No strong influence of aspect ratio is visible in the tangential velocity profiles (Figure 100). In the tip region, strong effects of aspect ratio were found (compare for example Figures 45a,b and 54a,b). Thus, the strong influence of aspect ratio has vanished by $X/C=10$. This may be indicative of blockage, bubble probe interference, or of an initial condition which decays rapidly and warrants further investigation.

The tangential velocity profiles of Devenport, et.al.³⁷ are shown in Figure 69. The current results and their results are quite similar. Figures 101 and 102 compare the maximum tangential velocities and the core radii measured in the current study and those reported by Devenport, et.al.³⁷. The current maximum tangential velocity results are

within $.03U_{ref}$ of those reported by Devenport, et.al.³⁷ for all cases. The current core radii are at most $.007C$ from those reported by Devenport, et.al.³⁷, with much closer agreement above 3.75° angle of attack. The inflections of the tangential velocity profiles are present by 5.0° angle of attack for both data sets. The inflection also increases in severity with increasing angle of attack for both sets of data. Discussion and comparison of core parameters derived from the tangential velocity profiles follows.

4.3.4.1 Maximum Tangential Velocity

The variation of maximum tangential velocity with increasing angle of attack is plotted in Figure 101. For comparison purposes, the variations of maximum tangential velocity reported by Devenport, et.al.³⁷ are also presented. The maximum tangential velocity increases linearly with increasing angle of attack, increasing from approximately .14 at 2.5° angle of attack to approximately .44 at 7.5° angle of attack, at an aspect ratio of 2.5. Increasing aspect ratio appears to have little effect. These trends are in agreement with those of Devenport, et.al.³⁷. The rate of increase reported by Devenport, et.al.³⁷ appears to be slightly less than that of the current results, but the differences may be due to measurement errors.

4.3.4.2 Core Radius

The variations of core radii with increasing angle of attack are presented in Figure 102. Also plotted for comparison purposes is the data of Devenport, et.al.³⁷. Core radius increases with increasing angle of attack. The current data and that of Devenport, et.al.³⁷ are in agreement.

The appreciable increase between 3.75° and 5.0° angle of attack is curious. It appears to be associated with the appearance of the inflection in the tangential velocity profiles and the increased influence of the outer region, as shown in the axial velocity profiles. Regardless, the increase with angle of attack is linear above 5.0° angle of attack.

4.3.4.3 Core Circulation

The circulation of the vortex core was calculated assuming an axisymmetric vortex core, i.e.,

$$\Gamma_1 = 2\pi r_{1m} v_{\theta 1m} \quad (4.4)$$

where r_{1m} , $v_{\theta 1m}$, and Γ_1 are the core radius, maximum tangential velocity, and core circulation, measured and calculated from the corrected for wandering profiles, respectively. The current results, at aspect ratios 2.5, 2.75, and 3.0, at $X/C=10$, and chord Reynolds number 330000 are plotted in Figure 103. The data of Devenport, et.al.³⁷, at aspect ratio 4.33, $X/C=10$, and chord Reynolds number 530000, are also plotted in Figure

103. The core region circulation increases with increasing angle of attack. The circulation also shows an interesting jump in magnitude between 3.75° and 5.0° angle of attack. This too could be a reflection of the development of two regions in the vortex core. Circulation increases linearly from 5.0° to 7.5° angle of attack, increasing at the same rate for both the current data and that of Devenport, et.al.³⁷. However, the current results are slightly higher in magnitude than those of Devenport, et.al.³⁷. The differences may be due to differences in chord Reynolds number. The value of the circulation appears to increase slightly with increasing aspect ratio.

4.4 Axial Vorticity

Axial vorticity was computed by differentiating the tangential velocity profiles, assuming (rv_θ) was only a function of r . That is, the axial vorticity was computed as

$$\omega_z \approx \frac{1}{r} \frac{d(rv_\theta)}{dr} \quad (4.6)$$

The axial vorticity profiles are plotted in Figure 104. At 2.5° and 3.75° angle of attack, the axial vorticity behaves as a Gaussian, decreasing from a peak and approaching 0 in the wake. The sharpness of the peak increases with increasing angle of attack, indicating a rapid change in the streamwise alignment of vorticity with increasing radial distance. Again, the variations of aspect ratio have no apparent effect at this streamwise location.

The peak streamwise vorticity is plotted versus angle of attack in Figure 105. The peak axial vorticity occurs at $r/C=.004$ for all cases. The peak axial vorticity increases linearly with increasing angle of attack.

Quite interestingly, the axial vorticity profiles show clearly the existence of an inner and outer core region. The differentiation of the regions becomes apparent by 5.0° angle of attack. The initial concave inflection occurs at about $r/C=.022$; and the convex curvature begins at about $r/C=.03$. The magnitude of vorticity at which the inflection occurs increases with angle of attack. At 7.5° angle of attack, the inflection in the axial vorticity curve forms a plateau at approximately $\omega_x C/U_{ref} = -18.2$. This increasingly strong region of axial vorticity remains at approximately the same radial location. The inner region increases in strength with increasing angle of attack more rapidly than the outer region.

4.5 Vortex Core Model

The existence of differentiated regions of the vortex core, becoming increasingly differentiated with increasing angle of attack, has been shown. The axial velocity profiles hint at the existence of such. The tangential velocity profiles show the existence of such regions. And the axial vorticity profiles define the strength of the regions. But what is the cause of the separate regions?

The tip flow results show the existence of a secondary vortex which co-rotates with the primary vortex core. As the pair proceeds downstream, the secondary vortex becomes increasingly deformed under the influence of the stronger primary vortex core. Ultimately, it is conjectured, the secondary vortex becomes an "annulus of vorticity" about the primary vortex core, and the spiral path of the primary vortex will have decayed to a straight line.

This model, if correct, would be able to be tested. At some downstream location, the existence of such an annulus of vorticity about the primary vortex would be able to be measured. The annulus would appear in tangential velocity profiles as an inflection, as the circulation of the secondary vortex would be added to the circulation of the primary vortex at any further outboard locations. The secondary vortex annulus of vorticity would also show itself as an inflection, or if strong enough an increase, in the local vorticity profile that would otherwise behave as a Gaussian. These are all occurrences or trends that have been herein reported.

The tip flow results indicate that the separation of the primary and second tip vortices increases with angle of attack. The vorticity plots do not show any convincing evidence of the separation of the primary and secondary regions increasing with angle of attack, though certainly the initial separation of the vortices would not be preserved as they move downstream. The tip flow results show an increase in primary vortex strength with increasing angle of attack, and the secondary vortex strength appeared to remain relatively constant with angle of attack. The inner and outer core regions at X/C both increase in

strength with increasing angle of attack, but the inner region certainly increases in strength at a faster rate. The secondary tip vortex did not appear in the photographs until 5.0° angle of attack. The differentiated core regions appear by 5.0° angle of attack.

The degree to which the regions are differentiated would tend to decrease with downstream location. The vorticity associated with the secondary vortex would tend to diffuse under the continued shearing of the primary vortex, and ultimately the vorticity would be absorbed by the primary vortex core. The data of Devenport, et.al.³⁷ show exactly such a disappearance of the differentiated regions by $X/C=30$. Their data indicate that the differentiation is strongest at $X/C=5$, and by $X/C=30$ their tangential velocity results fail to show any signs of a secondary region.

The heuristic model that is being proposed is shown in Figure 106. The flow near the tip is dominated by the coherent primary and secondary vortices. Under the influence of the strongly 3-dimensional tip flowfield, the secondary vortex begins to co-rotate with the primary vortex. As they travel downstream, the vortex pair traces a straight-line path; but the individual vortices appear to trace a spiral path. Under the shearing forces of the primary vortex, the secondary vortex deforms into an annulus of vorticity about the primary vortex. Initially, the vorticity originally associated with the secondary vortex forms a distinct region of vorticity. However, at further downstream locations, the vorticity diffuses and merges with the vorticity of the primary vortex. At that point, the regions are no longer differentiable.

Any successful model of the trailing vortex core from a blunt tipped NACA 0012 will have to describe various downstream regions of the trailing vortex. In the near tip region,

the model will have to be able to describe the strongly 3-dimensional flowfield dominated by two separate but interacting coherent vortices. Between that region and the farfield, the model will have to describe the two/three disparate regions: the inner core region dominated by the primary vortex core characteristics, the outer core region dominated by the secondary vortex vorticity, and any region which may exist between the two comprised, in characteristics, of the inner and outer regions. Though no rigorous mathematical model has been herein developed, the evidence strongly suggests that the differentiated regions are indeed artifacts of the two vortex tip flowfield described in Chapter 3. Further work should be aimed at developing a mathematical model. Such a model would facilitate calculation of the trailing vortex flows and possibly enable improvements in trailing vortex control.

5. Conclusions and Future Work

The 3'x2' Subsonic Wind Tunnel has been setup, and the flow quality has been determined through the use of single sensor hot wires. The test section potential core flow is closely uniform over the tunnel cross section at both the entrance and exit planes. The mean velocity varies approximately .4% at both the entrance and exit planes. The turbulence intensity is approximately .17% at the entrance and .14% at the exit. The potential core region shrinks by the test section exit plane due to growth of the boundary layers. The tunnel centerline axial velocity accelerates approximately 6% due to the boundary layer growth along the test section length of 20'11". Unsteadiness contributes significantly to the potential core turbulence level, approximately doubling the perceived axial stress.

The tunnel was used for trailing vortex flow visualization and hot-wire measurements. The trailing vortex flowfield was found to be very similar to that produced in the Virginia Tech Stability Wind Tunnel facility, thus proving the viability of the 3'x2' Subsonic Wind Tunnel for trailing vortex studies.

The major conclusions to be drawn from the tip flow visualizations are:

1. A secondary vortex is generated on the wingtip endcap.
2. The rotational sense of the secondary tip vortex is the same as that of the primary vortex.

3. The secondary vortex crosses to the suction side surface before passing from the trailing edge of the wing.
4. The secondary vortex and the primary vortex form a co-rotating pair, the interaction of the two causing the helical path of the primary vortex core.
5. The ratio of primary to secondary vortex circulation increases with increasing angle of attack. Increasing aspect ratio moderates the effect of increasing angle of attack. No particular dependence upon chord Reynolds number was found.
6. Primary core circulation increases with increasing angle of attack and chord Reynolds number. The increase is moderated with increasing aspect ratio.
7. The secondary vortex circulation appears to decrease with increasing angle of attack. The decrease is greater at high aspect ratios. The circulation appears to decrease slightly with increasing chord Reynolds number.
8. The maximum separation of the primary and secondary vortices is strongly dependent upon aspect ratio, increasing with angle of attack at low aspect ratios and decreasing with increasing angle of attack at higher aspect ratios.
9. Angle of attack strongly affects the vertical position of the primary vortex core above the wing surface at the trailing edge. The vertical position tends to increase with increasing aspect ratio. No particular dependence upon chord Reynolds number was found.
10. Spanwise displacement from the endcap of the primary vortex core is strongly dependent upon chord Reynolds number, increasing with increasing chord Reynolds

number. The displacement increases slightly with increasing angle of attack and decreases slightly with increasing aspect ratio.

11. No visible probe interference associated with the traversing of a quad-wire through the vortex core was found.

12. Flow angles on the endcap on the order of 20° were found with the PIV analysis.

Flow angles in excess of 25° relative to the local horizontal were found in the near tip regions with the helium-bubble flow visualization.

The major conclusions drawn from the quad-hot-measurements are:

14. The vortex generated in the 3'x2' Subsonic Wind Tunnel is similar to the vortices generated in the VA Tech Stability Wind Tunnel.

15. Vortex core wandering was approximately 1/2 that found in similar VA Tech Stability Wind Tunnel studies.

16. Two regions in the vortex core can be characterized, an inner region and an outer region, distinguishable above 3.75° angle of attack.

17. The inner region is similar to the primary tip vortex, and the outer region is similar to the secondary tip vortex.

18. The strong aspect ratio variations seen in the tip flow visualization results vanish by $X/C=10$.

19. An heuristic model has been developed describing the evolution of the differentiated regions in terms of the primary and secondary wingtip vortices.

In the future, work needs to be done to examine certain of these features further.

Among the investigations needed are:

1. The cause of the flow acceleration on the tunnel walls at the entrance needs to be determined.
2. The cause of the relatively large floor boundary layer at the test section entrance needs to be determined.
3. The effects of flow blockage on the tip flow structures needs to be quantitatively determined by single and multiple point hot-wire measurements in the tip regions.
4. Further experiments are needed to determine the effects of tip modifications and aspect ratio variations on the relative strengths of the tip structures. Large changes in aspect ratio, on the order of $1.5 \rightarrow 5.0$, need to be tested. Careful design of the experiments will be needed to isolate the effects of blockage from the effects of aspect ratio variation. A variety of tip modifications would also allow testing of planform changes.
5. Further analysis of the core regions is needed to determine the exact nature of the regions, determining unequivocally any relation of the tip structures to the regions. Multiple point measurements at the tip and at downstream locations would allow for the complete turbulence characterization of the inner and outer core regions.
6. Rigorous mathematical modeling will be needed to describe the formation and evolution of the inner and outer core regions.

References

1. Karamcheti, K., 1966, *Principles of Ideal Fluid Aerodynamics*, copyright 1966, John Wiley & Sons, inc.
2. Betz, A., 1932, "Behavior of Vortex Systems", NACA-TM-713.
3. Lowson, M.V., 1989, "Visualization Measurements of Vortex Flows", AIAA-89-0191.
4. Hoffmann, E.R. and Joubert, P.N., 1963, "Turbulent Line Vortices", Journal of Fluid Mechanics, vol. 16, pp.395.
5. Batchelor, G.K., 1964, "Axial Flow in Trailing Line Vortices", Journal of Fluid Mechanics, vol. 20, pp.645.
6. Moore, D.W. and Saffman, P.G., 1973, "Axial Flow in Laminar Trailing Vortices", Proceedings of the Royal Society of London, A.333, pp.491.
7. Phillips, W.R.C., 1981, "The Turbulent Trailing Vortex During Roll-up", Journal of Fluid Mechanics, vol. 105, pp.451.
8. Owen, P.R., 1970, "The Decay of a Turbulent Trailing Vortex", The Aeronautical Quarterly, February 1970.
9. Zeman, O., 1993, "Toward Modeling Wingtip Vortices", Center for Turbulence Research, Annual Research Briefs, 1993.
10. Devenport, W.J., Rife, M.C., et.al., 1994, "Turbulent Trailing Vortices", AIAA Paper 94-0404.
11. Uberoi, M.S., 1979, "Mechanisms of Decay of Laminar and Turbulent Vortices", Journal of Fluid Mechanics, vol. 90, pp.241.
12. Corsiglia, V.R., et.al., 1973, "Rapid Scanning, Three-Dimensional Hot-Wire Anemometer Surveys of Wing-Tip Vortices", Journal of Aircraft, vol. 10, no. 12.
13. Singh, P.I. and Uberoi, M.S., 1976, "Experiments on Vortex Stability", The Physics of Fluids, vol. 19, no. 12, December 1976.
14. Wu, C., Farokhi, S., and Taghavi, R., 1992, "Spatial Instability of a Swirling Jet-Theory and Experiment", AIAA Journal, vol. 30, no. 6, June 1992.

15. Smits, A.J., and Kummer, R.P., 1985, "The Interaction and Merging of Two Turbulent Line Vortices", AIAA-85-0046.
16. Chevalier, H., 1973, "Flight Test Studies of the Formation and Dissipation of Trailing Vortices", Society of Automotive Engineers, 730295.
17. Wentz, W.H., jr., and Kohlman, D.L., "Vortex Breakdown on Slender Sharp-Edged Wings", Journal of Aircraft, vol. 8, no. 3, pp.156.
18. Sarpkaya, T., 1992, "Three-Dimensional Interactions of Vortices with a Free Surface", AIAA-92-0059.
19. Melander, M.V. and Hussain, F., 1991, "Coherent Structure Dynamics: Interaction Between Large and Fine Scales", Eighth Symposium on Turbulent Shear Flows, 28-5, 1991.
20. Tsai, C. and Widnall, S.E., 1976, "The Stability of Short Waves on a Straight Vortex Filament in a Weak Externally Imposed Strain Field", Journal of Fluid Mechanics, vol. 73, part 4, pp.721.
21. Maxworthy, T., 1988, "Waves on Vortex Cores", Fluid Dynamics Research 3, pp.52.
22. Bandyopadhyay, P.R., et.al., 1991, "Organized Nature of a Turbulent Trailing Vortex", AIAA Journal vol. 29, no. 10, October 1991, pp.1627.
23. Green, S.I. and Acosta, A.J., 1991, "Unsteady Flow in Trailing Vortices", Journal of Fluid Mechanics, vol. 227, pp.107.
24. Sarpkaya, T., 1971, "Vortex Breakdown in Swirling Conical Flows", AIAA Journal, vol. 9, no. 9, pp.1792.
25. Saffman, P.G., 1973, "Structure of Turbulent Line Vortices", The Physics of Fluids, vol. 16, no. 8, August 1973.
26. Hoffman, J.D., Velkoff, H.R., "Vortex Flow over Helicopter Rotor Tips", J. Aircraft, Vol. 8, No. 9, pp. 739.
27. Francis, T.B., Katz, J., "Observations on the Development of a Tip Vortex on a Rectangular Hydrofoil", Transactions of the ASME, Vol. 110, June 1988, pp. 208.

28. Francis, M.S., Kennedy, D.A., "Formation of a Trailing Vortex", *J. Aircraft*, Vol. 16, No. 3, pp. 148.
29. Katz, J., Bueno Galdo, J., "Effect of Roughness on Rollup of Tip Vortices on a Rectangular Hydrofoil", *J. Aircraft*, Vol. 26, No. 3, March 1989, pp. 247.
30. Arndt, R.E.A., et.al., "Some Observations of Tip-Vortex Cavitation", *J. Fluid Mech.*, Vol. 229, pp. 269.
31. Chow, J.S., Zilliac, G.G., Bradshaw, P., "Measurements in the Near-Field of a Turbulent Wingtip Vortex," AIAA-93-0551.
32. Chow, J.S., Zilliac, G.G., Bradshaw, P., "Turbulence Measurements in the Near-Field of a Wingtip Vortex," ASME Forum on Turbulence in Complex Flows, 1994.
33. Chigier, N.A., Corsiglia, V.R., "Tip Vortices-Velocity Distributions," NASA TM X-62,087, September 1971.
34. Spivey, R.F., "Blade Tip Aerodynamics, Profile and Planform Effects," 24th Annual National Forum of the American Helicopter Society, May 1968.
35. Carlin, G., Dadone, L., Spencer, R., "Results of an Experimental Investigation of Blade Tip Vortex Modification Devices," NASA CR-181853, June 1989.
36. Green, S.I., "Correlating Single Phase Flow Measurements with Observations of Trailing Vortex Cavitation," *Journal of Fluids Engineering*, Vol. 113, 1991, pp. 125-129.
37. Devenport, et.al., "Turbulence Structure and Scaling in Trailing Vortices", 1995, AIAA 95-0588.
38. Chow, et.al., "Initial Roll-up of a Wingtip Vortex", FAA International Wake Vortex Symposium, October 1991.
39. Thompson, David H., "Experimental Study of Axial Flow in Wing Tip Vortices", 1975, *Journal of Aircraft*, Vol. 12, No. 11, pp. 910.
40. Higuchi, et.al., "Vortex Roll-Up from an Elliptic Wing at Moderately Low Reynold's Numbers", 1986, AIAA 86-0562.
41. Stinebring, et.al., "The Structure of a Three-Dimensional Tip Vortex at High Reynolds Numbers", *Transactions of the ASME*, Vol. 113, September 1991.

42. Winkelmann, A.E., "Flow Visualization Studies of the Tip Vortex System of a Semi-Infinite Wing", 1989, AIAA
43. Corsiglia, et.al., "Experimental Study of the Effect of Span Loading on Aircraft Wakes", 1975, Journal of Aircraft, Vol. 13, No. 12, pp. 968.
44. Steger, J.L. and Kutler, P., "Implicit Finite-Difference Procedures for the Computation of Vortex Wakes", 1976, AIAA.
45. Corsiglia, et.al., "Laser Velocimeter Surveys of Merging Vortices in a Wind Tunnel", AIAA 78-107.
46. Brandt, S.A., and Iversen, J.D., "Merging of Aircraft Trailing Vortices", Journal of Aircraft, Vol. 14, No. 12, pp.1212.
47. Accardo, et.al., "
48. Zsolodos, J.S. and Devenport, W.J., 1992, "An Experimental Investigation of Interacting Wingtip Vortex Pairs," M.S. Thesis, VPI-AOE-191, VPI&SU, Blacksburg, VA.
49. Zsolodos, J. S. and Devenport, W.J., 1991, "Flow Visualizations of Interacting Wingtip Vortex Pairs," Report VPI-AOE-188, VPI&SU, Blacksburg, VA.
50. Devenport, W.J. and Sharma, G., 1990, "Flow Visualizations of a Wingtip Vortex in the Presence of a Probe," Report VPI-AOE-177, VPI&SU, Blacksburg, VA.
51. Bearman, P.W., 1971, "Corrections for the Effect of Ambient Temperature Drift on Hot-Wire Measurements in Incompressible Flow", DISA Information, vol. 11, pp. 25-30.
52. Mironer, A., 1971, "Accelerated Diffusion of Wing-Tip Vortices by Heating", AIAA Paper 71-616.
53. Weinstein, L.M., 1991, "An Improved Large Field Focusing Schlieren System", AIAA 91-0567.
54. Weinstein, L.M., 1993, "Large-Field High-Brightness Focusing Schlieren System", AIAA Journal, vol. 31, no. 7, July 1993.
55. Collicott, S.H. and Salyer, T.R., 1994, "Quantification of Noise Reduction in Multiple-Source Schlieren Systems", AIAA 94-0279.

56. Holder, D.W. and North, R.J., 1956, "Optical Methods for Examining the Flow in High-Speed Wind Tunnels, part 1: Schlieren Methods", AGARDograph 23, November 1956.
57. Holder, D.W. and North, R.J., 1963, "Schlieren Methods", Notes on Applied Science, no. 31.
58. Longhurst, R.S., 1962, *Geometrical and Physical Optics*,
59. Jenkins, F.A. and White, H.E., 1976, *Fundamentals of Optics*, 4th. edition,
60. Mason, W.H., and Marchman, J.F., 1972, "Far-Field Structure of an Aircraft Trailing Vortex", NASA CR 62078.

APPENDIX I. Operation Procedures

The following is a guideline to the use of the 3'x2' subsonic wind tunnel facility. These guidelines, if followed, will allow safe and repeatable usage of the facility, with no degradation to the tunnel and surroundings.

1. Fan blades should be periodically visually checked for cracks or other signs of fatigue.
2. Bearings supporting the fan prop shaft (Fig. 8a) should be greased every 50 to 100 fan hours.
3. When not to be run for a considerable period of time, the wall disconnect should be thrown.
4. All objects in the test section must be firmly secured to prevent slippage into the fan.
5. All modifications done to the tunnel must be done such that there are no leaks, which would show up as changes to the static pressure variations documented later in the calibration sections.
6. All modifications must be done such that the tunnel may be easily returned to its original state.

Appendix 2: Schlieren Flow-Visualization

A2.1 Purpose

The purpose of the investigation was to examine the instantaneous structure of a trailing vortex core. Many theories exist to describe the instantaneous structure, but little substantial evidence exists to support or refute the theories. The focusing schlieren was chosen over more conventional schlieren methods because of the sharp focusing capabilities, and the system is much more easily set-up and less expensive than more sensitive schemes, such as interferometry methods.

A2.2 History

The general methodology behind any of the variety of schlieren methods is relatively simple: density gradients across a system cause varied deflections of the incident light beams; and a cutoff removes the extraneous deflected light beams, thus giving an image of the flowfield that has varied light intensities. Depending upon the actual schlieren system employed, the density gradients may be represented as bright or as dark regions upon a dark or a light background, respectively. Such systems were originally employed in Germany to detect faults in glass, termed schlieren⁵⁶. More recently a wide variety of schlieren systems have been developed to analyze subsonic, transonic, and supersonic

flows, reacting flows, and many of the other complex flowfields of interest to researchers. Though a number of attempts have been made to develop quantitative schlieren systems⁵⁶,⁵⁷, schlieren visualization is used mostly for qualitative investigations. Though schlieren systems have certain inherent limitations, recent advances, in particular the development of the focusing schlieren system, have opened the flow visualization scheme to ever more complex flow analysis.

A2.2 Principles of Schlieren Systems

Many sources exist which describe in great detail all of the principles behind schlieren systems (see for example references 56 and 57). Therefore, the following discussion is rather restricted to the employment of such systems to the current investigations of trailing vortices in a subsonic wind tunnel facility.

A typical Toepler schlieren arrangement is depicted in Figure 107. The deflections of the incident light beam are proportional to the refractive index gradient in the direction normal to the path of the light beam. In Figure 107, the light beam is in the z direction. Thus the gradients are assumed to be in the x-z and y-z planes, and the angular deflections are thus

$$\epsilon_x = (1/n_o) \int (\partial n / \partial x) dz$$

$$\epsilon_y = (1/n_o) \int (\partial n / \partial y) dz$$

where n_0 is the refractive index of air, n is the refractive index of the test section medium, and ε_x' and ε_y' are the angles that the deflected light path makes with the x and y axes, respectively.

These equations illuminate the most significant problem inherent in the employment of standard Toepler schlieren methods, as well as many other schlieren schemes: the image formed is due to the integrated effects of all optical disturbances along the path of the beam. Especially when considering complex three dimensional flow features, such integration effects can obscure all of the important flow features.

North, et.al.^{56,57} showed that the contrast, C' , of the deflected part of an image with the background light can be given by

$$C' = \delta I / I = f_2 \delta \varepsilon / a$$

and the contrast sensitivity, S , by

$$S = dC' / d\varepsilon = f_2 / a$$

where I is the illumination of the screen, f_2 is the focal length of the second mirror, ε is again the angular deviation of the beam from its original path, and a is the height of the image passing by the knife edge (Figure 108)⁵⁶. Associated with the contrast and sensitivity is a range of beam deflection, beyond which increased beam deflection will have no effect upon the image contrast and the system sensitivity. The maximum range of angular deflection, $(\delta \varepsilon)'$, associated with this range is thus given by⁵⁶

$$(\delta \varepsilon)' = (h / f_1)$$

where h is the height of the light source being employed. With the system designed such that the range is equivalent for deflections towards and away from the cutoff, the corresponding height, a , of the source image above the cutoff is thus⁵⁶

$$a=5f_2(\delta\varepsilon)$$

Because such high refractive indices are present in subsonic wind tunnels (in comparison to the low refractive indices available in supersonic and hypersonic wind tunnels), the typical problem is usually associated with achieving an acceptable working range^{56, 57}. The range of the Toepler schlieren apparatus being employed can be improved by increasing the height, h , of the source or by decreasing the focal length of the first mirror, f_1 .

An alternative setup, called a focusing schlieren, greatly reduces the depth of focus of the schlieren system, thus diminishing the integration length^{53, 54}. A brief history of the focusing schlieren methodology and recent developments are outlined in several papers by Weinstein^{53, 54}. A typical focusing schlieren system, based upon the design of Weinstein⁵³, is drawn in Figure 109.

To uniformly illuminate the flowfield, light from the source first passes through a diffuser. The exit light then uniformly illuminates the source grid. The light which passes through the source grid is passes through a focusing lens. The purpose of the focusing lens is to project an ever decreasing cone of light through the test section, thus uniformly illuminating the flowfield. The cone is optimally focused to the diameter of the primary receiving lens. Light incumbent upon the receiving lens is thus transmitted to the cutoff

grid. Ideally, only deflected light passes through the cutoff grid. The image of the flowfield gradients is thus formed at the image plane.

The source grid may be of any geometrical design, though for simplicity the grid considered herein is constructed of parallel lines. The cutoff grid is thus the photographic negative image of the source grid. In a focusing schlieren system, an image is formed from several different light sources: the image is in focus if the images corresponding to each light source overlap and is thus out of focus if they do not overlap (Figure 110). Movement of the image plane location allows for traversing of the plane in focus through the flowfield.

The sensitivity of a focusing schlieren system is given by^{53, 54}

$$(\delta\epsilon)' = 2aL/(L'(L-l))$$

where L is the distance from the source grid to the primary receiving lens, l is the distance from the flowfield to the receiving lens, and L' is the distance from the receiving lens to the cutoff grid.

Because L' tends to be small and the term $L/(L-l)$ tends to be large, the source image height $2a$ needs to be very small to achieve a satisfactory system sensitivity. The ability of the receiving optics to resolve such fine grid lines is a stringent requirement.

The resolution attainable with the focusing schlieren system employing grid lines is dependent upon the resolution power of a slit aperture. From Longhurst [*Geometrical and Physical Optics*, p.282], objects are resolved if the separation of their geometrical images is equal to the distance from the center of one (airy) pattern to the first minimum.

That is, objects are considered resolved if they are separated by a distance h' ⁵⁸ (Figure 110),

$$h' = \lambda / (2n' \sin U')$$

where λ is the wavelength of the light, n' is the refractive index of the medium, and U' is the angle the light cone makes with the horizontal. This can be simplified by assuming small angular displacements ($\sin U' \approx U'$) and assuming the medium is air ($n=1$),

$$h' = \lambda / (2U')$$

Substituting from Figure 110 for the known geometrical parameters, this becomes

$$h' = \lambda (l' - L') / b$$

where b is the cutoff grid slit height.

Considering the magnification, m , from the flowfield to the image screen,

$$m = l'/l$$

the resolution, w , becomes

$$w = h' / m$$

$$w = \lambda (l' - L') l / (b l')$$

which is the same expression found by Weinstein⁵³.

One of the most attractive features of a focusing schlieren system is the ability to analyze a slice of the complex 3-dimensional flowfield. Thus, one must define two depths of focus associated with the focusing schlieren, termed "sharp focus depth" and "unsharp focus depth" by Weinstein^{53, 54}. The first refers to the system being out of focus because the object is at a depth which exceeds the resolution capability of the system. And the

second indicates that an object of a specified arbitrary size is unresolvable due to it being at a depth too far from the particular focal plane in the flowfield.

An unsharp depth of focus is defined by Longhurst [*Geometrical and Physical Optics*, pp.287-288] in terms of the Rayleigh 1/4 - wave limit, i.e., there will be no appreciable deterioration of the image, i.e., no marked change from the airy pattern, provided the maximum phase difference between disturbances arriving at the center of the pattern does not exceed $\pi/2$, which corresponds to a reduction in intensity at the center of the pattern of 20-30%. From Figure 111a, this limitation becomes (with $\delta l' \ll A'B'$)

$$\delta l' = \pm \lambda / (8n' \sin^2(U'/2))$$

A less strict definition follows from Figure 111b,

$$\delta l' = \pm r / \tan(U')$$

with r defined as a limit to the radius of the circular patch of light induced by shifting the image plane a distance $\delta l'$ from the focus point, B' , of a point image [Longhurst, *Geometrical and Physical Optics*, pp.287-288]. Thus, based upon these criteria, the double sided depth of unsharp focus is

$$DOF_U = 2\delta l' = 2r / \tan(U')$$

and assuming small angles ($\tan U' \approx U'$),

$$\begin{aligned} DOF_U &= 2r/U' \\ &= 2r/((D_m/2)/l') \\ &= 4rl'/D_m \end{aligned}$$

The unsharp depth of focus is directly related to the resolution power of the focusing schlieren system, which in the current investigation is controlled by the resolution power of the slit apertures comprising the cutoff grid. From Longhurst [*Geometrical and Physical Optics*, pp. 282], the limit of resolution due to a slit is such that objects are resolved if the separation of their geometrical images is equal to the distance from the center of one (Airy) pattern to the first minimum (of the second airy pattern). That is, two point sources are considered resolved if they are separated by a distance h' ,

$$\begin{aligned}
 h' &= .5\lambda/(n'\sin U') \\
 h' &= \lambda/2U' \\
 &= \lambda/2((b/2)/(l'-L')) \\
 &= \lambda(l'-L')/b
 \end{aligned}$$

And, considering the magnification from the flowfield to the image screen, $m=l'/l$,

$$\begin{aligned}
 \text{Res} &= h'/m \\
 \text{Res} &= \lambda(l'-L')l/(bl')
 \end{aligned}$$

Thus, the depth of sharp focus, as defined by Weinstein^{53, 54}, is

$$\begin{aligned}
 \text{DOF}_s &= \text{Res} * l/D_m \\
 \text{DOF}_s &= \lambda(l'-L')l^2 / (bl'D_m)
 \end{aligned}$$

A2.3 Instrumentation/Results

The employment of any schlieren system requires the existence of density gradients in the flowfield to be examined. In the current investigation, the wingtip was heated. The heated air was centrifuged to the lower pressure vortex core, thus imposing a thermal gradient between the vortex core and the surrounding wake structures. Other studies have utilized similar vortex heating to track the downstream development of trailing vortices¹⁵. Numerical studies by Mironer⁵² have shown that heating of the vortex core does not increase the dissipation of vorticity from the core, thus a heated core would be a good representative of a non-heated vortex. Helium injection was considered for the introduction of a refractive index gradient, but mass injection from a wingtip has been shown to cause rapid expansion of the vortex core⁶⁰. Thus, heating of the wingtip was chosen.

The current investigation was conducted in the 3'x2' subsonic wind tunnel. The wing model employed was the same NACA 0012 airfoil used in the flow visualization and quad-hot-wire experiments. It has a chordlength of 8" and was mounted at an aspect ratio of 3.0 (Figure 38). The boundary layer was tripped with a uniform 20-40% trip consisting of .5mm glass beads glued to the surface of the wing model with an average bead density of 200 beads/cm².

The wingtip was heated by the insertion of a ni-chrome heater coil into a hollow NACA 0012 wingtip affixed to the end of the test wing. The heater was powered by a

variable wattage power supply with a range from 0-300 watts. The 14 gauge wires connecting the heater and the power supply passed inside a trough on the pressure side surface of the wing underneath the trip.

The light source chosen was a 45 Watt pulsed copper vapor laser produced by Oxford Lasers. The laser was mounted to a fixed height table. A mirror mounting system was attached to the table to allow elevation changes of the laser beam (Figure 112). Mirror stands were built that allowed for passage of the light beams through the centerline of the tunnel test section.

Many different focusing and regular schlieren system configurations were employed in the study. Several of the different variations are presented in Figures 113 and 114. Each of the systems were employed to fix various technical problems. Most of the problems encountered concerned alignment of several mirrors separated by many meters. However, the greatest difficulty, and one which turned out to be insurmountable, involved making an acceptable source and cutoff grid. The source grid is supposed to consist of alternating clear and opaque lines, and the cutoff grid is supposed to be the photographic negative image of the source grid at the cutoff location. The difficulty associated with making an acceptable source grid was relatively easily overcome, as an opaque source grid can be mechanically made. The ability to make an acceptable cutoff grid, however, managed to elude us. For a diffuse light source, a photographic negative may be sufficient⁵³. However, in the current investigation, the bright laser light transmitted through all regions of the negative. Thus, the contrast in the image plane was almost imperceptible except in

the most extreme of circumstances. Such an extreme circumstance included viewing of a heater element in the optical path (see for example Figure 115).

To eliminate the difficulty associated with the formation of the cutoff grid, a typical Toepler schlieren system was formed (Figure 116). As previously discussed, a major disadvantage of the Toepler schlieren system is the optical path integration inherent with all such systems. That is, any and all optical defects in the path of the light beam affects the image quality. Thus, the tunnel walls distorted the light beam and the image. The tunnel walls in the beam path were replaced with 3/8" plate glass, but the glass quality still adversely affected the image quality. Only with a heater element directly in the beam path could density gradients be viewed.

A2.4 Conclusions

A heated wingtip has been constructed. Several mirror mounts and a laser table have also been constructed. Though many variations of both focusing and Toepler style schlieren systems were tested, only limited results were obtained. The primary difficulty encountered was in making an acceptable cutoff grid. Future work should concern alternative means for making a cutoff grid with alternating clear and extremely opaque areas.

Tables

Table 1. Measurements from Tip Flow Visualizations

AR	Rec x1000	Angle of Attack (deg.)	(X/2)/C	(2a)/C	(2b)/C	Gamma 1 / Gamma 2	Site/C	Ste/C	Max. Vtible Flow Angle (deg.)	Gamma 1 / Unif.Cmeas	Gamma 2 / Unif.Cmeas
3	130	2.5	5	0.33071749	0.0336323	0.0805	0.0874439	2.6	0.0401	0.0446	
			7.5	0.33022573	0.027088	0.0497	0.0722348	2.67	0.0435	0.0453	24.01
260		2.5						0.0635		0.1579	0.0607
			5	0.32735426	0.0336323	0.0538	0.072991	2.2	0.0614	0.063	0.118
			7.5	0.30361174	0.027088	0.0519	0.0767494	2.83	0.0432	0.0514	0.0442
335		2.5						0.0508		0.12	
			5	0.326223318	0.029148			0.0641	0.0502	31.66	0.0546
			7.5	0.31715576	0.0248307	0.0655	0.106948	4.27	0.0435	0.0535	0.0457
2.5	130	2.5						0.055		27.4	0.0506
			5	0.33983008	0.0344828	0.039	0.0434783	1.26	0.043	0.0297	0.2162
			7.5	0.32028112	0.0251004	0.0577	0.0903614	3.6	0.0653	0.0631	0.0392
260		2.5						0.0657		31.5	0.0391
			5	0.33358321	0.0304848	0.04	0.0494753	1.62	0.0332		0.0446
			7.5	0.30271084	0.0190763	0.0592	0.0939916	5.21	0.039		
335		2.5						0.0577		0.0586	0.0361
			5	0.34107946	0.0289855	0.039	0.0489755	1.69	0.0327	0.1918	0.0368
			7.5	0.31551205	0.0210843	0.0417	0.062249	2.95	0.0375	0.0553	0.0322
								0.0537		42.07	0.0275
								0.0912		0.0812	

Table 2. Errors and Uncertainties Associated with the Tip Flow Analysis

	X/C	(2a)/C	r/C	$\frac{\Gamma_1}{\Gamma_2} = \frac{(2b)}{(2a)}$	H_n	S_n	Γ_1	Γ_2	Maximum Flow Angle
Uncertainty									
r.s.s. Error	.045	0.006	0.006	0.237	0.00224	0.00212	0.0107	0.008	+5°

Table 3. Vortex Core Parameters

Case	$U_\infty c/v$	α	AR	x/c	r_e/c	$V_{\theta e}/U_\infty$	$U_p/V_{\theta e}$	r_p/c	$V_{\theta p}/U_\infty$	$\Gamma_e/U_\infty c$	$\Gamma_p/U_\infty c$	σ_e/c	σ_p/c
1 ^a 0	33000	5.0°	2.5	10									
2	"	5.0°	"	"	.038	.304	.1458	.02174	.2656	.0726	.0363	.003	.004
3	"	3.75°	"	"	.028	.23	.1782	.028	.23	.0405	.0405	.004	.005
4	"	6.25°	"	"	.0435	.378	.1083	.0203	.2920	.1033	.0372	.003	.003
5	"	7.5°	"	"	.048	.44	.07242	.02163	.3274	.1327	.0445	.003	.003
6	"	2.5°	"	"	.025	.143	.1453	.025	.143	.0220	.0220	.007	.008
7	"	5.0°	2.75	"	.038	.308	.1454	.02174	.2691	.0735	.0363	.003	.004
8	"	5.0°	3.0	"	.039	.312	.1413	.02227	.2656	.0764	.0372	.004	.004
9 ^b		5.0°	3.0	12									

^aQuad-hot-wire grid survey.

^bSingle hot-wire grid survey.

Figures

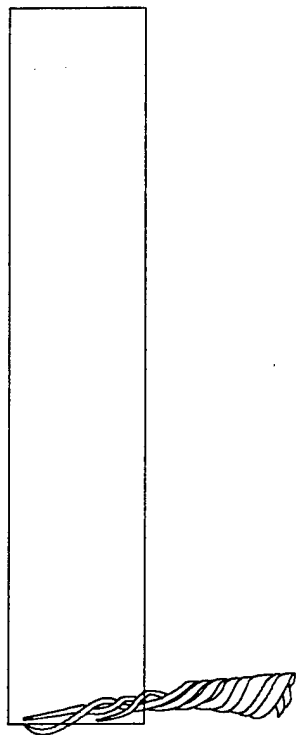
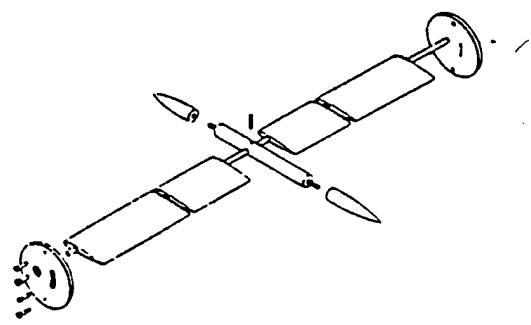


Figure 1. Coalescence of a General System of Wingtip Vortices



Model assembly showing flow aligned cylinder and airfoils.

Figure 2. Experimental Model of Bandyopadhyay, et.al.²²

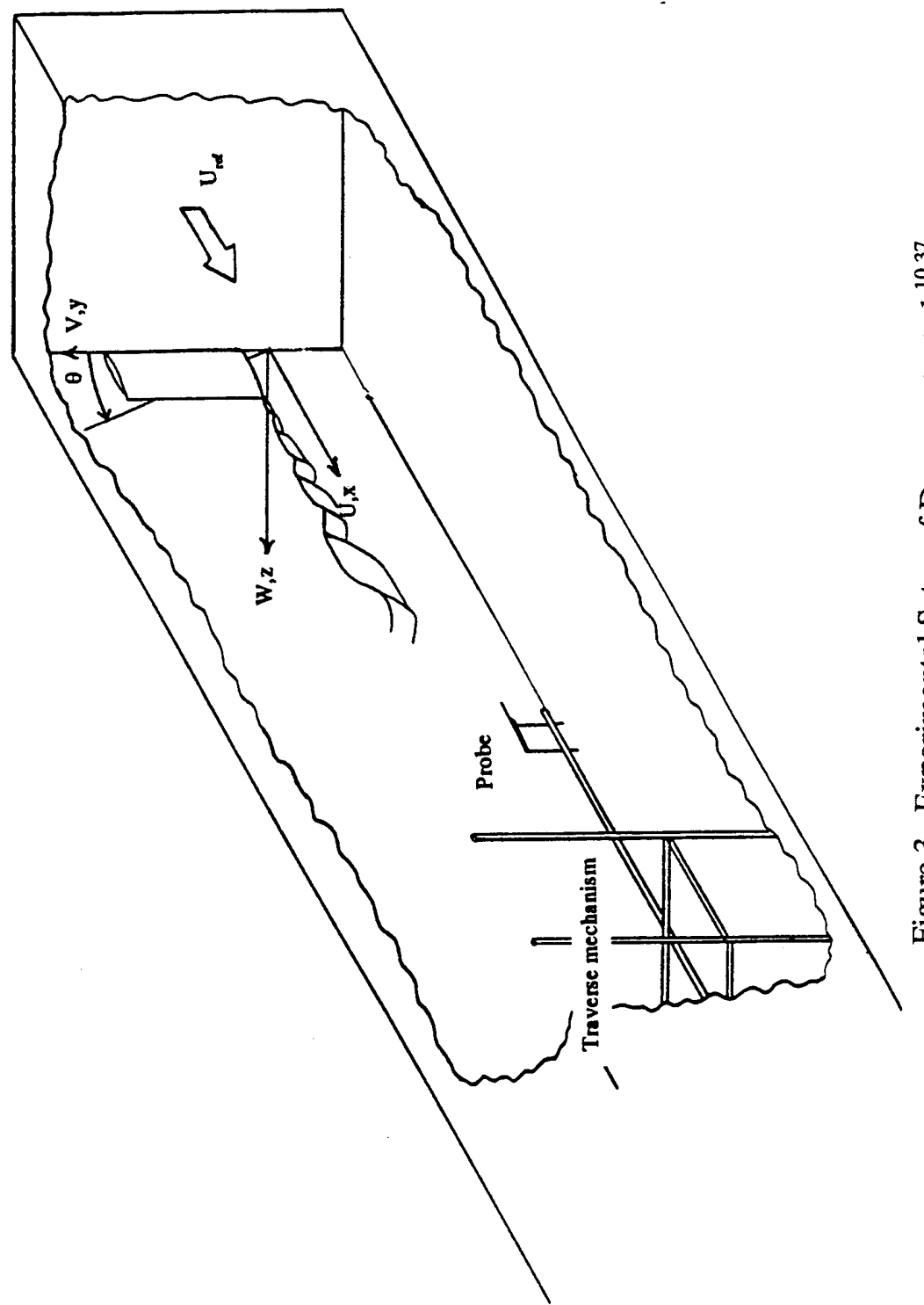


Figure 3. Experimental Setup of Devenport, et.al. ^{10,37}

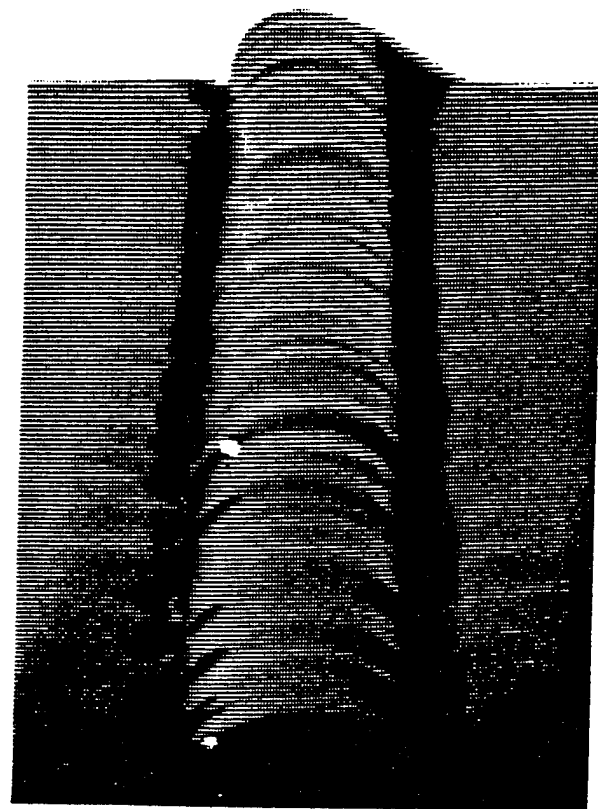


Figure 4. Vortex/Free-Surface Interaction (Sarpkaya¹⁸)

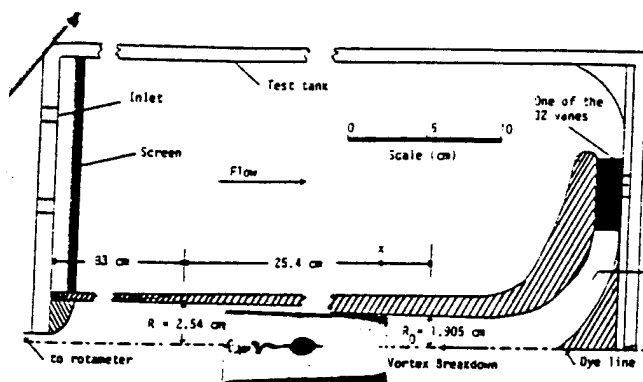
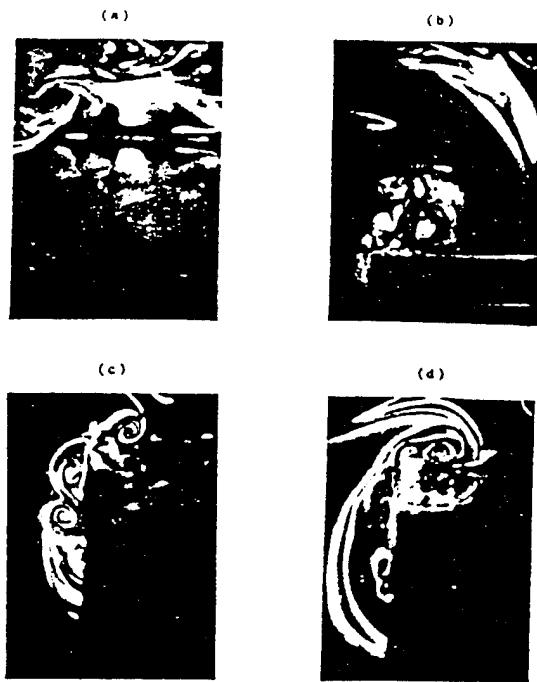


Figure 5. Experimental Setup of Sarpkaya²⁴

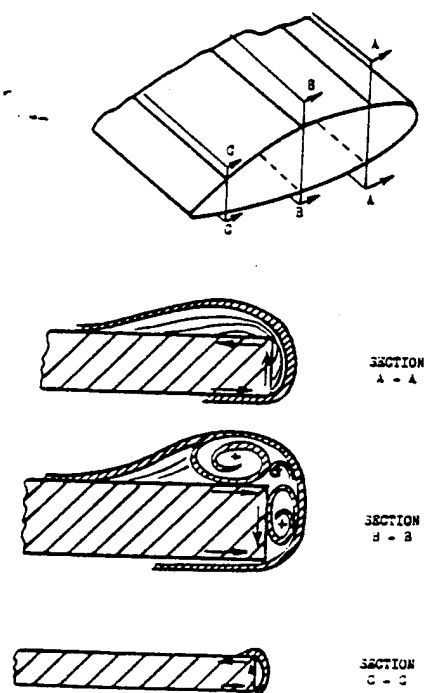


A series of photographs of the primary and several secondary vortex structures around the tip of the hydrofoil.

- (a) $V = 0.46 \text{ m/s}$, $\alpha = 2 \text{ deg}$, $X/C = 0.70$
- (b) $V = 0.12 \text{ m/s}$, $\alpha = 5 \text{ deg}$, $X/C = 0.92$
- (c) $V = 0.05 \text{ m/s}$, $\alpha = 12 \text{ deg}$, $X/C = 0.46$
- (d) $V = 0.46 \text{ m/s}$, $\alpha = 2 \text{ deg}$, $X/C = 0.70$

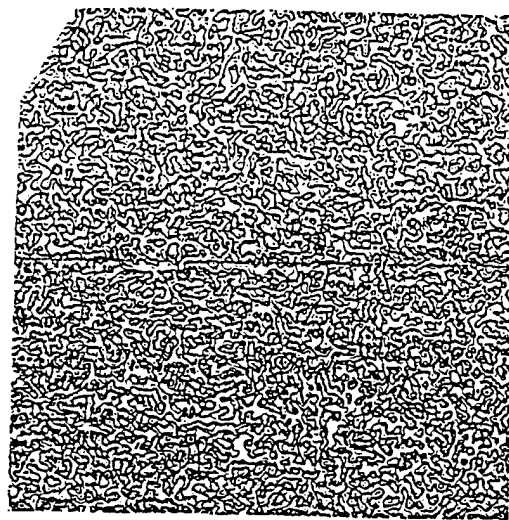
The actual size of the image shown in each photograph is 10.4 cm. The primary structure is the clockwise rotating vortex which is located above the foil.

Figure 6. Complex Wingtip Vortex System about a Blunt Tip Hydrofoil (Francis and Katz²⁷)

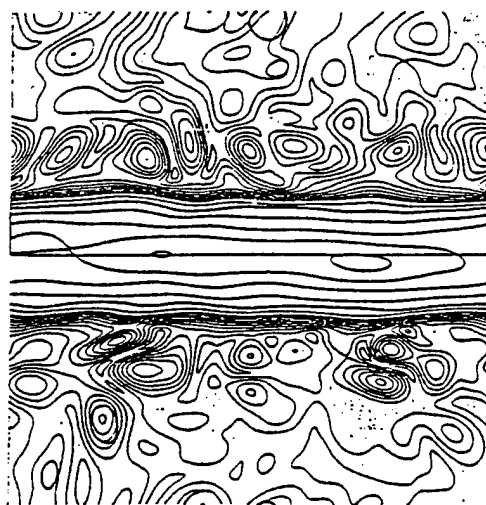


Sketch of flow patterns around square tip.

Figure 7. Schematic of Shear Layer System about a Blunt Tip Airfoil (Hoffman and Velkoff²⁶)



a.



b.

Contours of vorticity.

- a. $t=0$
- b. $t=85.15$

Figure 8. Coherent Structure Organization of Fine Scale Turbulence
(Melander and Hussain¹⁹)

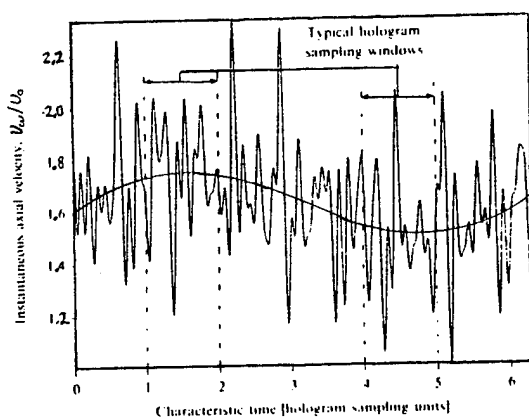


Figure 9. "Slow" Time Dependent Axial Velocities of a Trailing Vortex Core (Green and Acosta²³)

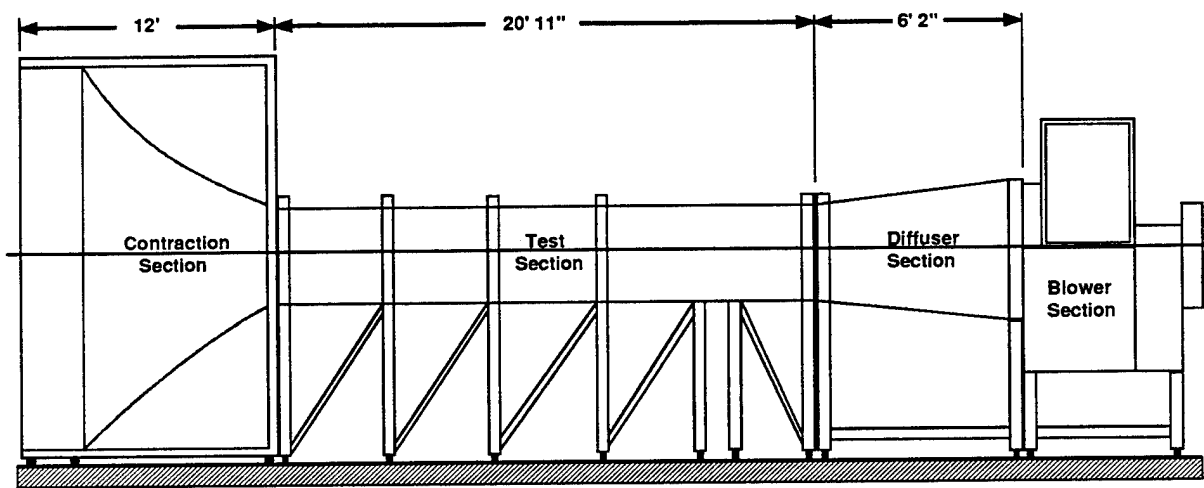


Figure 10. 3'x2' Subsonic Wind Tunnel Profile Sketch

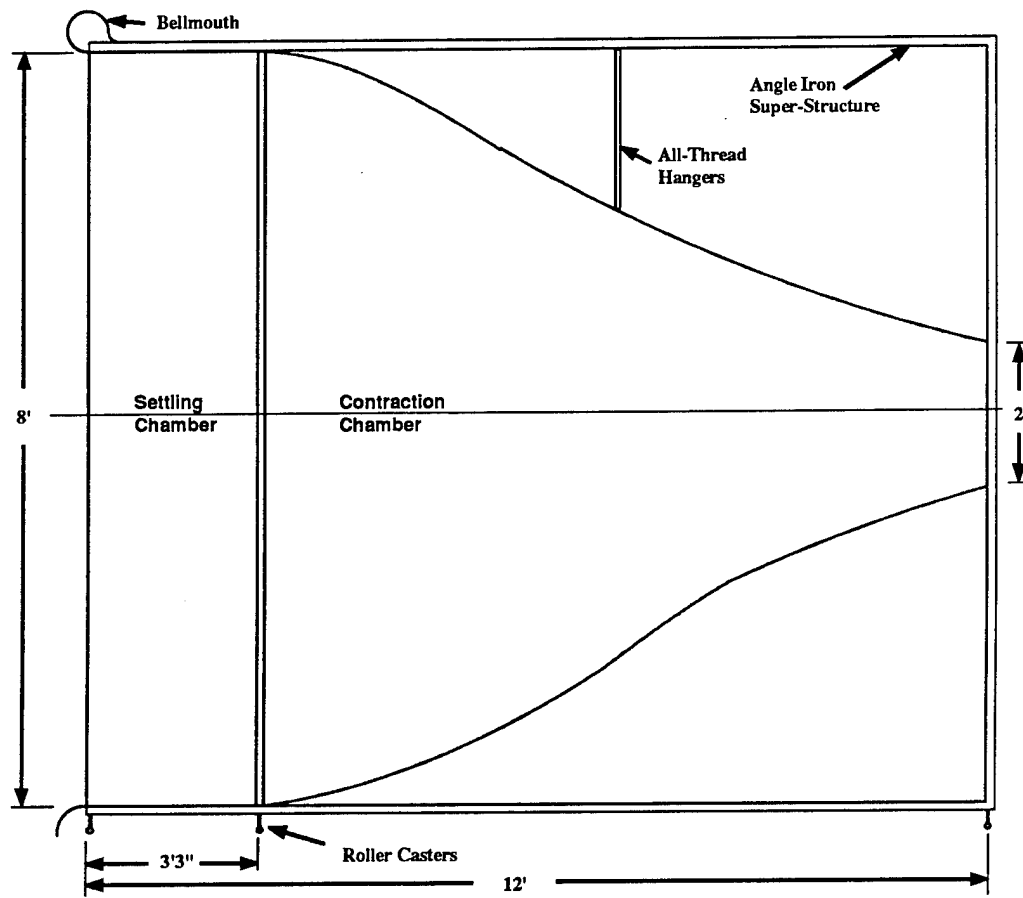


Figure 11. Contraction Sideview

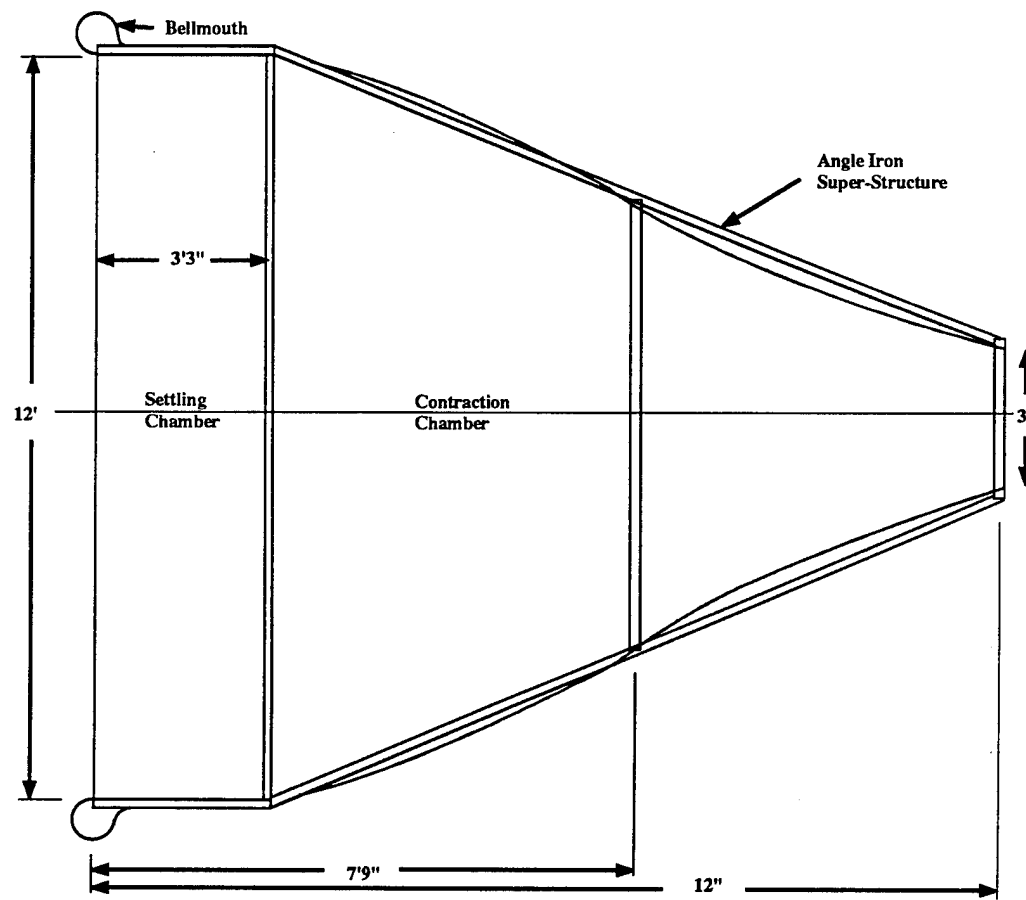


Figure 12. Contraction Topview

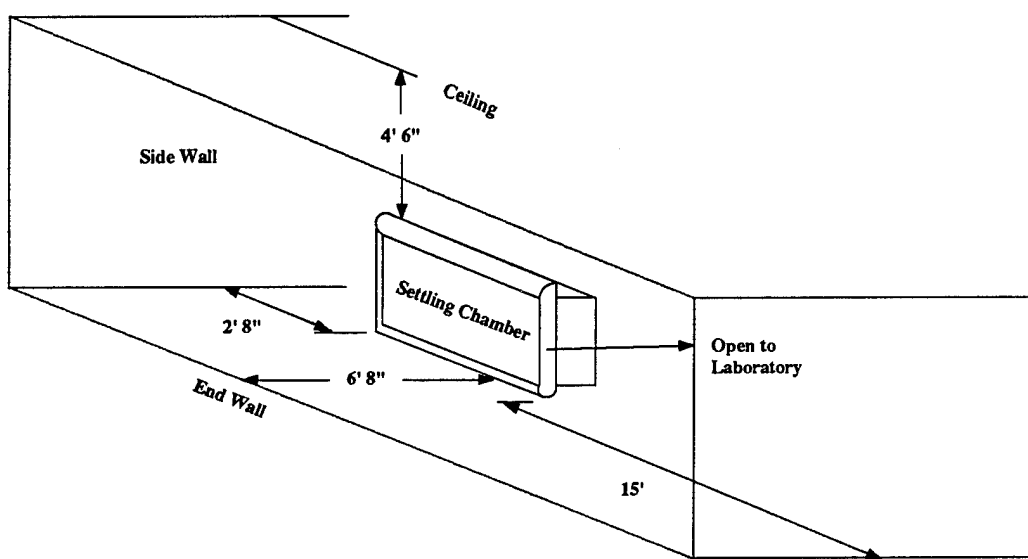


Figure 13. Inlet Proximity to Laboratory Walls

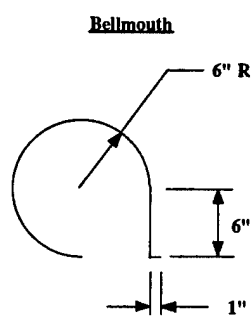
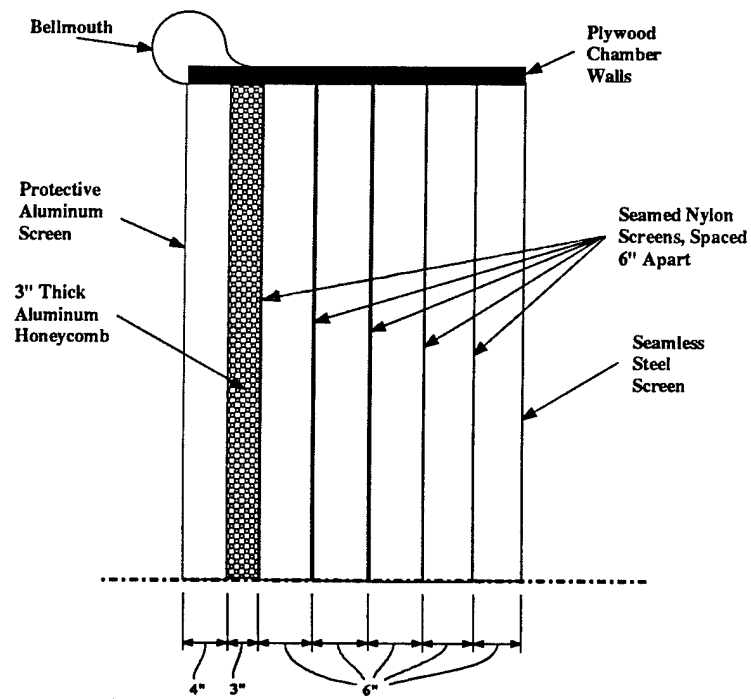
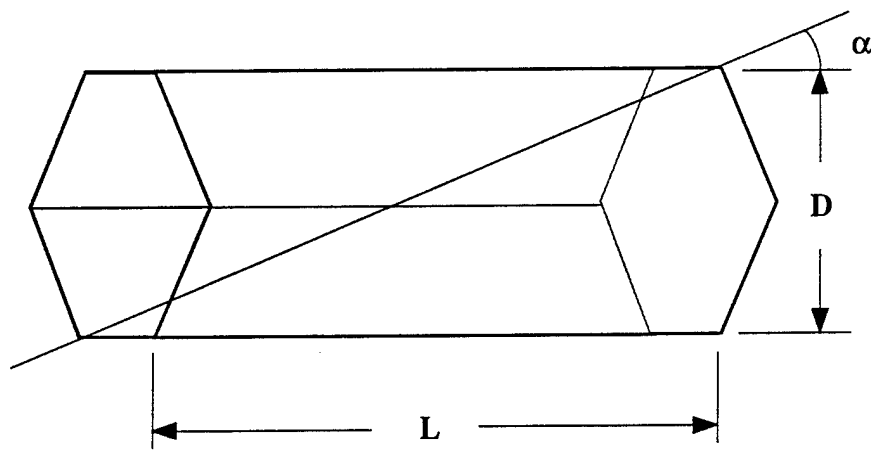
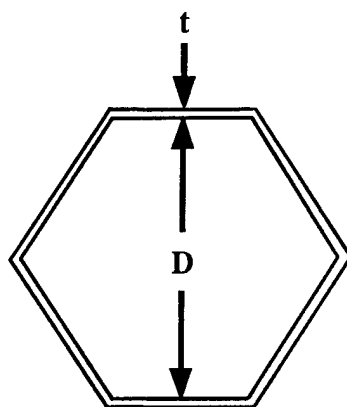


Figure 14. Settling Chamber with Bellmouth



$$\alpha = \tan^{-1}(D/L)$$



$D = .260''$
 $L = 3.0''$
 $t = .0007''$

$$\text{Closed Area/Open Area Ratio} = \frac{\text{Area of } 1/2 \text{ Wall Thickness}}{\text{Internal Area}}$$

Figure 15. Flow Angularity

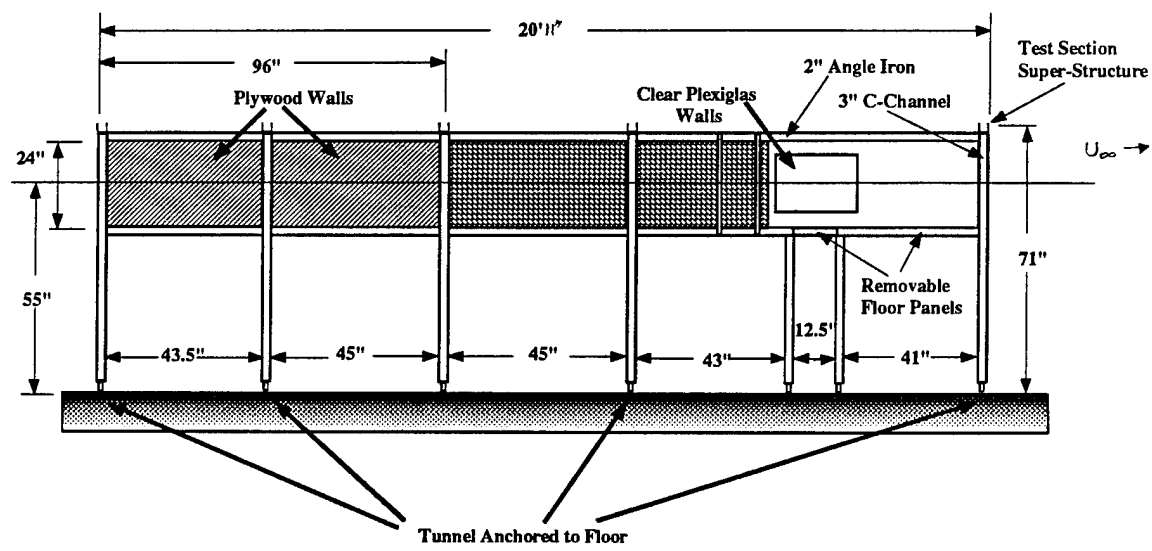


Figure 16. Test Section, Right Side

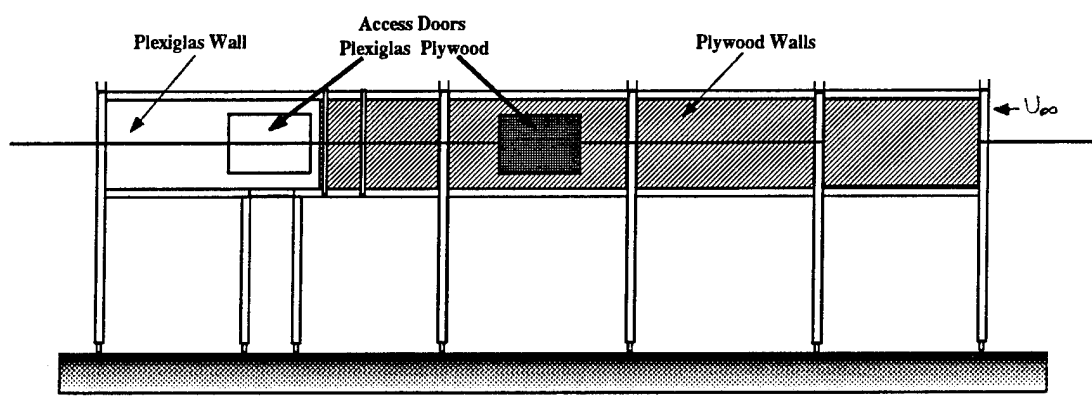


Figure 17. Test Section, Left Side

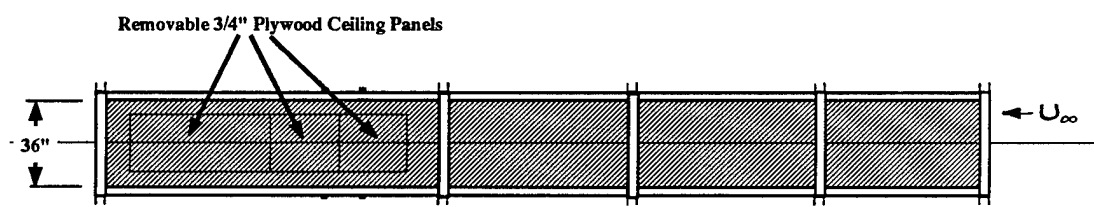


Figure 18. Test Section, Top View

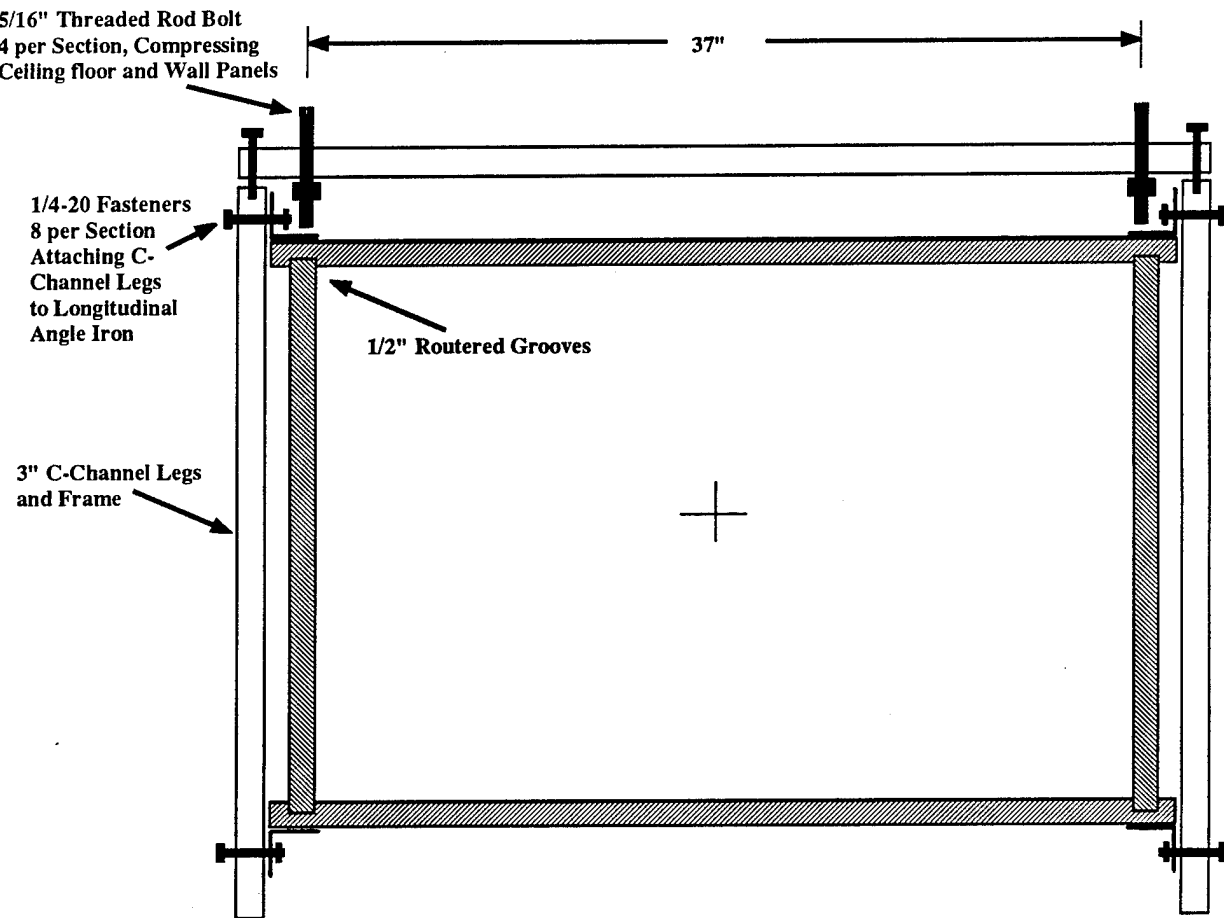


Figure 19. Wall, Ceiling, and Floor Compression

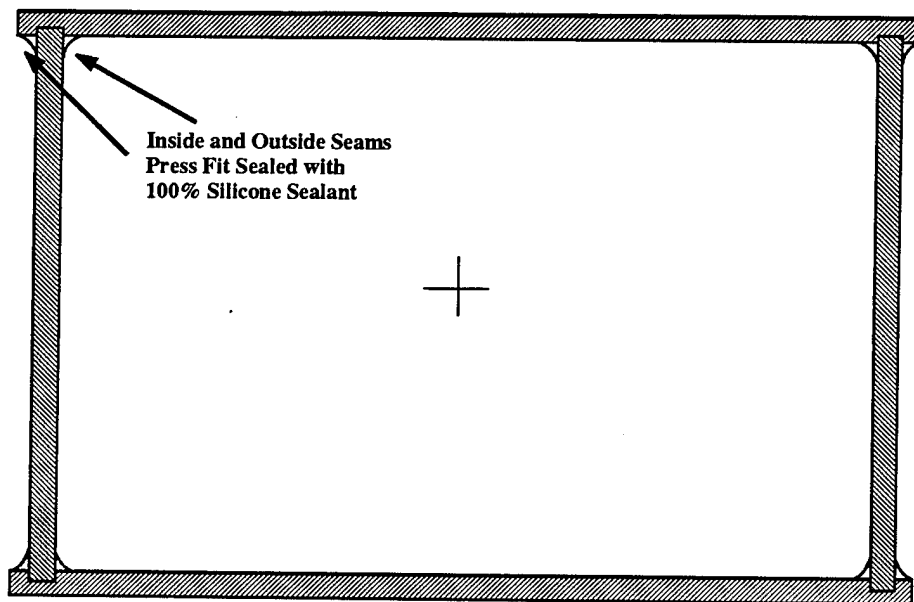


Figure 20. Inside and Outside Seam Sealant

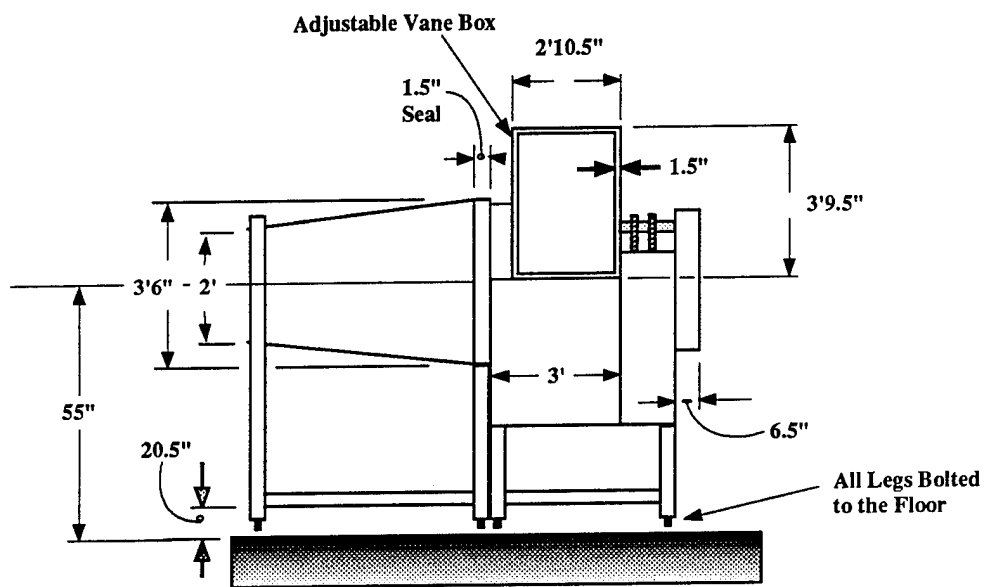


Figure 21. Blower and Diffuser Sections, Front View

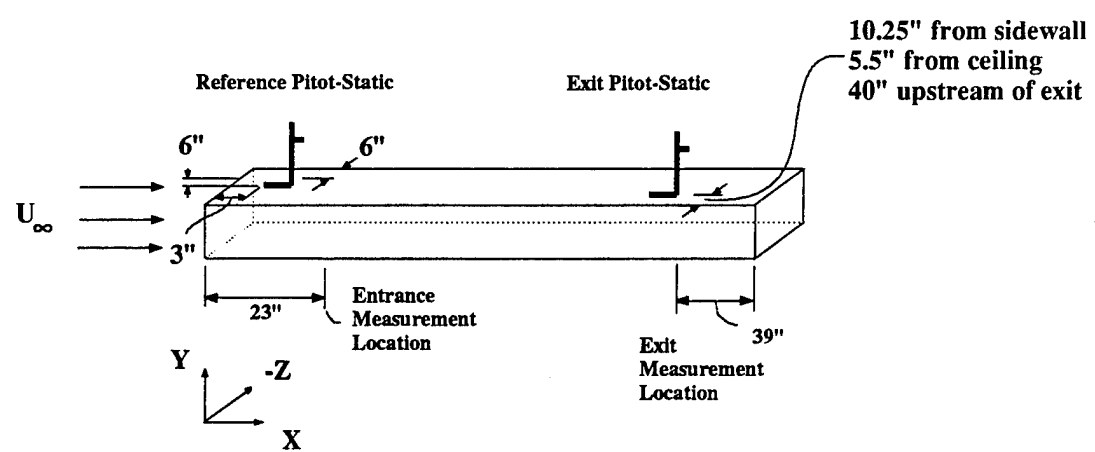


Figure 22. Test Section Coordinate System and Pitot-Static Locations

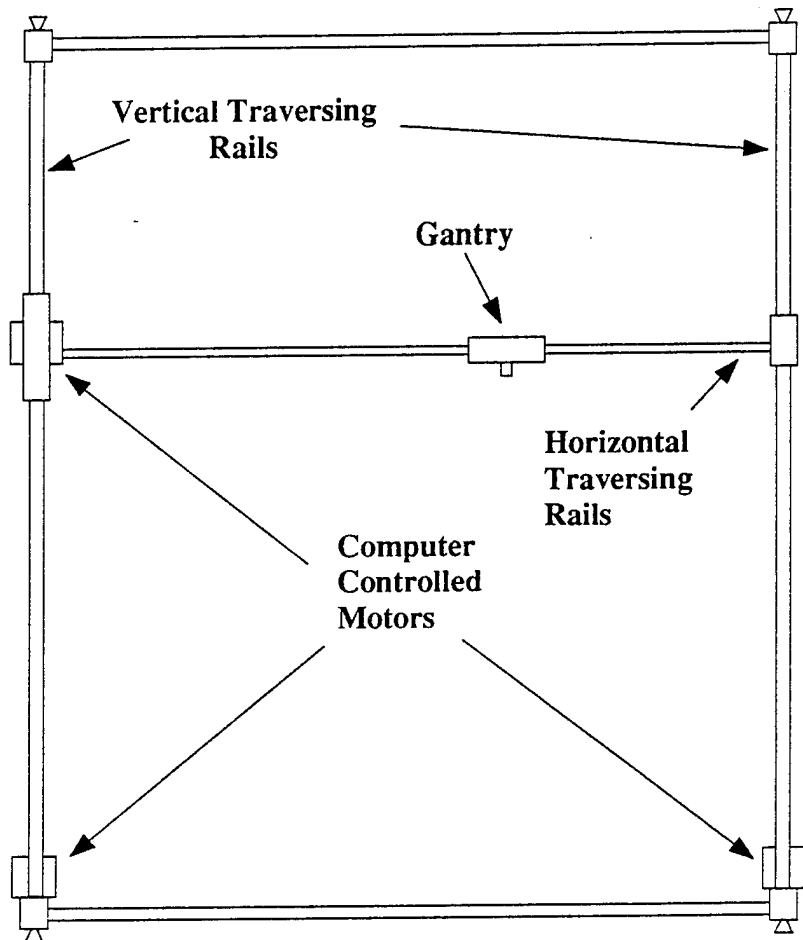
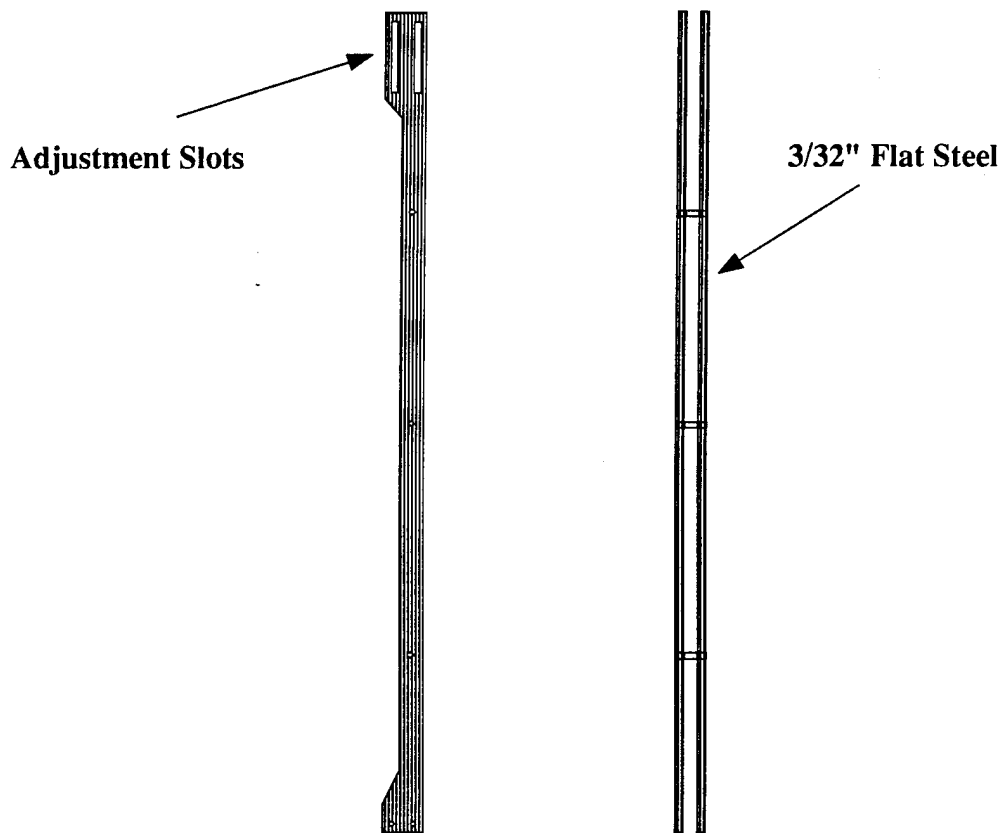


Figure 23. VA Tech Stability Tunnel 2-Axis Traverse

Vertical Probe Support



Streamlined Probe Holder

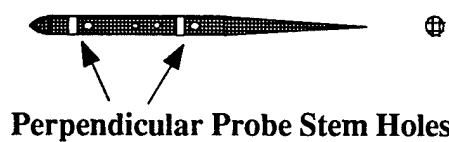


Figure 24. Probe Support

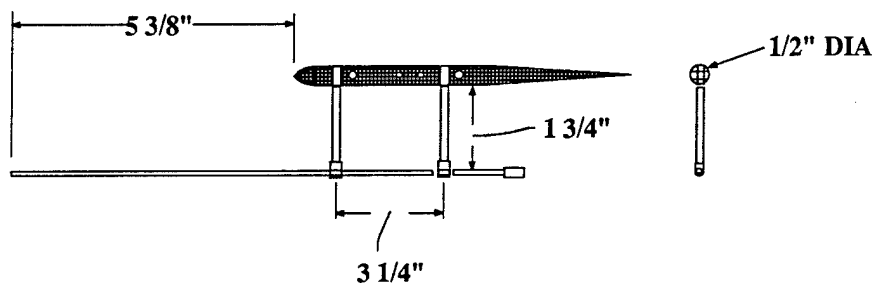


Figure 25. Hot-Wire Probe Offset

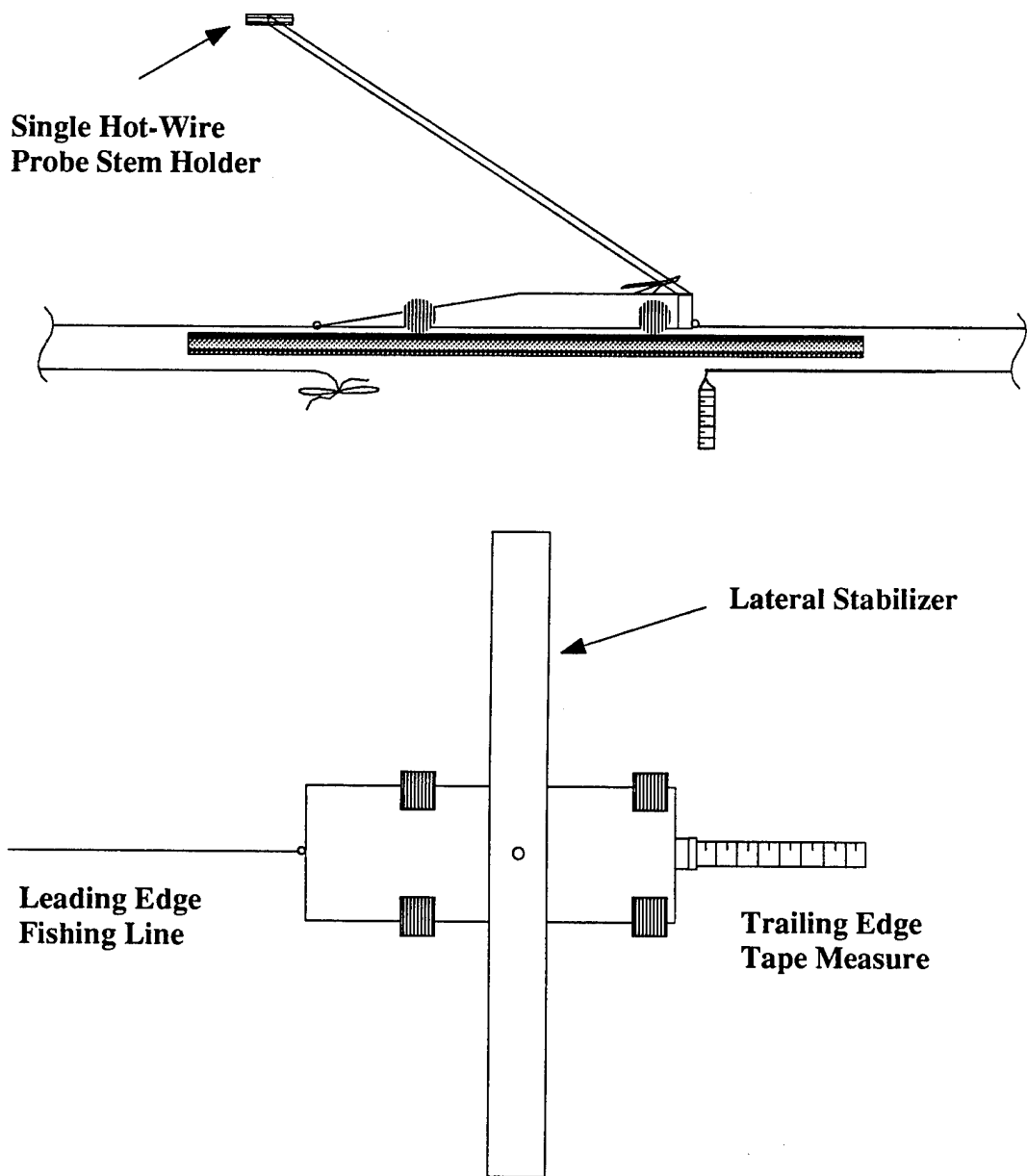


Figure 26. Streamlined Longitudinal Traverse

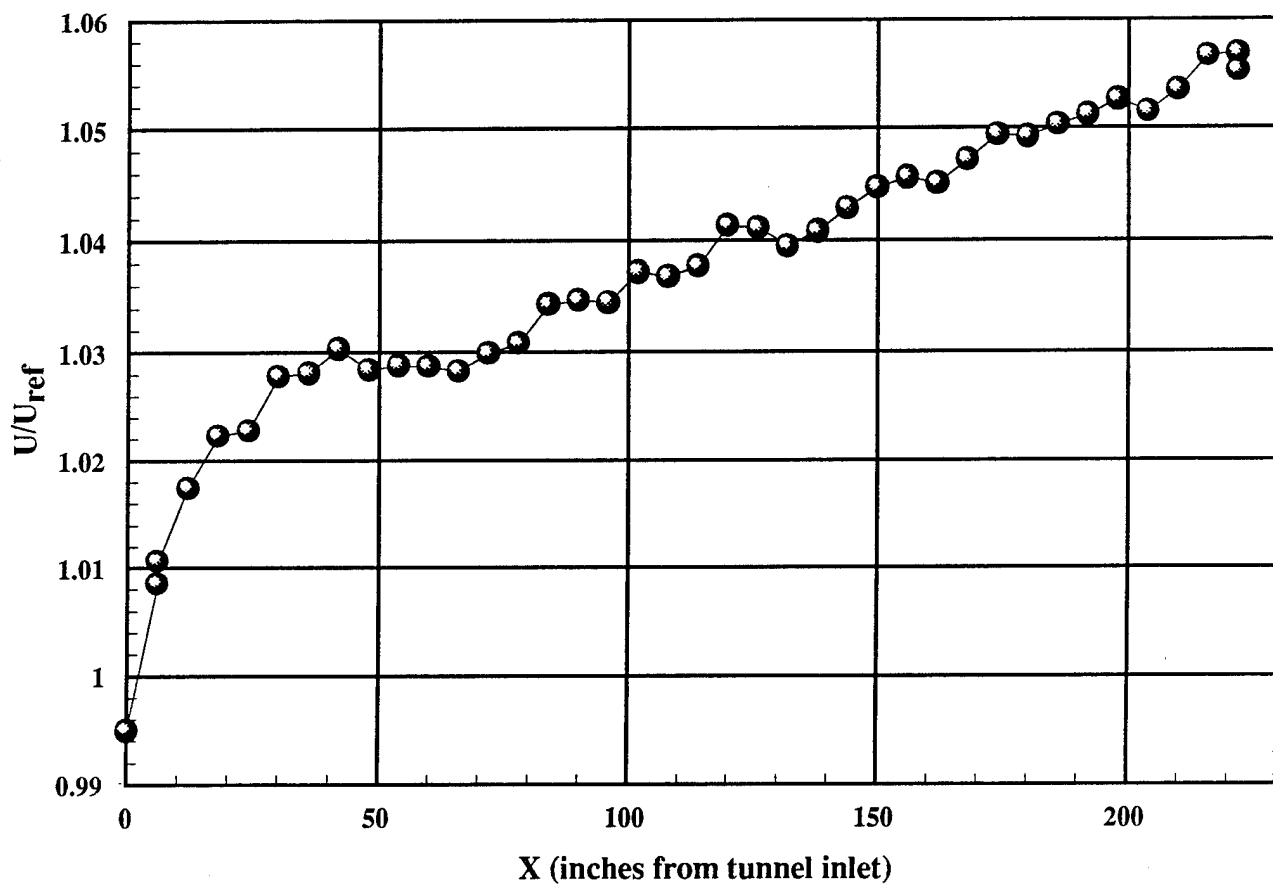


Figure 27. U/U_{ref} Variations along Tunnel Centerline, $Re_x=1.6 \times 10^6$

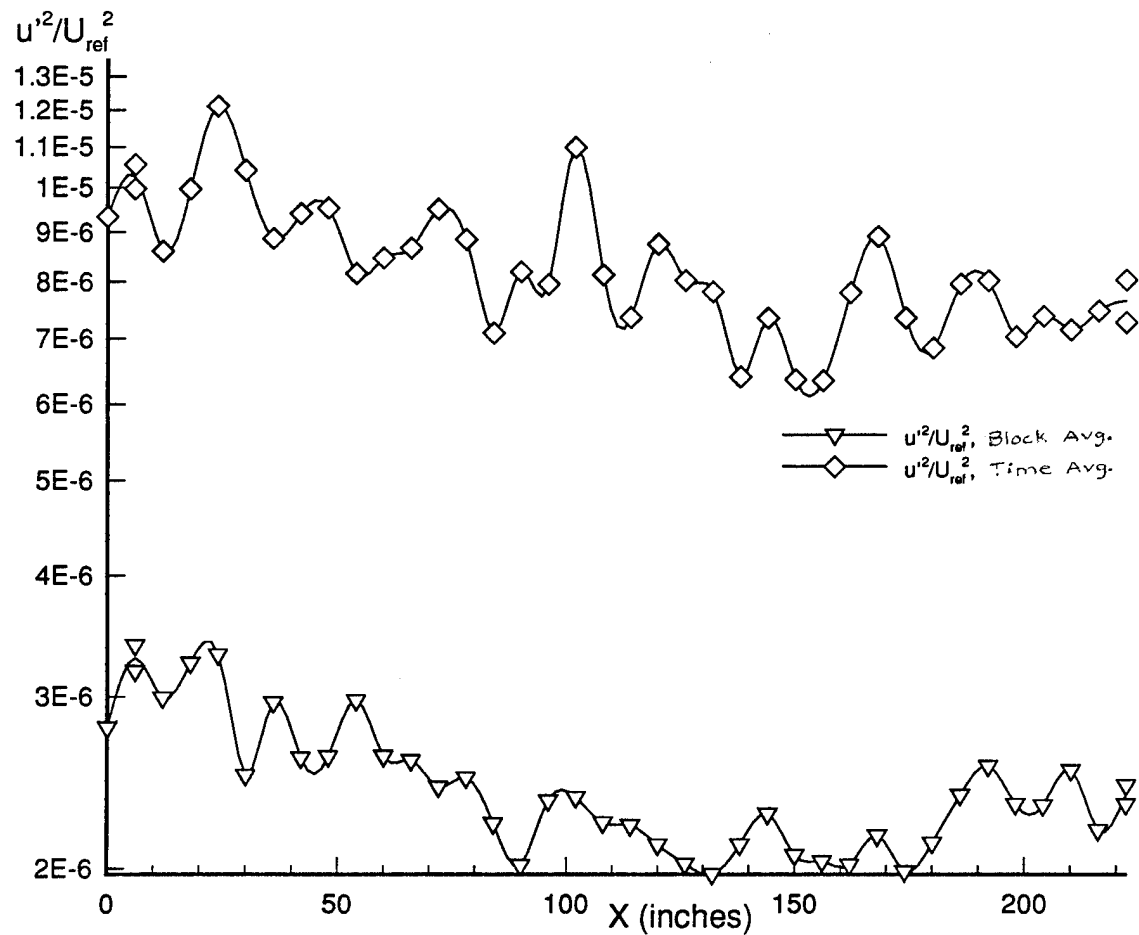


Figure 28. u'^2/U_{ref}^2 Variations along the Tunnel Centerline, $Re_x=1.6 \times 10^6$

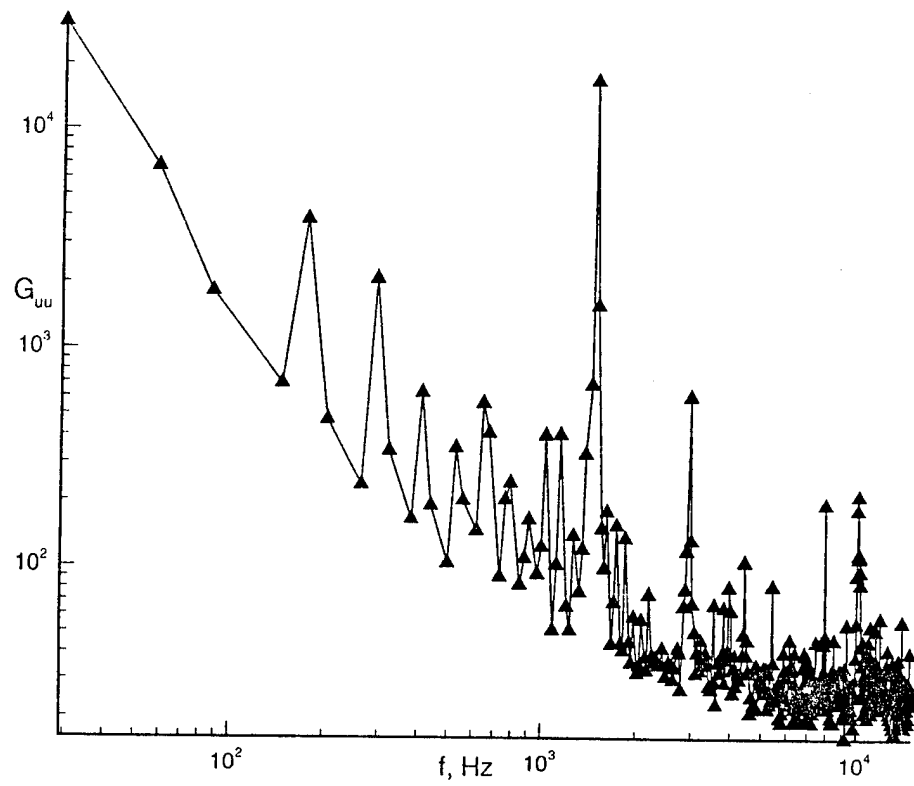


Figure 29. G_{uu} Power Spectrum at $X=0''$

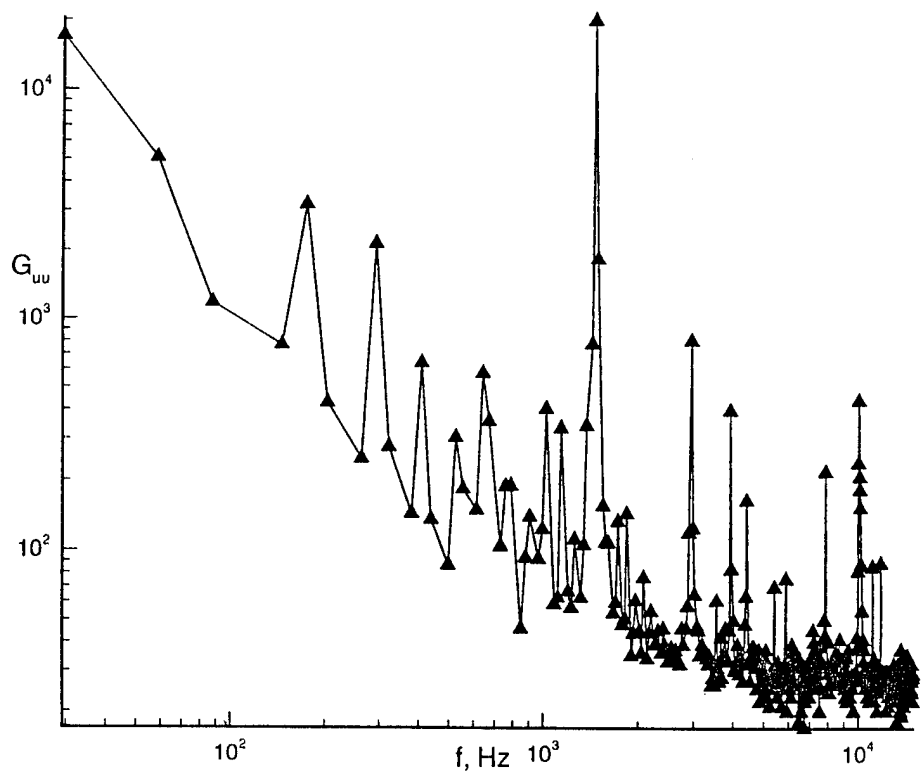


Figure 30. G_{uu} Power Spectrum at $X=114''$

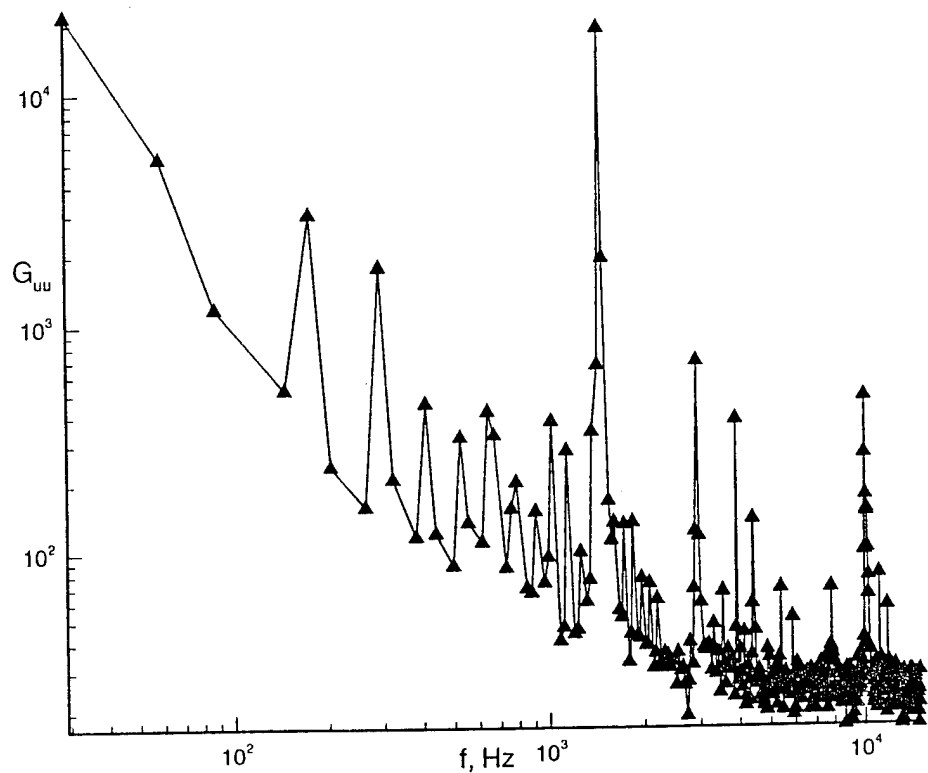


Figure 31. G_{uu} Power Spectrum at $X=216''$

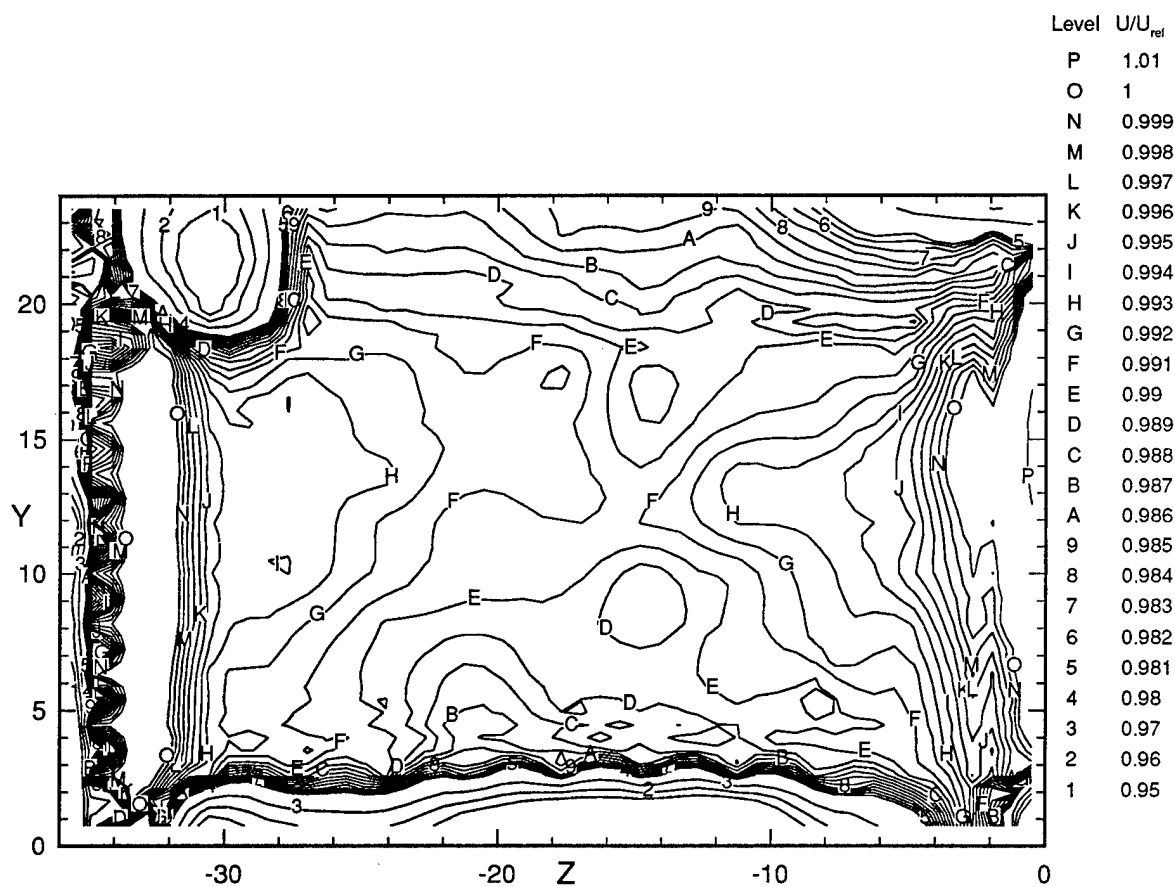


Figure 32. U/U_{ref} Variations across the Test Section Entrance

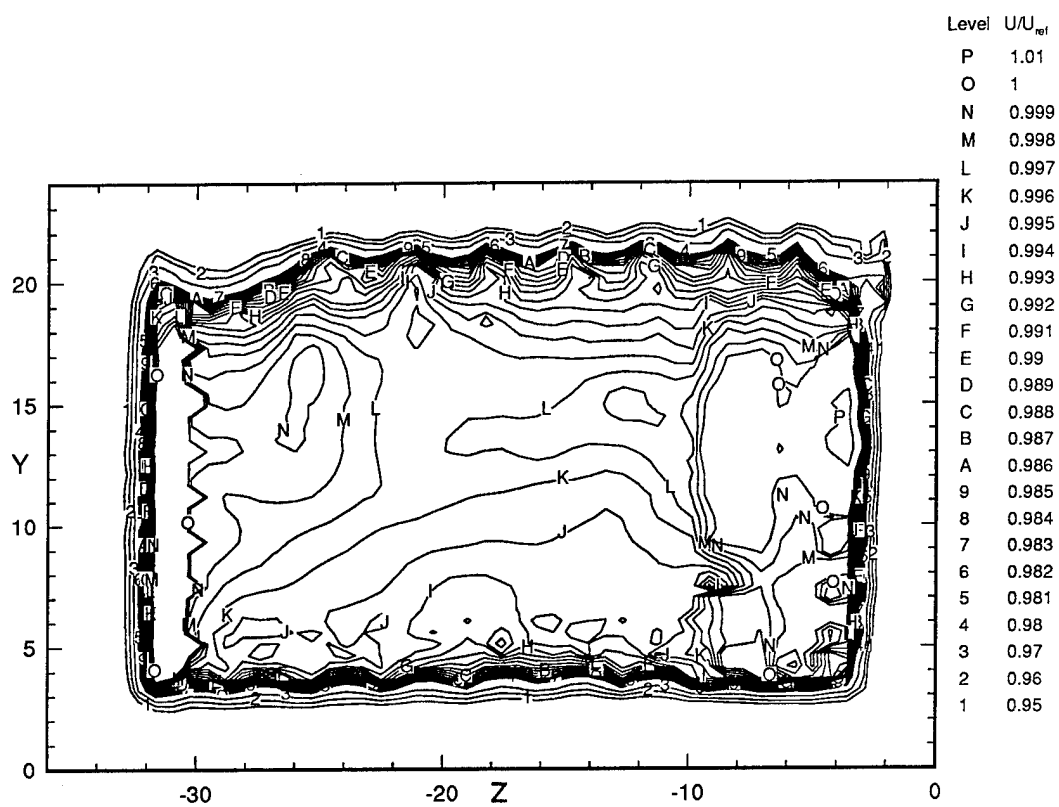


Figure 33. U/U_{ref} Variations across the Test Section Exit

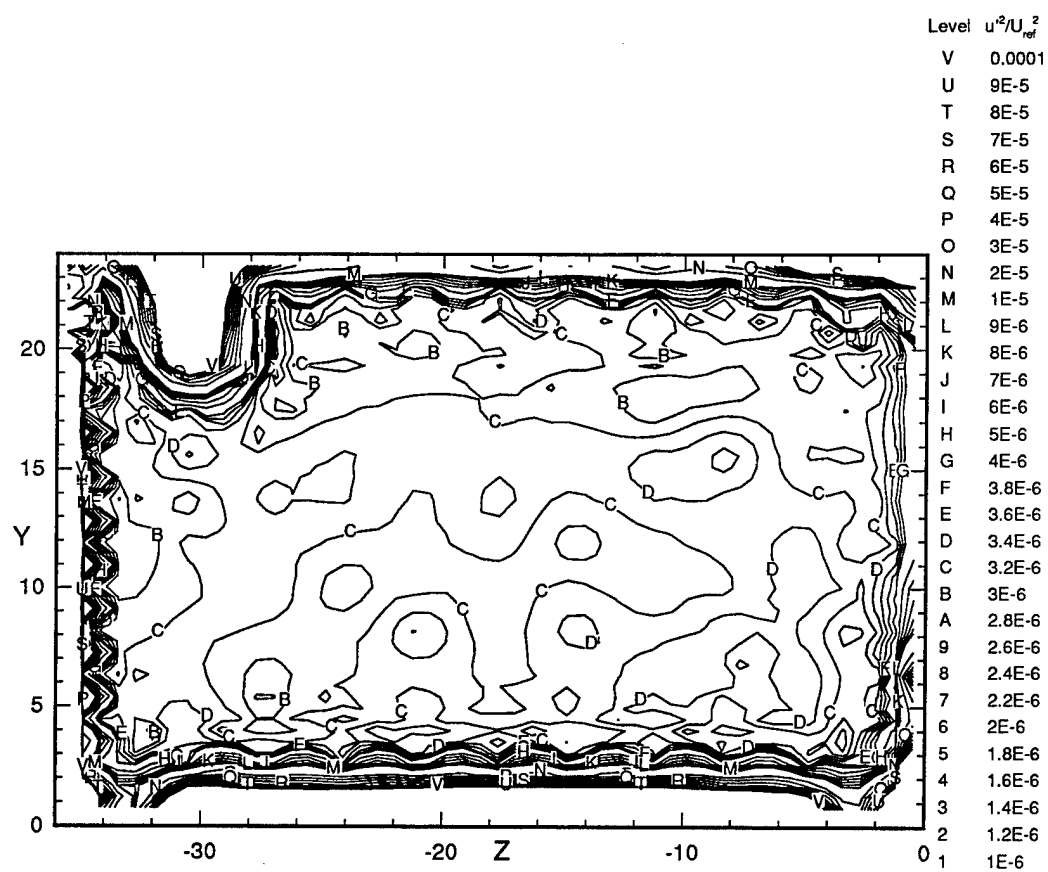
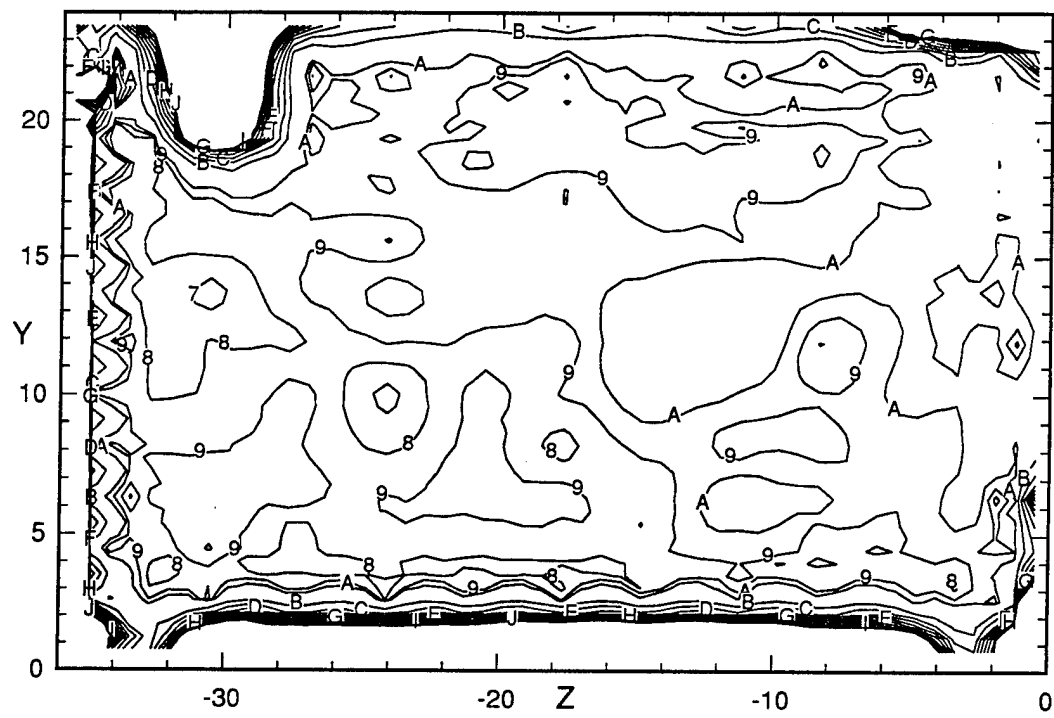


Figure 34. u^2 / U_{ref}^2 , Block Averaged, Variations across the Test Section Entrance



Level	u'^2/U^2_{ref}
J	0.0001
I	9E-5
H	8E-5
G	7E-5
F	6E-5
E	5E-5
D	4E-5
C	3E-5
B	2E-5
A	1E-5
9	9E-6
8	8E-6
7	7E-6
6	6E-6
5	5E-6
4	4E-6
3	3E-6
2	2E-6
1	1E-6

Figure 35. u'^2/U^2_{ref} , Time Averaged, Variations across the Test Section Entrance

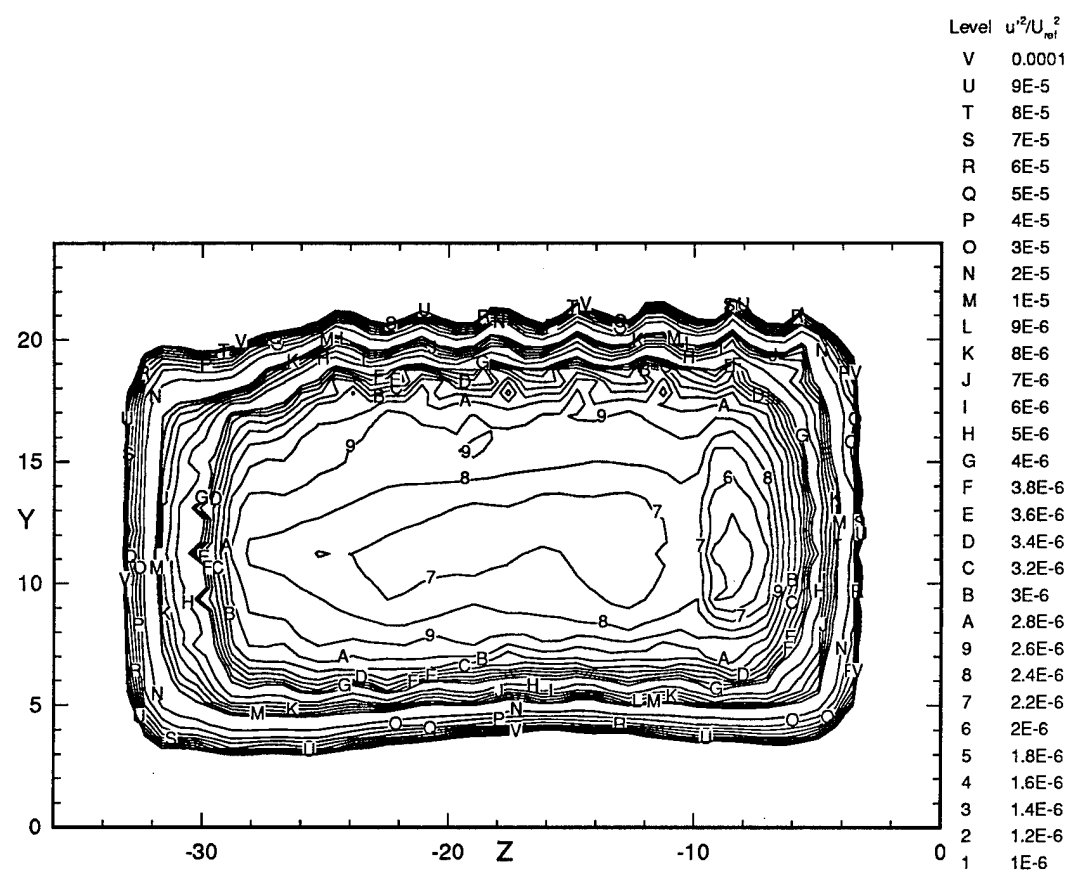
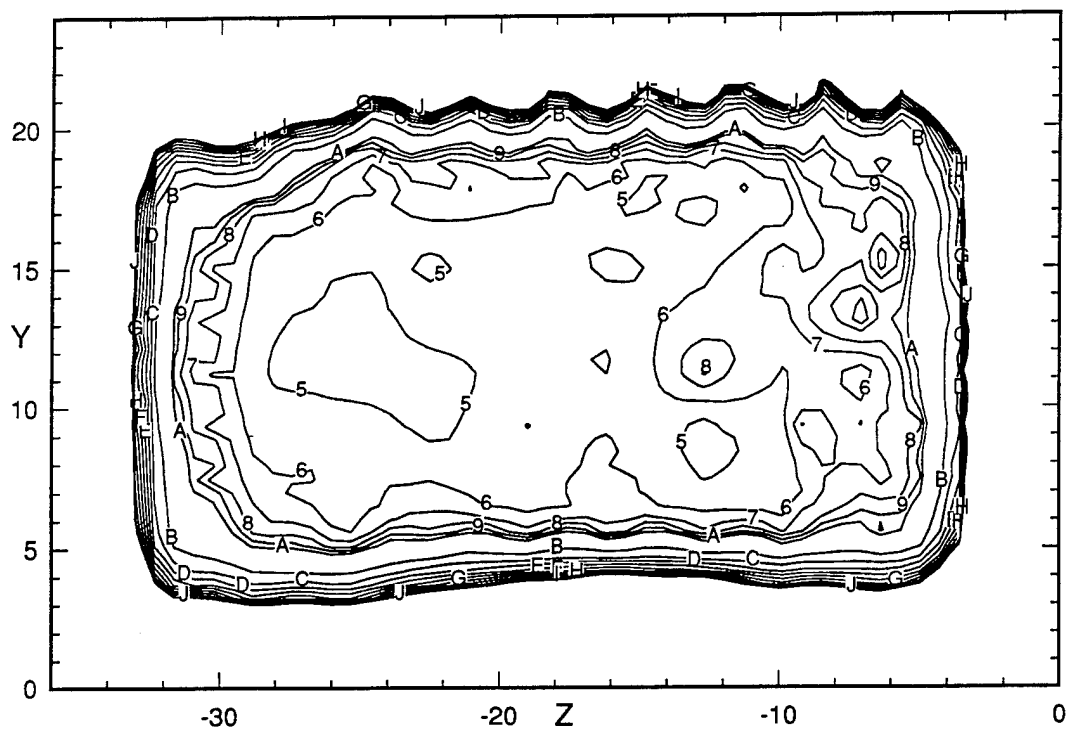


Figure 36. u^2/U_{ref}^2 , Block Averaged, Variations across the Test Section Exit



Level	u^2/U_{ref}^2
J	0.0001
I	9E-5
H	8E-5
G	7E-5
F	6E-5
E	5E-5
D	4E-5
C	3E-5
B	2E-5
A	1E-5
9	9E-6
8	8E-6
7	7E-6
6	6E-6
5	5E-6
4	4E-6
3	3E-6
2	2E-6
1	1E-6

Figure 37. u^2/U_{ref}^2 , Time Averaged, Variations across the Test Section Exit

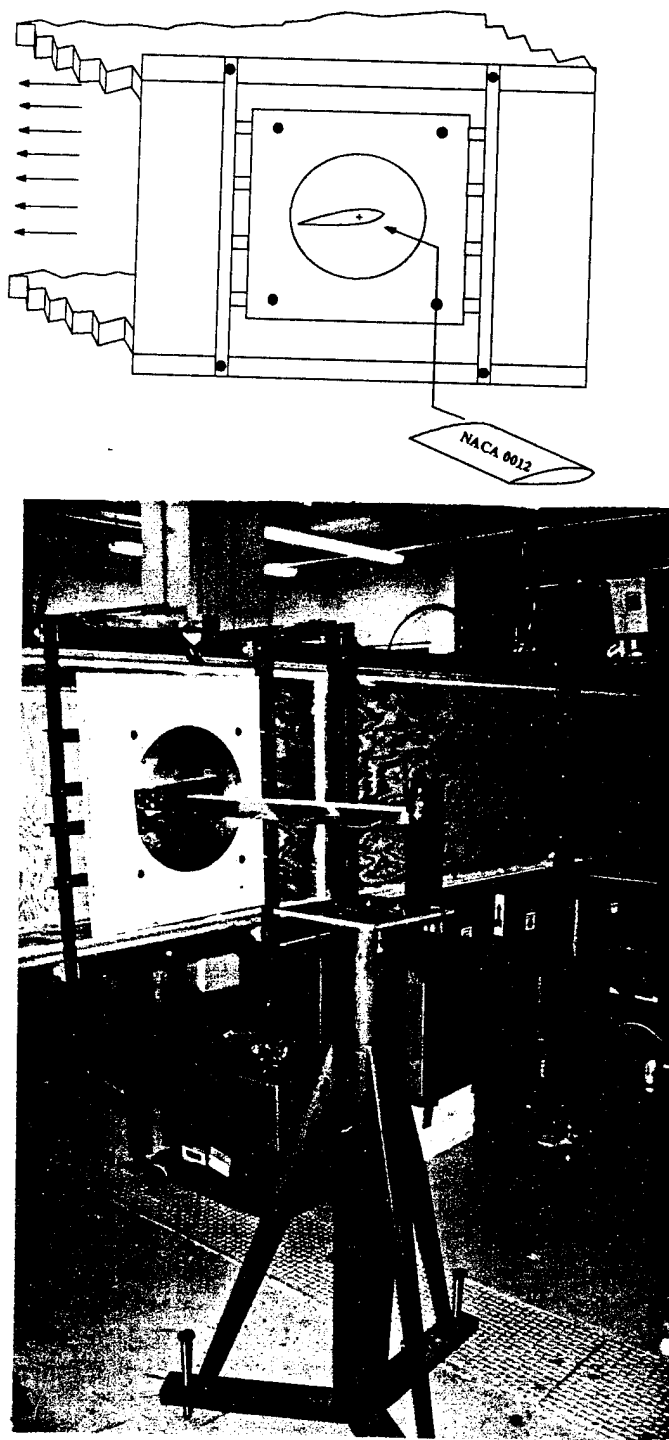


Figure 38. Over-Designed Wing Mount

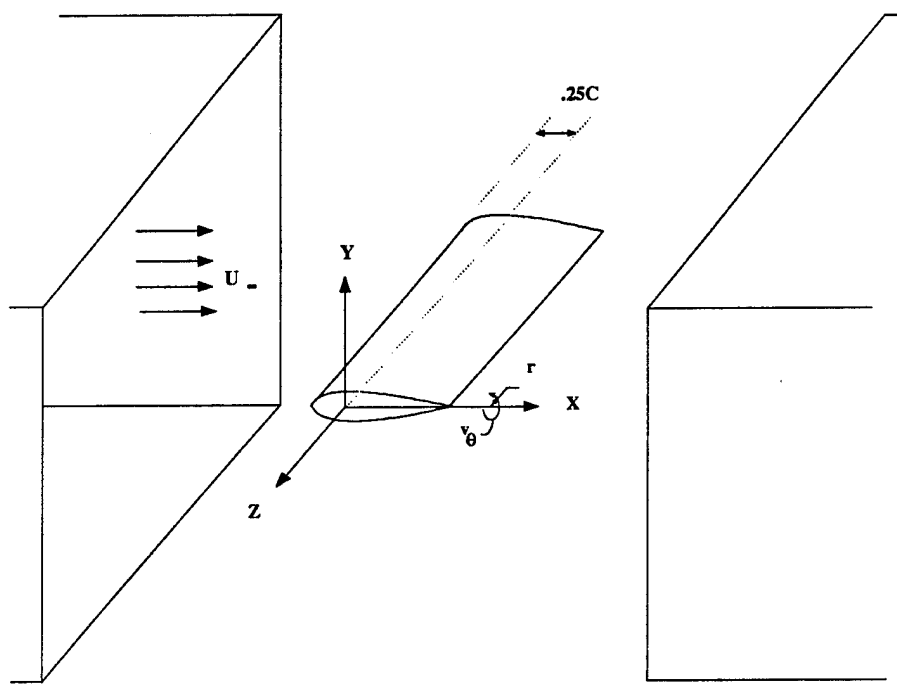
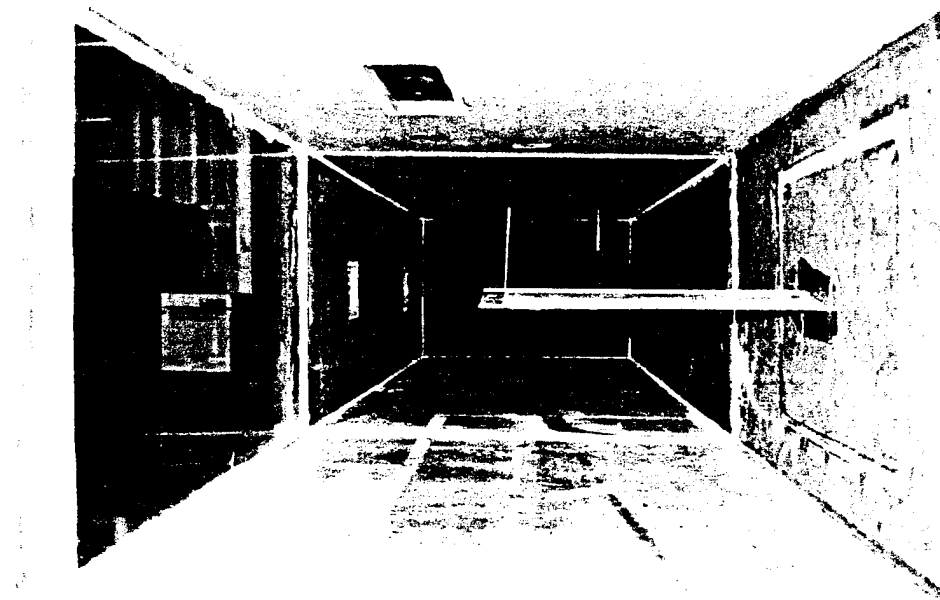
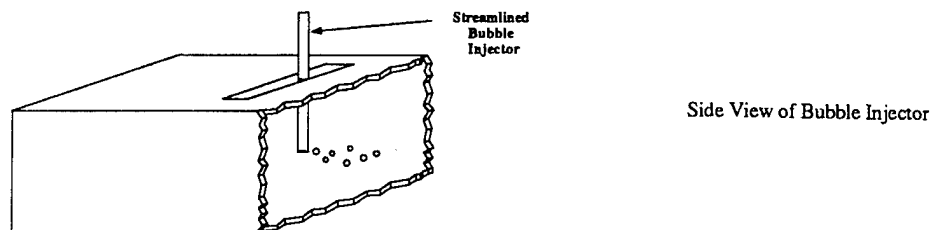
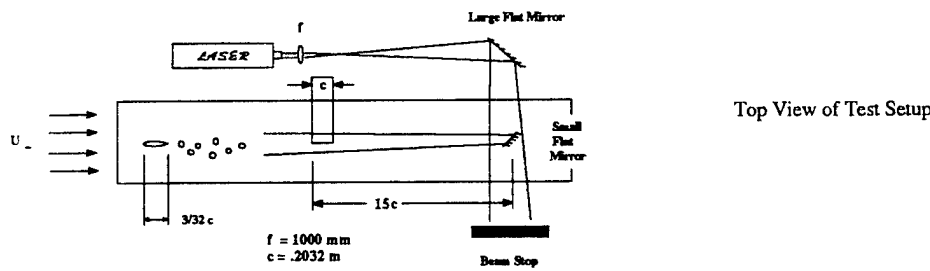
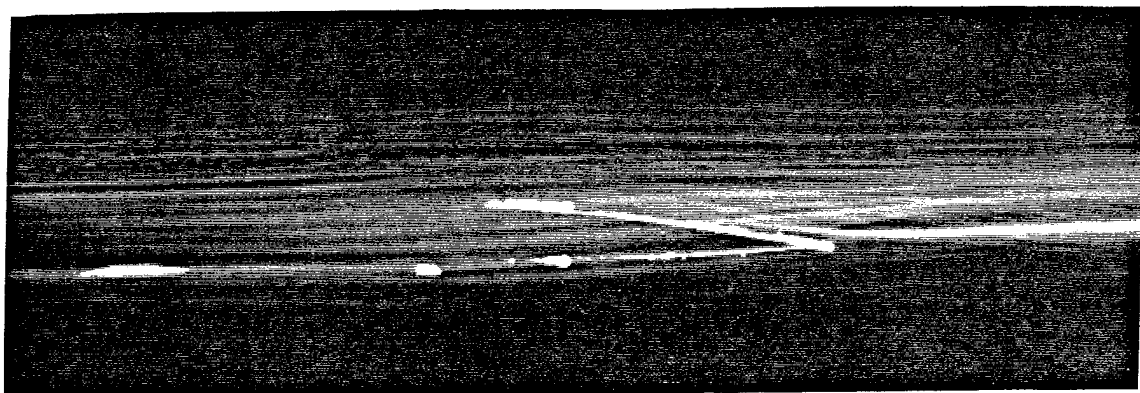


Figure 39. Coordinate System



View Looking Upstream of Wing, Bubble Probe to left of Center, and Tunnel Reference Pitot-Static at Upper Right. Note that Endcap Photos were taken through Window to Left of Wing and Suction Side Photos were taken from Window in Ceiling.

Figure 40. Flow Visualization Layout



a. Exposure Time = 1 sec.

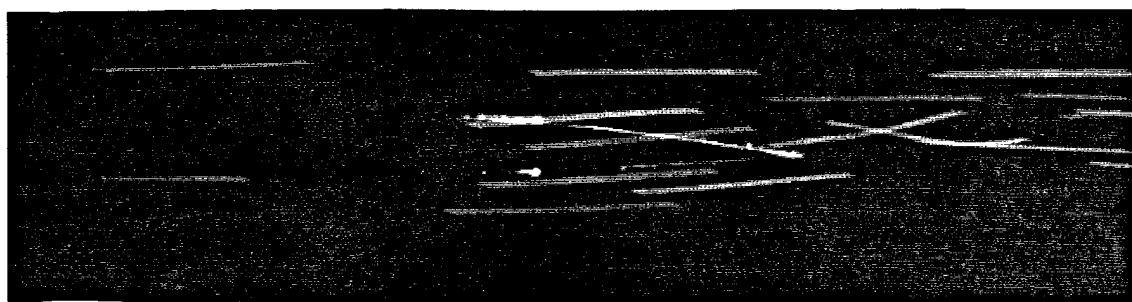


b. Exposure Time = 1/4 sec.

Figure 41. Tip Flow Visualizations, Endcap View
Aspect Ratio=3.0, Angle of Attack=2.5°, $Re_c=130000$

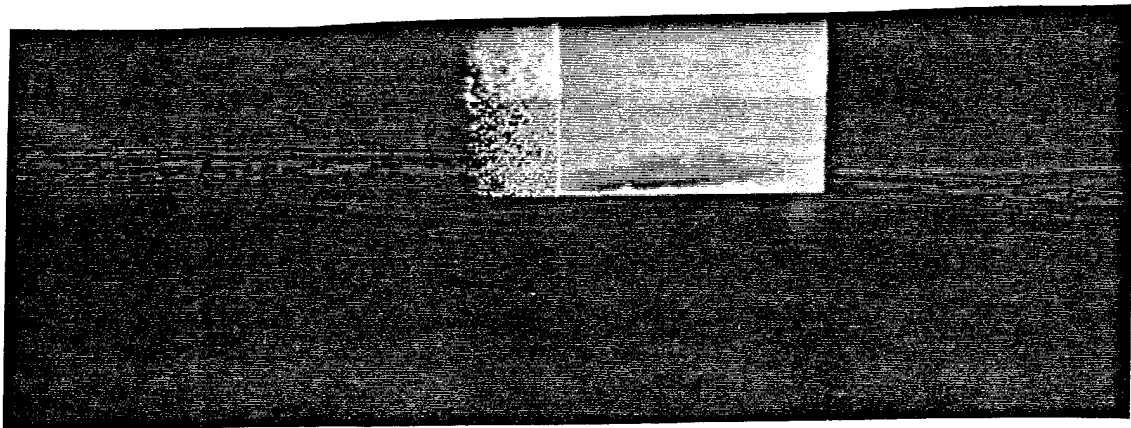


c. Exposure Time = 1/15 sec.

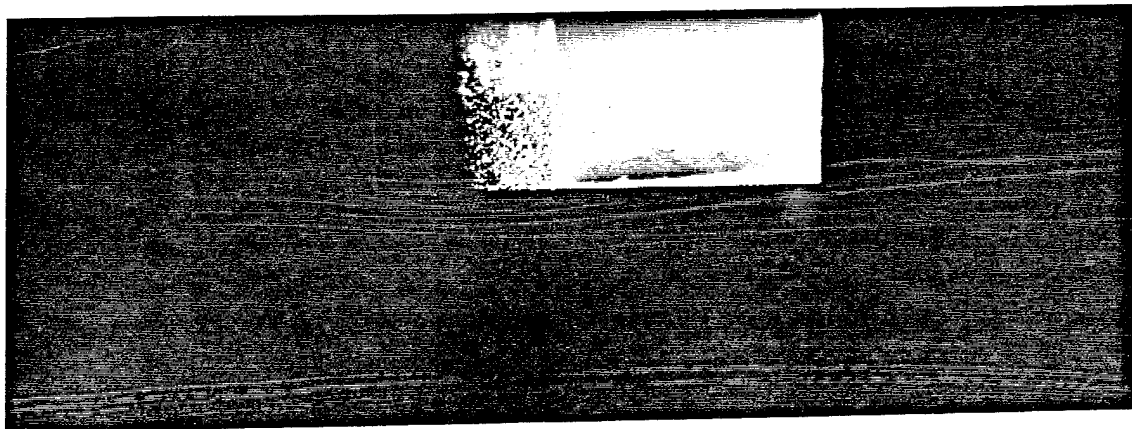


d. Exposure Time = 1/125 sec.

Figure 41. Tip Flow Visualizations, Endcap View
Aspect Ratio=3.0, Angle of Attack=2.5°, $Re_c=130000$

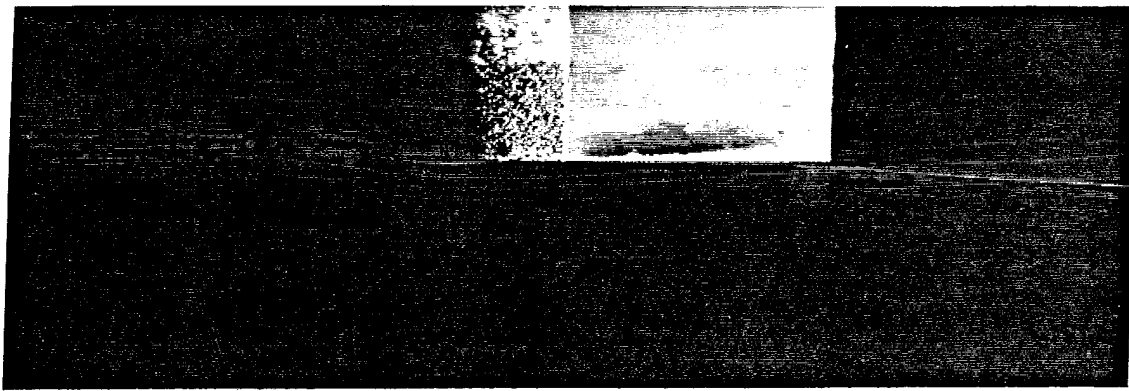


e. Exposure Time = 2 sec.

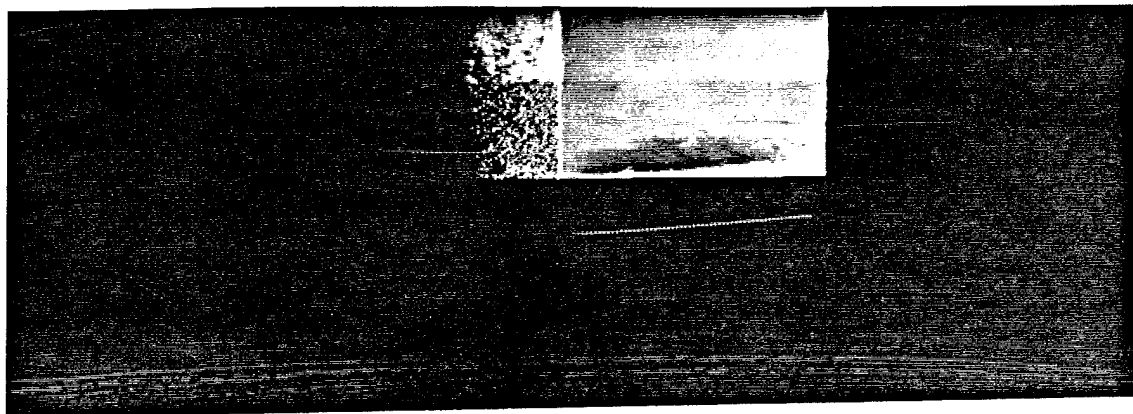


f. Exposure Time = 1/4 sec.

Figure 41. Tip Flow Visualizations, Suction Surface View
Aspect Ratio=3.0, Angle of Attack=2.5°, $Re_c=130000$

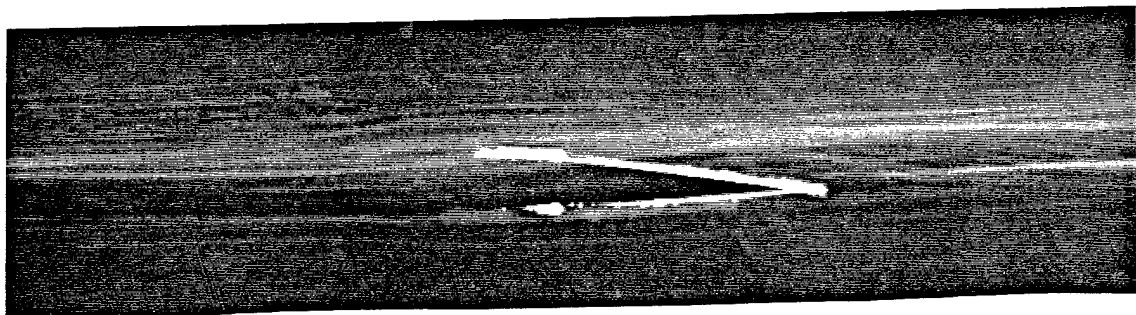


g. Exposure Time = 1/15 sec.

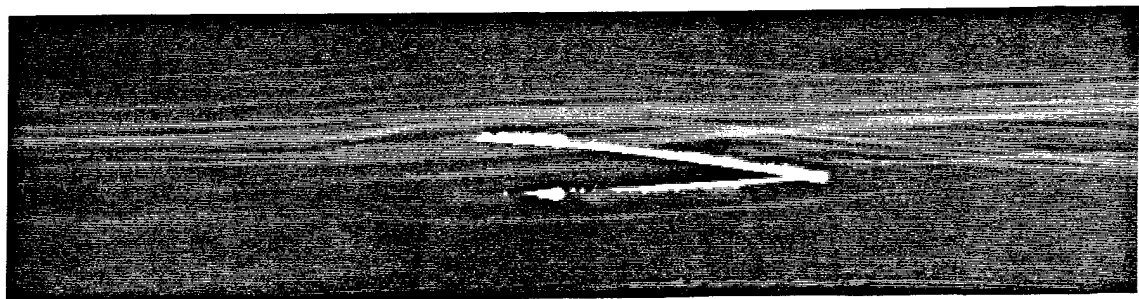


h. Exposure Time = 1/125 sec.

Figure 41. Tip Flow Visualizations, Suction Surface View
Aspect Ratio=3.0, Angle of Attack=2.5°, $Re_c=130000$



a. Exposure Time = 1 sec.

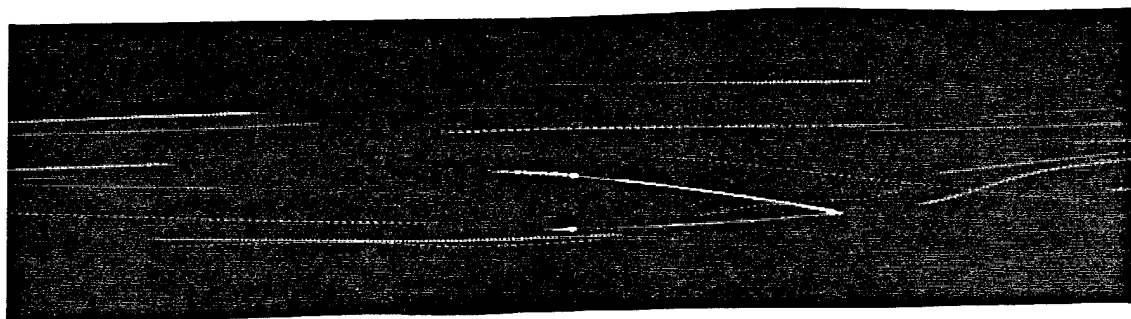


b. Exposure Time = 1/4 sec.

Figure 42. Tip Flow Visualizations, Endcap View
Aspect Ratio=3.0, Angle of Attack=2.5°, $Re_c=260000$

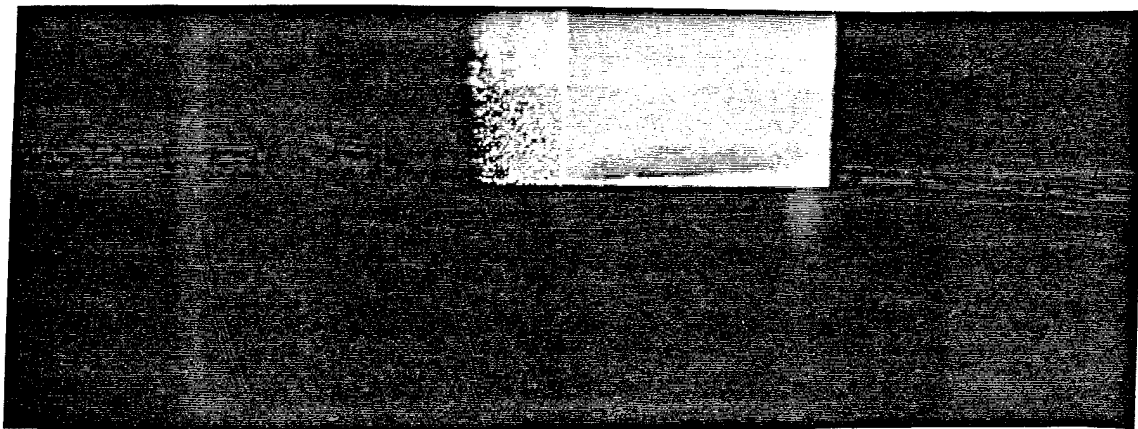


c. Exposure Time = 1/15 sec.

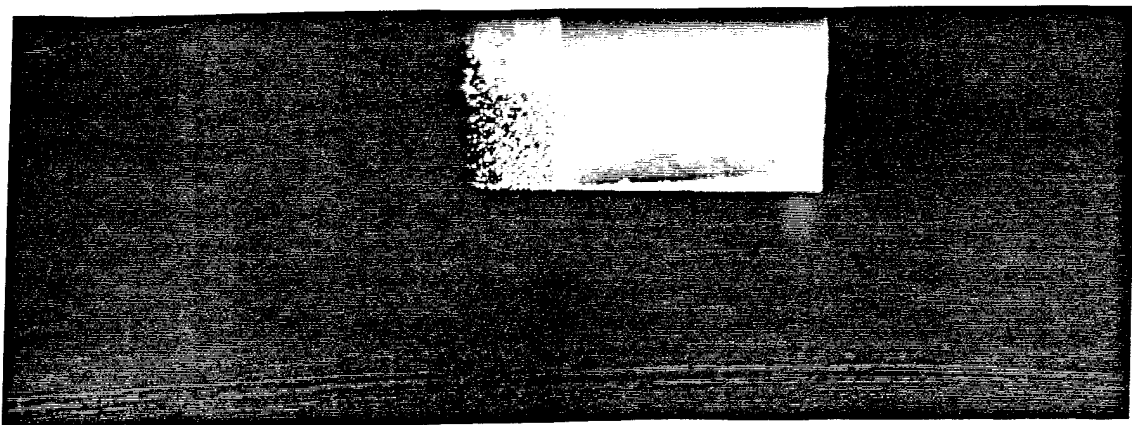


d. Exposure Time = 1/125 sec.

Figure 42. Tip Flow Visualizations, Endcap View
Aspect Ratio=3.0, Angle of Attack=2.5°, $Re_c=260000$

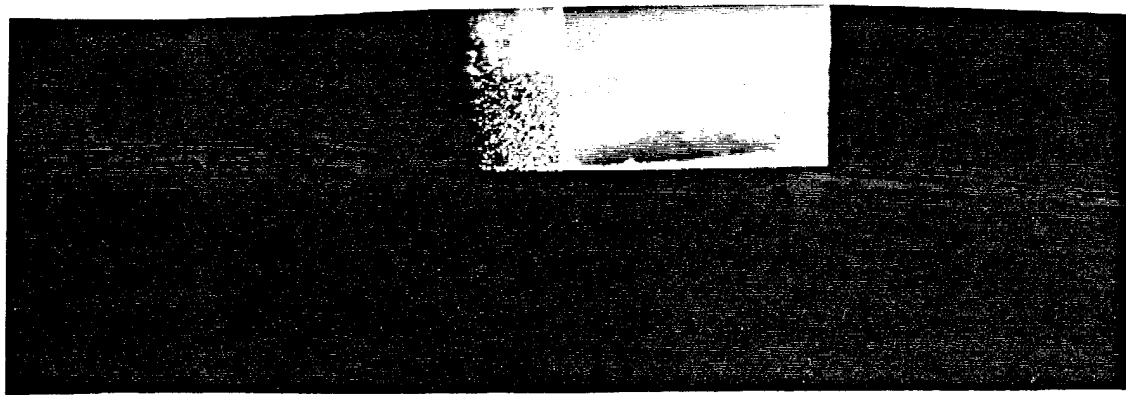


e. Exposure Time = 2 sec.

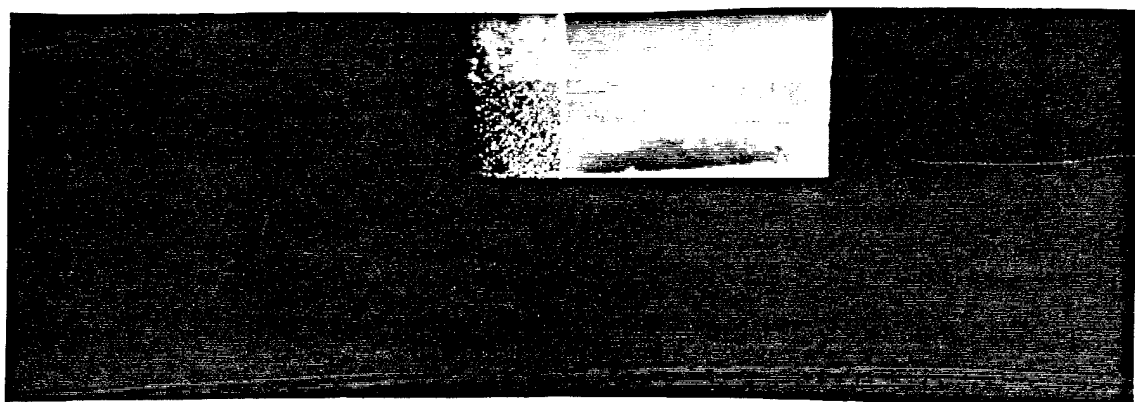


f. Exposure Time = 1/4 sec.

Figure 42. Tip Flow Visualizations, Suction Surface View
Aspect Ratio=3.0, Angle of Attack=2.5°, $Re_c=260000$

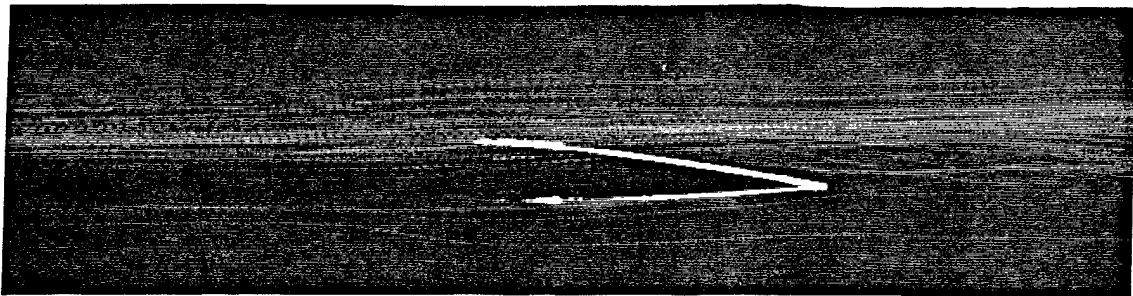


g. Exposure Time = 1/15 sec.

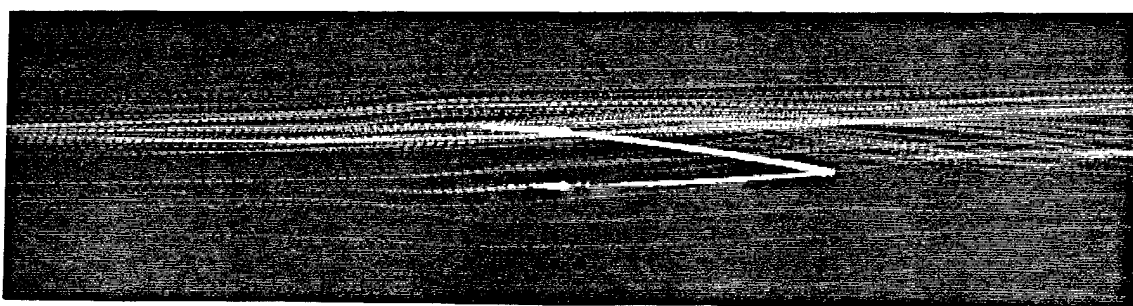


h. Exposure Time = 1/125 sec.

Figure 42. Tip Flow Visualizations, Suction Surface View
Aspect Ratio=3.0, Angle of Attack=2.5°, $Re_c=260000$

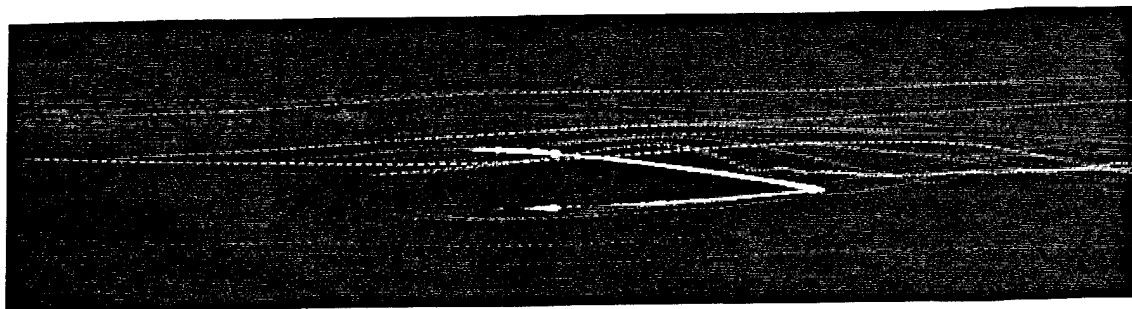


a. Exposure Time = 1 sec.

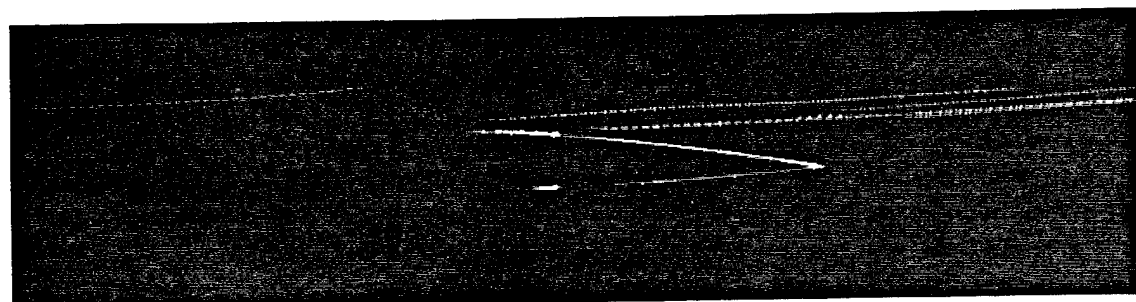


b. Exposure Time = 1/4 sec.

Figure 43. Tip Flow Visualizations, Endcap View
Aspect Ratio=3.0, Angle of Attack=2.5°, $Re_c=335000$

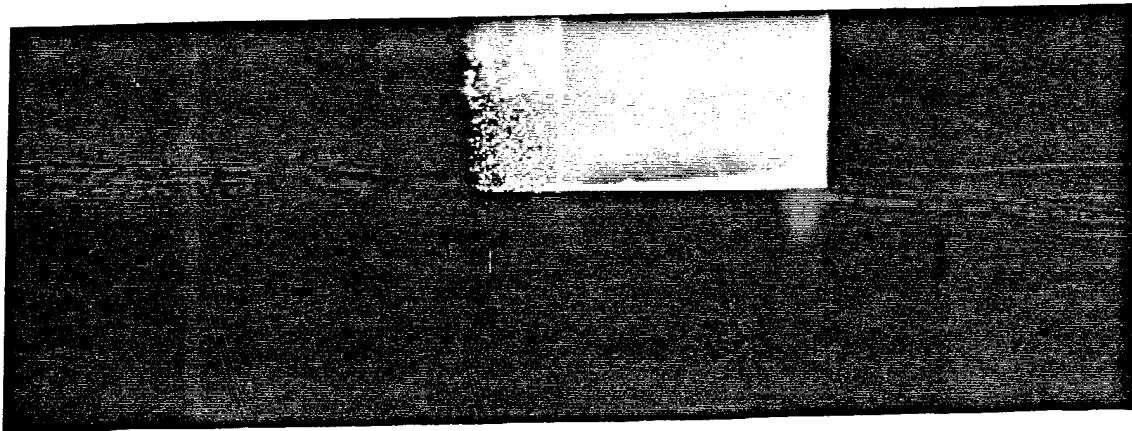


c. Exposure Time = 1/15 sec.

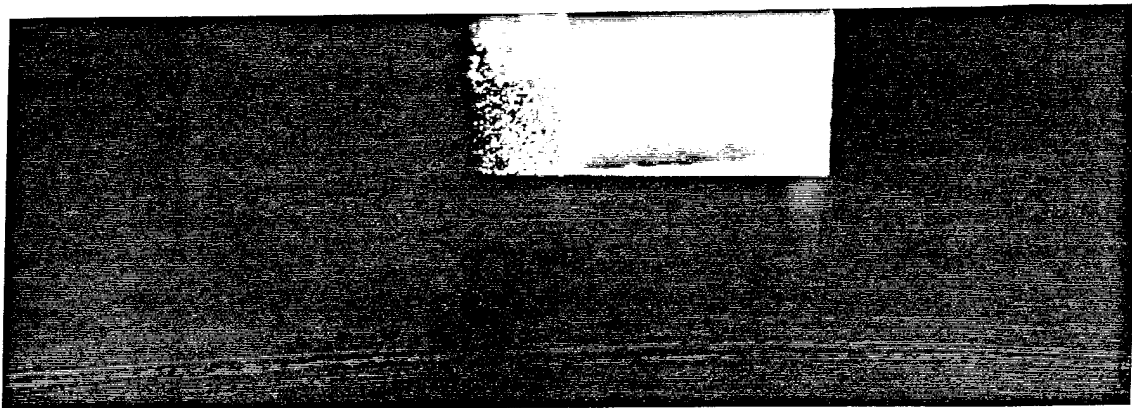


d. Exposure Time = 1/125 sec.

Figure 43. Tip Flow Visualizations, Endcap View
Aspect Ratio=3.0, Angle of Attack=2.5°, $Re_c=335000$

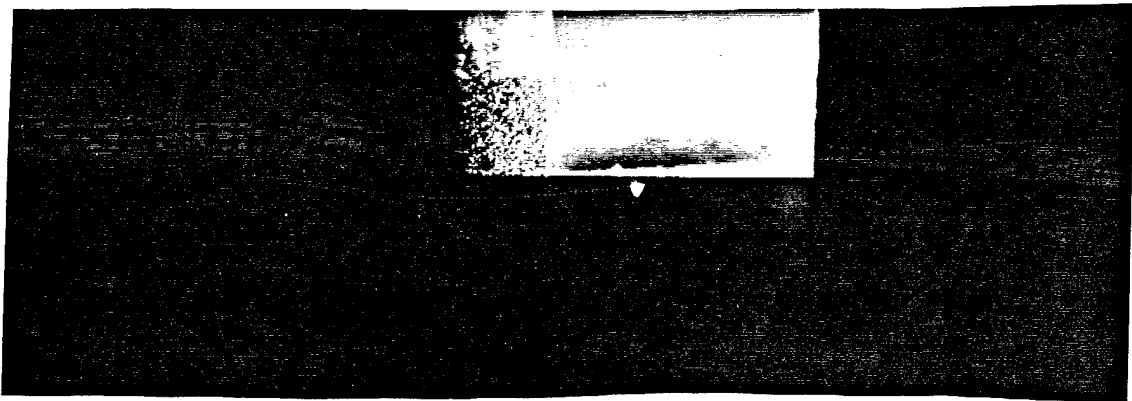


e. Exposure Time = 2 sec.

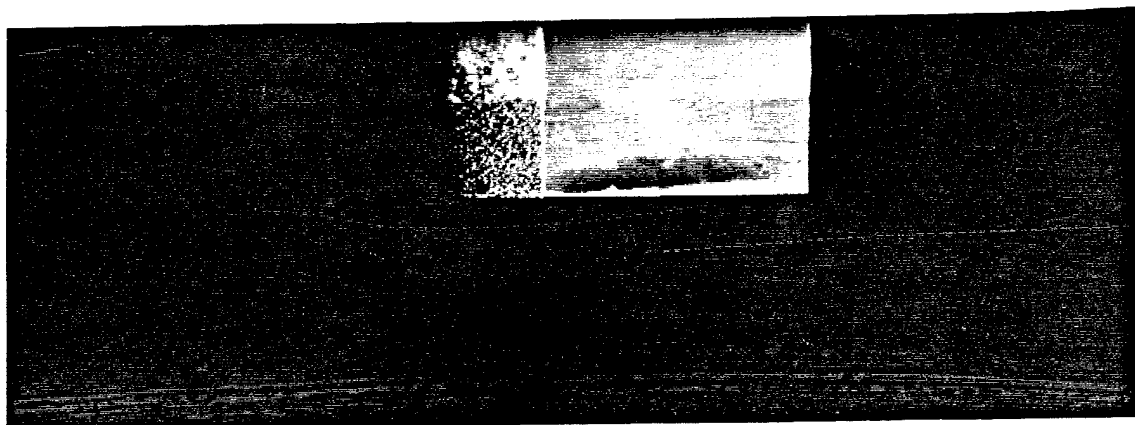


f. Exposure Time = 1/4 sec.

Figure 43. Tip Flow Visualizations, Suction Surface View
Aspect Ratio=3.0, Angle of Attack=2.5°, $Re_c=335000$

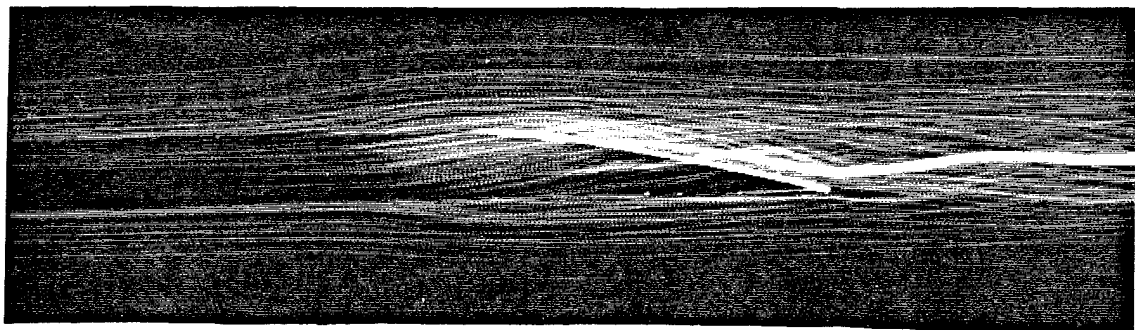


g. Exposure Time = 1/15 sec.

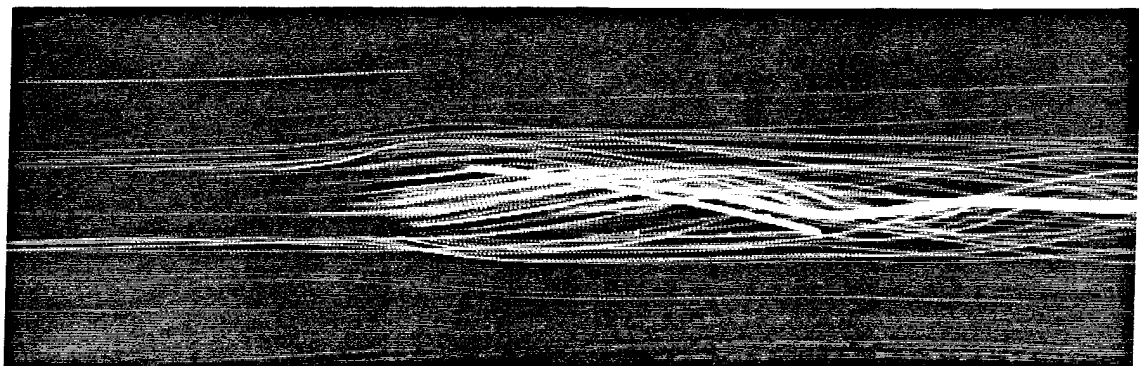


h. Exposure Time = 1/125 sec.

Figure 43. Tip Flow Visualizations, Suction Surface View
Aspect Ratio=3.0, Angle of Attack=2.5°, $Re_c=335000$

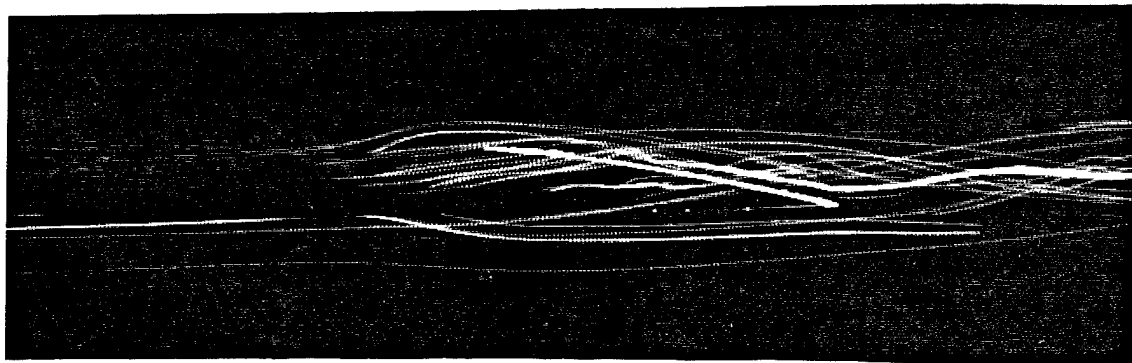


a. Exposure Time = 1 sec.

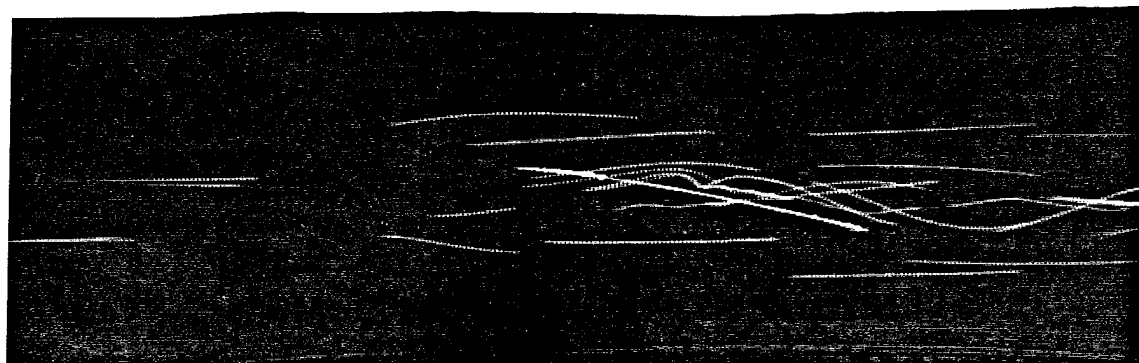


b. Exposure Time = 1/4 sec.

Figure 44. Tip Flow Visualizations, Endcap View
Aspect Ratio=3.0, Angle of Attack=5.0°, $Re_c=130000$

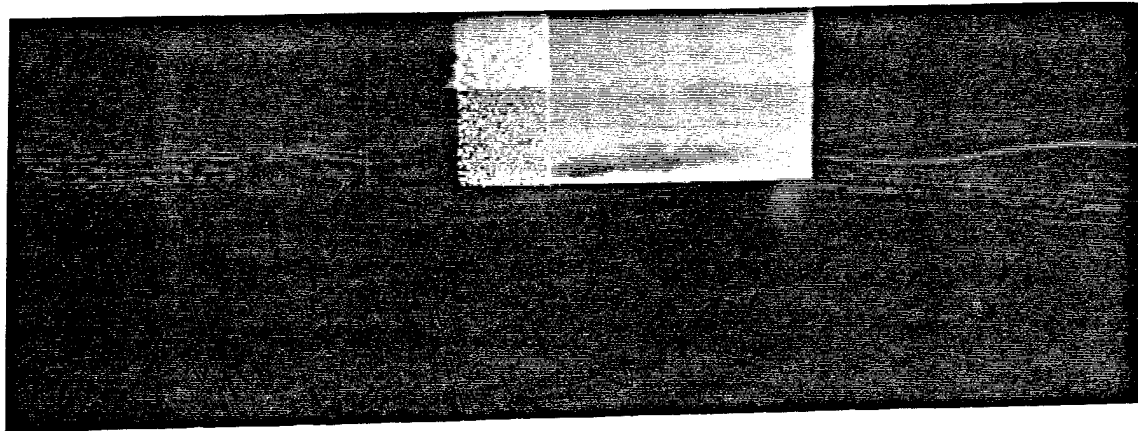


c. Exposure Time = 1/15 sec.

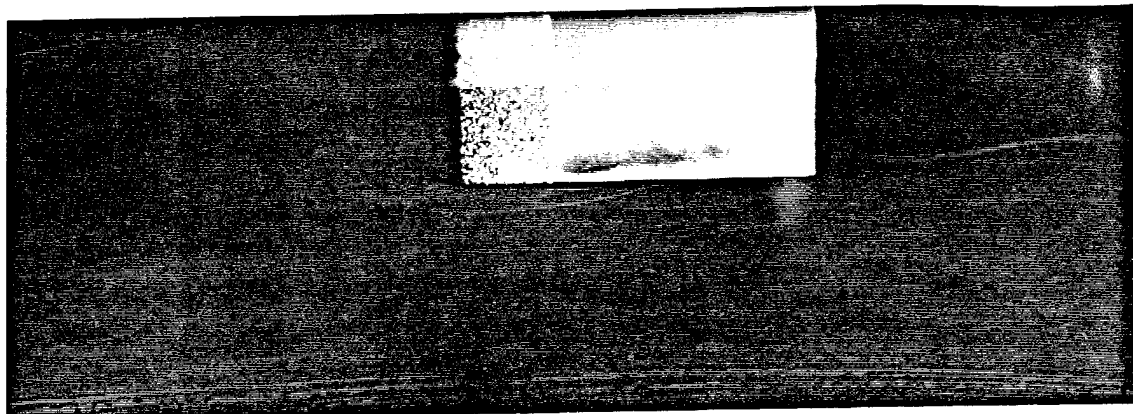


d. Exposure Time = 1/125 sec.

Figure 44. Tip Flow Visualizations, Endcap View
Aspect Ratio=3.0, Angle of Attack=5.0°, $Re_c=130000$

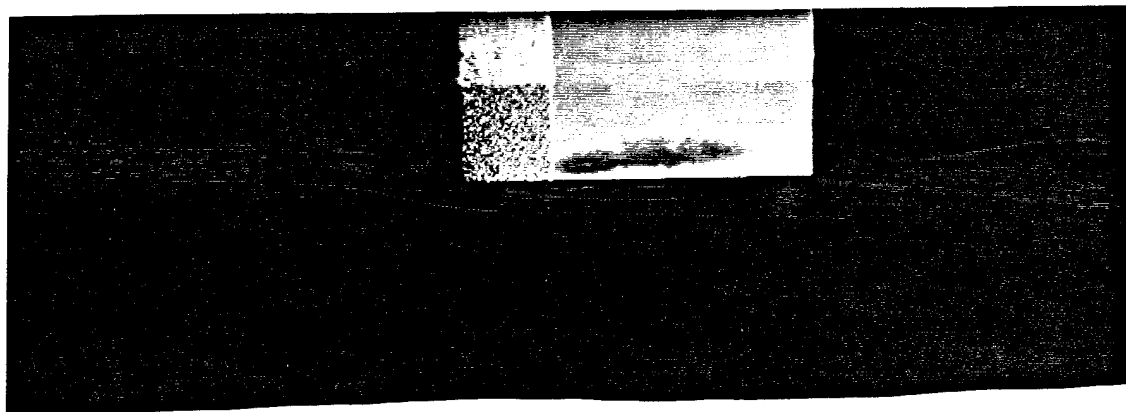


e. Exposure Time = 2 sec.

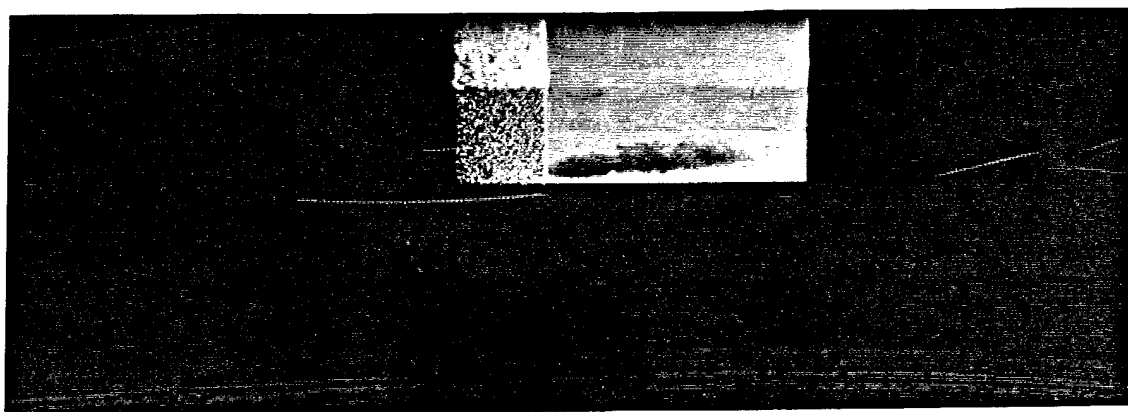


f. Exposure Time = 1/4 sec.

Figure 44. Tip Flow Visualizations, Suction Surface View
Aspect Ratio=3.0, Angle of Attack=5.0°, $Re_c=130000$

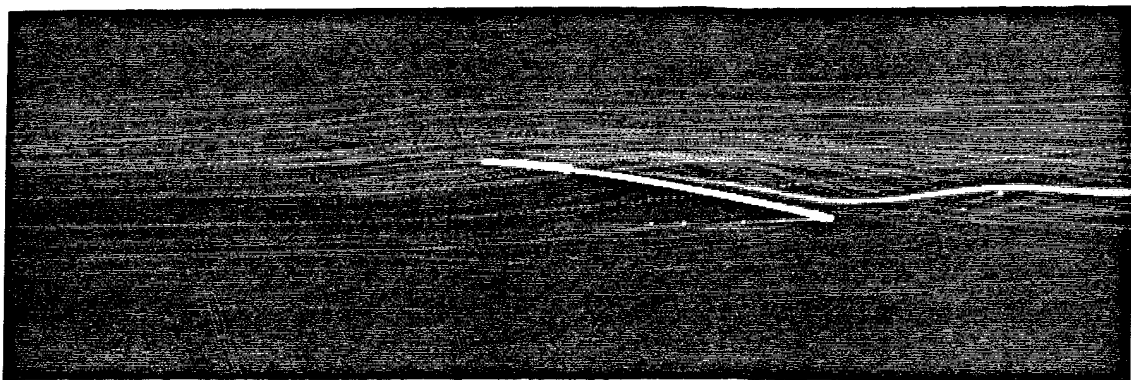


g. Exposure Time = 1/15 sec.

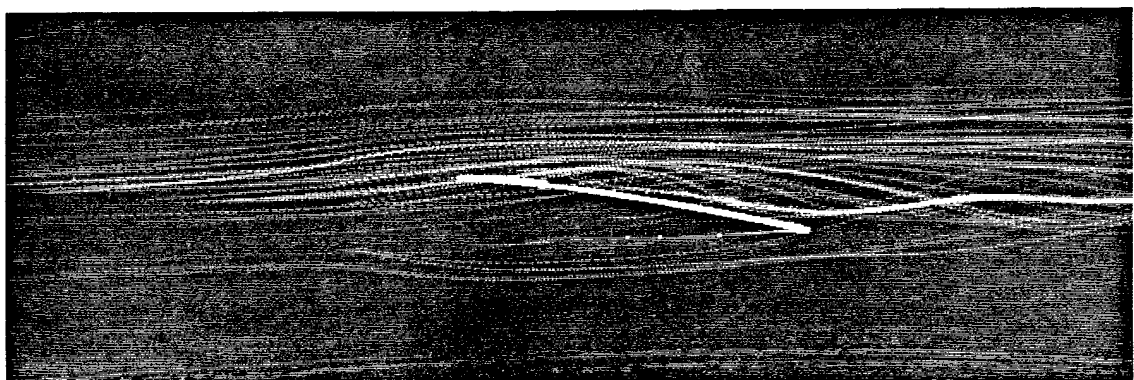


h. Exposure Time = 1/125 sec.

Figure 44. Tip Flow Visualizations, Suction Surface View
Aspect Ratio=3.0, Angle of Attack=5.0°, $Re_c=130000$

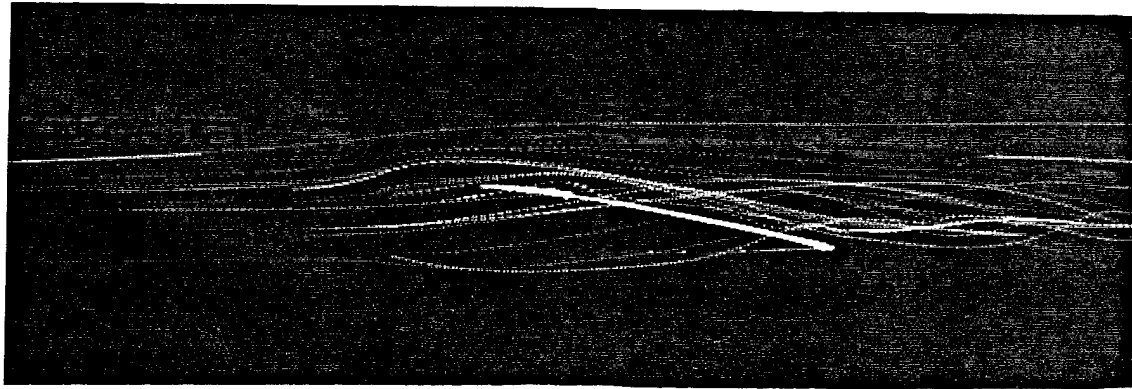


a. Exposure Time = 1 sec.

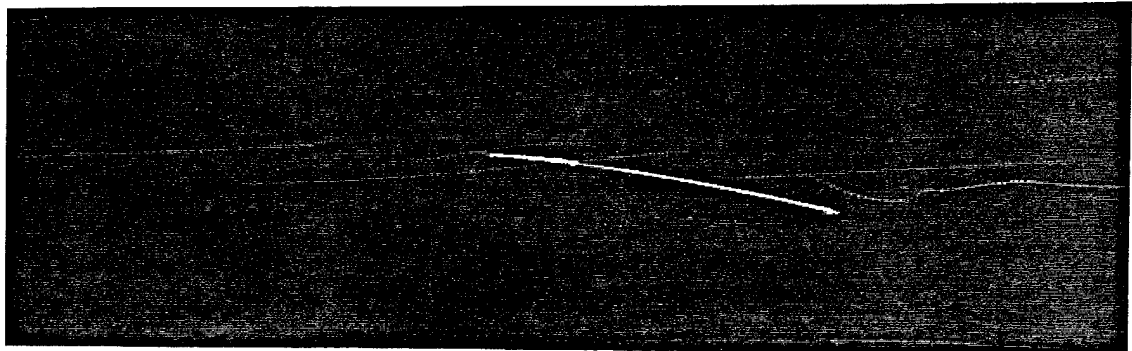


b. Exposure Time = 1/4 sec.

Figure 45. Tip Flow Visualizations, Endcap View
Aspect Ratio=3.0, Angle of Attack=5.0°, $Re_c=260000$

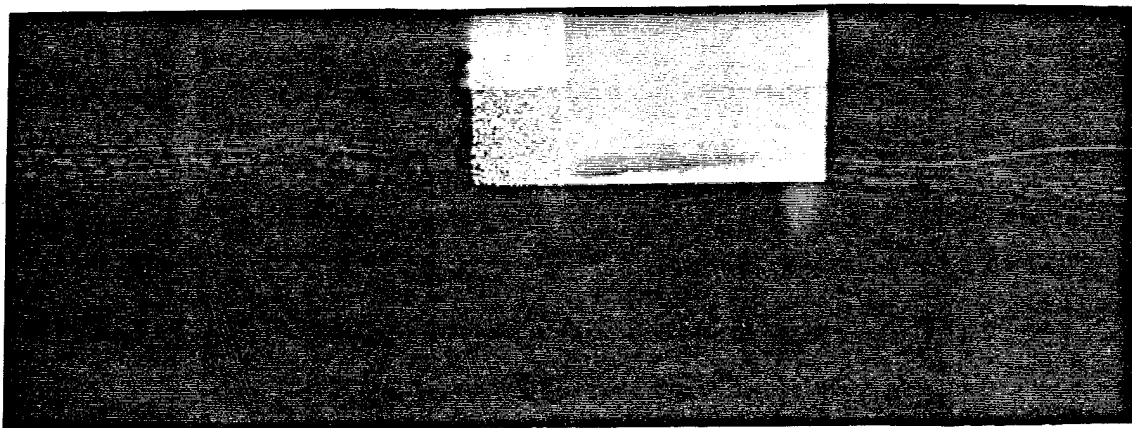


c. Exposure Time = 1/15 sec.

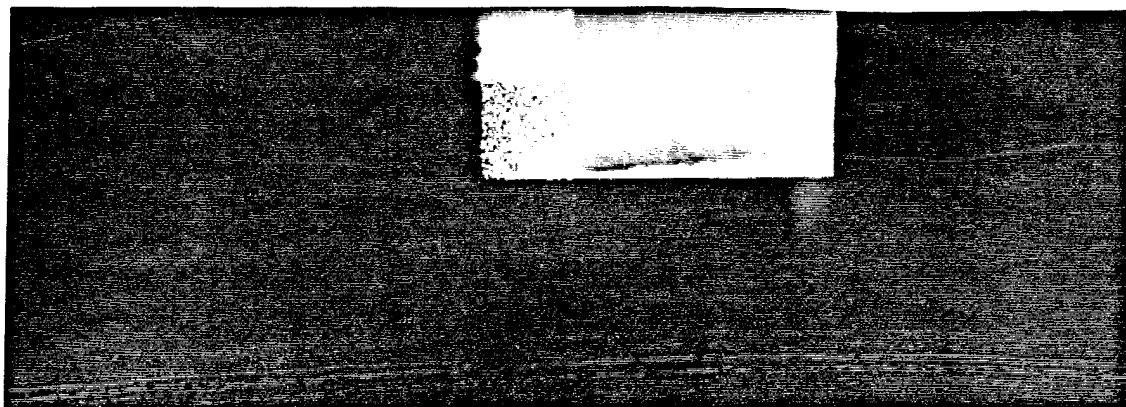


d. Exposure Time = 1/125 sec.

Figure 45. Tip Flow Visualizations, Endcap View
Aspect Ratio=3.0, Angle of Attack=5.0°, $Re_c=260000$

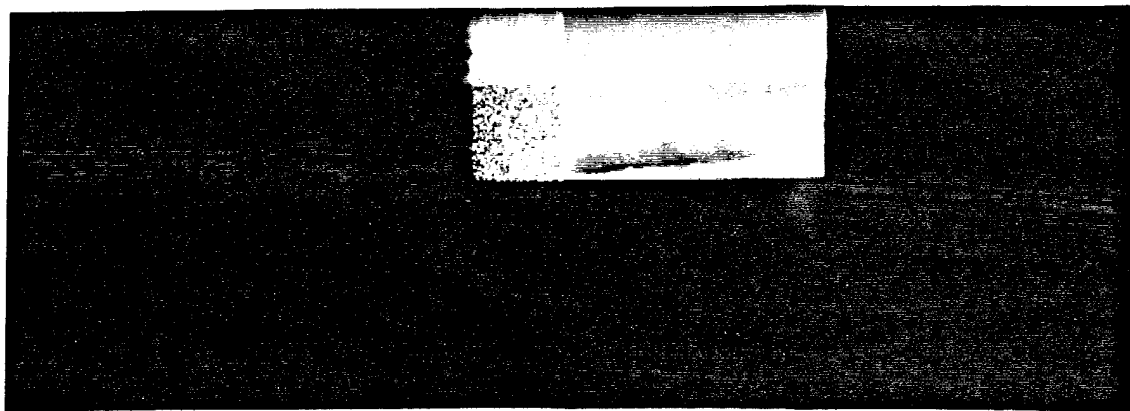


e. Exposure Time = 2 sec.

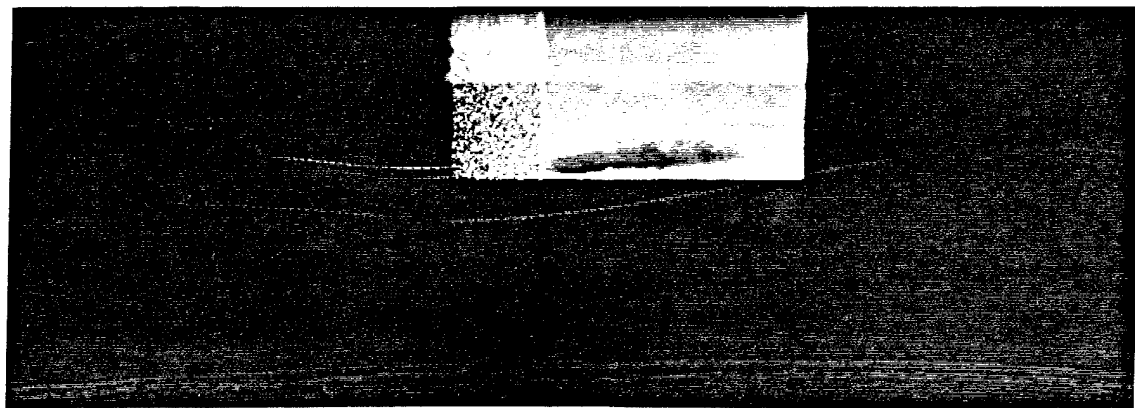


f. Exposure Time = 1/4 sec.

Figure 45. Tip Flow Visualizations, Suction Surface View
Aspect Ratio=3.0, Angle of Attack=5.0°, $Re_c=260000$

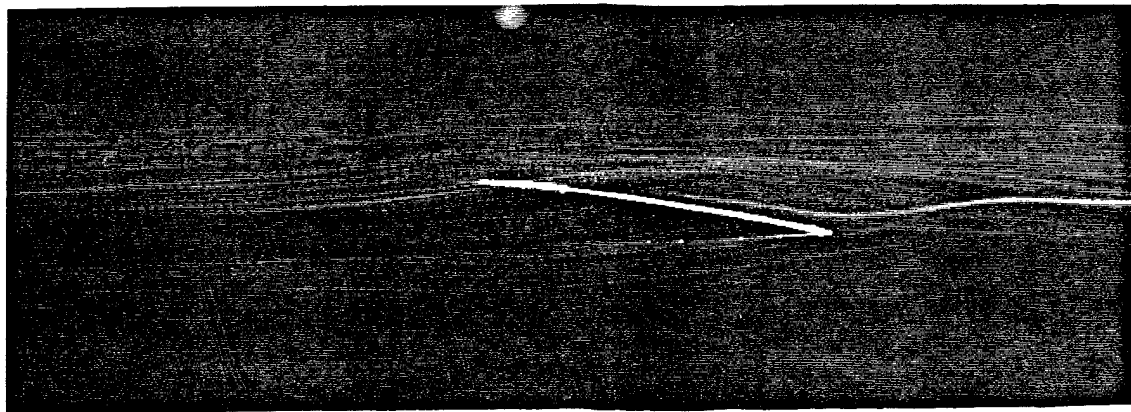


g. Exposure Time = 1/15 sec.

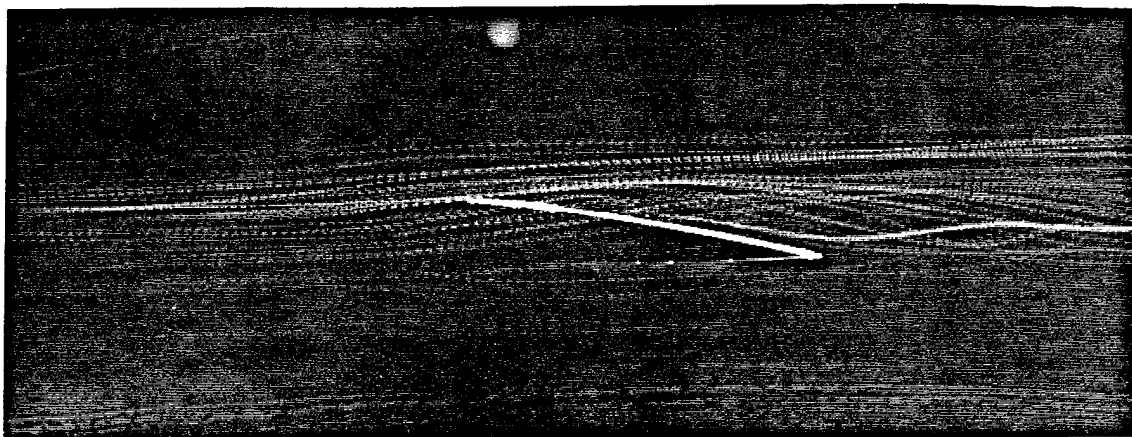


h. Exposure Time = 1/125 sec.

Figure 45. Tip Flow Visualizations, Suction Surface View
Aspect Ratio=3.0, Angle of Attack=5.0°, $Re_c=260000$

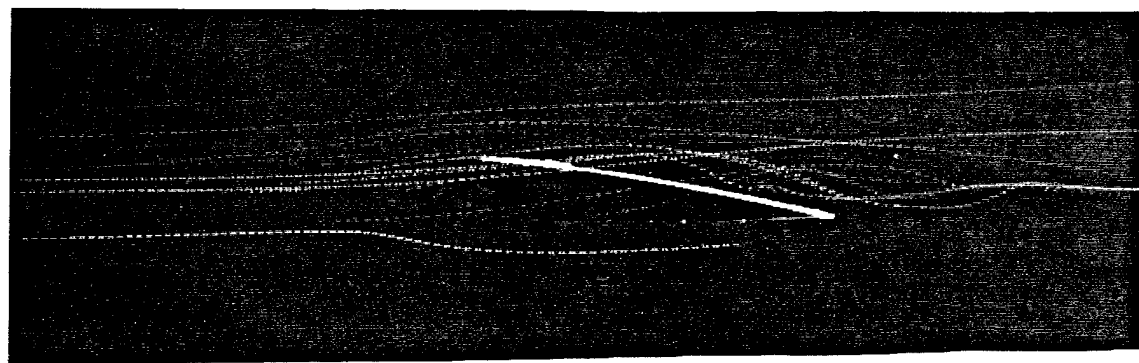


a. Exposure Time = 1 sec.



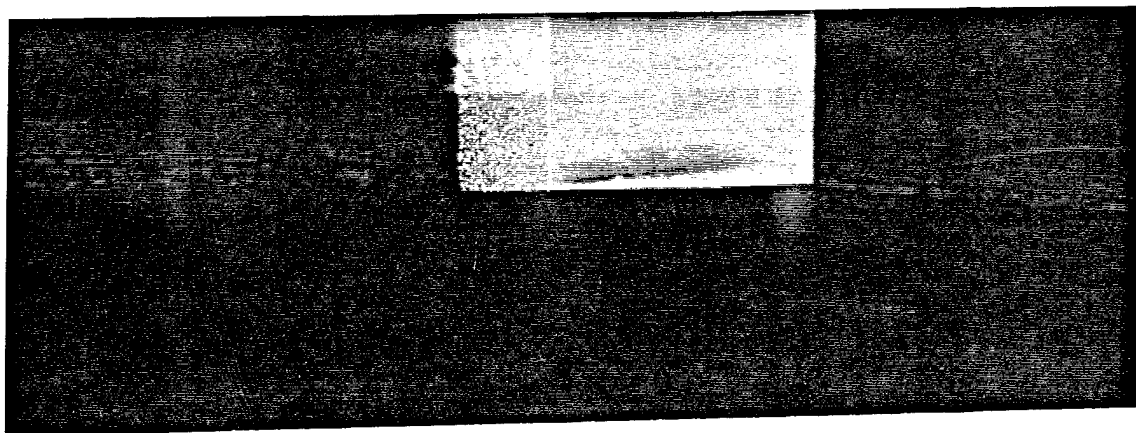
b. Exposure Time = 1/4 sec.

Figure 46. Tip Flow Visualizations, Endcap View
Aspect Ratio=3.0, Angle of Attack=5.0°, $Re_c=335000$

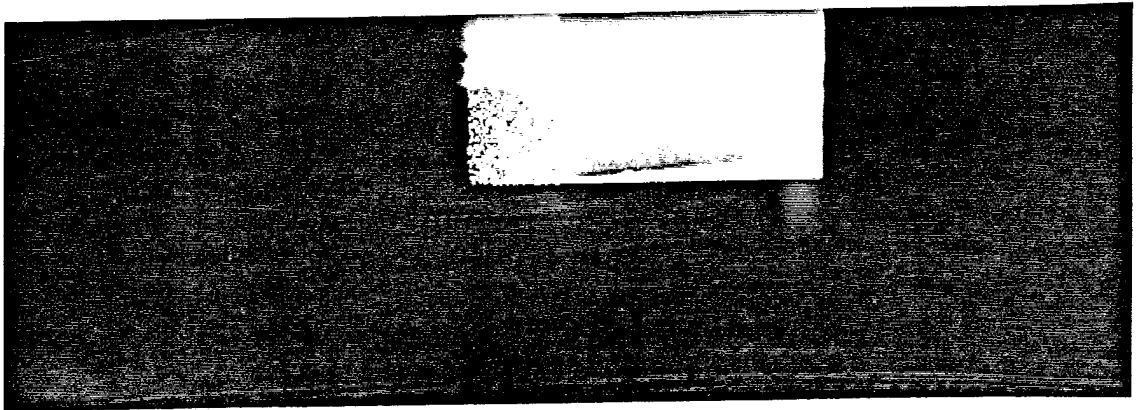


c. Exposure Time = 1/15 sec.

Figure 46. Tip Flow Visualizations, Endcap View
Aspect Ratio=3.0, Angle of Attack=5.0°, $Re_c=335000$

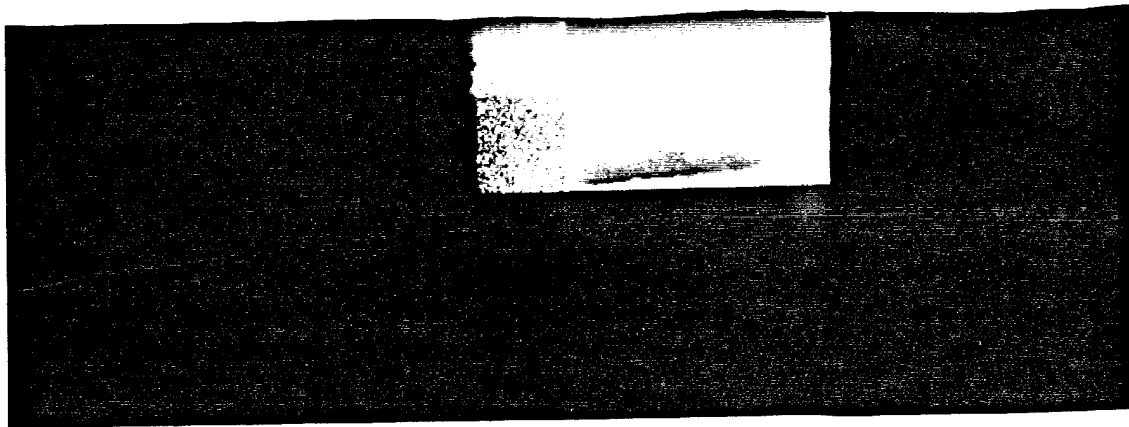


e. Exposure Time = 2 sec.



f. Exposure Time = 1/4 sec.

Figure 46. Tip Flow Visualizations, Suction Surface View
Aspect Ratio=3.0, Angle of Attack=5.0°, $Re_c=335000$



g. Exposure Time = 1/15 sec.

Figure 46. Tip Flow Visualizations, Suction Surface View
Aspect Ratio=3.0, Angle of Attack=5.0°, $Re_c=335000$

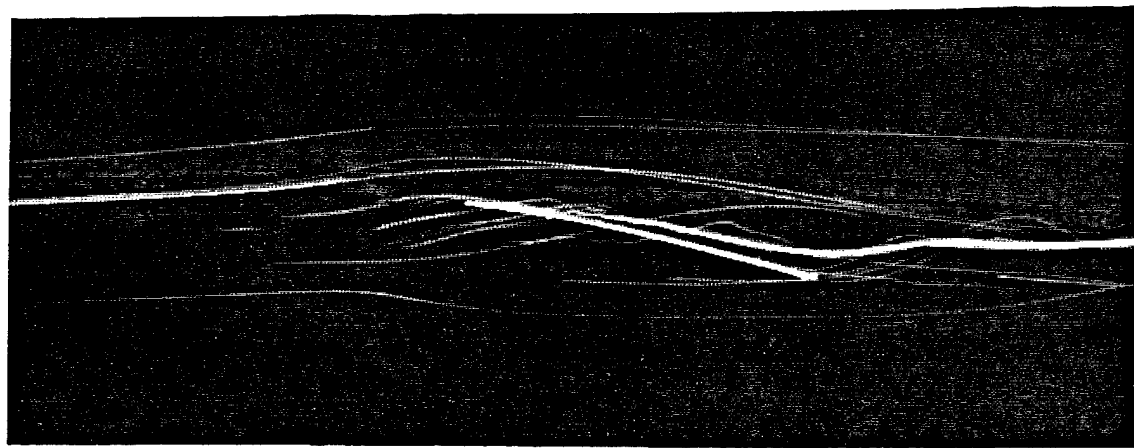


a. Exposure Time = 1 sec.

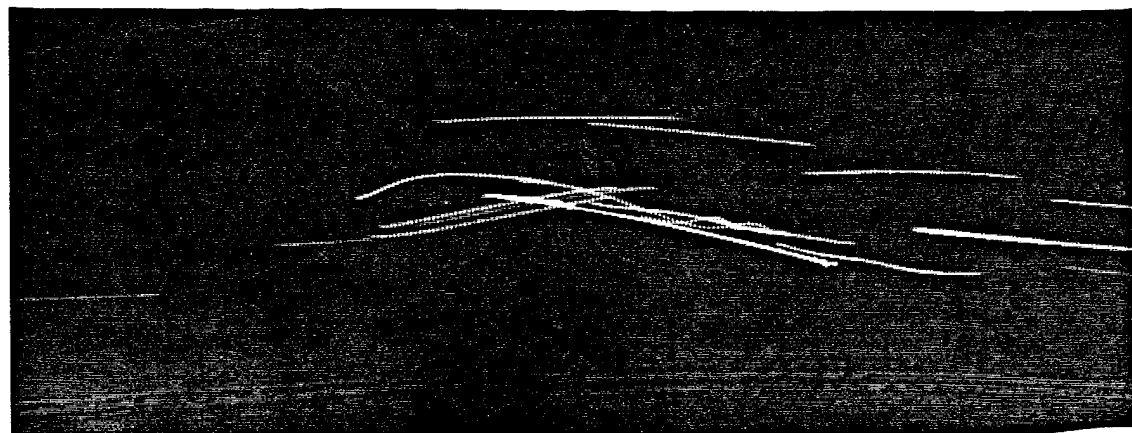


b. Exposure Time = 1/4 sec.

Figure 47. Tip Flow Visualizations, Endcap View
Aspect Ratio=3.0, Angle of Attack=7.5°, $Re_c=130000$

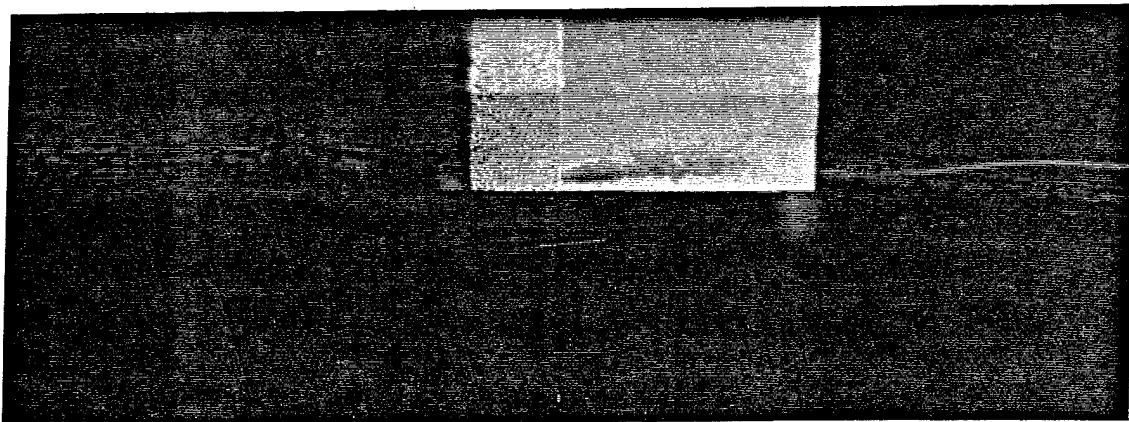


c. Exposure Time = 1/15 sec.

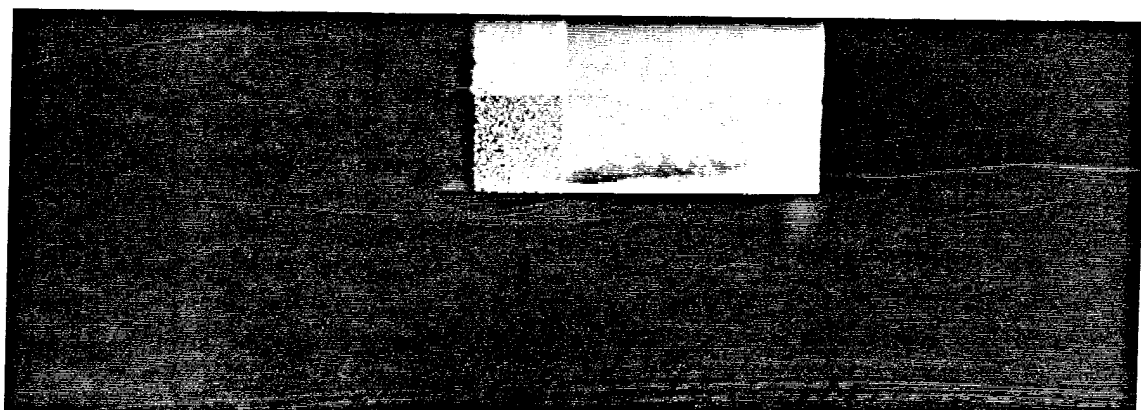


d. Exposure Time = 1/125 sec.

Figure 47. Tip Flow Visualizations, Endcap View
Aspect Ratio=3.0, Angle of Attack=7.5°, $Re_c=130000$

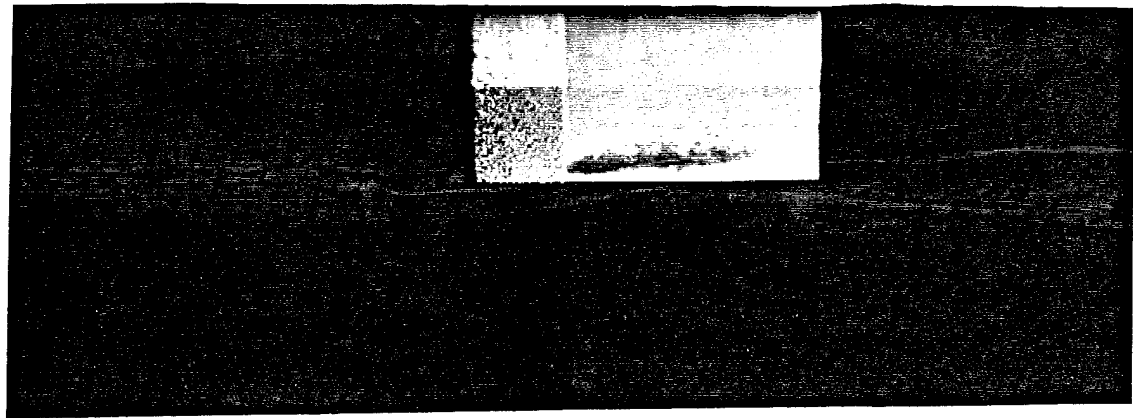


e. Exposure Time = 2 sec.

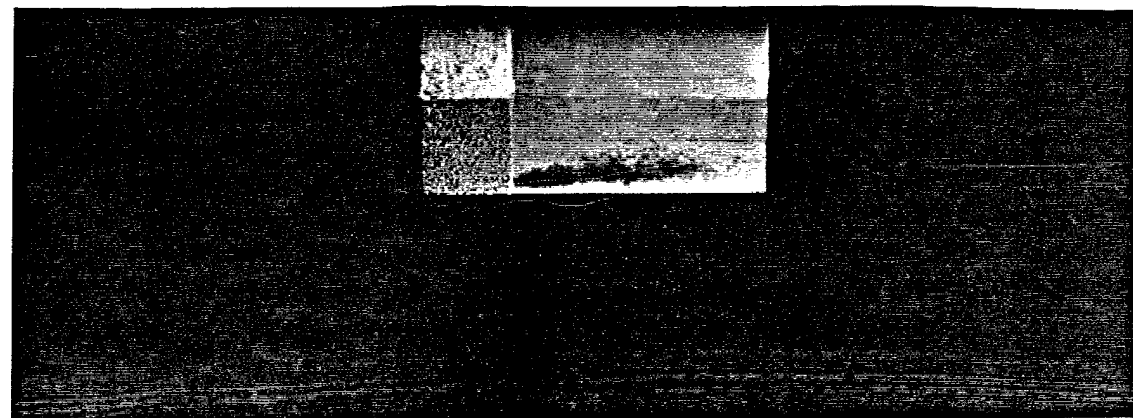


f. Exposure Time = 1/4 sec.

Figure 47. Tip Flow Visualizations, Suction Surface View
Aspect Ratio=3.0, Angle of Attack=7.5°, $Re_c=130000$

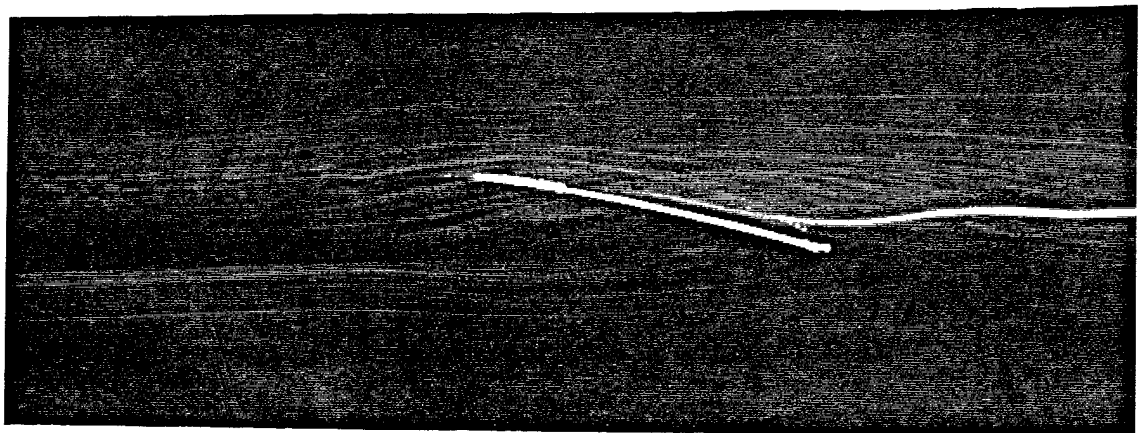


g. Exposure Time = 1/15 sec.

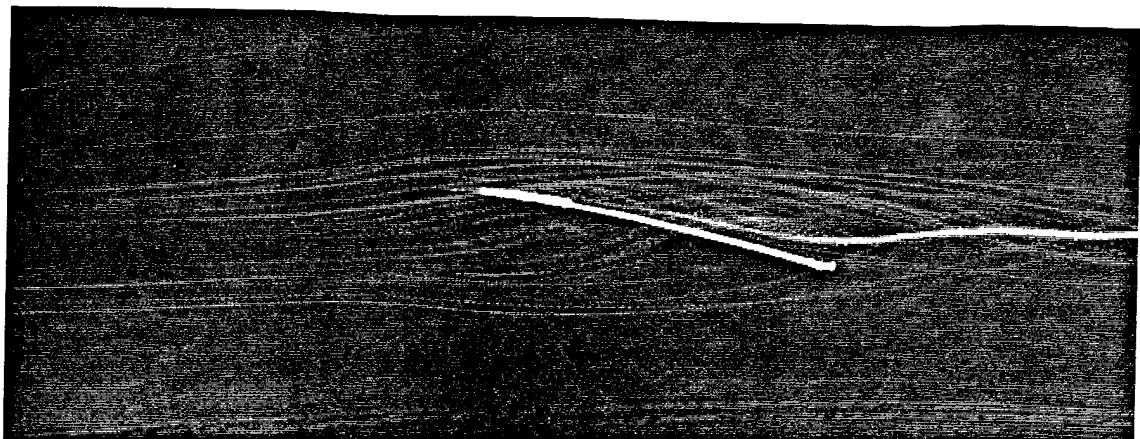


h. Exposure Time = 1/125 sec.

Figure 47. Tip Flow Visualizations, Suction Surface View
Aspect Ratio=3.0, Angle of Attack=7.5°, $Re_c=130000$

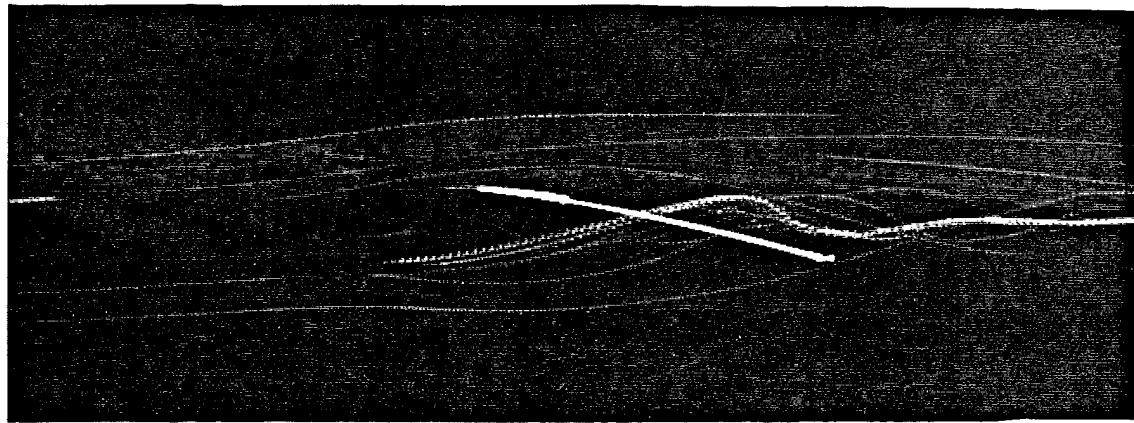


a. Exposure Time = 1 sec.

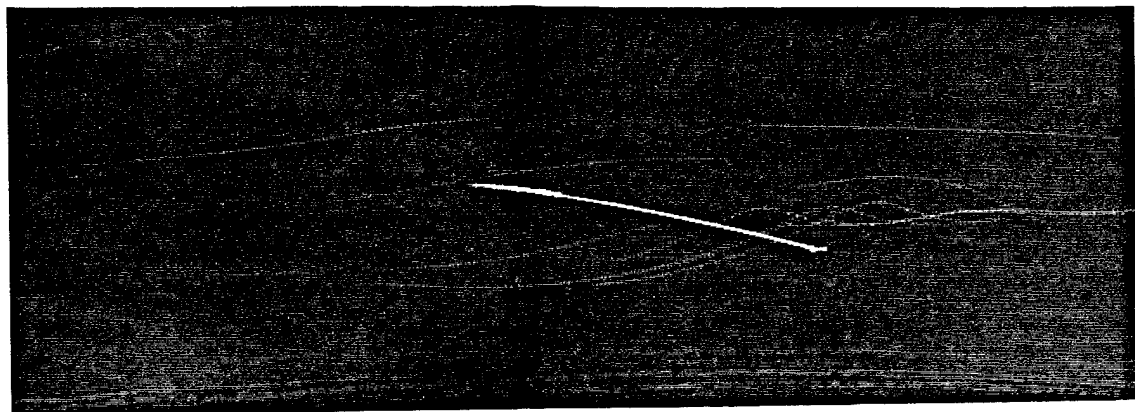


b. Exposure Time = 1/4 sec.

Figure 48. Tip Flow Visualizations, Endcap View
Aspect Ratio=3.0, Angle of Attack=7.5°, $Re_c=260000$

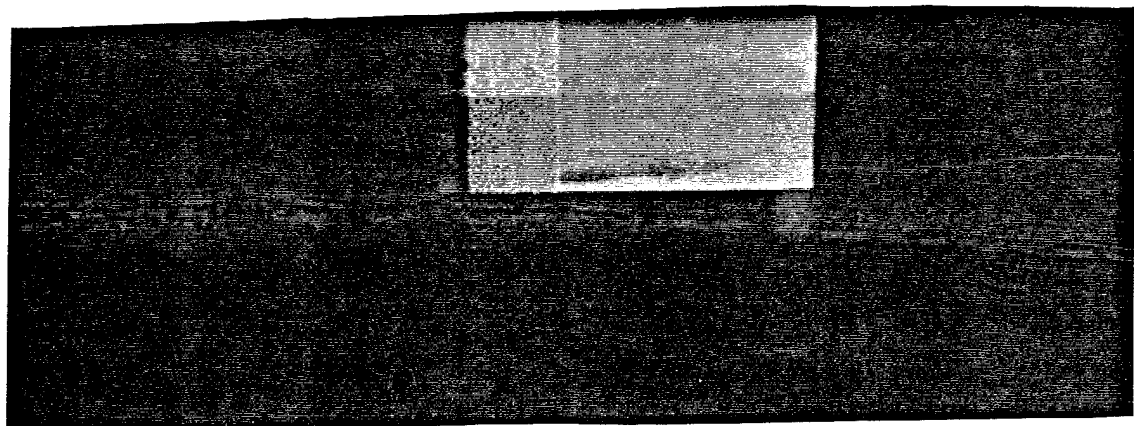


c. Exposure Time = 1/15 sec.

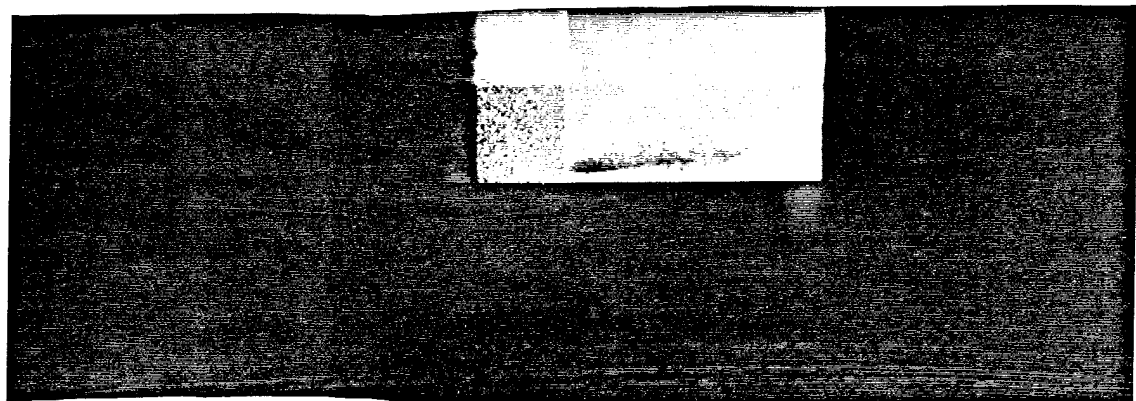


d. Exposure Time = 1/125 sec.

Figure 48. Tip Flow Visualizations, Endcap View
Aspect Ratio=3.0, Angle of Attack=7.5°, $Re_c=260000$

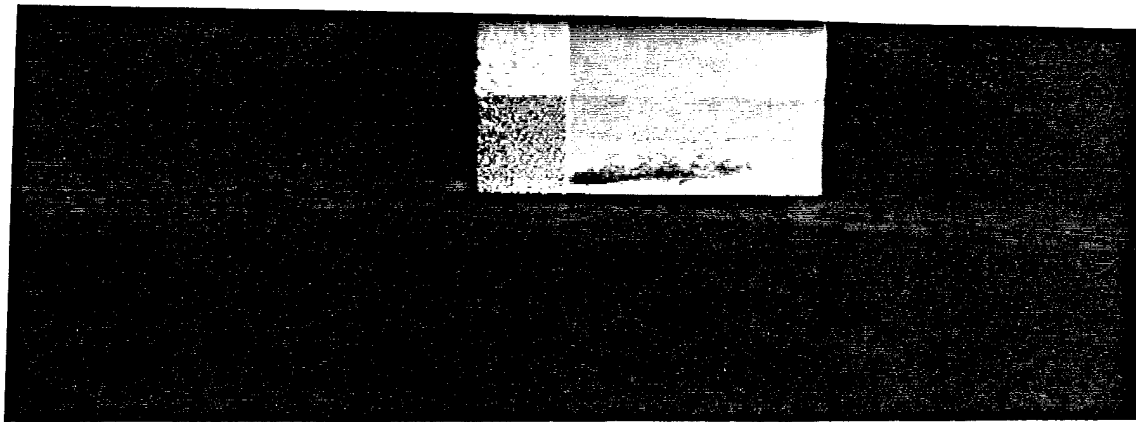


e. Exposure Time = 2 sec.

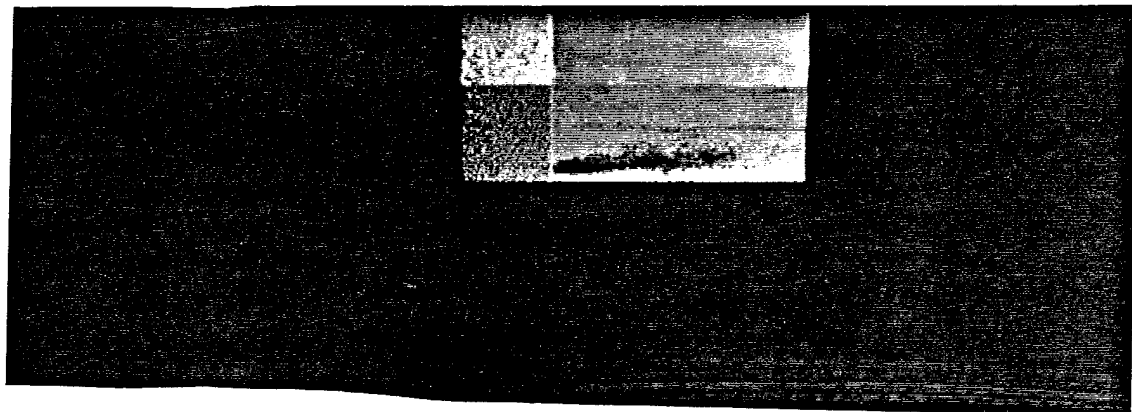


f. Exposure Time = 1/4 sec.

Figure 48. Tip Flow Visualizations, Suction Surface View
Aspect Ratio=3.0, Angle of Attack=7.5°, $Re_c=260000$

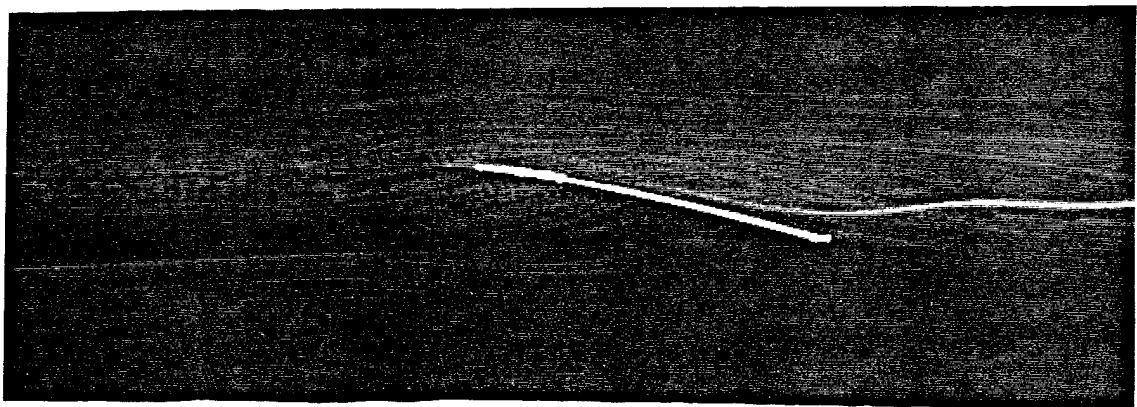


g. Exposure Time = 1/15 sec.

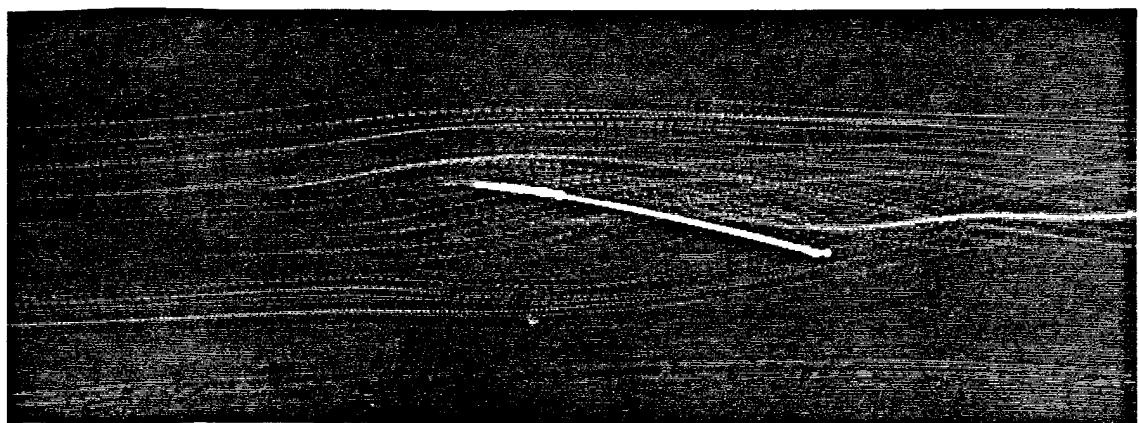


h. Exposure Time = 1/125 sec.

Figure 48. Tip Flow Visualizations, Suction Surface View
Aspect Ratio=3.0, Angle of Attack=7.5°, $Re_c=260000$

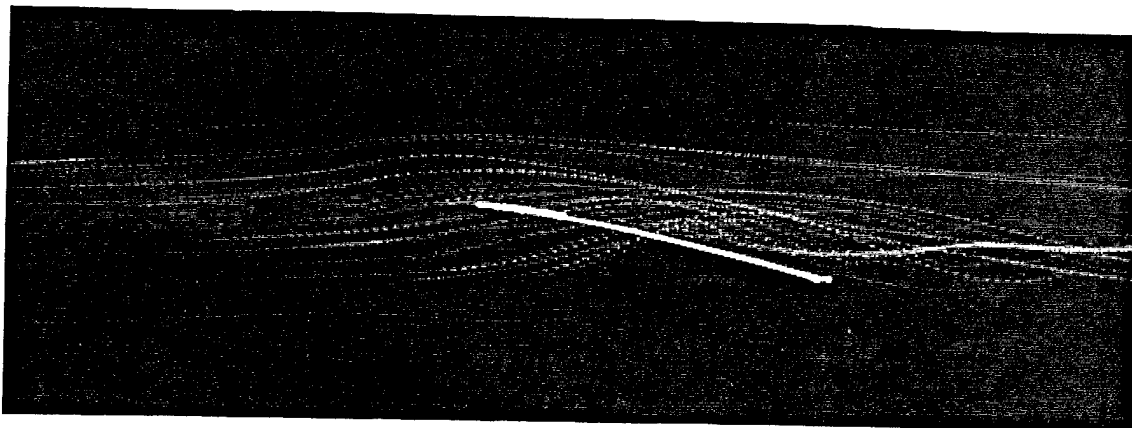


a. Exposure Time = 1 sec.

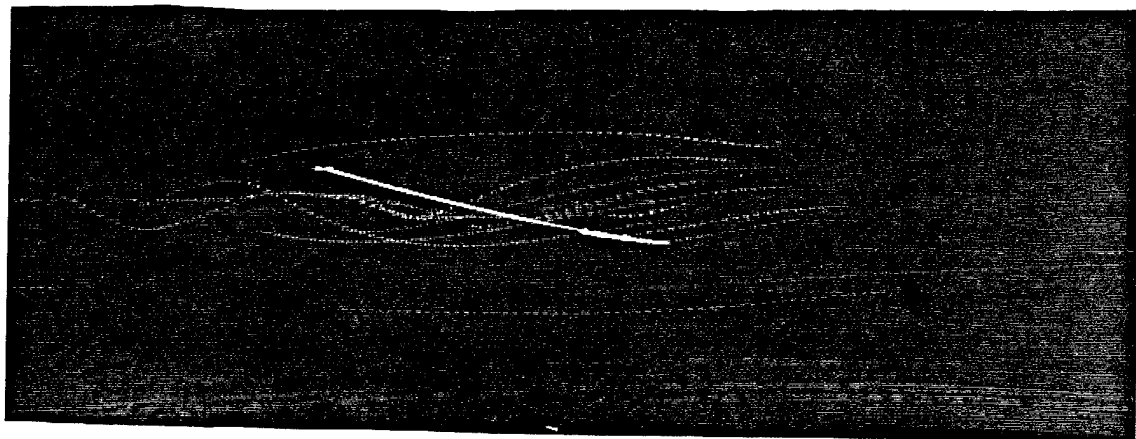


b. Exposure Time = 1/4 sec.

Figure 49. Tip Flow Visualizations, Endcap View
Aspect Ratio=3.0, Angle of Attack=7.5°, $Re_c=335000$

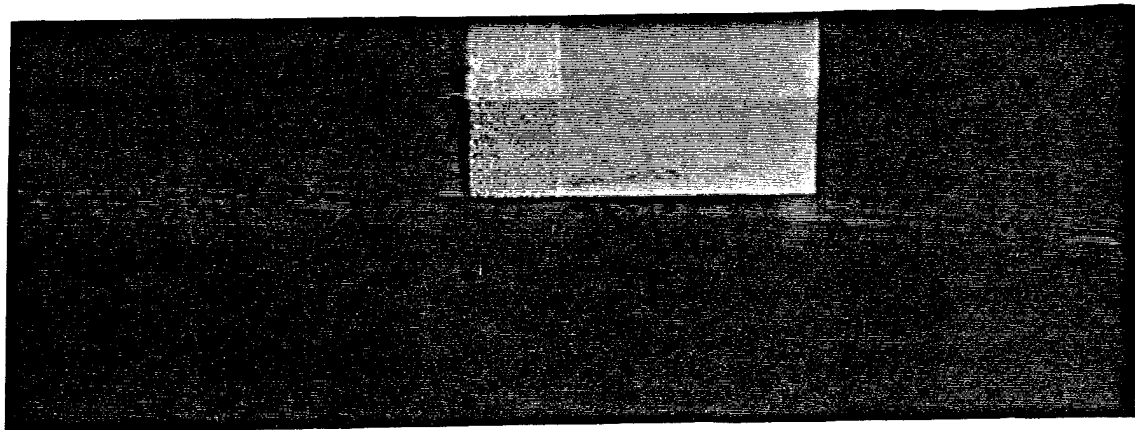


c. Exposure Time = 1/15 sec.

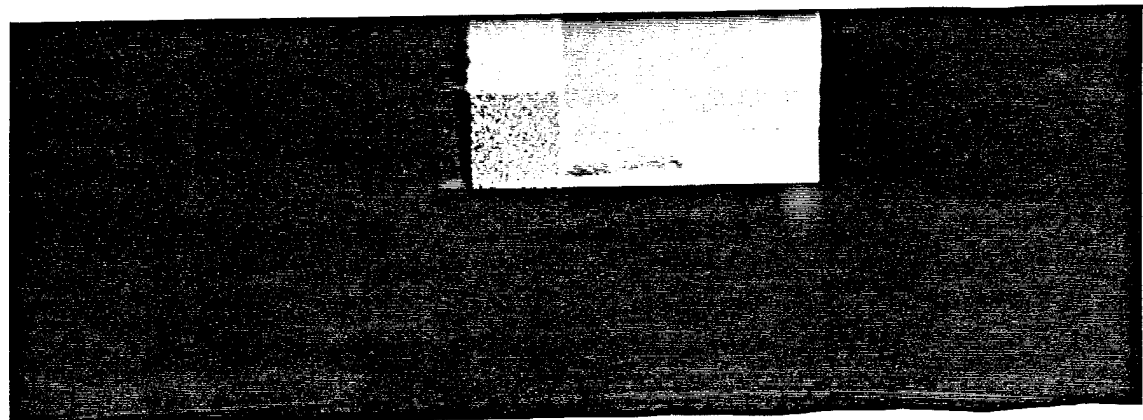


d. Exposure Time = 1/125 sec.

Figure 49. Tip Flow Visualizations, Endcap View
Aspect Ratio=3.0, Angle of Attack=7.5°, $Re_c=335000$

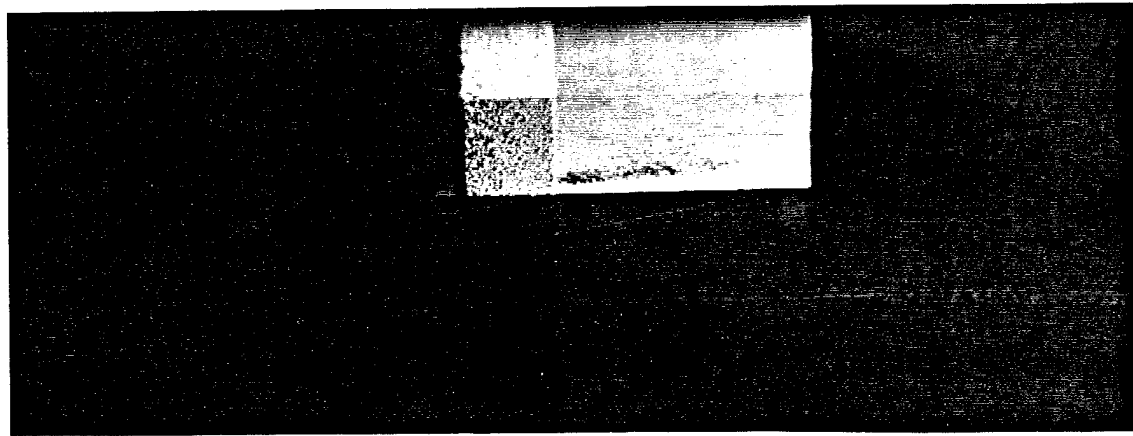


e. Exposure Time = 2 sec.



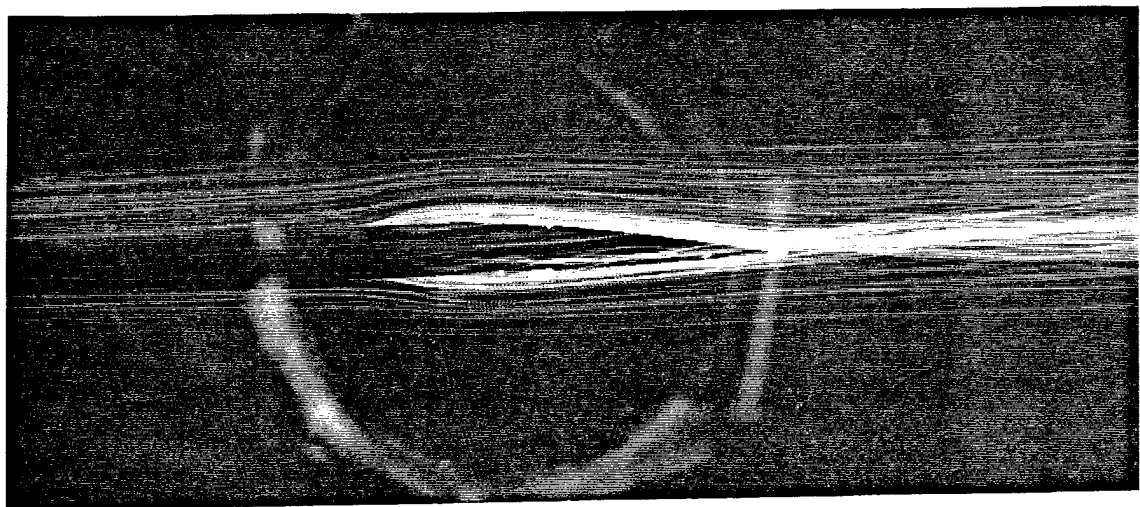
f. Exposure Time = 1/4 sec.

Figure 49. Tip Flow Visualizations, Suction Surface View
Aspect Ratio=3.0, Angle of Attack=7.5°, $Re_c=335000$

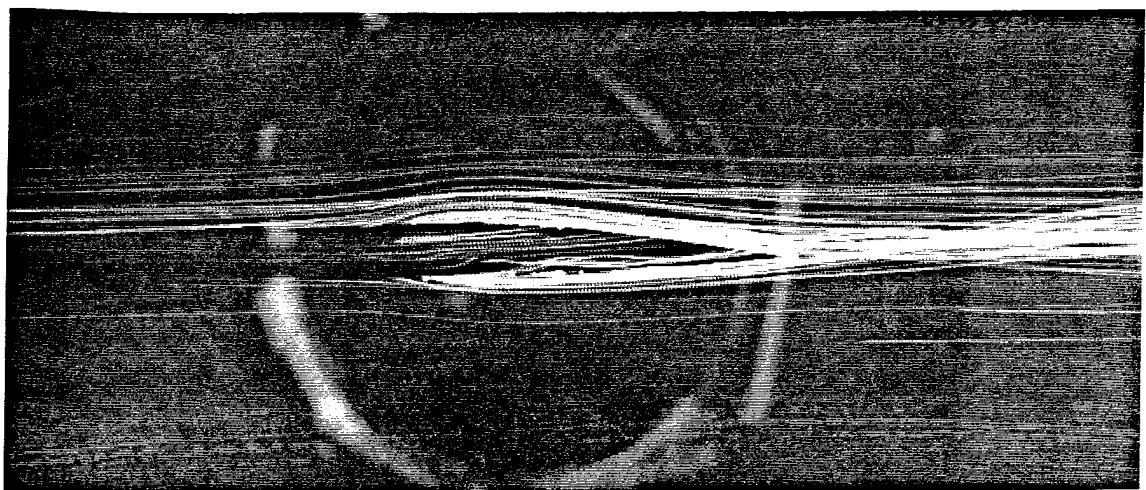


g. Exposure Time = 1/15 sec.

Figure 49. Tip Flow Visualizations, Suction Surface View
Aspect Ratio=3.0, Angle of Attack=7.5°, $Re_c=335000$

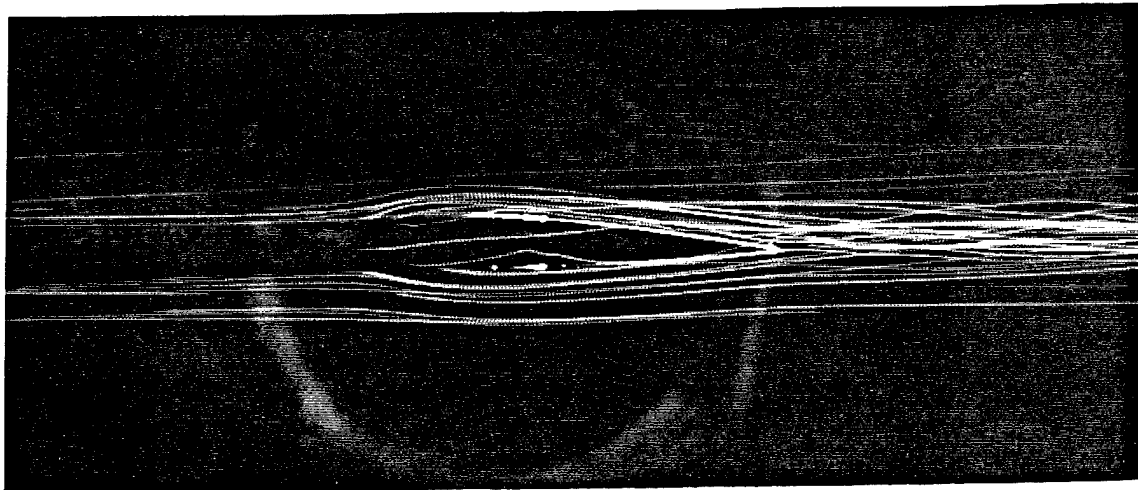


a. Exposure Time = 1 sec.

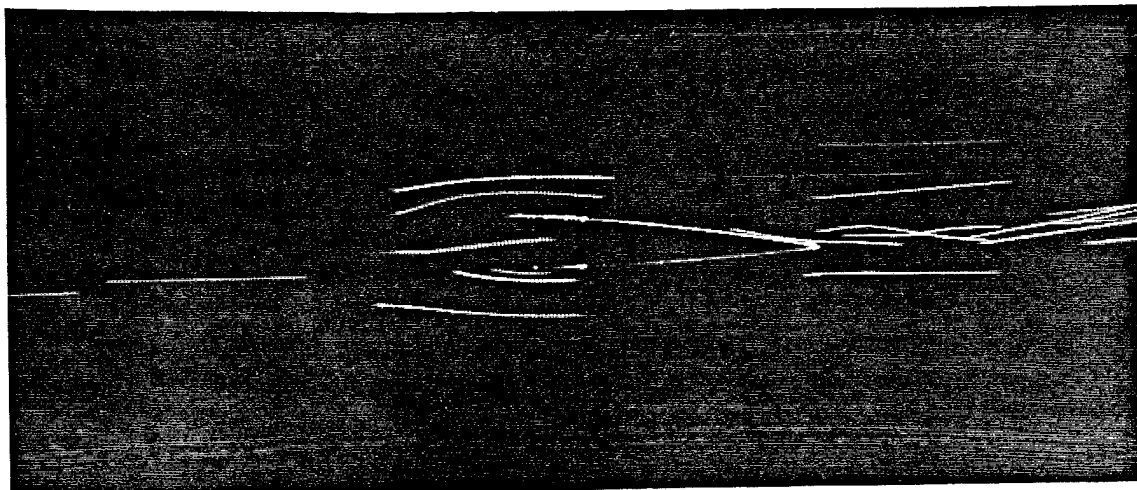


b. Exposure Time = 1/4 sec.

Figure 50. Tip Flow Visualizations, Endcap View
Aspect Ratio=2.5, Angle of Attack=2.5°, $Re_c=130000$

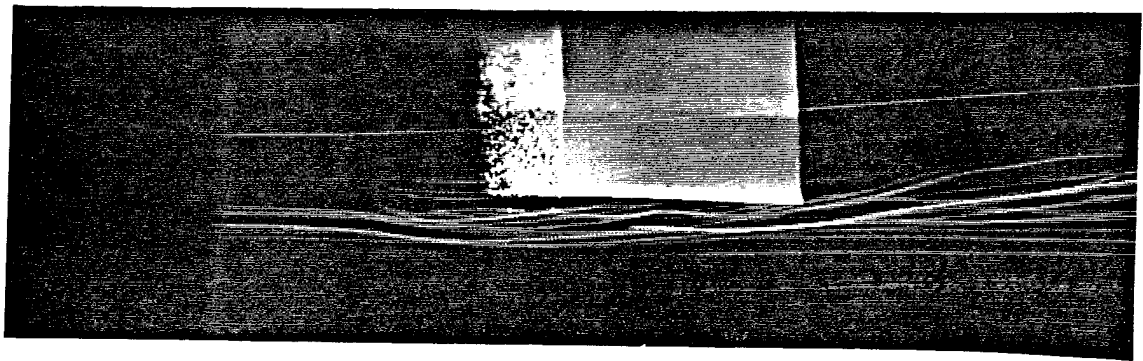


c. Exposure Time = 1/15 sec.



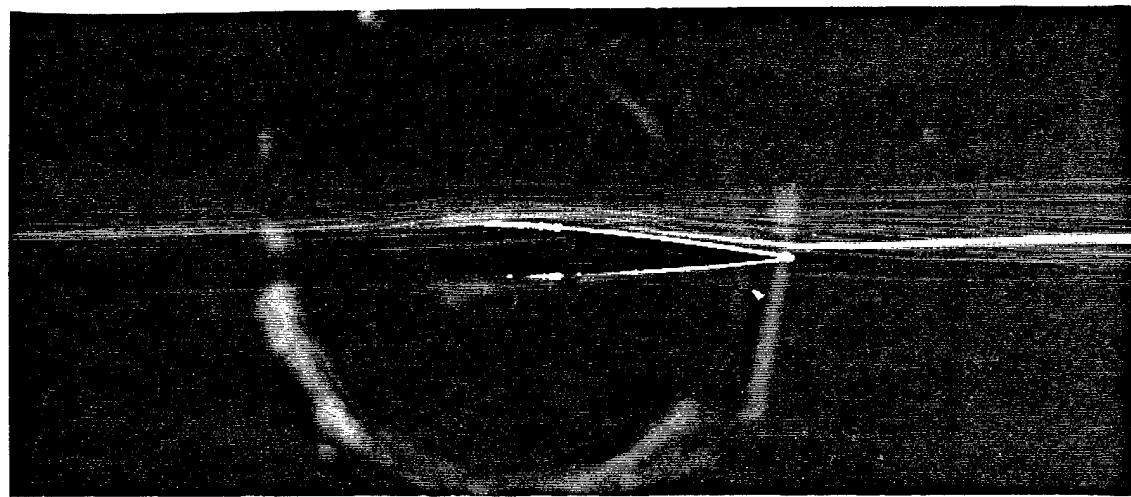
d. Exposure Time = 1/125 sec.

Figure 50. Tip Flow Visualizations, Endcap View
Aspect Ratio=2.5, Angle of Attack=2.5°, $Re_c=130000$

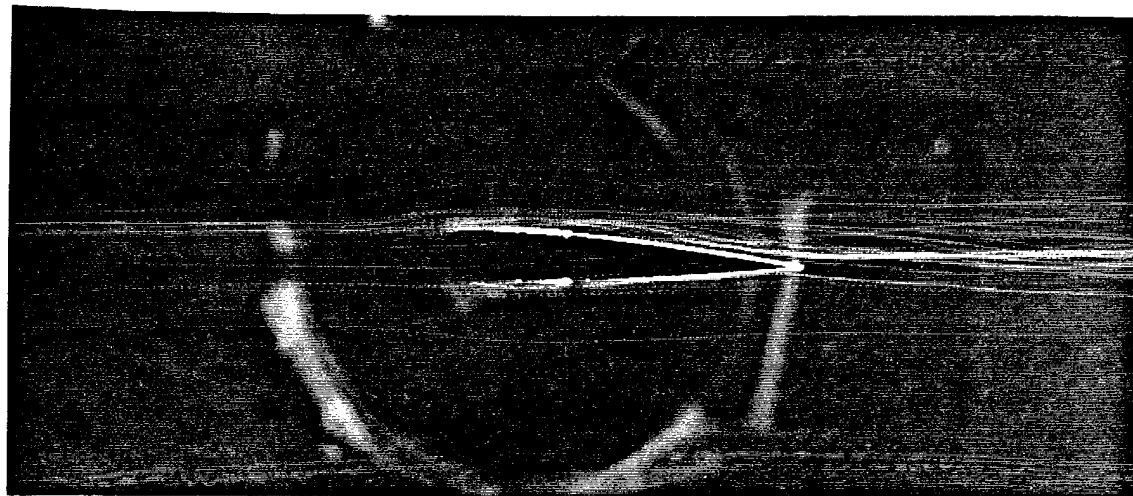


e. Exposure Time = 1 sec.

Figure 50. Tip Flow Visualizations, Suction Surface View
Aspect Ratio=2.5, Angle of Attack=2.5°, $Re_c=130000$

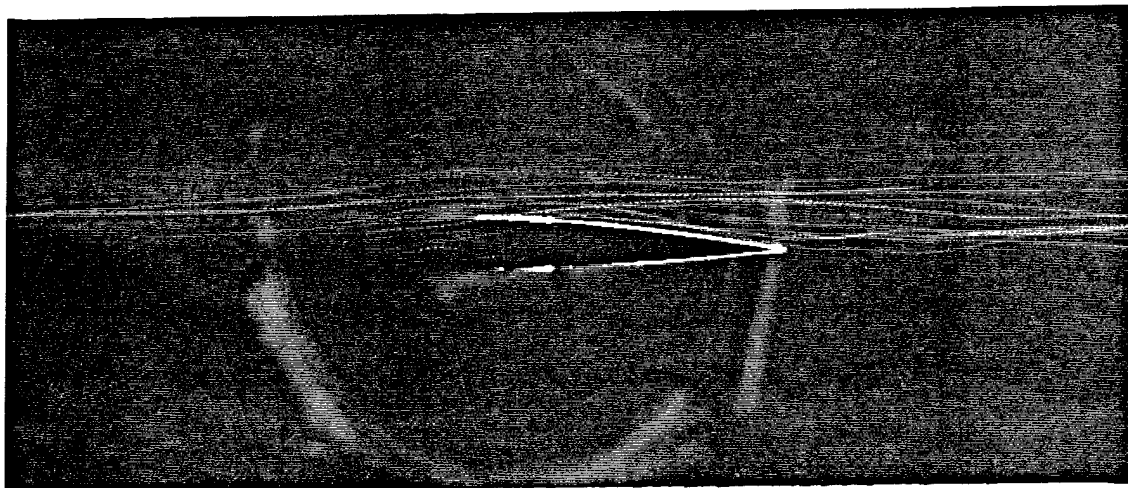


a. Exposure Time = 1 sec.

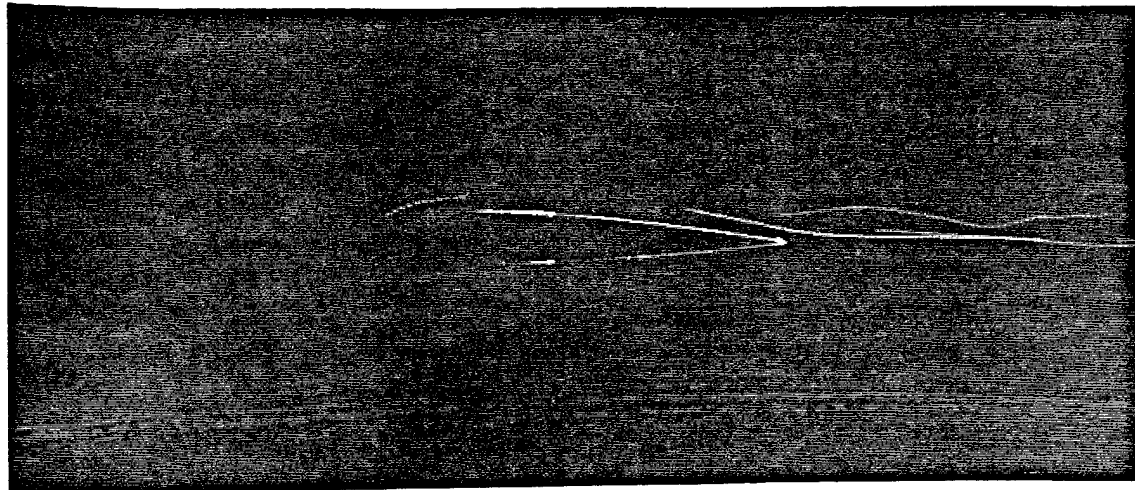


b. Exposure Time = 1/4 sec.

Figure 51. Tip Flow Visualizations, Endcap View
Aspect Ratio=2.5, Angle of Attack=2.5°, $Re_c=260000$

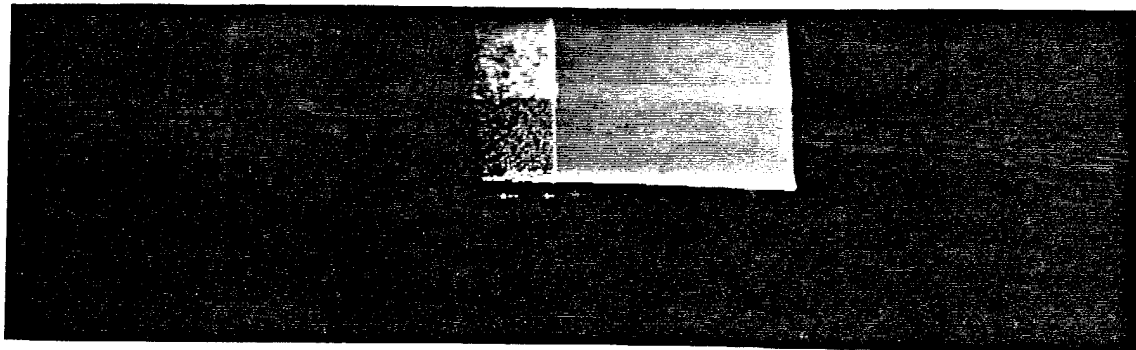


c. Exposure Time = 1/15 sec.

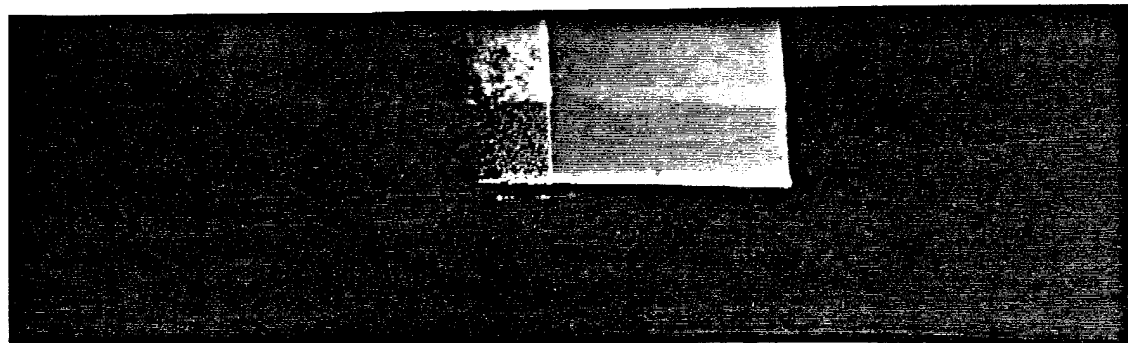


d. Exposure Time = 1/125 sec.

Figure 51. Tip Flow Visualizations, Endcap View
Aspect Ratio=2.5, Angle of Attack=2.5°, $Re_c=260000$

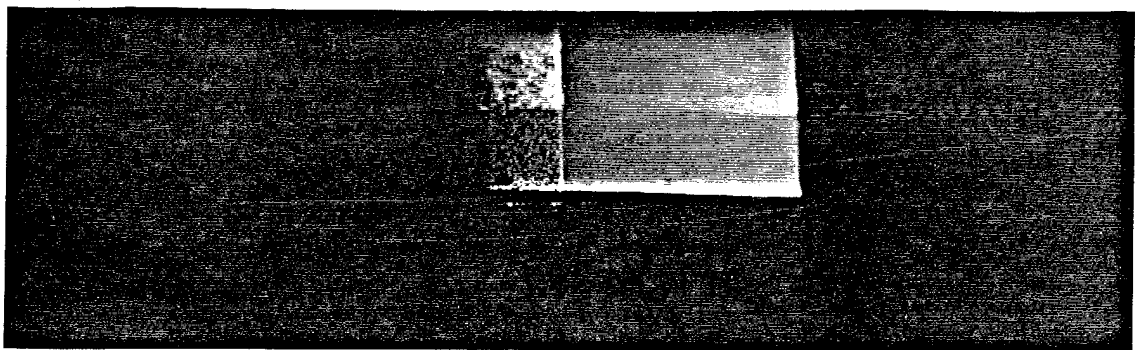


e. Exposure Time = 1 sec.



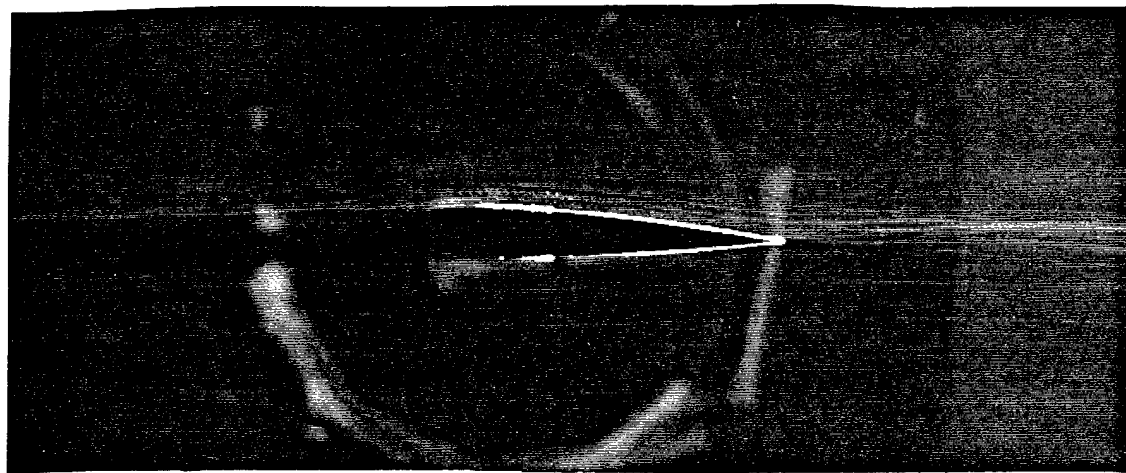
f. Exposure Time = 1/4 sec.

Figure 51. Tip Flow Visualizations, Suction Surface View
Aspect Ratio=2.5, Angle of Attack=2.5°, $Re_c=260000$

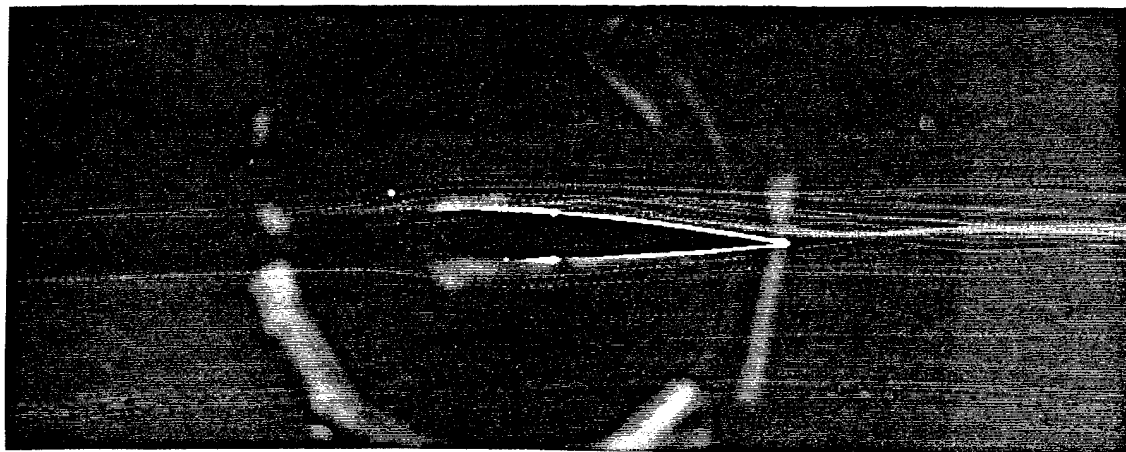


g. Exposure Time = 1/15 sec.

Figure 51. Tip Flow Visualizations, Suction Surface View
Aspect Ratio=2.5, Angle of Attack=2.5°, $Re_c=260000$

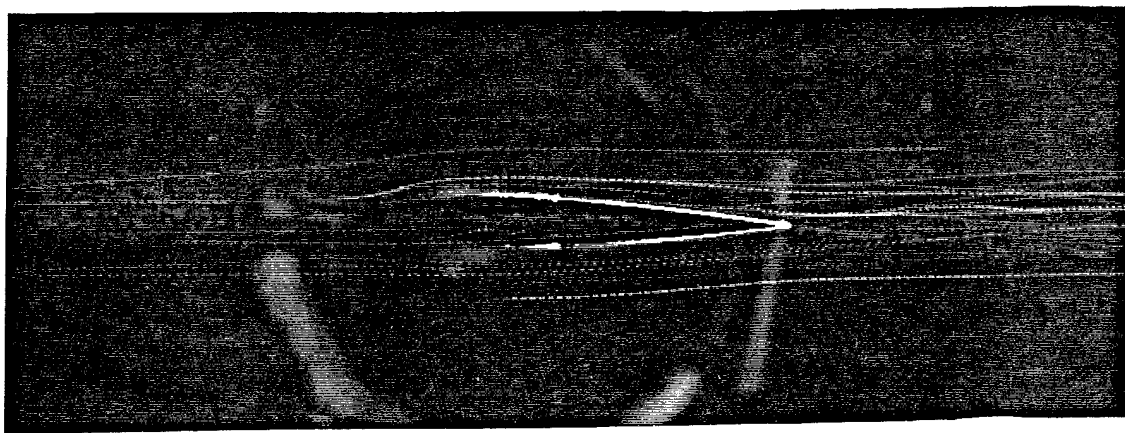


a. Exposure Time = 1 sec.

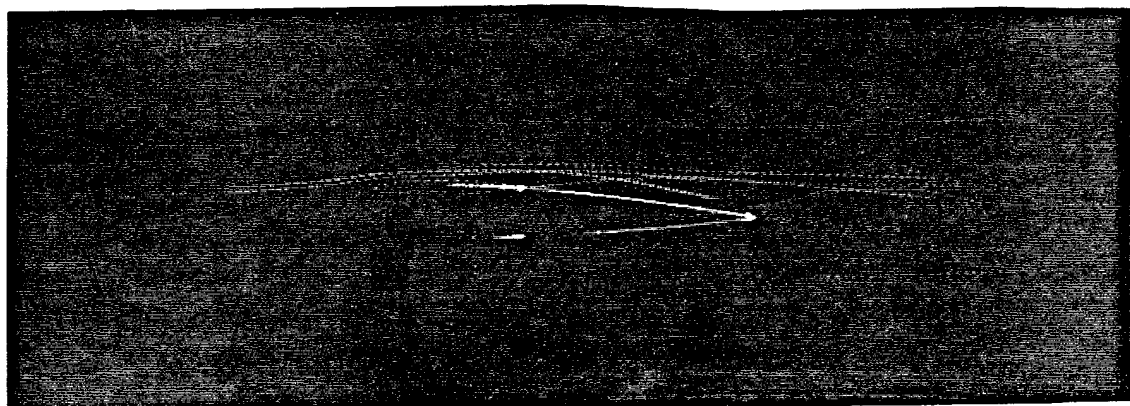


b. Exposure Time = 1/4 sec.

Figure 52. Tip Flow Visualizations, Endcap View
Aspect Ratio=2.5, Angle of Attack=2.5°, $Re_c=335000$

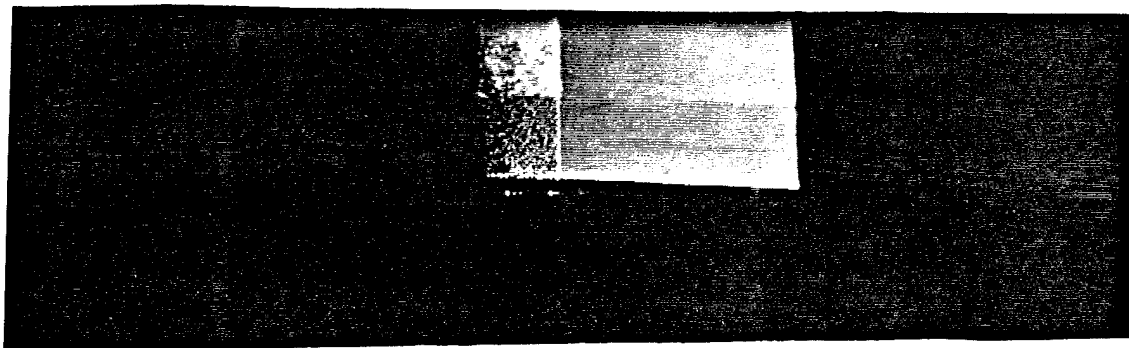


c. Exposure Time = 1/15 sec.

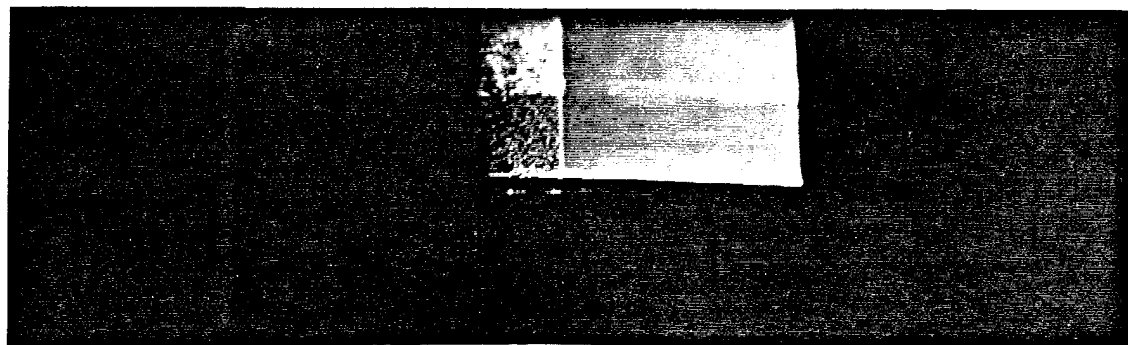


d. Exposure Time = 1/125 sec.

Figure 52. Tip Flow Visualizations, Endcap View
Aspect Ratio=2.5, Angle of Attack=2.5°, $Re_c=335000$

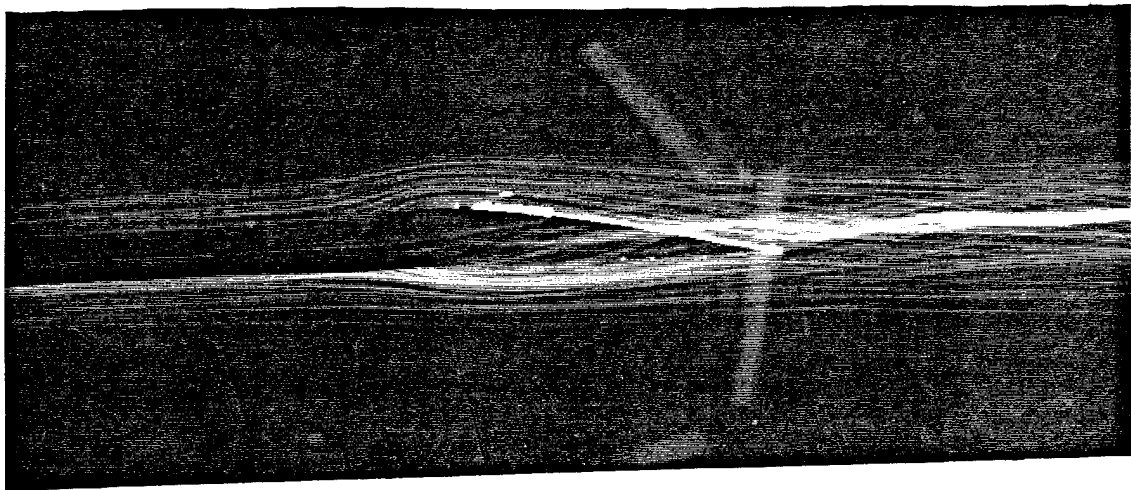


e. Exposure Time = 1 sec.

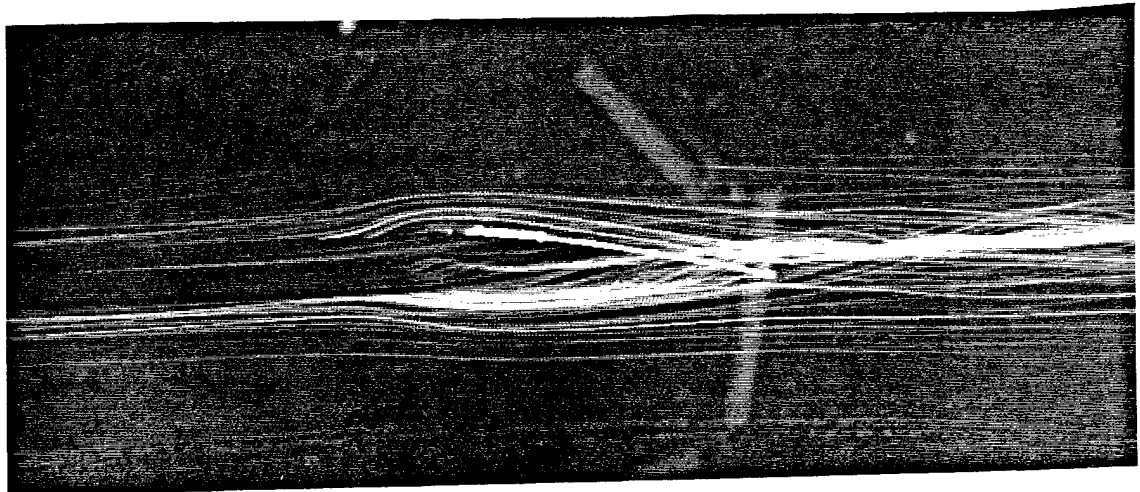


f. Exposure Time = 1/4 sec.

Figure 52. Tip Flow Visualizations, Suction Surface View
Aspect Ratio=2.5, Angle of Attack=2.5°, $Re_c=335000$

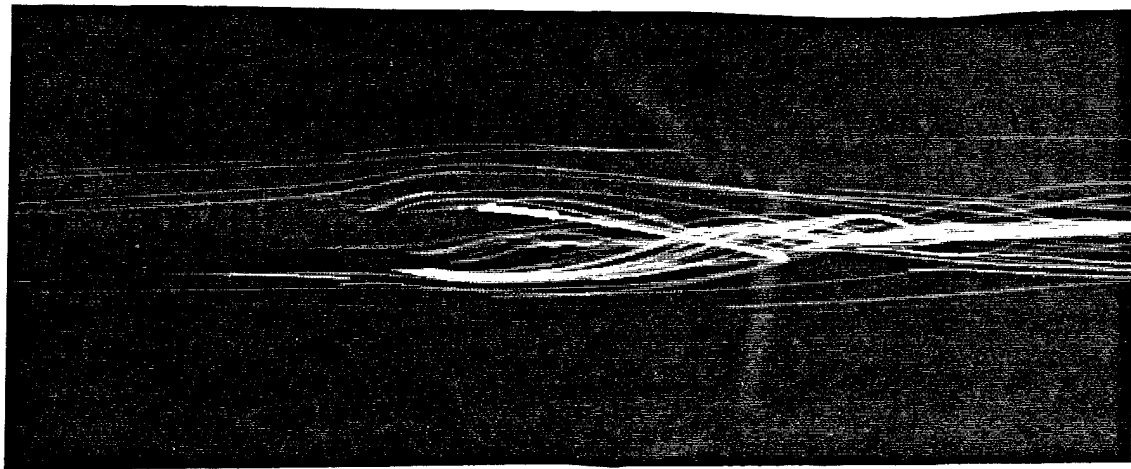


a. Exposure Time = 1 sec.

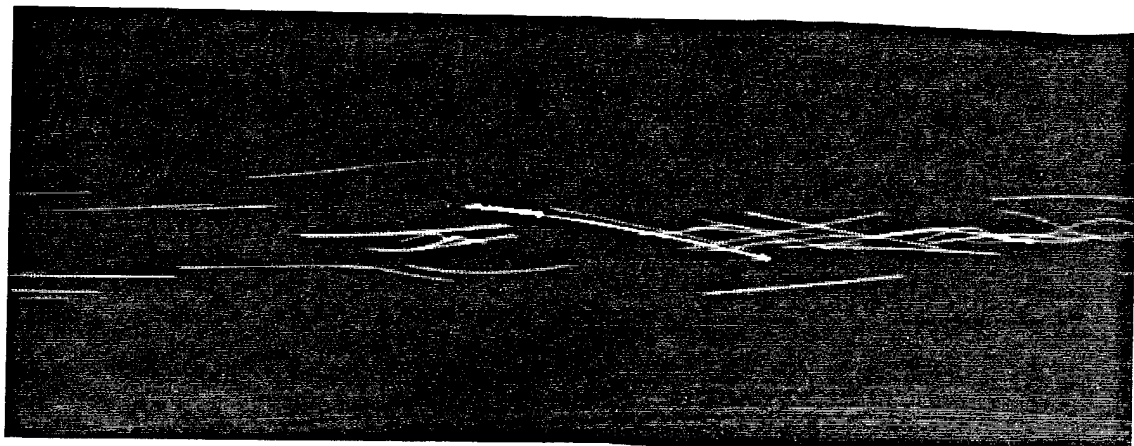


b. Exposure Time = 1/4 sec.

Figure 53. Tip Flow Visualizations, Endcap View
Aspect Ratio=2.5, Angle of Attack=5.0°, $Re_c=130000$

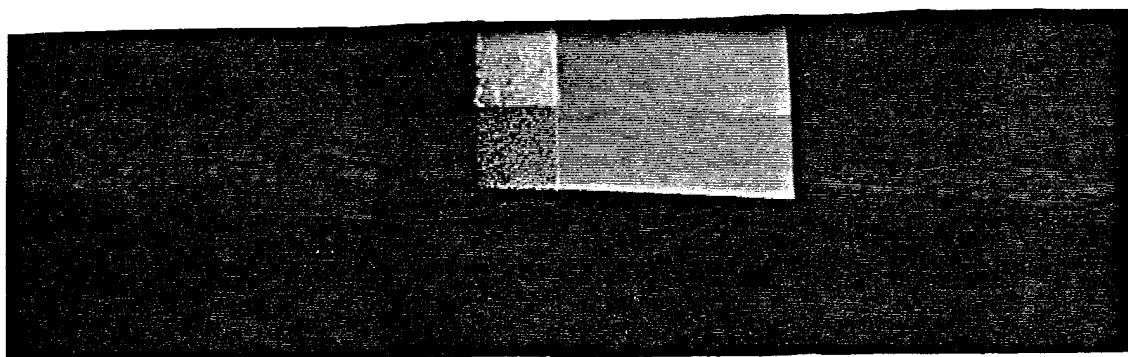


c. Exposure Time = 1/15 sec.

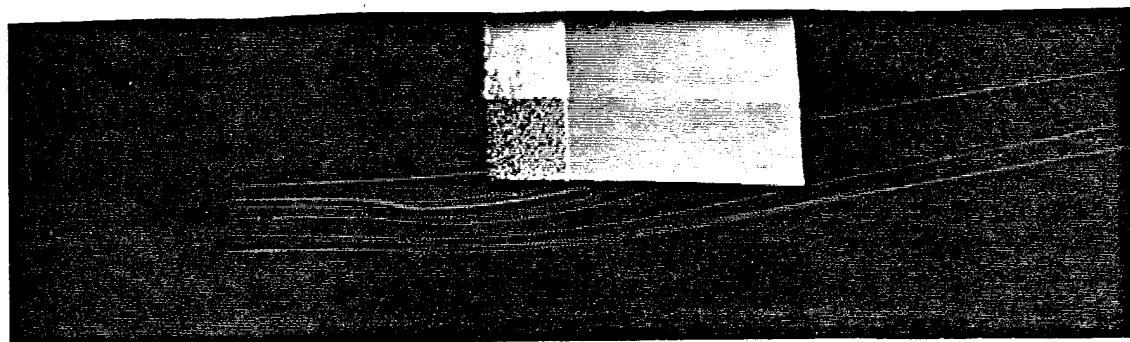


d. Exposure Time = 1/125 sec.

Figure 53. Tip Flow Visualizations, Endcap View
Aspect Ratio=2.5, Angle of Attack=5.0°, $Re_c=130000$

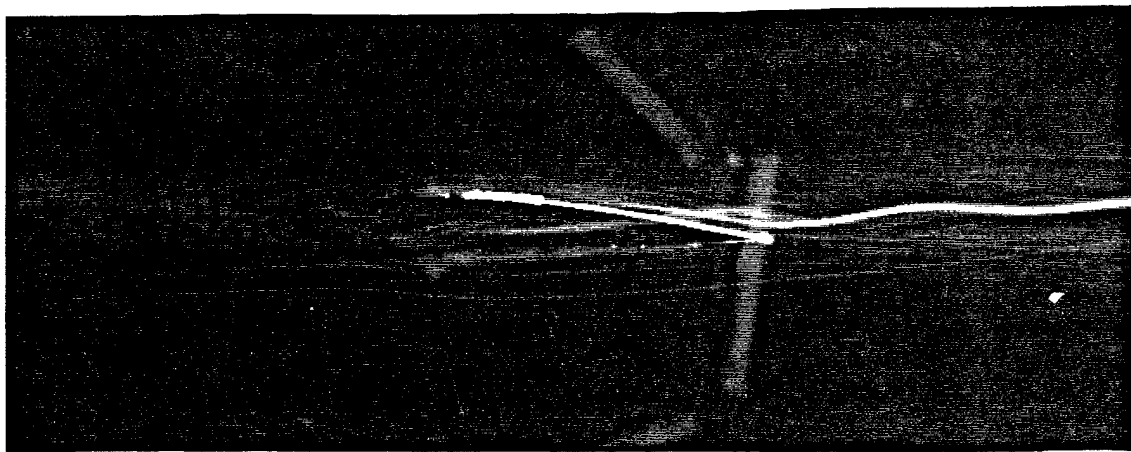


e. Exposure Time = 1 sec.

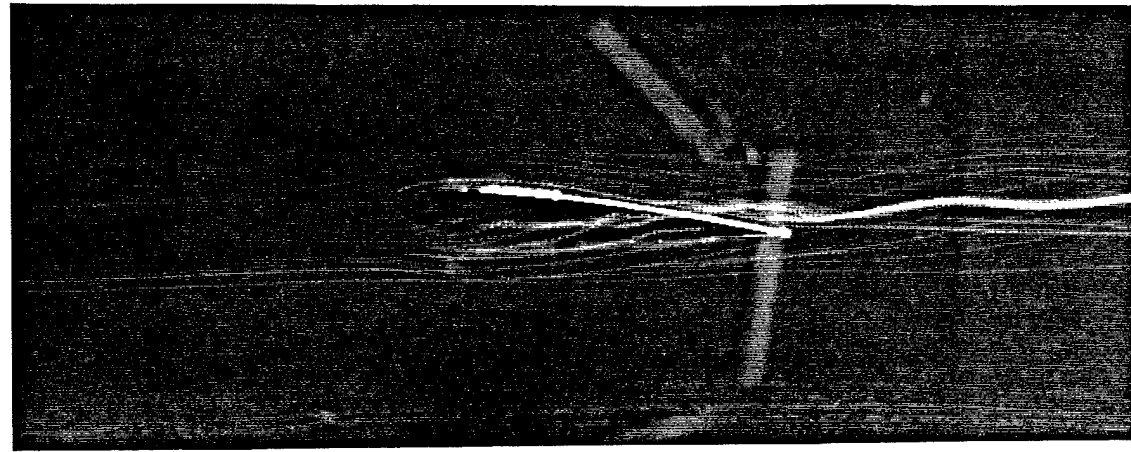


f. Exposure Time = 1/4 sec.

Figure 53. Tip Flow Visualizations, Suction Surface View
Aspect Ratio=2.5, Angle of Attack=5.0°, $Re_c=130000$

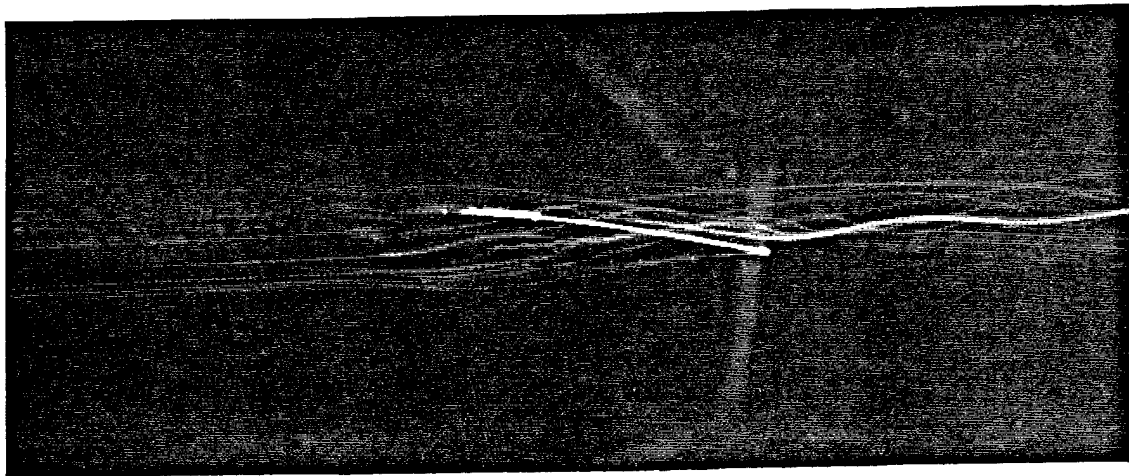


a. Exposure Time = 1 sec.

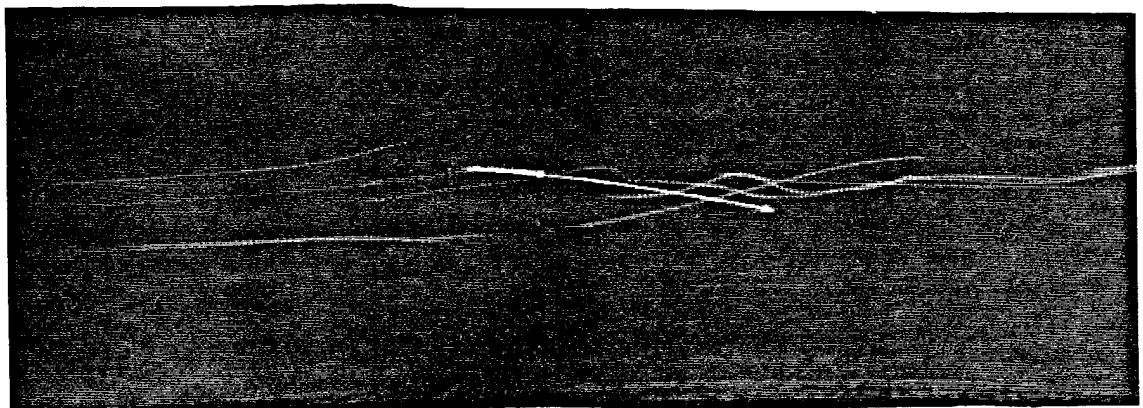


b. Exposure Time = 1/4 sec.

Figure 54. Tip Flow Visualizations, Endcap View
Aspect Ratio=2.5, Angle of Attack=5.0°, $Re_c=260000$

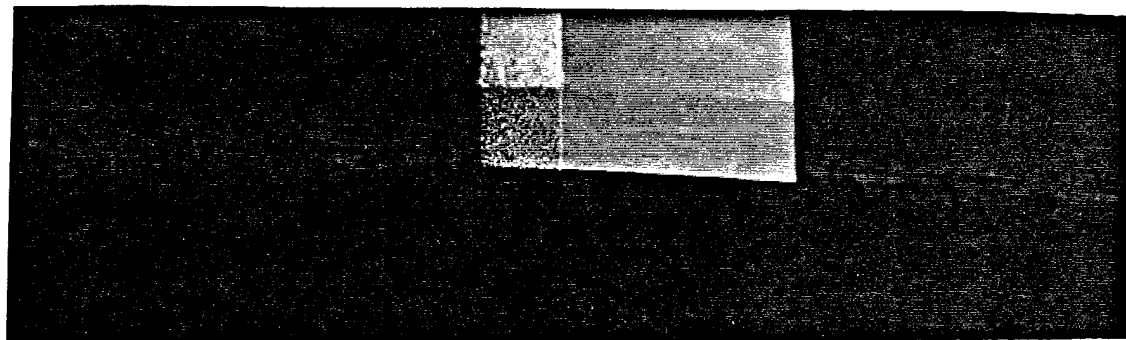


c. Exposure Time = 1/15 sec.

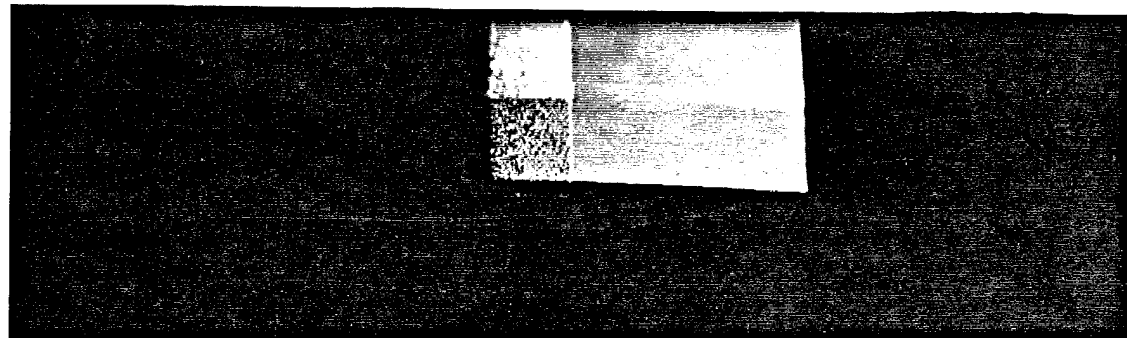


d. Exposure Time = 1/125 sec.

Figure 54. Tip Flow Visualizations, Endcap View
Aspect Ratio=2.5, Angle of Attack=5.0°, $Re_c=260000$

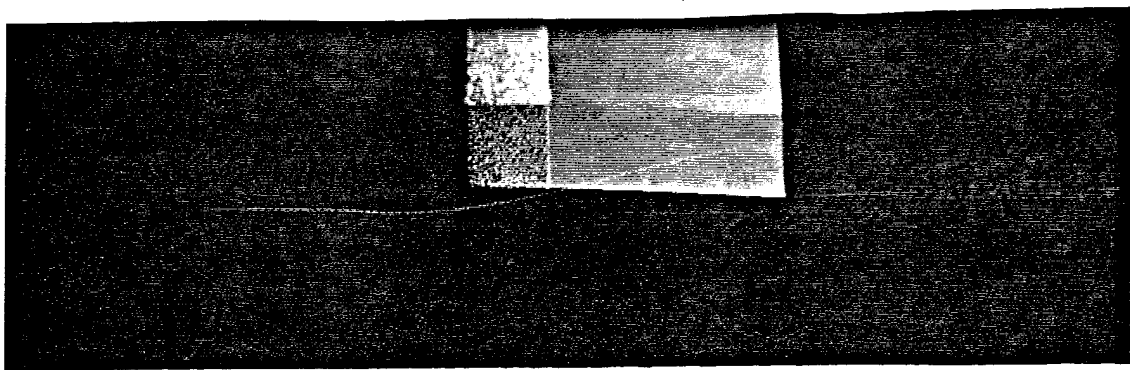


e. Exposure Time = 1 sec.



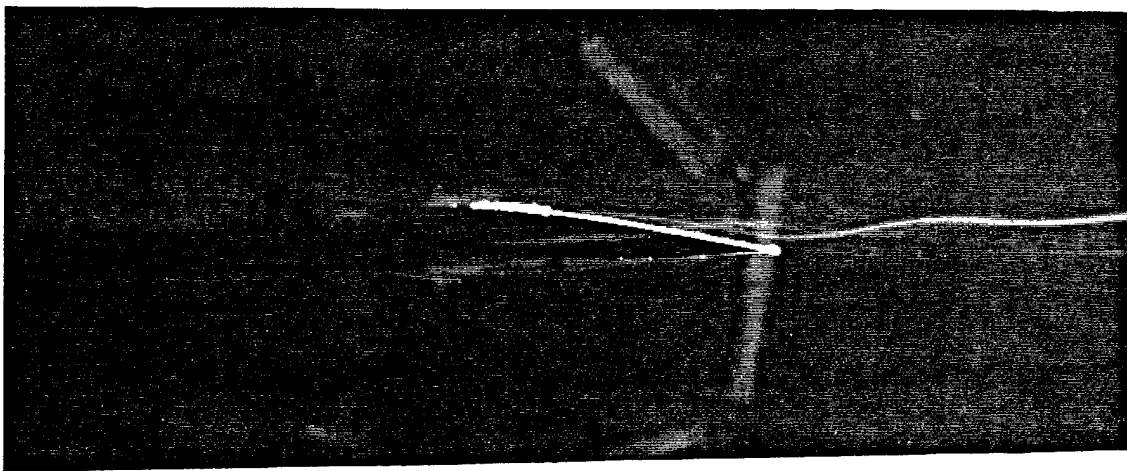
f. Exposure Time = 1/4 sec.

Figure 54. Tip Flow Visualizations, Suction Surface View
Aspect Ratio=2.5, Angle of Attack=5.0°, $Re_c=260000$

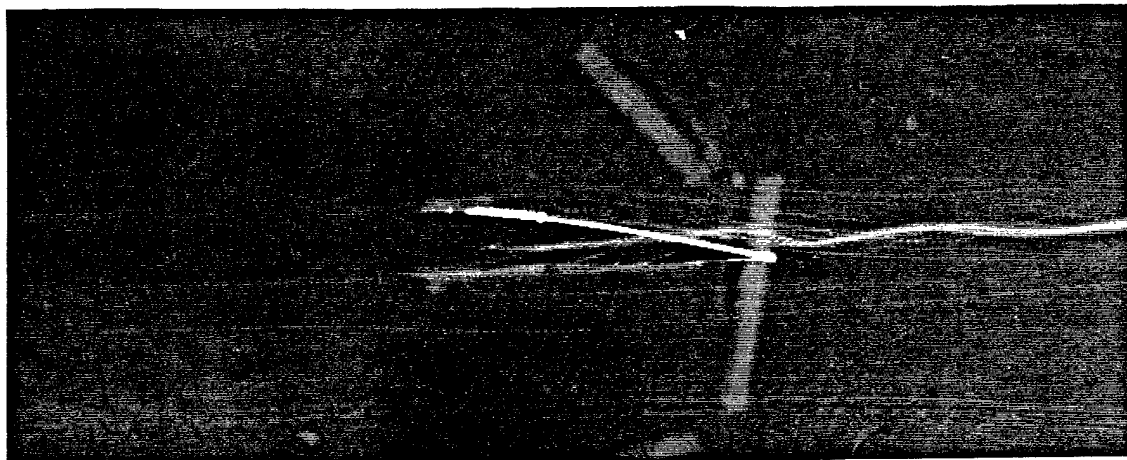


g. Exposure Time = 1/15 sec.

Figure 54. Tip Flow Visualizations, Suction Surface View
Aspect Ratio=2.5, Angle of Attack=5.0°, $Re_c=260000$

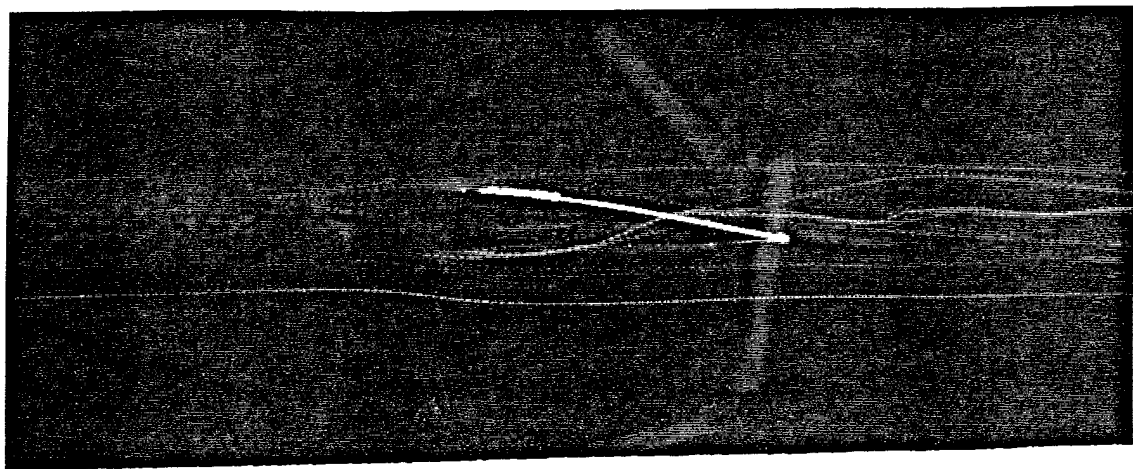


a. Exposure Time = 1 sec.

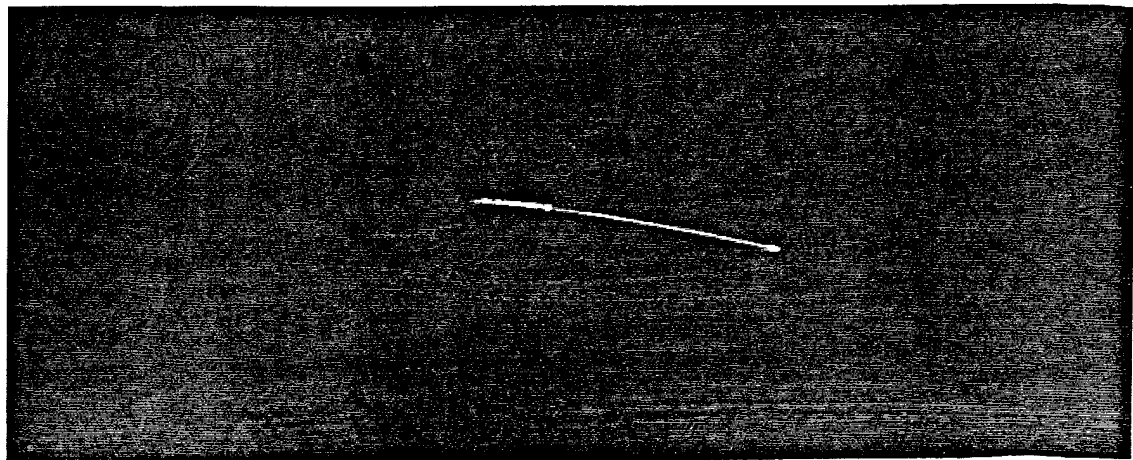


b. Exposure Time = 1/4 sec.

Figure 55. Tip Flow Visualizations, Endcap View
Aspect Ratio=2.5, Angle of Attack=5.0°, $Re_c=335000$

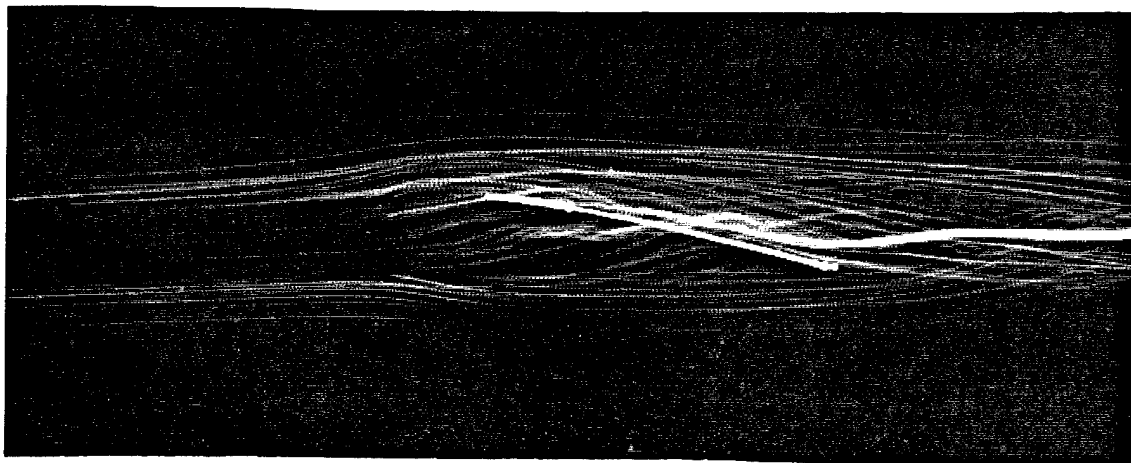


c. Exposure Time = 1/15 sec.

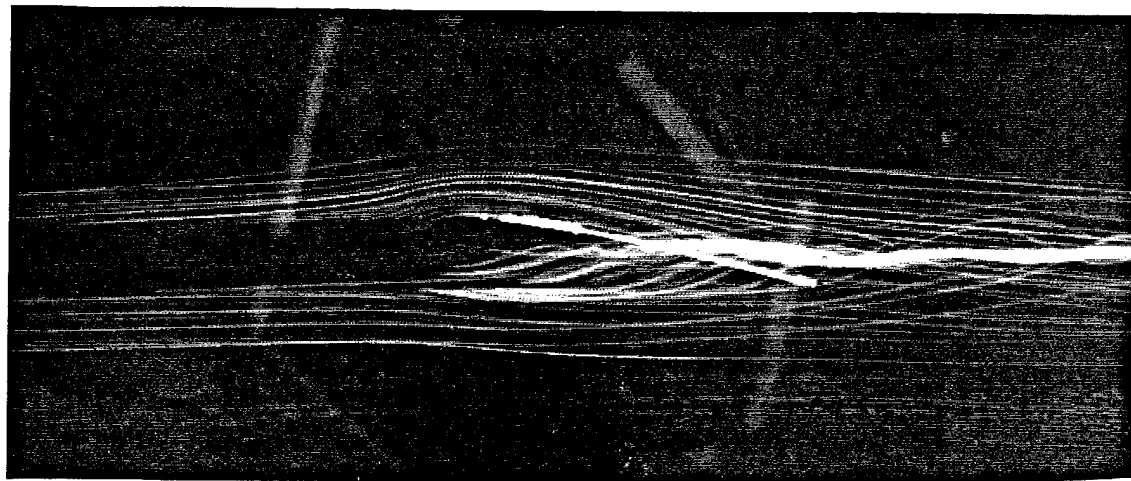


d. Exposure Time = 1/125 sec.

Figure 55. Tip Flow Visualizations, Endcap View
Aspect Ratio=2.5, Angle of Attack=5.0°, $Re_c=335000$

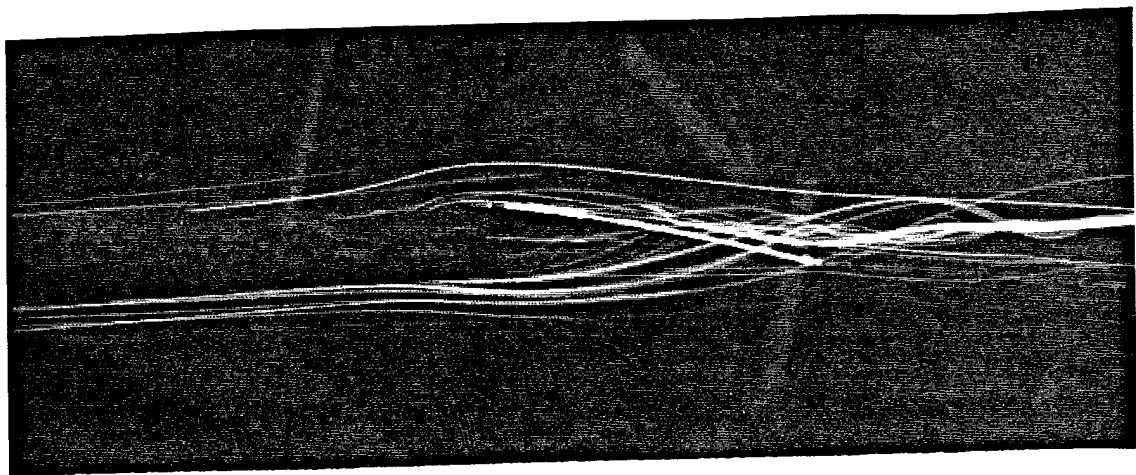


a. Exposure Time = 1 sec.

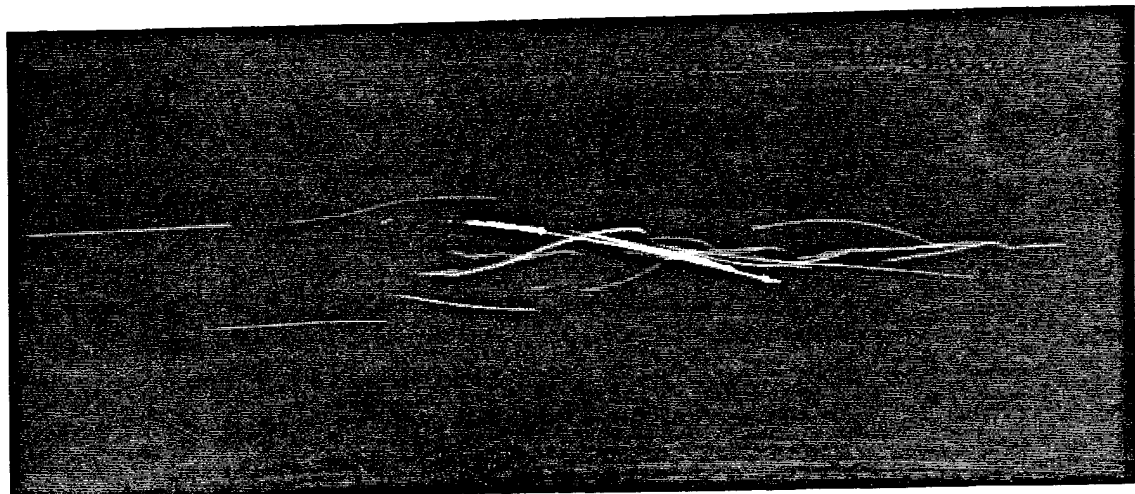


b. Exposure Time = 1/4 sec.

Figure 56. Tip Flow Visualizations, Endcap View
Aspect Ratio=2.5, Angle of Attack= 7.5° , $Re_c=130000$

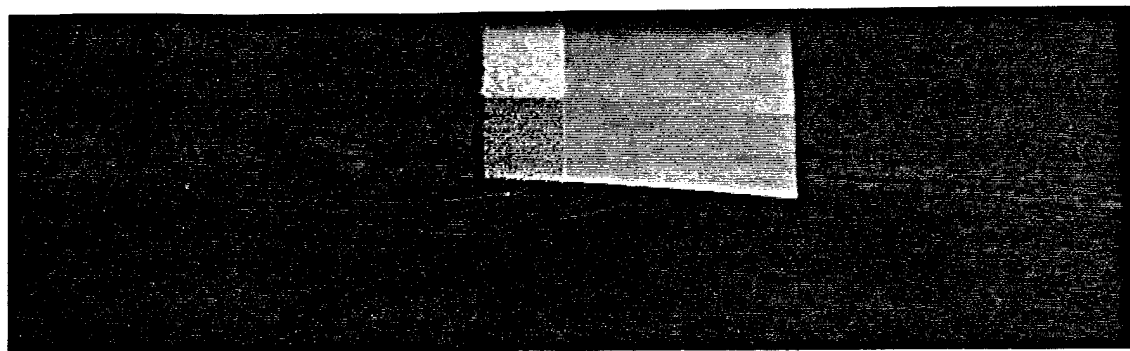


c. Exposure Time = 1/15 sec.

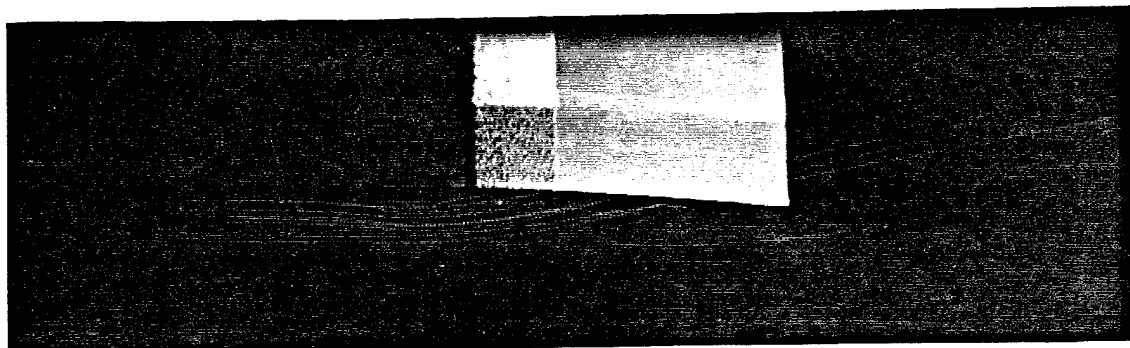


d. Exposure Time = 1/125 sec.

Figure 56. Tip Flow Visualizations, Endcap View
Aspect Ratio=2.5, Angle of Attack=7.5°, $Re_c=130000$

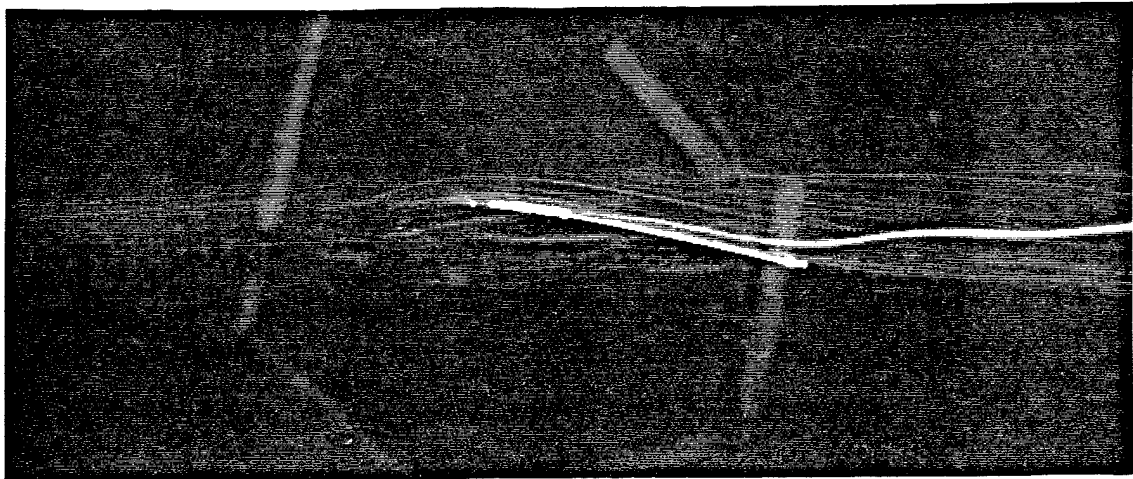


e. Exposure Time = 1 sec.



f. Exposure Time = 1/4 sec.

Figure 56. Tip Flow Visualizations, Suction Surface View
Aspect Ratio=2.5, Angle of Attack=7.5°, $Re_c=130000$

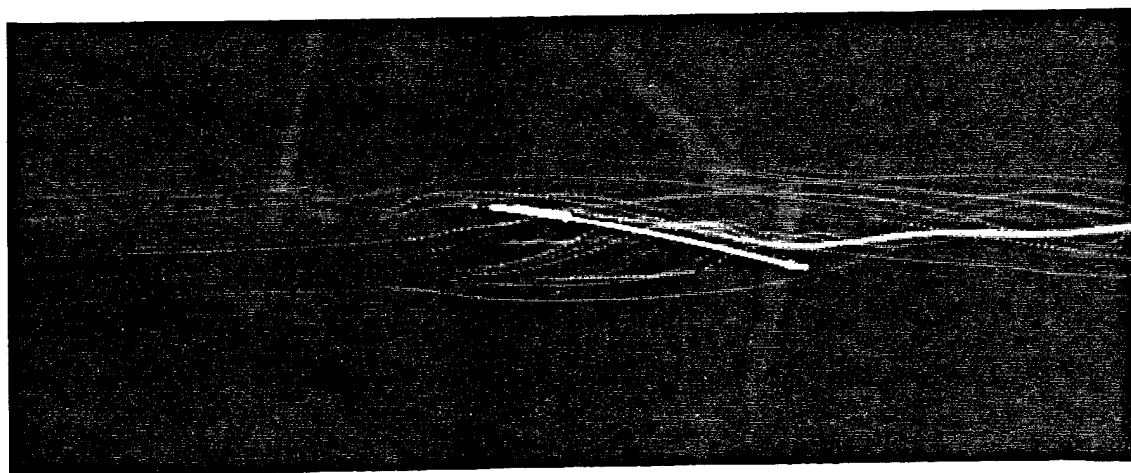


a. Exposure Time = 1 sec.

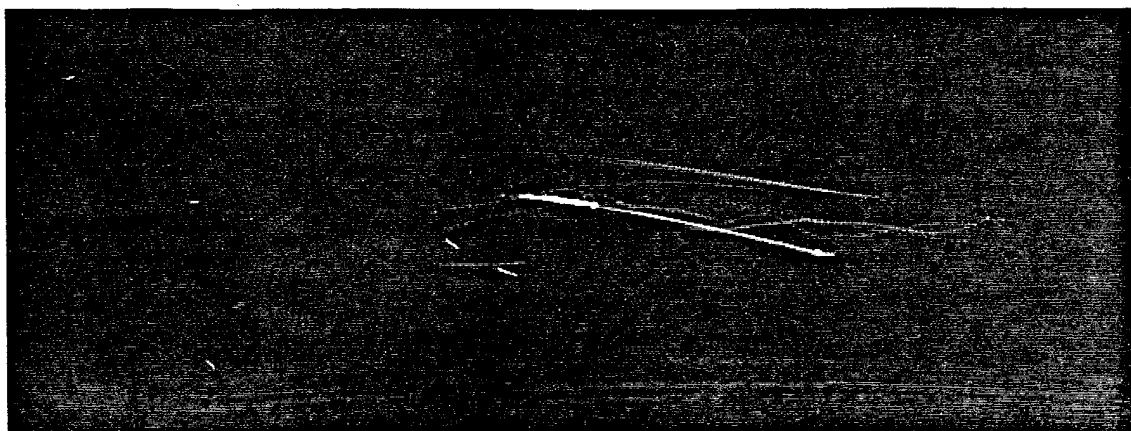


b. Exposure Time = 1/4 sec.

Figure 57. Tip Flow Visualizations, Endcap View
Aspect Ratio=2.5, Angle of Attack=7.5°, $Re_c=260000$



c. Exposure Time = 1/15 sec.

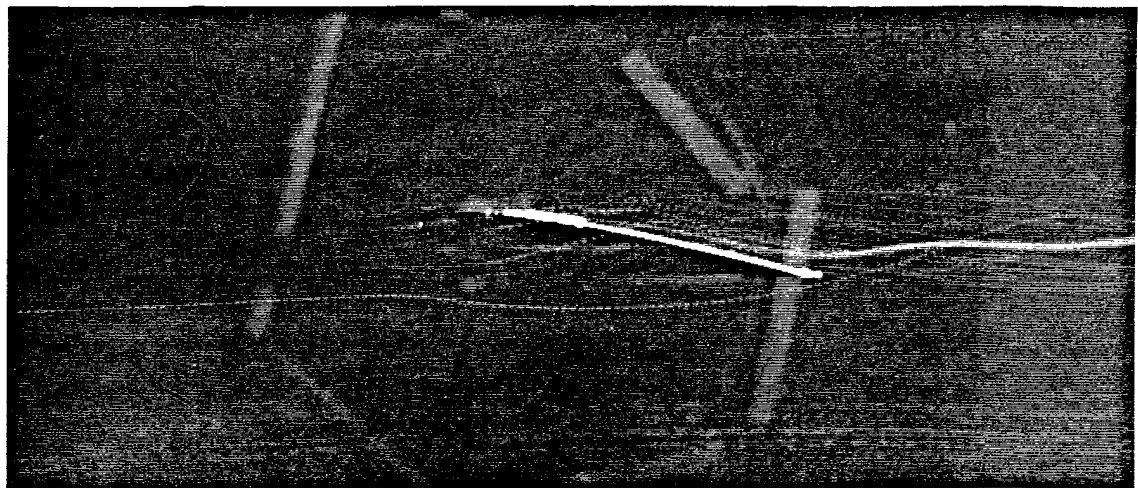


d. Exposure Time = 1/125 sec.

Figure 57. Tip Flow Visualizations, Endcap View
Aspect Ratio=2.5, Angle of Attack= 7.5° , $Re_c=260000$

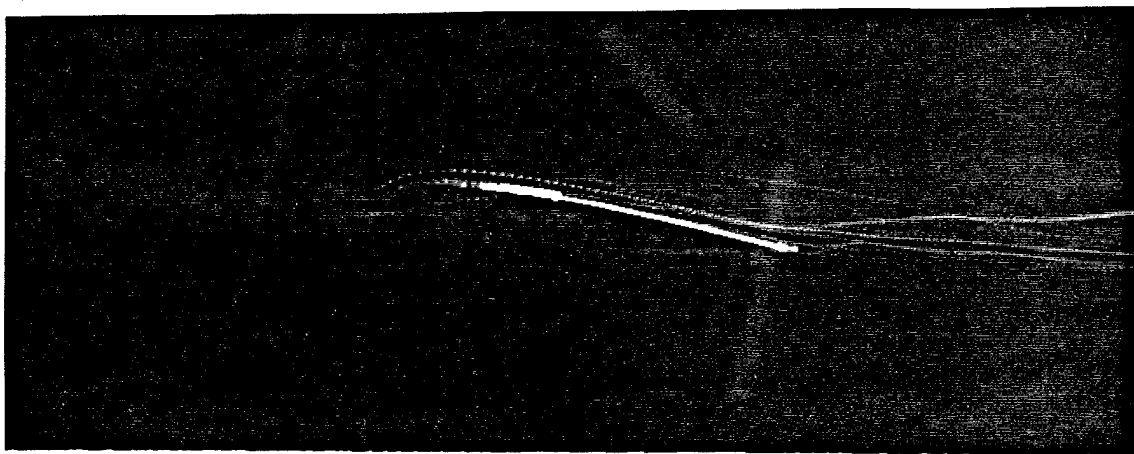


a. Exposure Time = 1 sec.

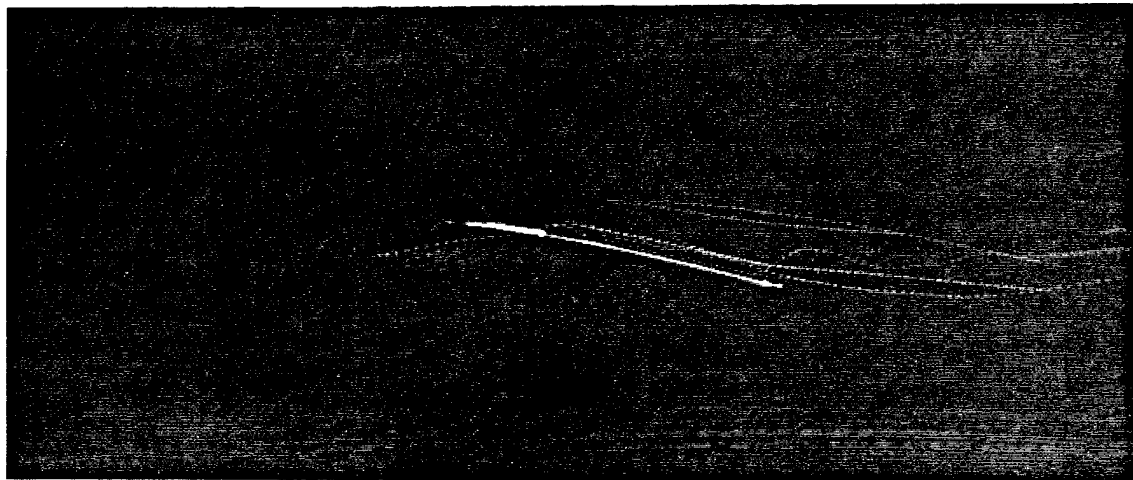


b. Exposure Time = 1/4 sec.

Figure 58. Tip Flow Visualizations, Endcap View
Aspect Ratio=2.5, Angle of Attack=7.5°, $Re_c=335000$



c. Exposure Time = 1/15 sec.



d. Exposure Time = 1/125 sec.

Figure 58. Tip Flow Visualizations, Endcap View
Aspect Ratio=2.5, Angle of Attack=7.5°, $Re_c=335000$

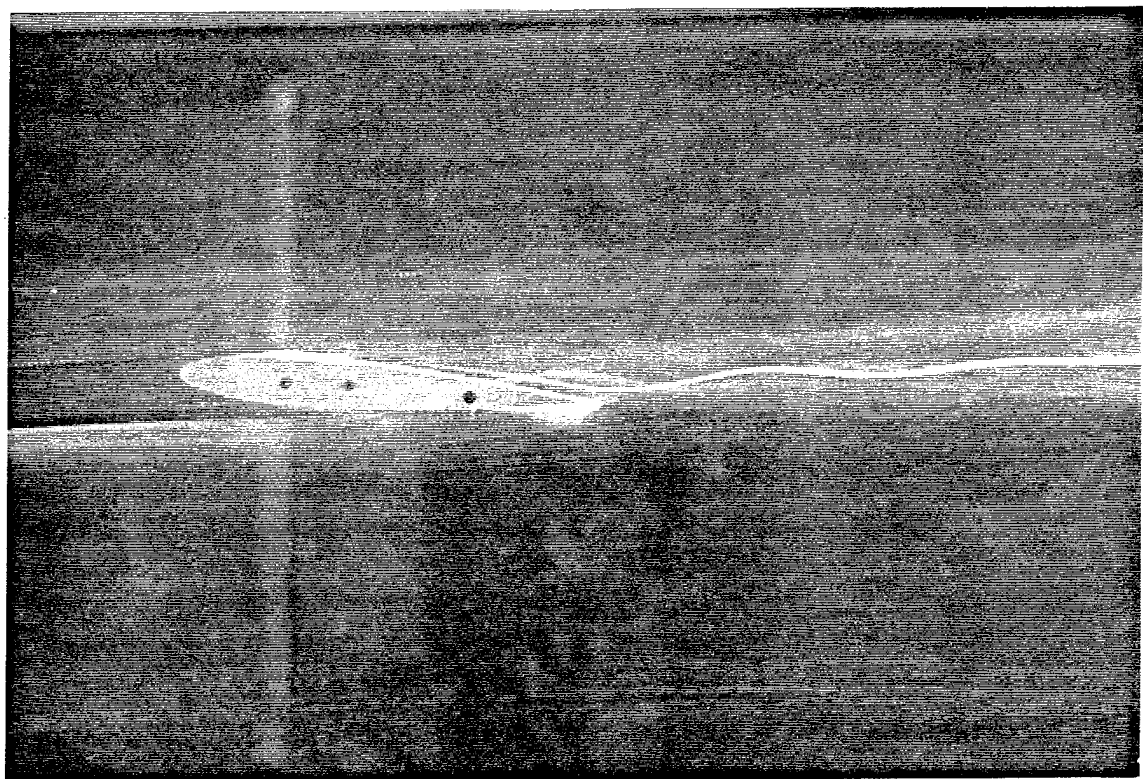


Figure 59. Co-Rotating Vortices
Aspect Ratio=3.0, Angle of Attack=5.0°, $Re_c=130000$

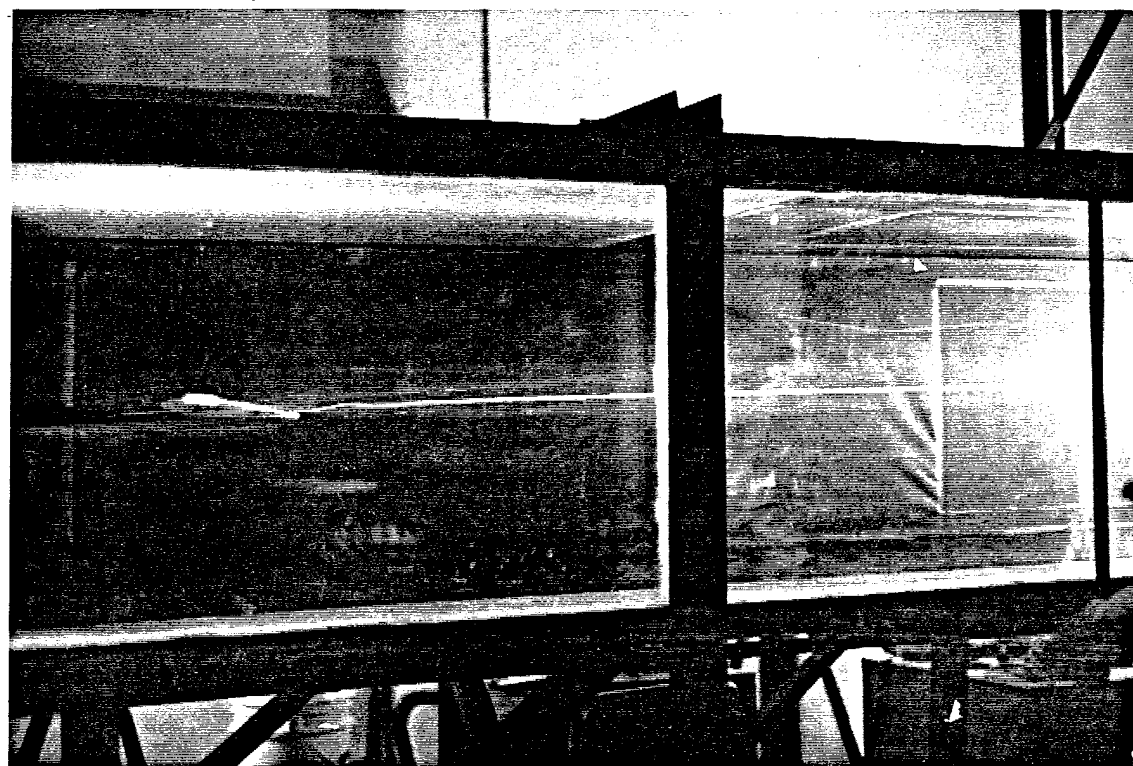
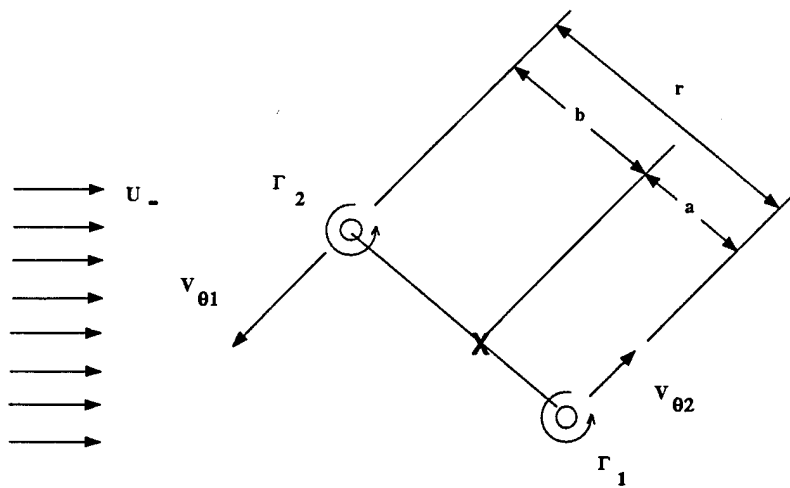
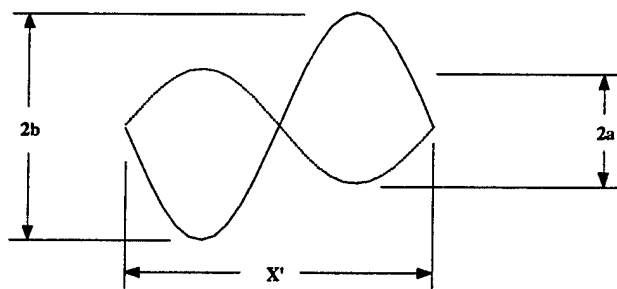


Figure 60. Diminishing Trailing Vortex Core Spiral Path
Aspect Ratio=3.0, Angle of Attack=5.0°, $Re_c=130000$

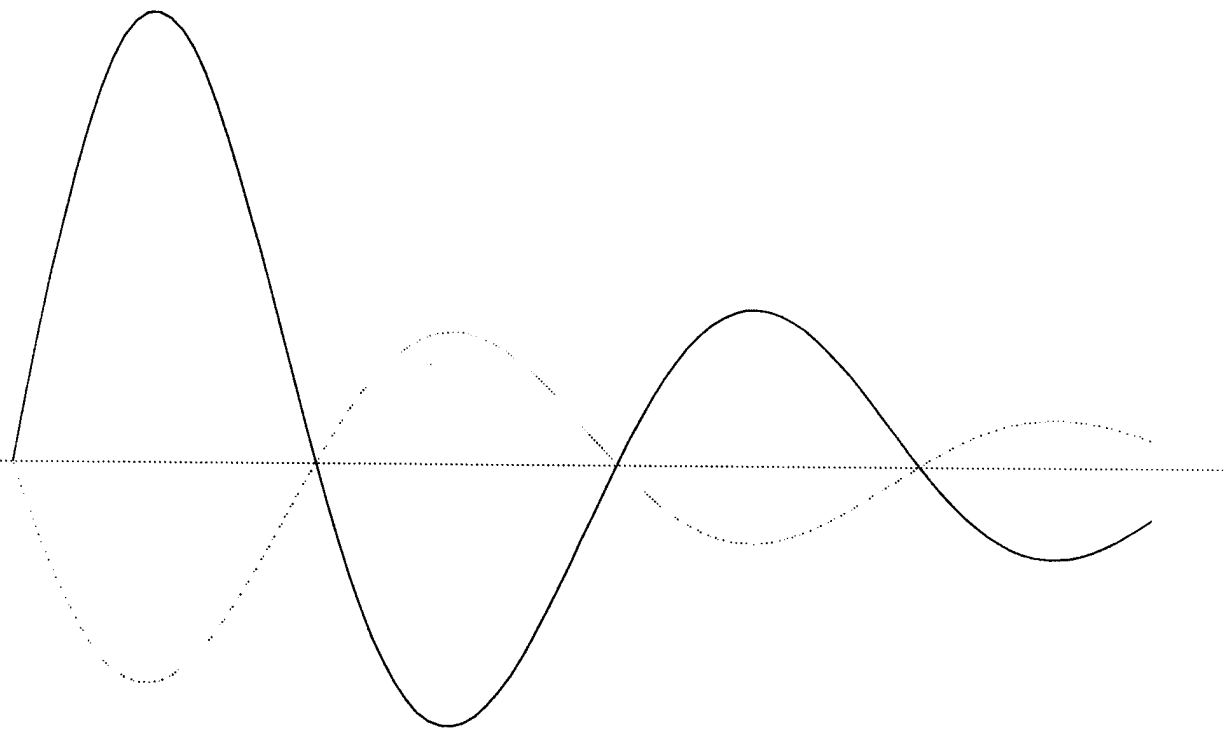


a. Ideal Point Vortices in a Uniform Freestream



b. Co-Rotating Ideal Point Vortices

Figure 61. Co-Rotating Ideal Point Vortices in a Uniform Freestream



Paths of ... 1. Center of Momentum
2. Strong Vortex
3. Weak Vortex

Figure 62. Model of Co-Rotating Non-Ideal Vortices

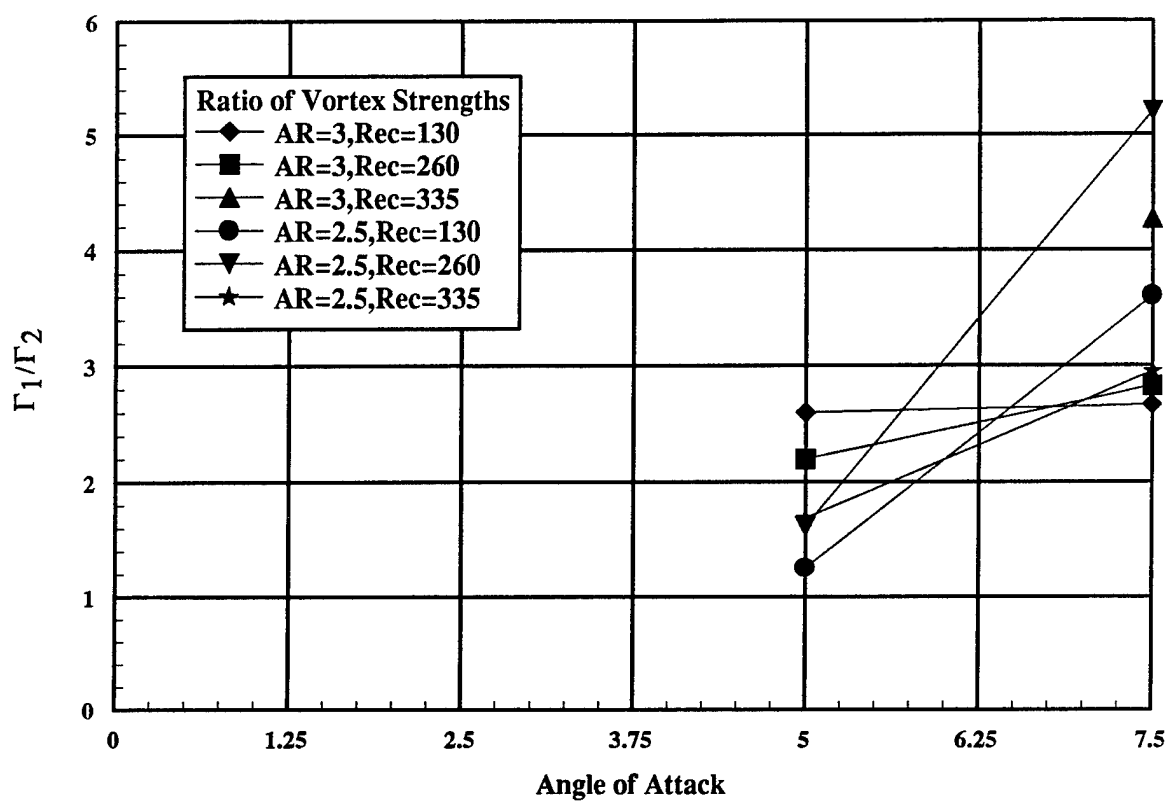


Figure 63. Ratio of Primary to Secondary Vortex Strengths as a Function of Angle of Attack

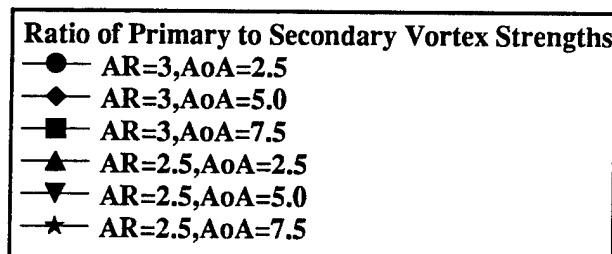
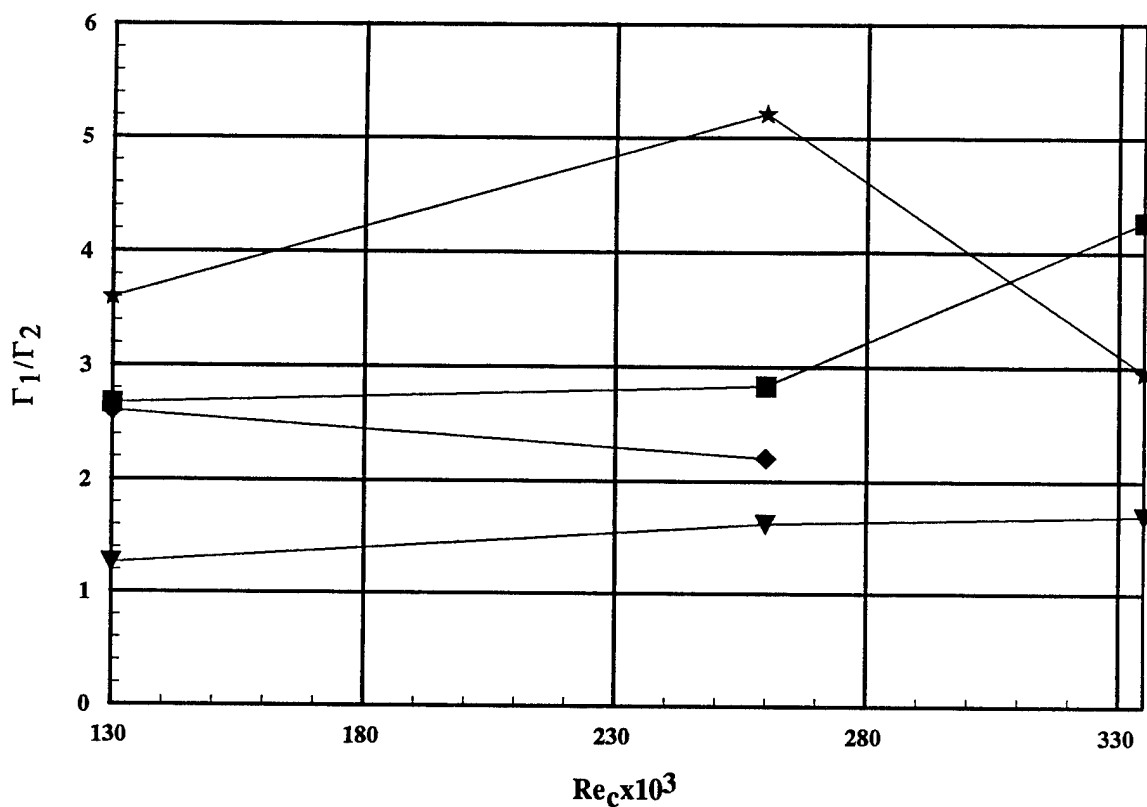


Figure 64. Ratio of Primary to Secondary Vortex Strengths as a Function of Chord Reynolds Number

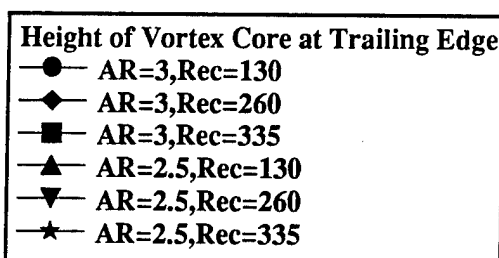
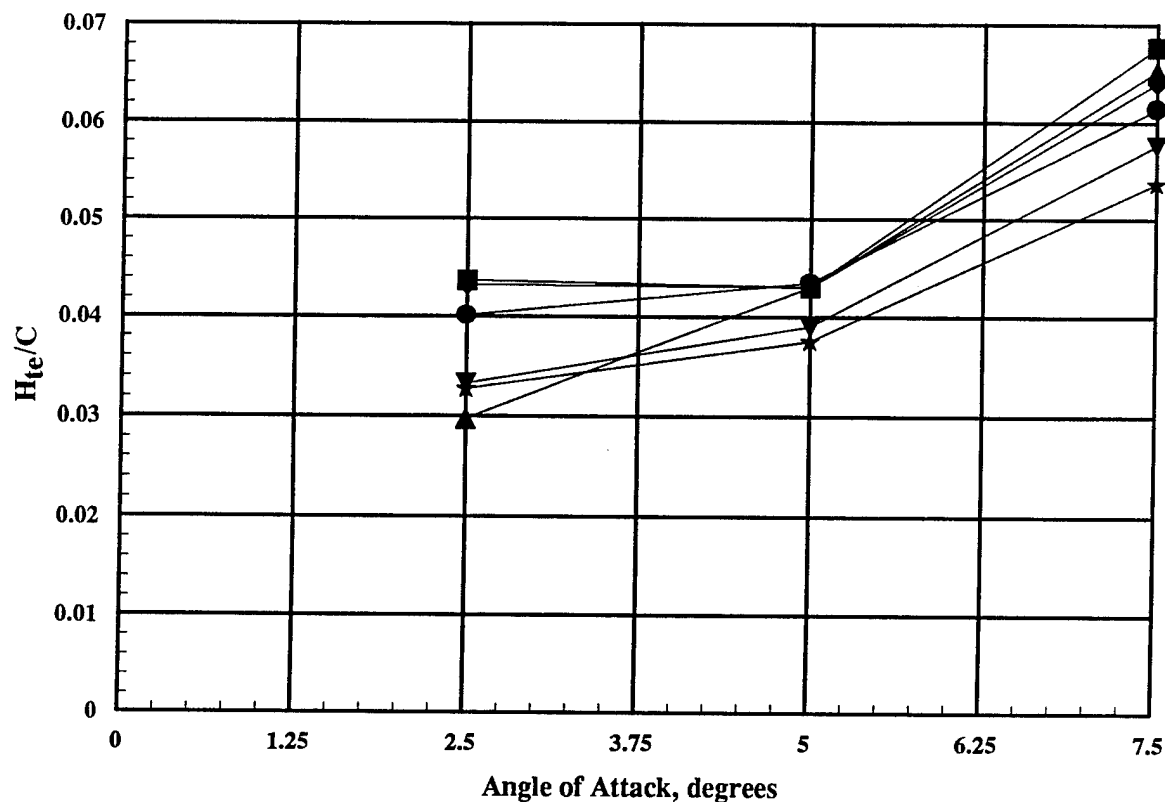


Figure 73. Height of the Primary Vortex Core above the Suction Surface at the Wing Trailing Edge as a Function of Angle of Attack

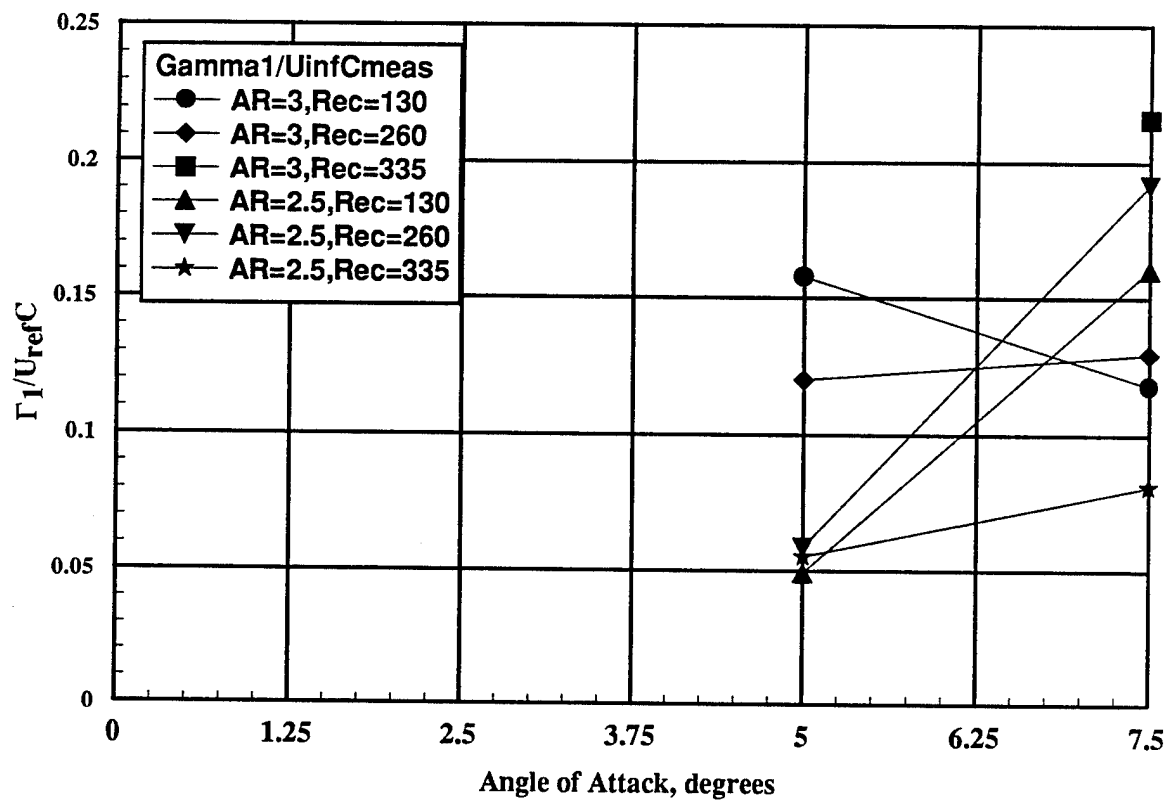


Figure 65. Normalized Primary Vortex Strength as a Function of Angle of Attack

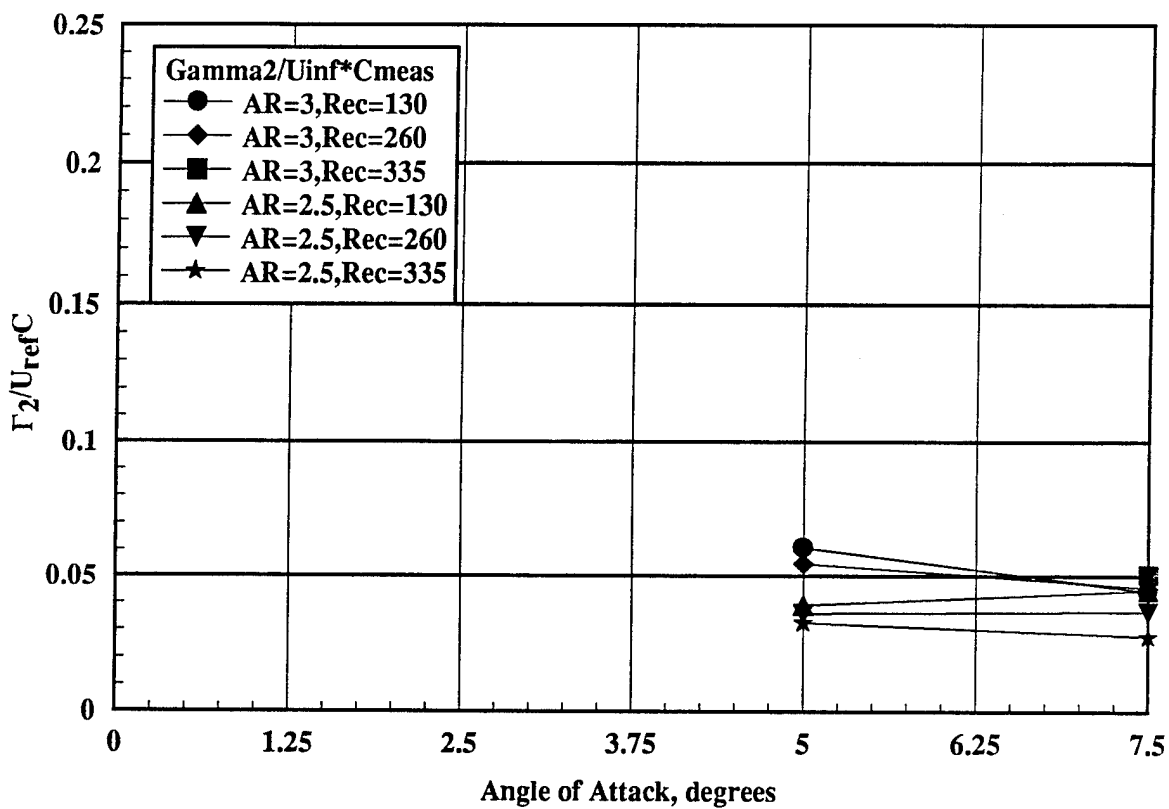
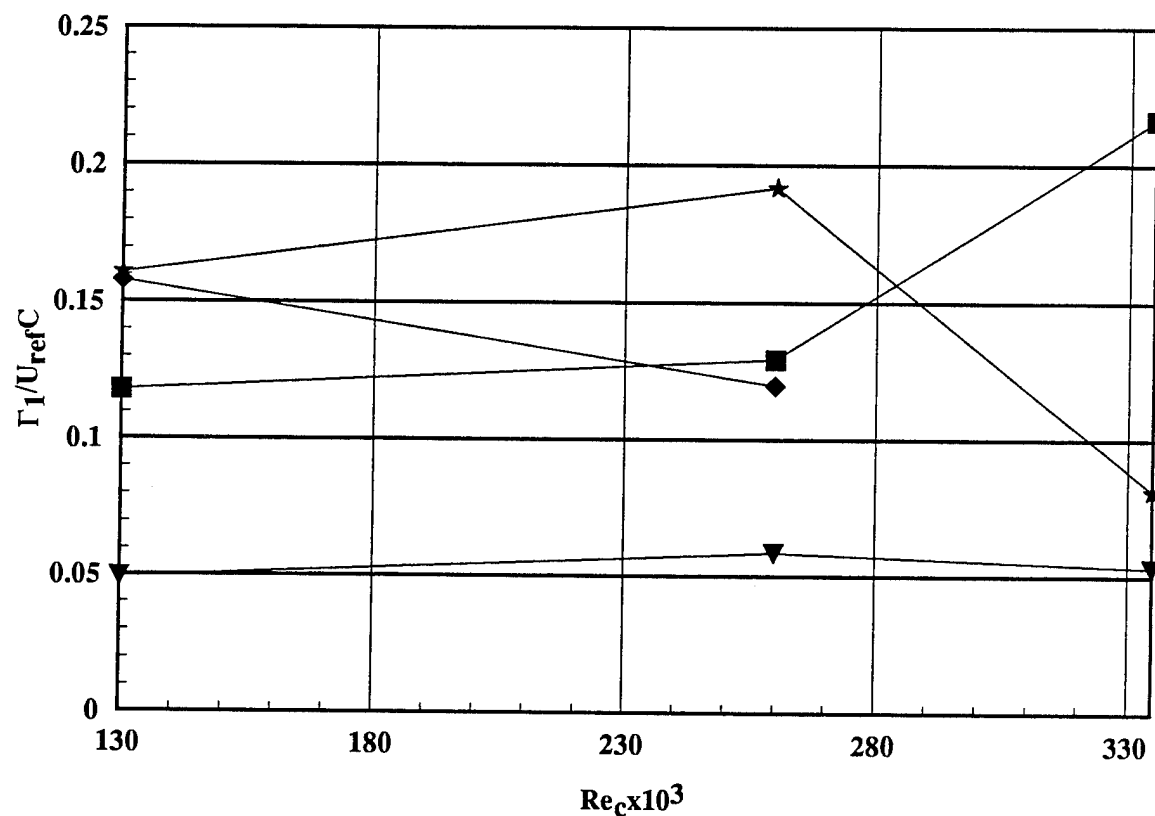


Figure 66. Normalized Secondary Vortex Strength as a Function of Angle of Attack



Primary Vortex Strength

- AR=3, AoA=2.5
- ◆ AR=3,AoA=5.0
- AR=3,AoA=7.5
- ▲ AR=2.5,AoA=2.5
- ▼ AR=2.5,AoA=5.0
- ★ AR=2.5,AoA=7.5

Figure 67. Normalized Primary Vortex Strength as a Function of Chord Reynolds Number

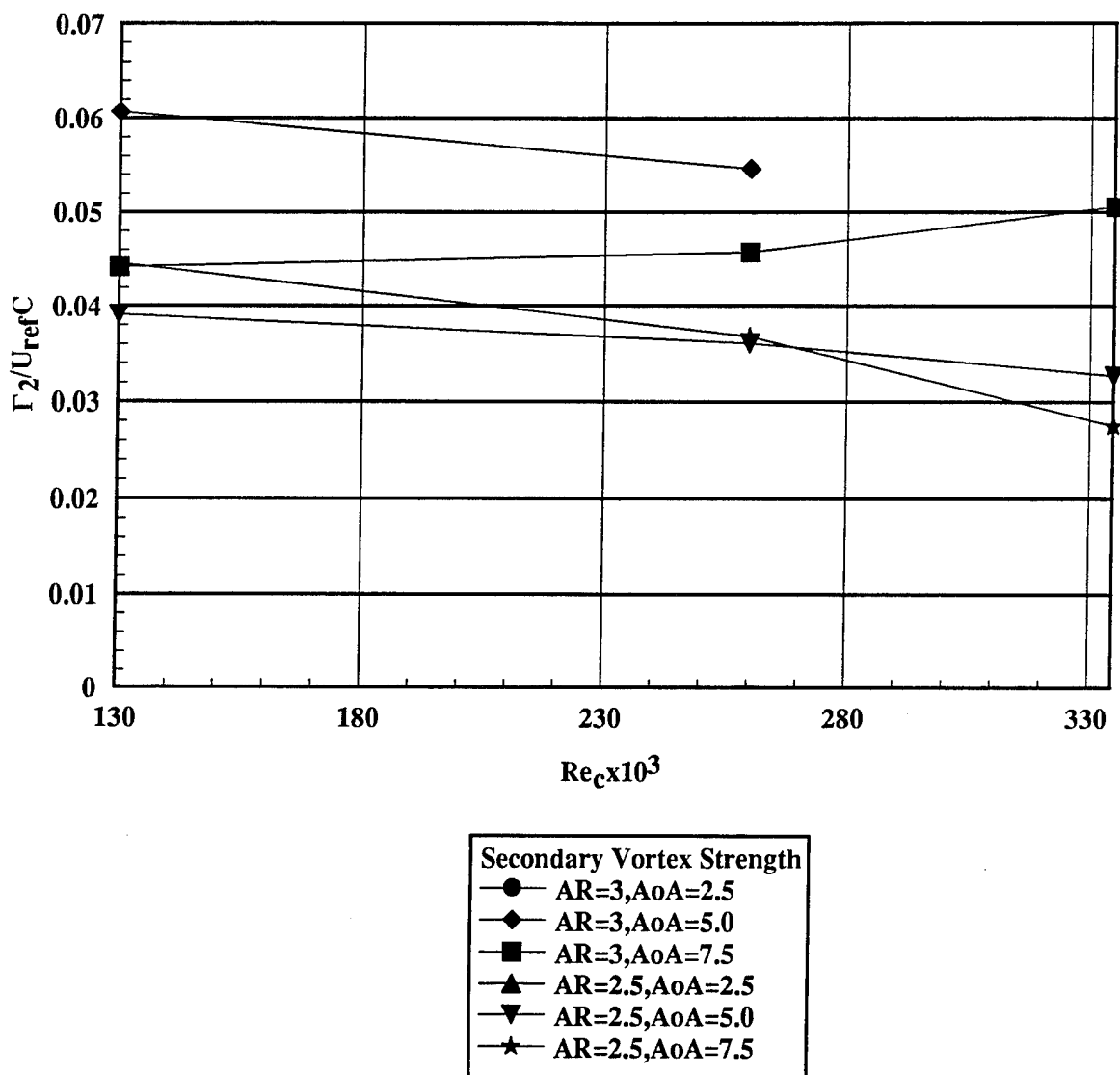


Figure 68. Normalized Secondary Vortex Strength as a Function of Chord Reynolds Number

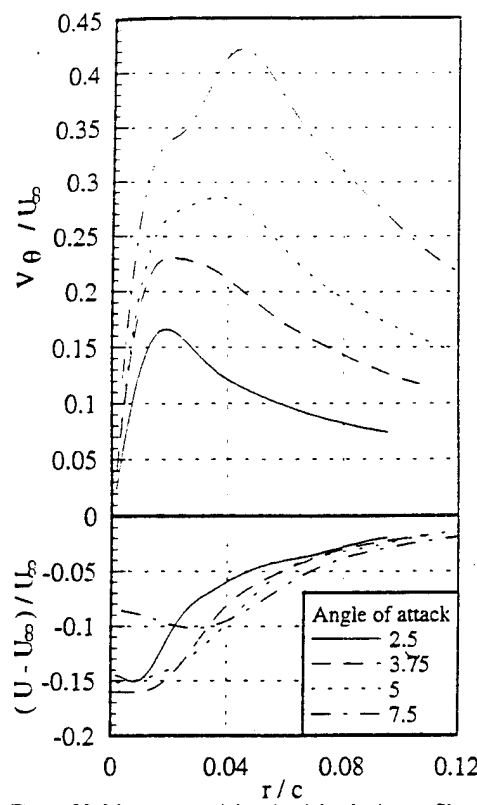


Figure 28. Mean tangential and axial velocity profiles through the core at $x/c=10$ as a function of angle of attack. Profiles corrected for the effects of wandering

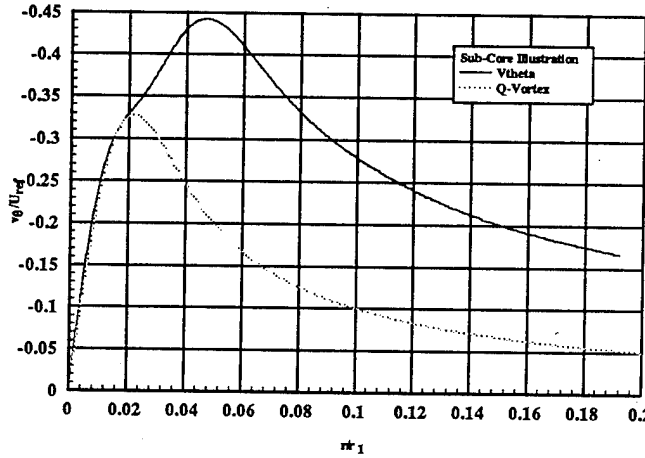


Figure 69. Data of Devenport, et.al.³⁷ Showing Development of Inner and Outer Core Regions and a Simplistic Model of the Inner Region as a Batchelor⁵ q-vortex

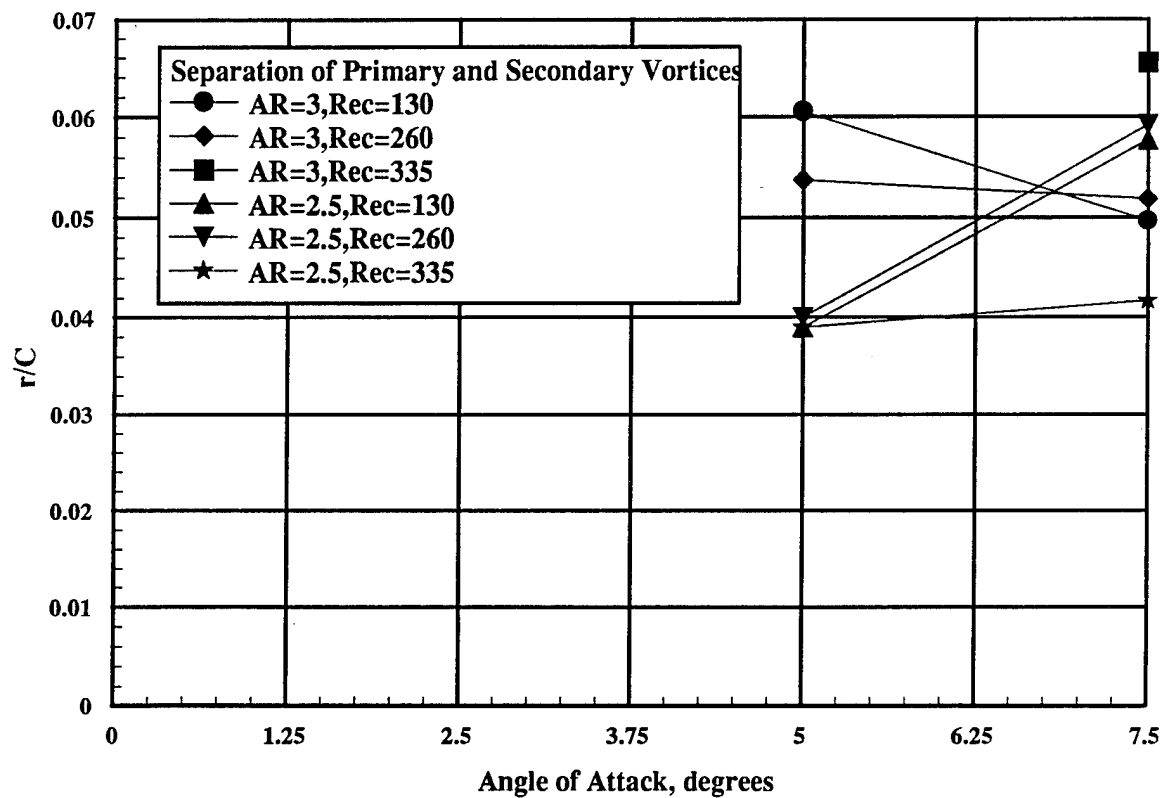
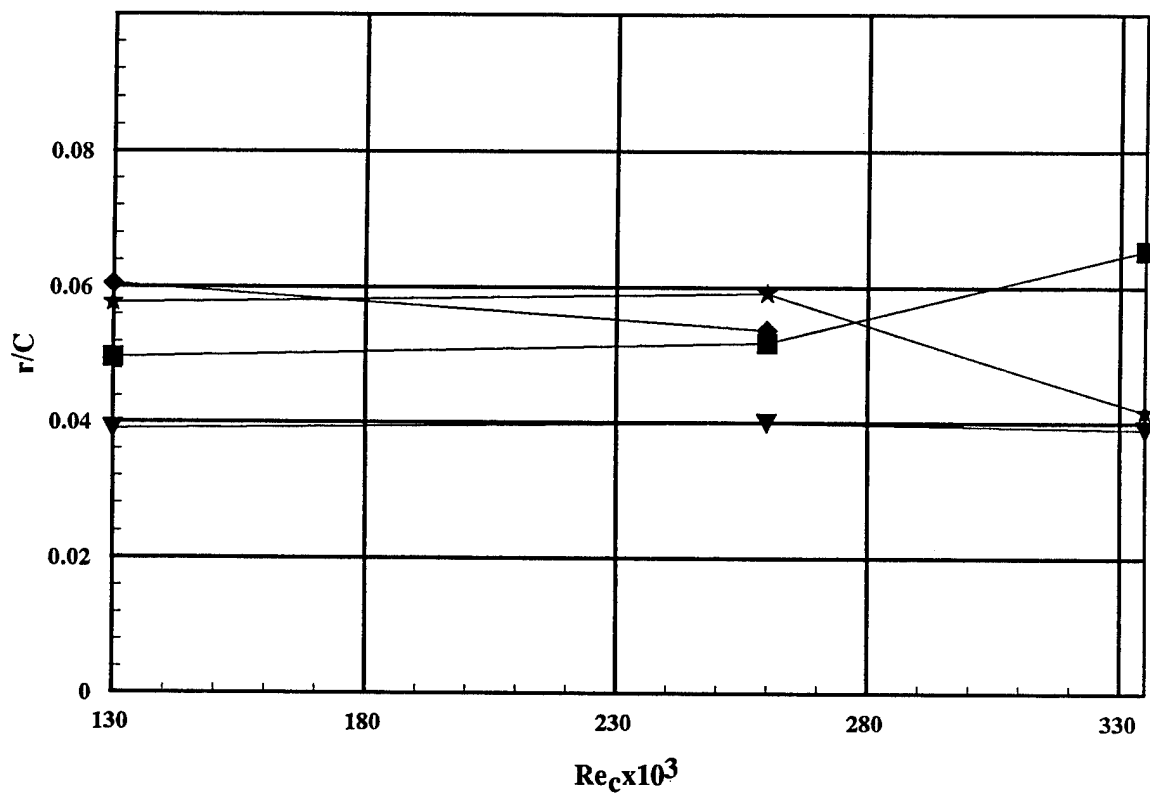


Figure 70. Separation of the Primary and Secondary Tip Vortices as a Function of Angle of Attack



Primary and Secondary Vortex Separation

- AR=3,AoA=2.5
- ◆ AR=3,AoA=5.0
- AR=3,AoA=7.5
- ▲ AR=2.5,AoA=2.5
- ▼ AR=2.5,AoA=5.0
- ★ AR=2.5,AoA=7.5

Figure 71. Separation of the Primary and Secondary Tip Vortices as a Function of Chord Reynolds Number

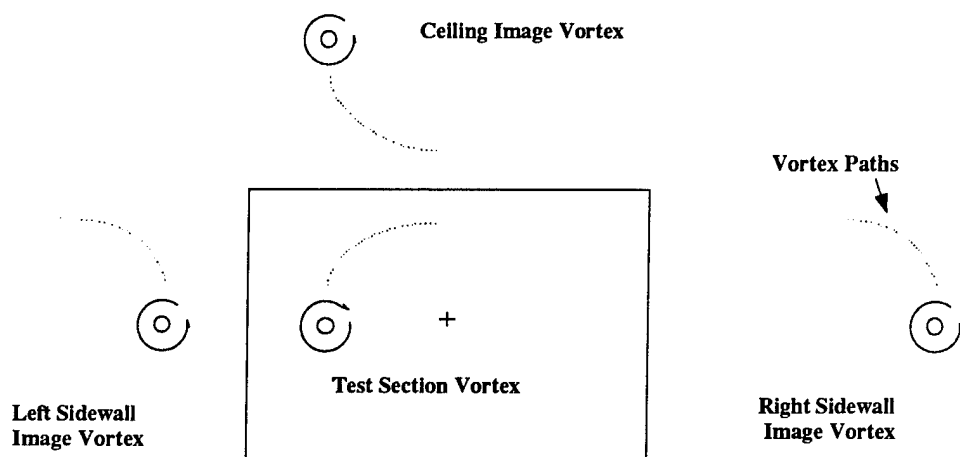


Figure 72. Test Section Wall Proximity Effects

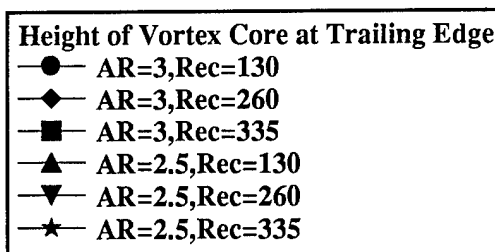
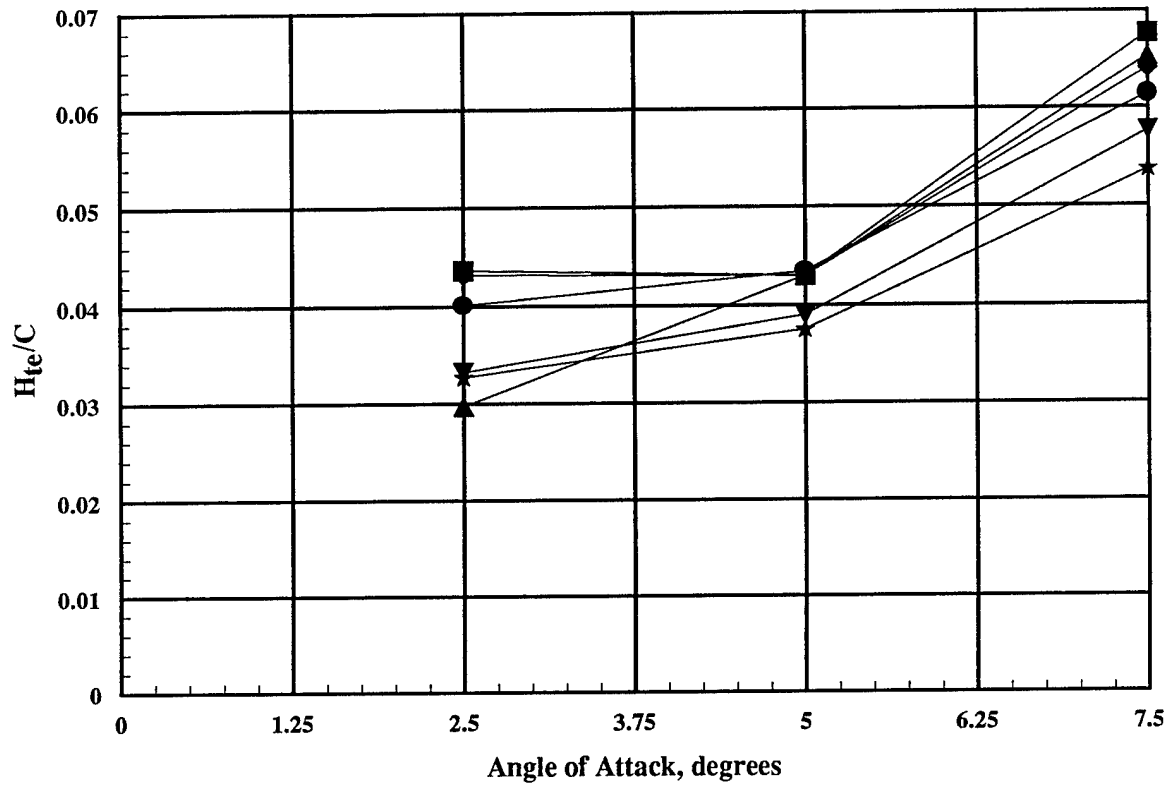


Figure 73. Height of the Primary Vortex Core above the Suction Surface at the Wing Trailing Edge as a Function of Angle of Attack

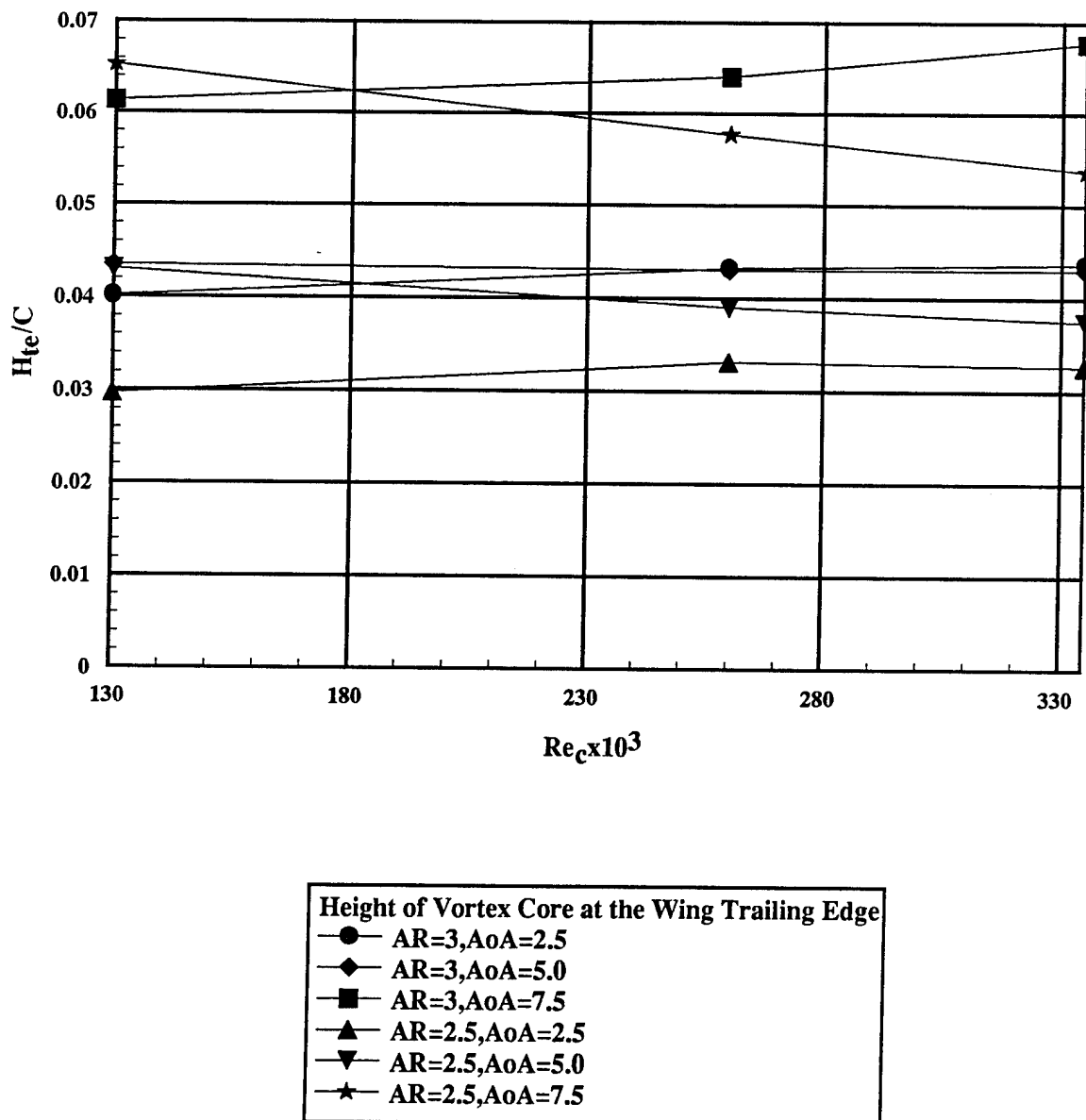


Figure 74. Height of the Primary Vortex Core above the Suction Surface at the Wing Trailing Edge as a Function of Chord Reynolds Number

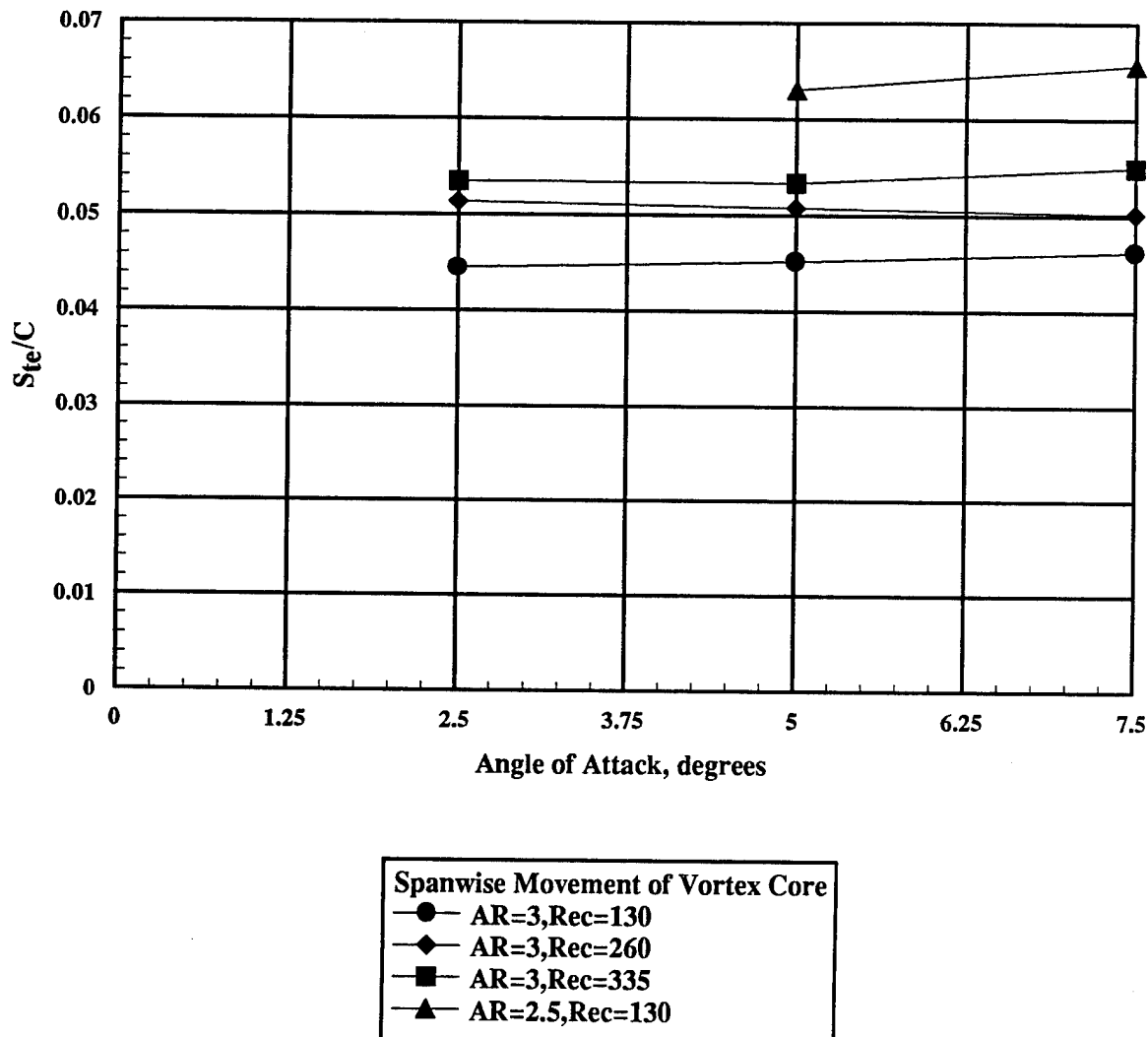
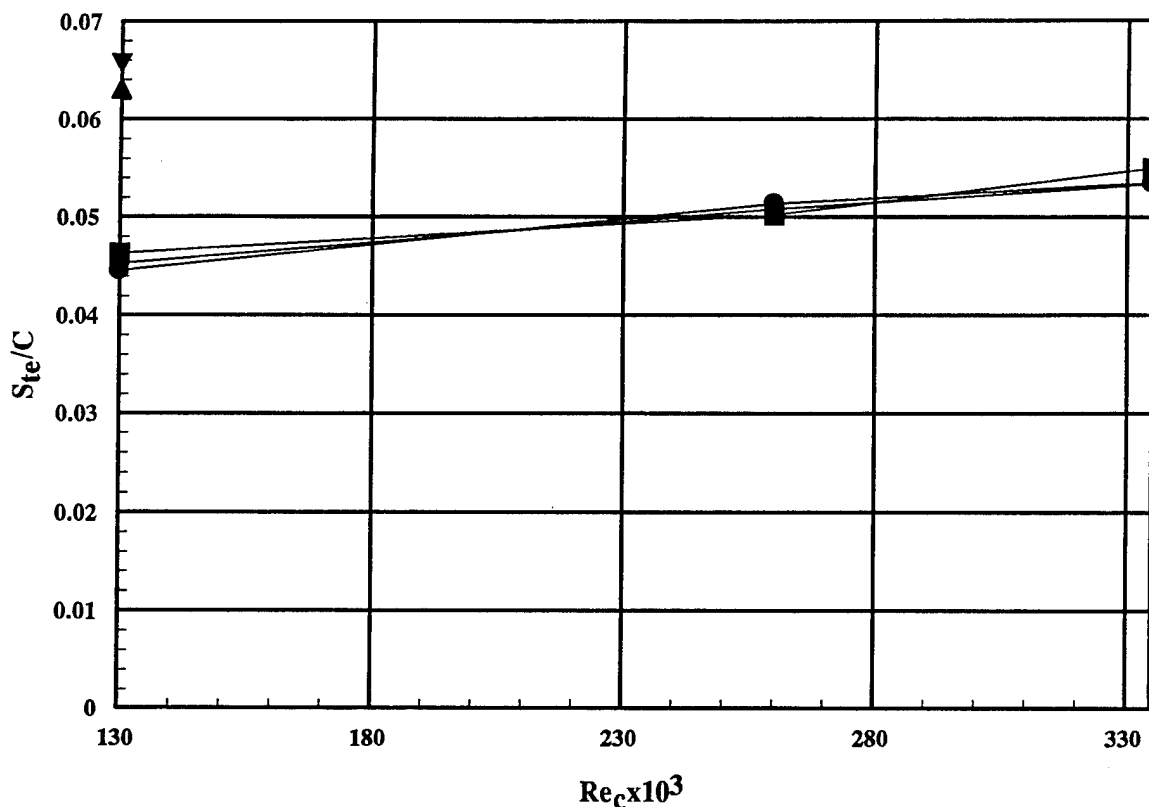


Figure 75. Spanwise Movement of the Primary Vortex Core Relative to the Endcap at the Wing Trailing Edge as a Function of Angle of Attack



Spanwise Movement of Vortex Core

- $AR=3, AoA=2.5$
- ◆ $AR=3, AoA=5.0$
- $AR=3, AoA=7.5$
- ▲ $AR=2.5, AoA=2.5$
- ▼ $AR=2.5, AoA=5.0$
- ★ $AR=2.5, AoA=7.5$

Figure 76. Spanwise Movement of the Primary Vortex Core Relative to the Endcap at the Wing Trailing Edge as a Function of Chord Reynolds Number

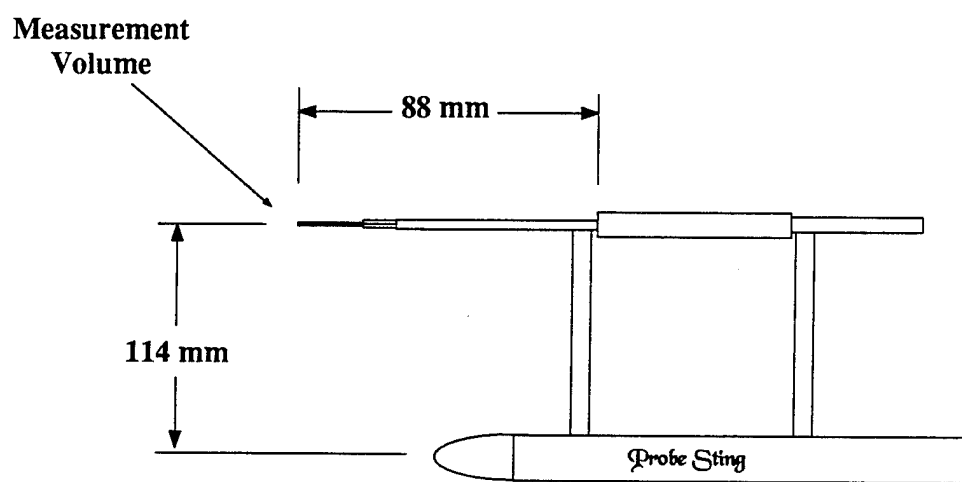


Figure 77. Quad-Hot-Wire Probe Configuration, as Used by Devenport, et.al^{10,37}

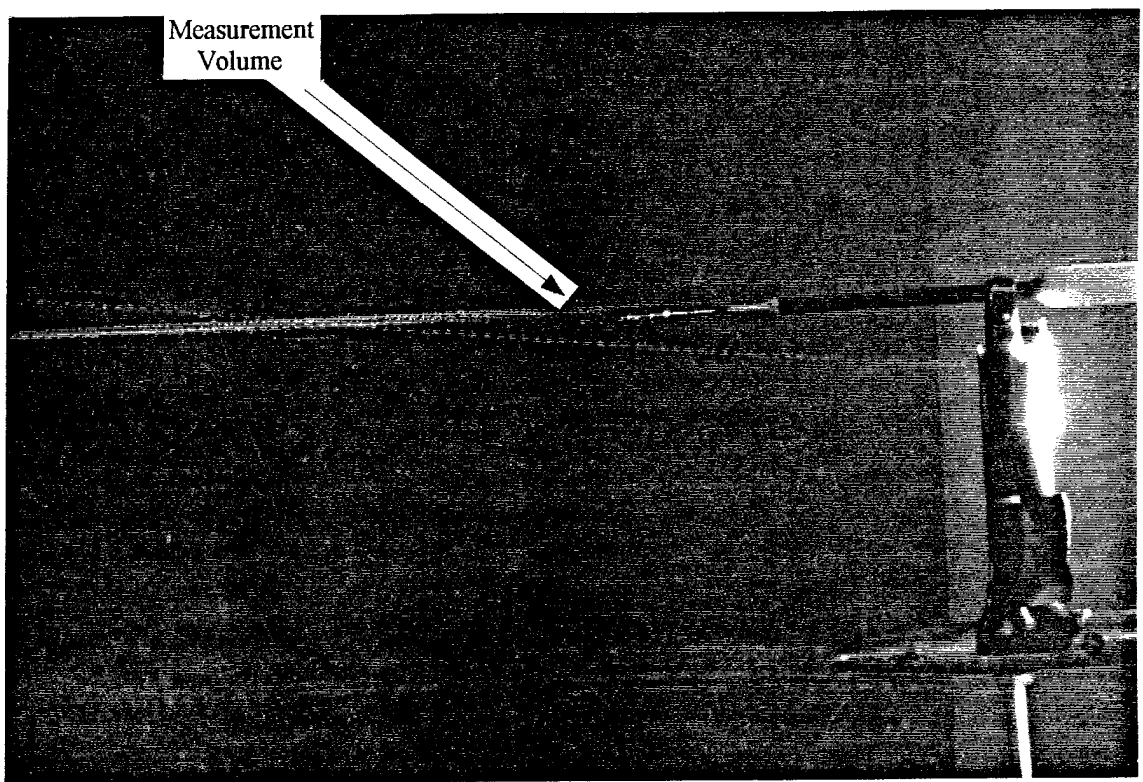


Figure 78. Quad-Hot-Wire Probe 1/8" below the Vortex Core Centerline
 $X/C=10$, $Re_c=130000$, Exposure Time=1/15 second

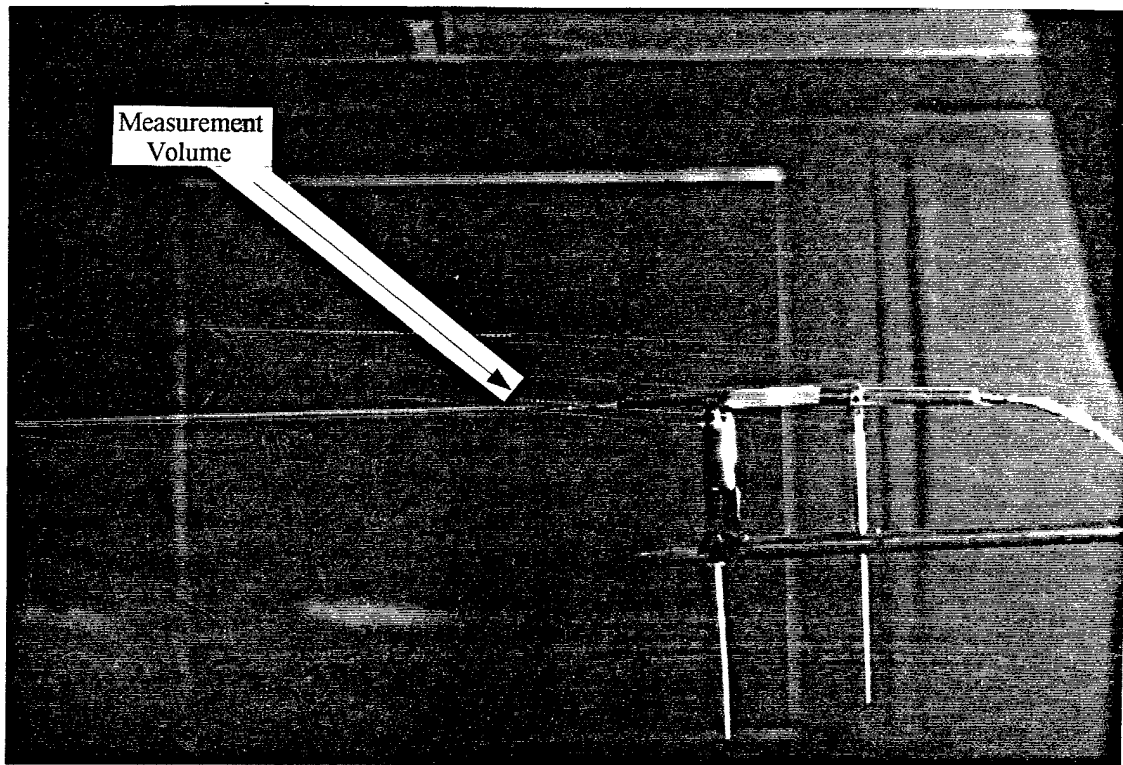


Figure 79. Quad-Hot-Wire Probe Centered in the Vortex Core
 $X/C=10$, $Re_c=130000$, Exposure Time=1/15 second

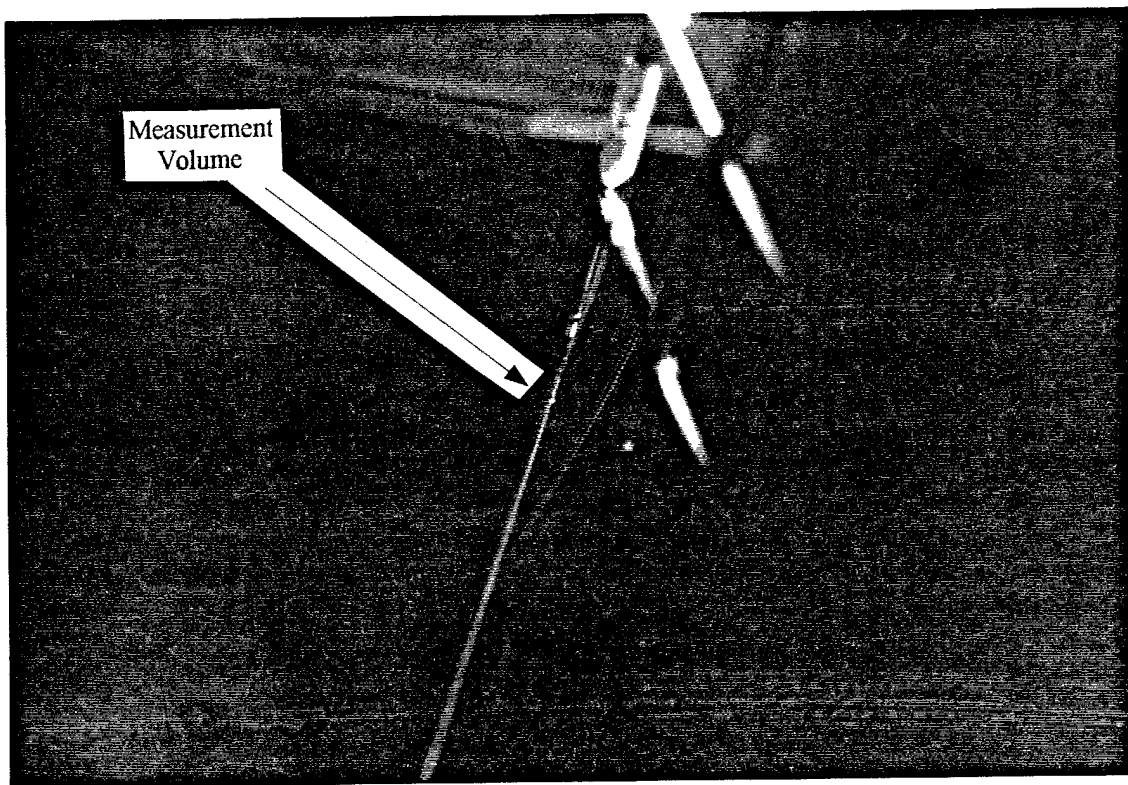


Figure 80. Quad-Hot-Wire Probe Centered in the Vortex Core, Viewed from below and behind the Probe. Flow is from the bottom of the Photograph to the Top.
 $X/C=10$, $Re_c=130000$, Exposure Time=1/15 second

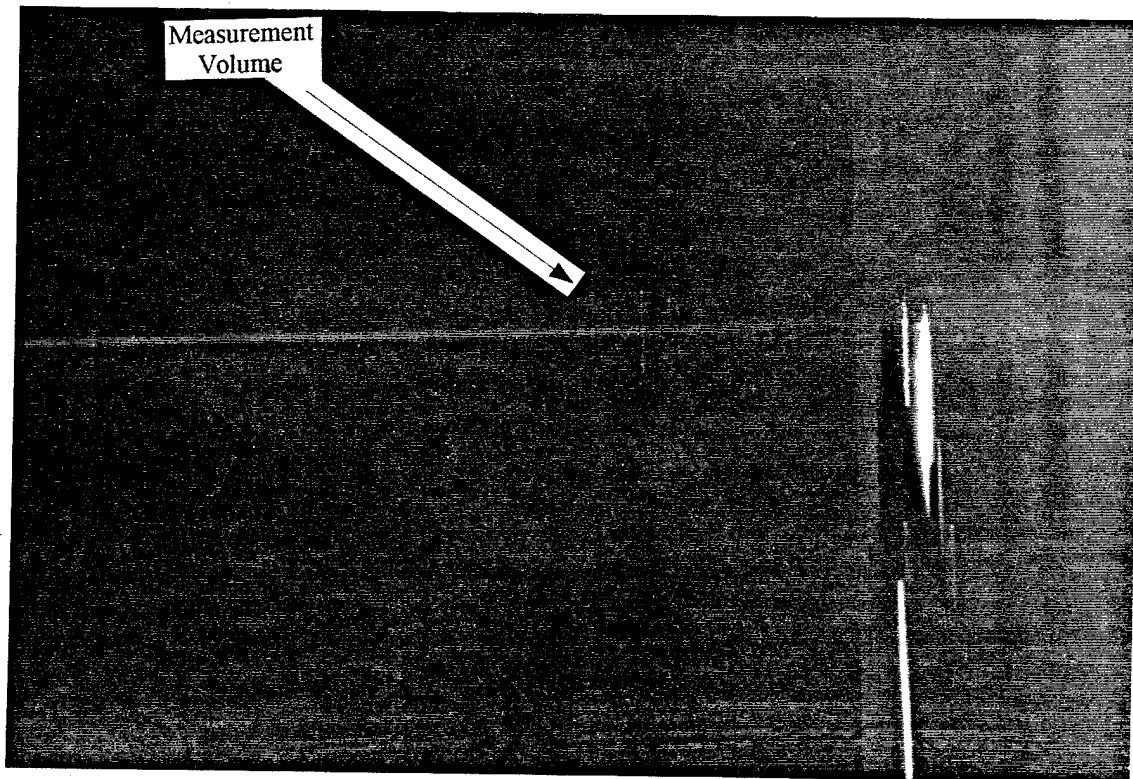


Figure 81. Quad-Hot-Wire Probe Traversing Through the Vortex Core
 $X/C=10$, $Re_c=130000$, Exposure Time=4 seconds

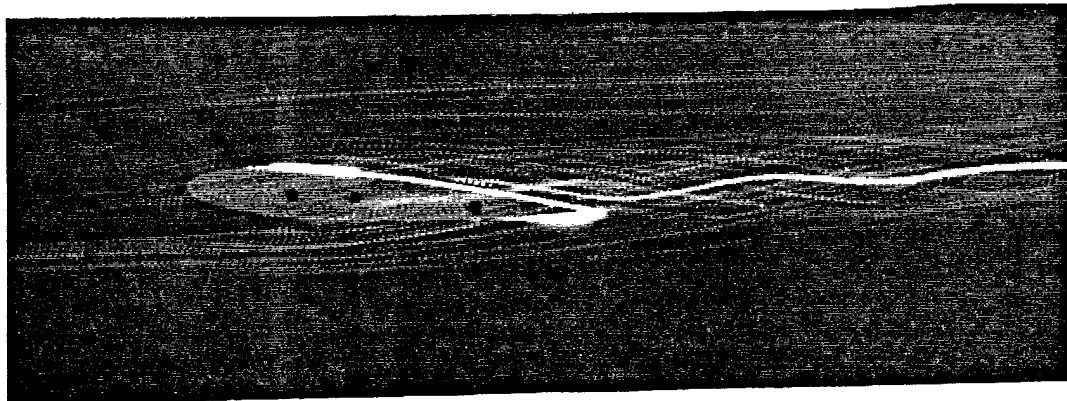
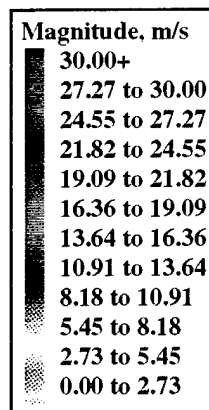
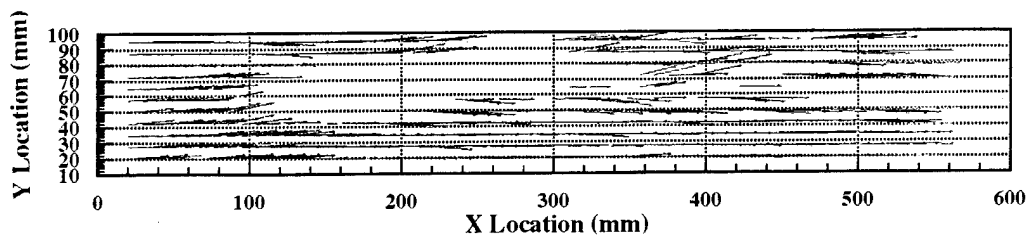


Figure 82. PIV Analysis

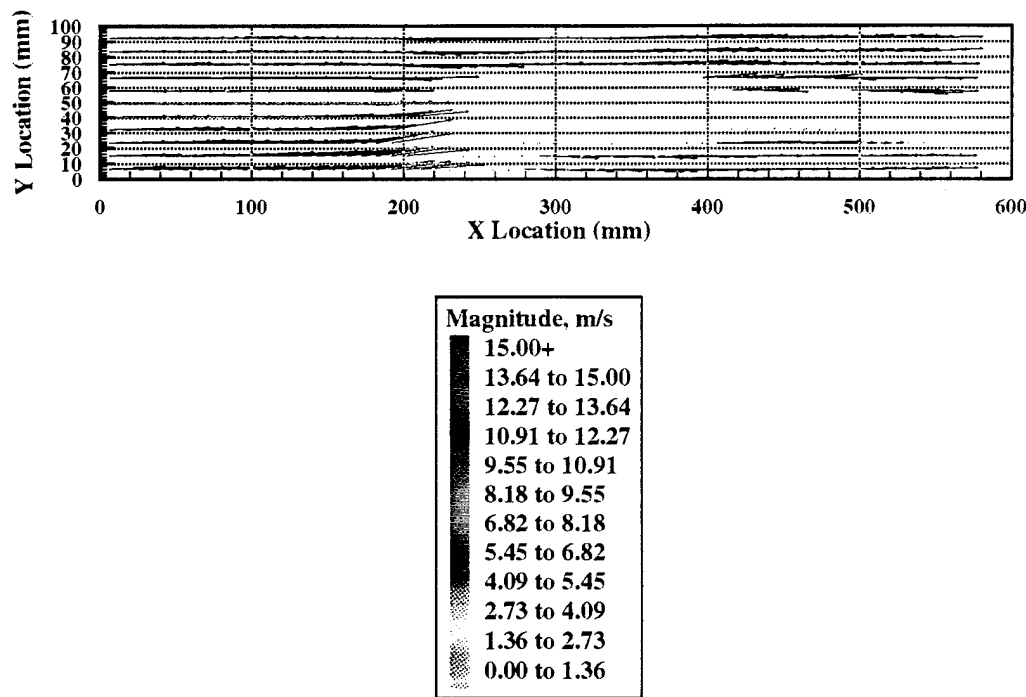


Figure 83. PIV Analysis of Figure 44a

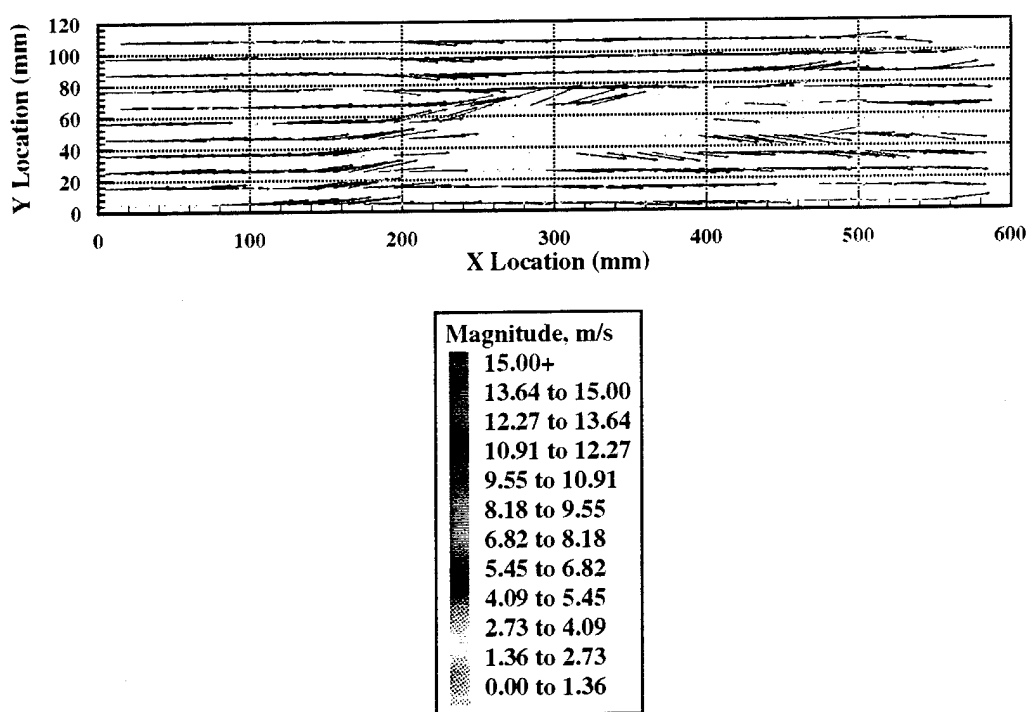


Figure 84. PIV Analysis of Figure 47a

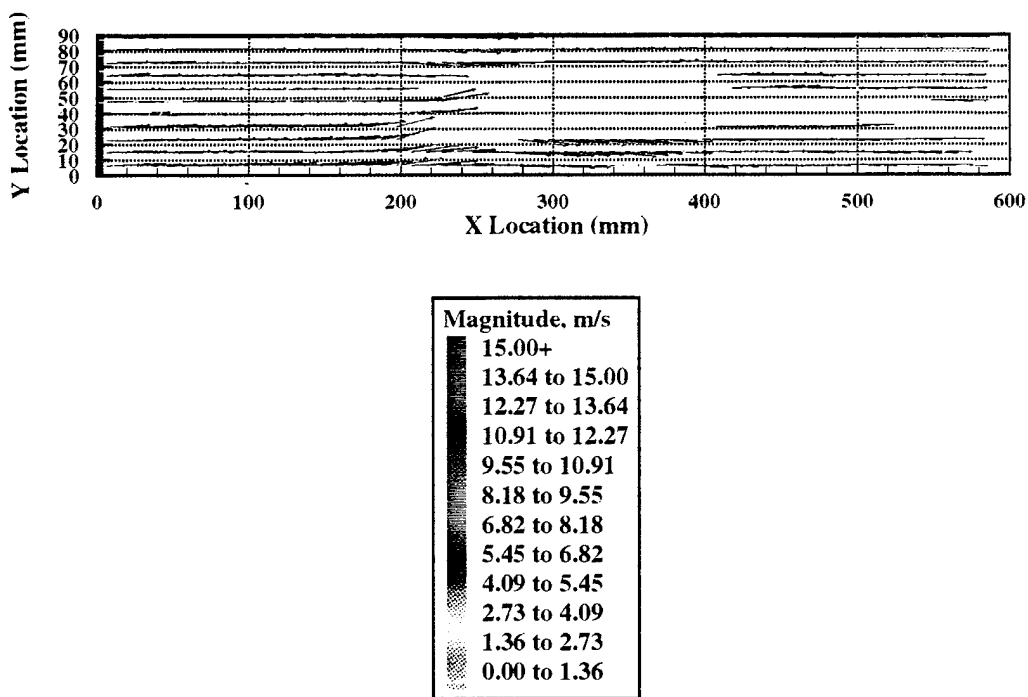


Figure 85. PIV Analysis of Figure 53a

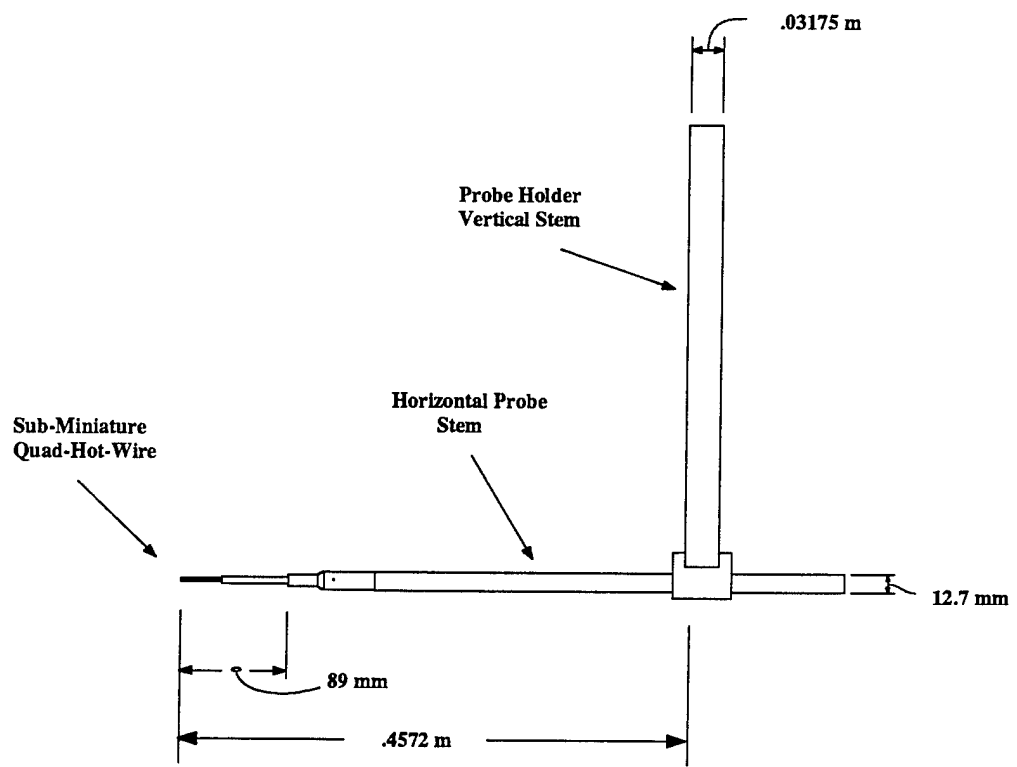


Figure 86. Quad-Hot-Wire Probe Holder

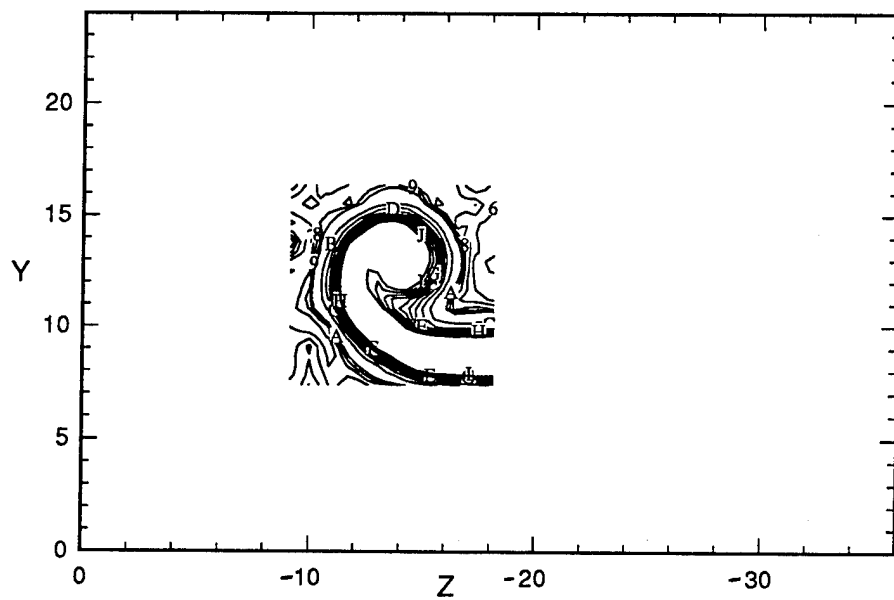


Figure 87. Location of Vortex with Respect to Test Section Walls
Single Sensor Hot-Wire Measurements of u^2 / U_{ref}^2
X/C=12, Aspect Ratio=3.0, Angle of Attack=5.0°, $Re_c=330000$

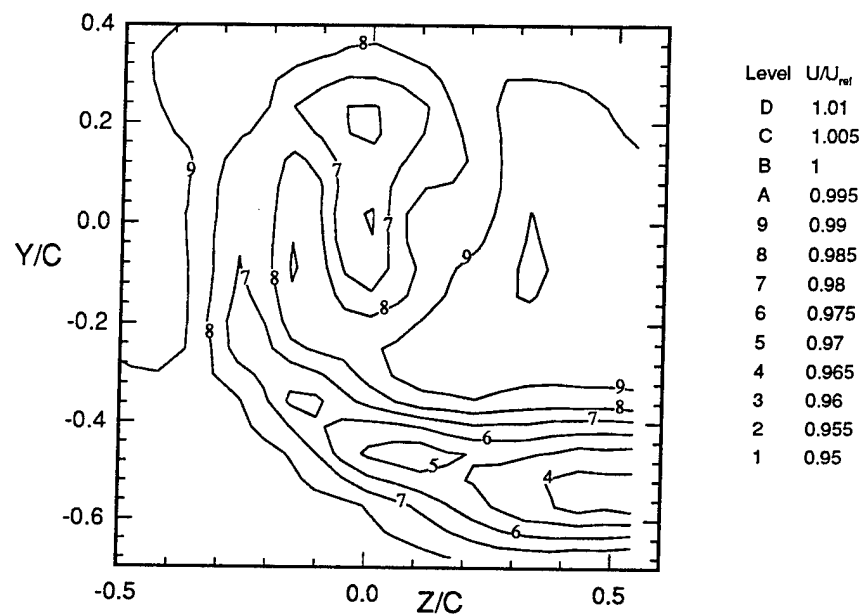


Figure 88. Contours of U/U_{ref} in Trailing Vortex
 Single Sensor Hot-Wire Measurements
 $X/C=12$, Aspect Ratio=3.0, Angle of Attack=5.0°, $Re_c=330000$

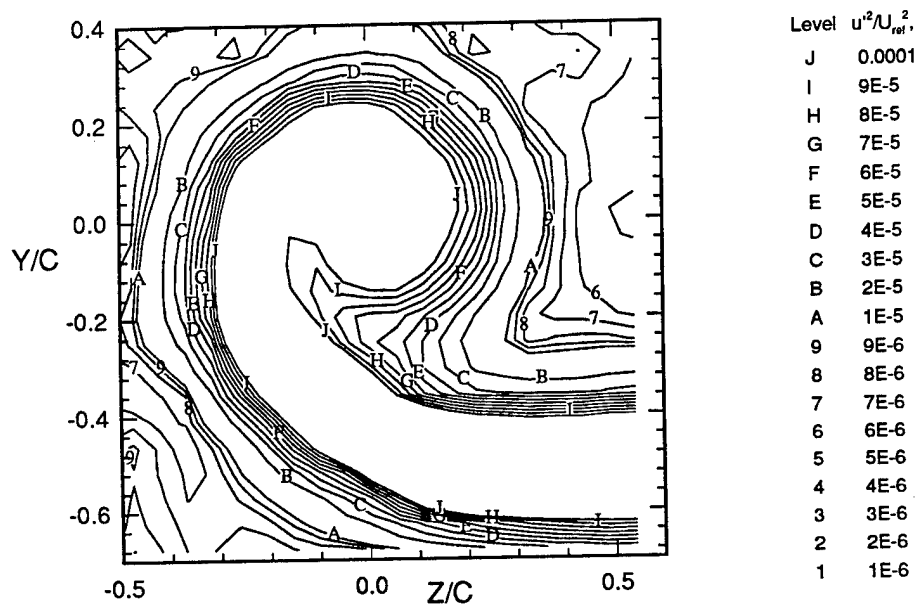


Figure 89. Contours of u^2 / U_{ref}^2 in Trailing Vortex
 Single Sensor Hot-Wire Measurements
 $X/C=12$, Aspect Ratio=3.0, Angle of Attack=5.0°, $Re_c=330000$

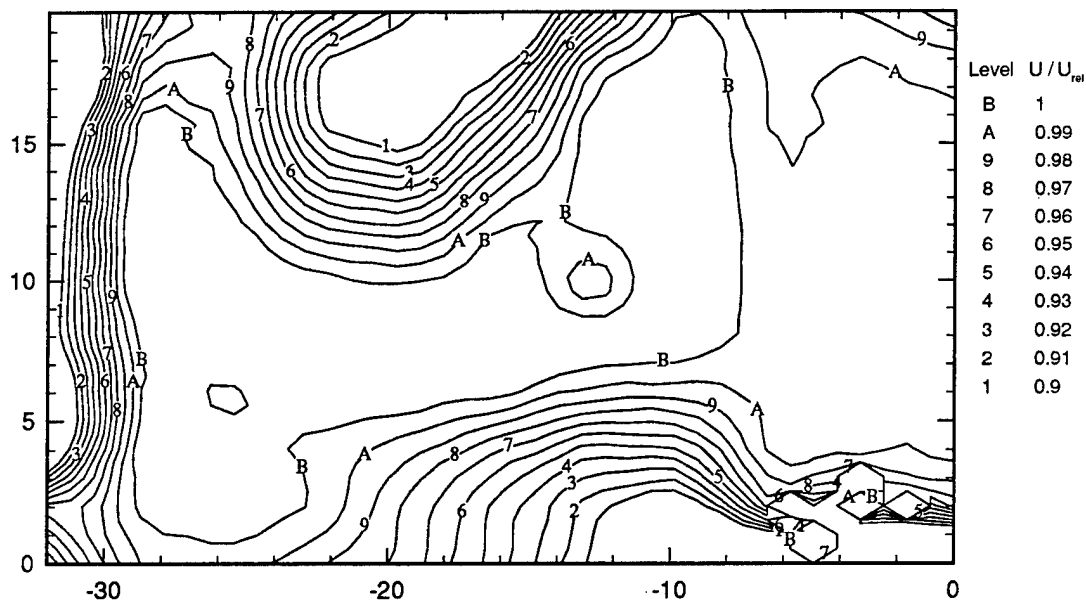


Figure 90. Contours of U/U_{ref} Showing no Evidence of an Organized Vortex
 Single Sensor Hot-Wire Measurements
 $X/C=25$, Aspect Ratio=3.0, Angle of Attack=5.0°, $Re_c=330000$

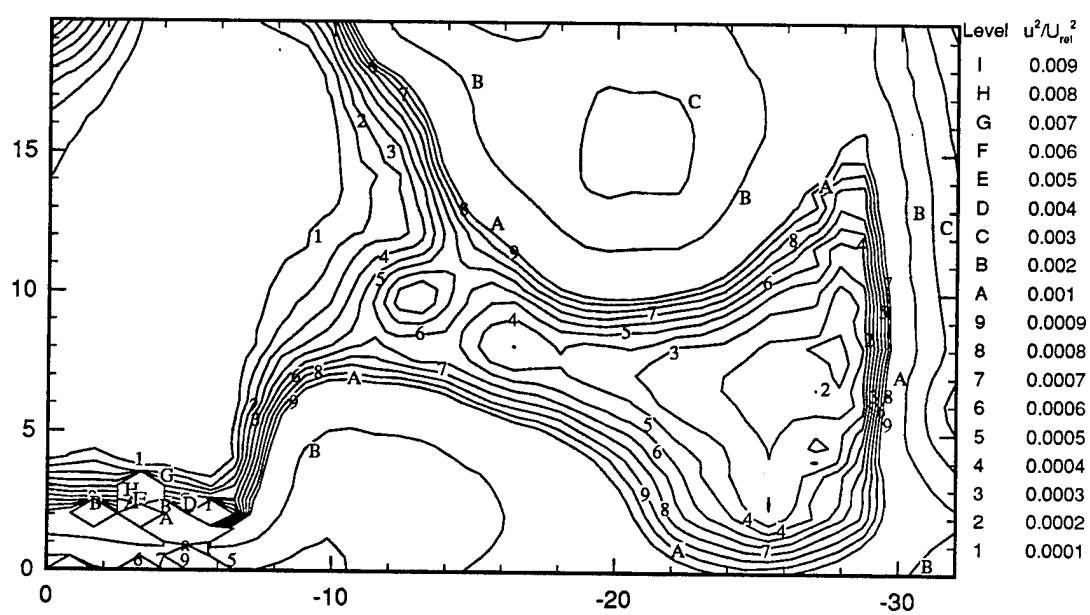


Figure 91. Contours of u^2/U_{ref}^2 Showing no Evidence of an Organized Vortex. Single Sensor Hot-Wire Measurements
 $X/C=25$, Aspect Ratio=3.0, Angle of Attack=5.0°, $Re_c=330000$

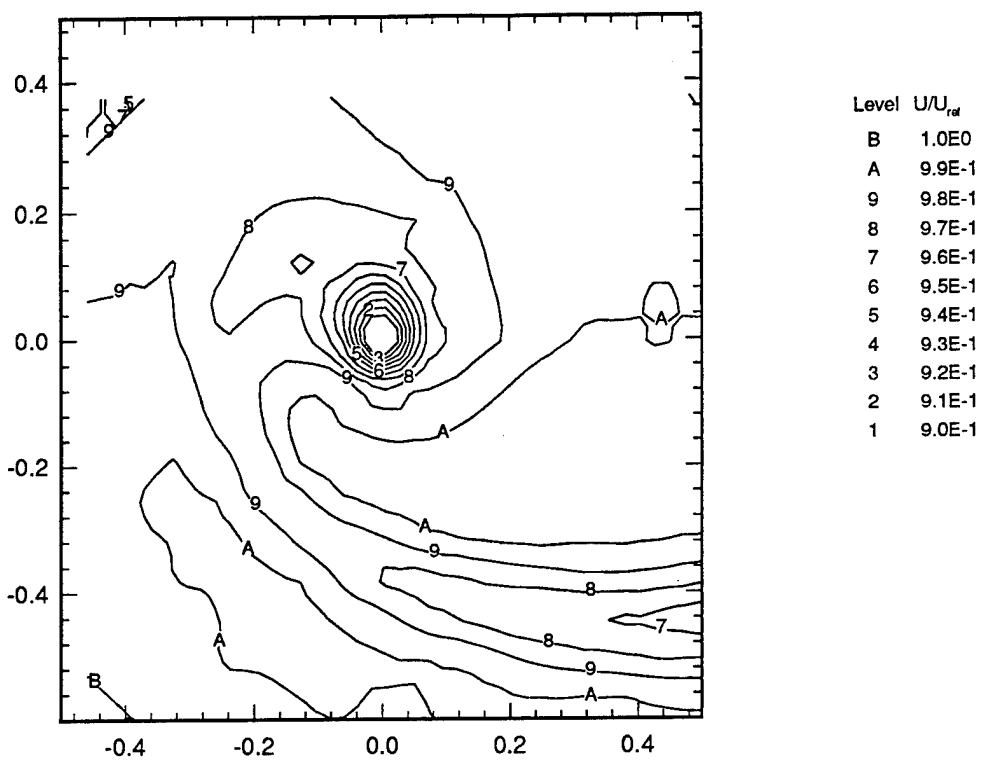


Figure 92. Contours of U/U_{ref} Showing a Well Organized Trailing Vortex
 Quad-Hot-Wire Measurements
 $X/C=10$, Aspect Ratio=2.5, Angle of Attack= 5.0° , $Re_c=330000$

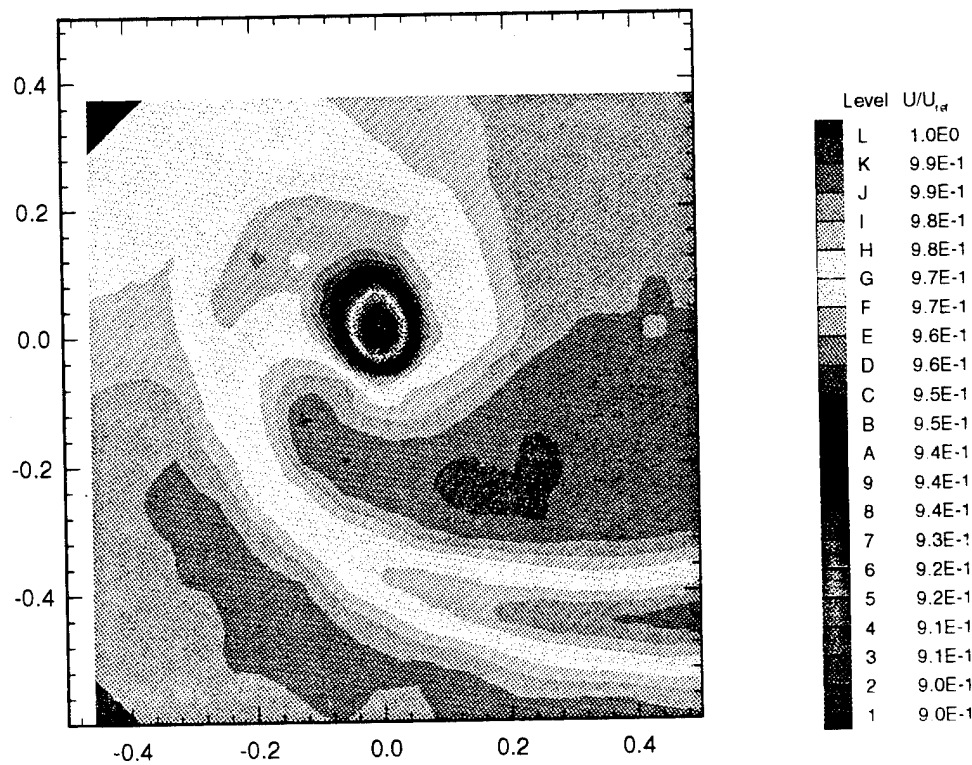


Figure 93. Color Contours of U/U_{ref} Showing Strong Axial Velocity Deficit at the Core Center. Quad-Hot-Wire Measurements
 $X/C=10$, Aspect Ratio=2.5, Angle of Attack=5.0°, $Re_c=330000$

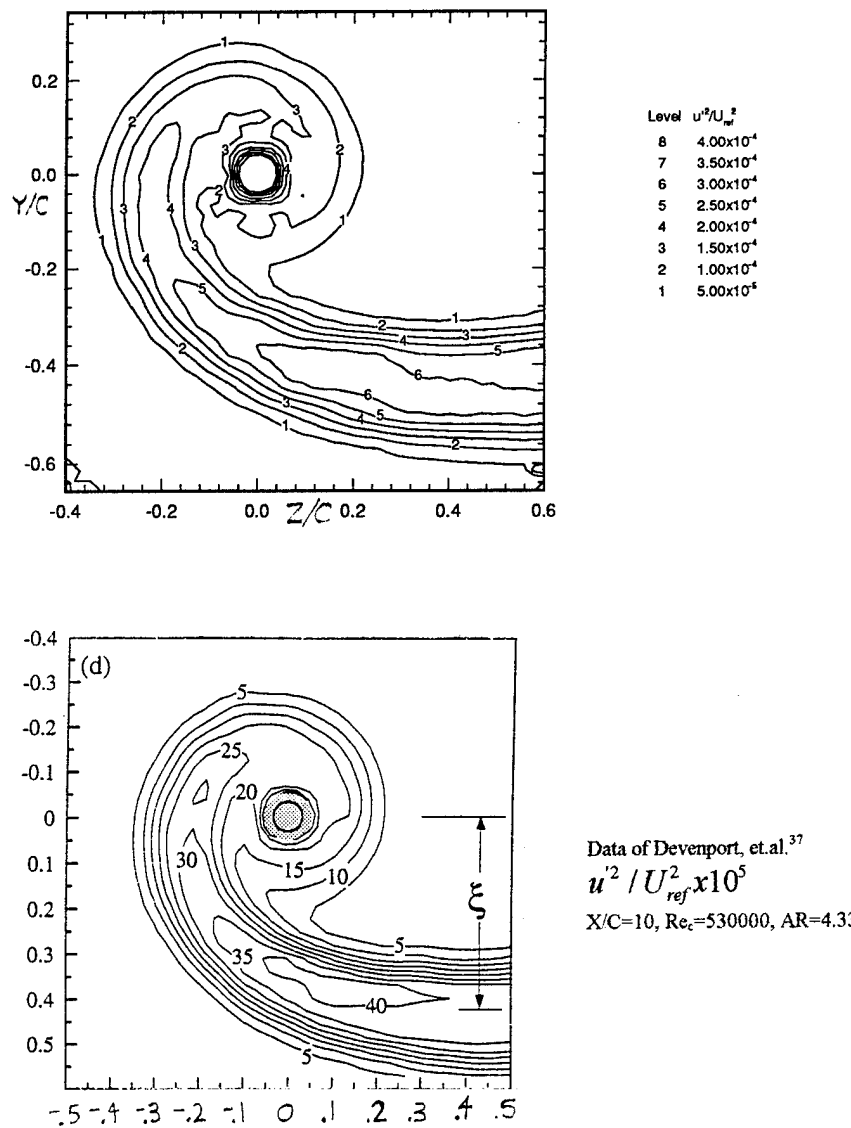


Figure 94. Contours of u'^2 / U_{ref}^2 Showing a Well Organized Trailing Vortex
 Quad-Hot-Wire Measurements
 $X/C=10$, Aspect Ratio=2.5, Angle of Attack=5.0°, $Re_c=330000$

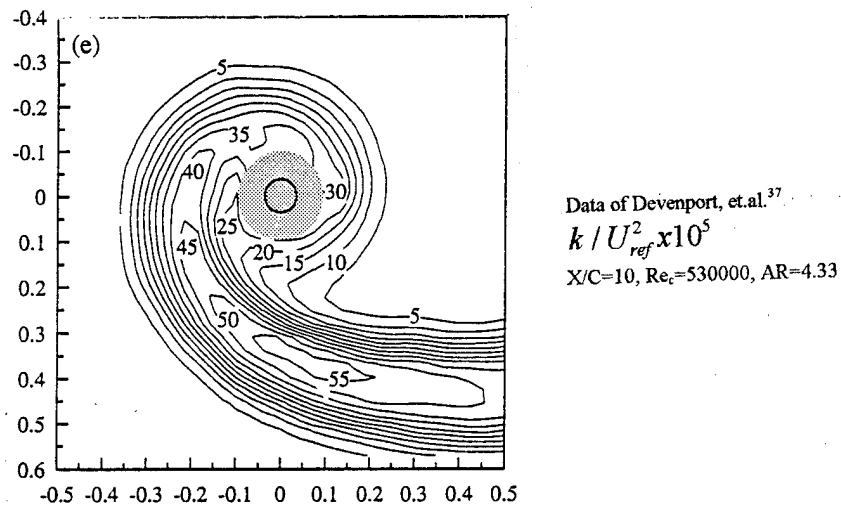
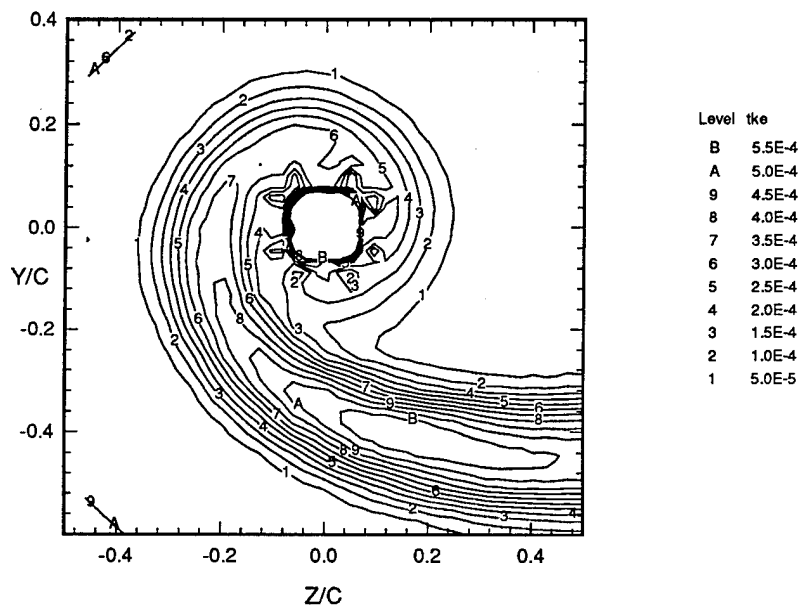


Figure 95. Contours of Turbulent Kinetic Energy (TKE)
 $X/C=10$, Aspect Ratio=2.5, Angle of Attack=5.0°, $Re_c=330000$

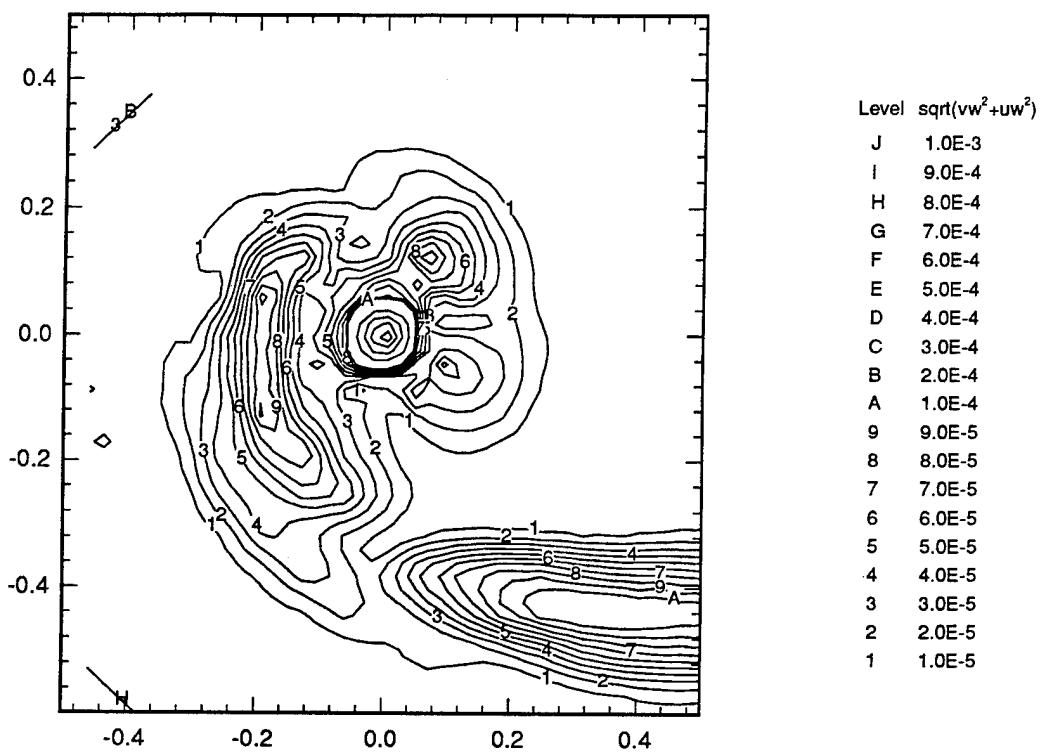


Figure 96. Contours of $\sqrt{(vw^2 + uw^2)}$
 $X/C=10$, Aspect Ratio=2.5, Angle of Attack=5.0°, $Re_c=330000$

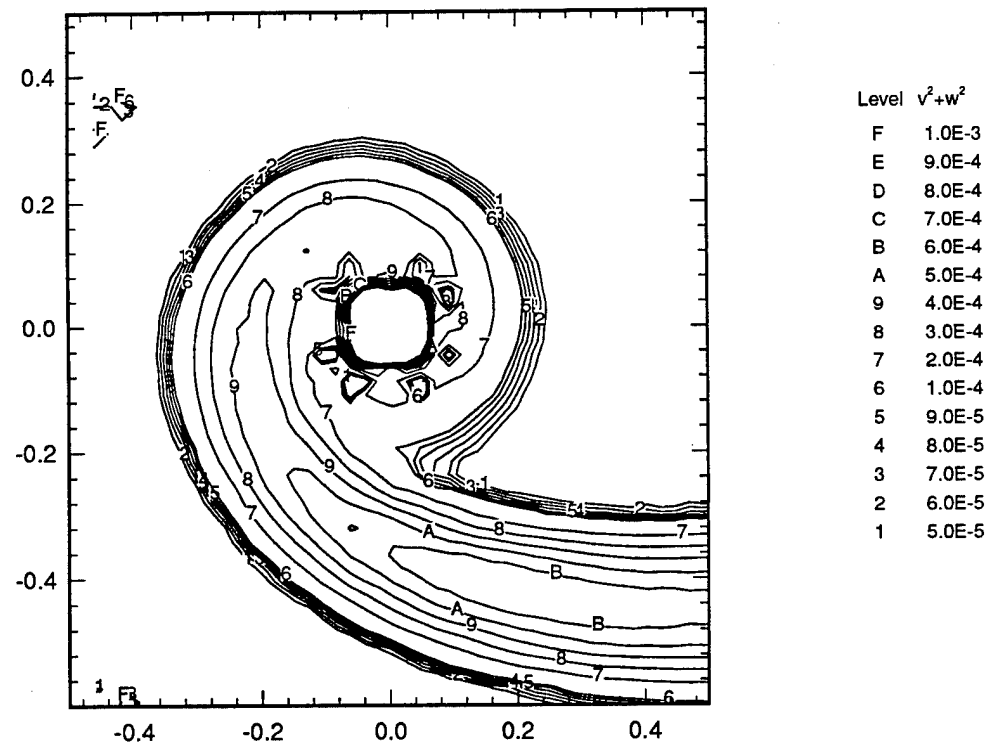
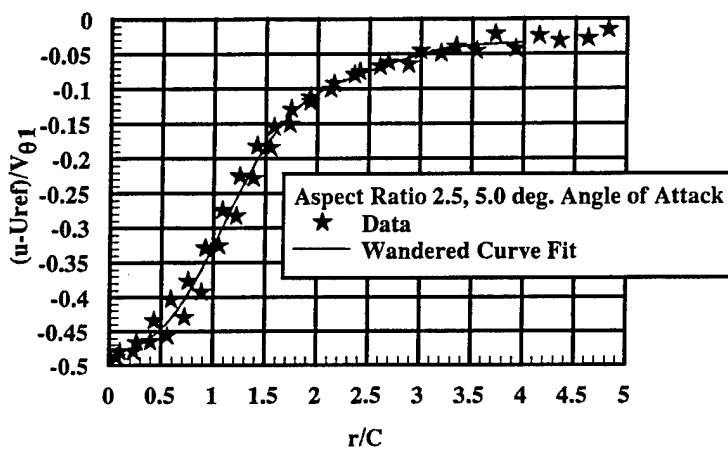
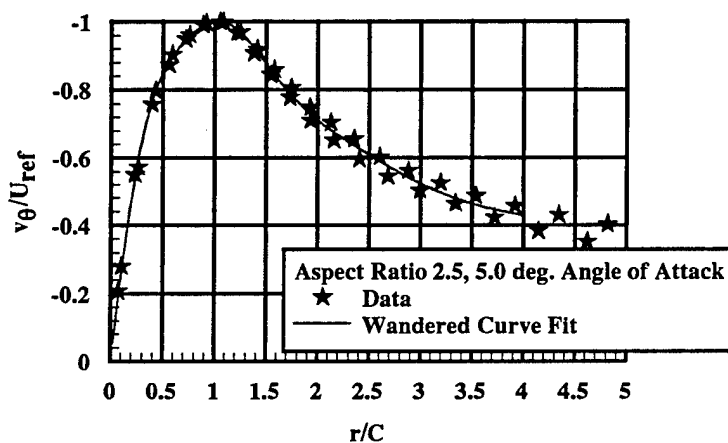


Figure 97. Contours of $(v^2 + w^2)$
 $X/C=10$, Aspect Ratio=2.5, Angle of Attack= 5.0° , $Re_c=330000$

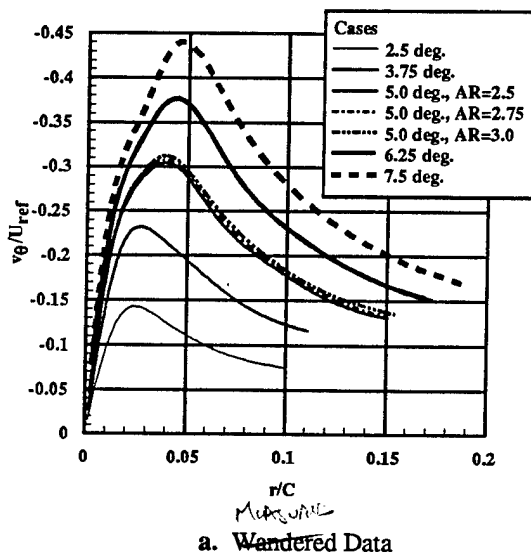


a: Curve Fit to Axial Profile Data

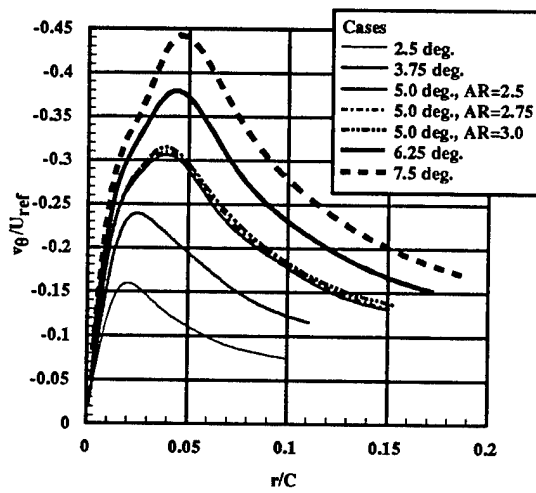


b: Curve Fit to Tangential Profile Data

Figure 98. A Typical Curve Fit to the Data
 $X/C=10$, Aspect Ratio=2.5, Angle of Attack=5.0°, $Re_c=330000$

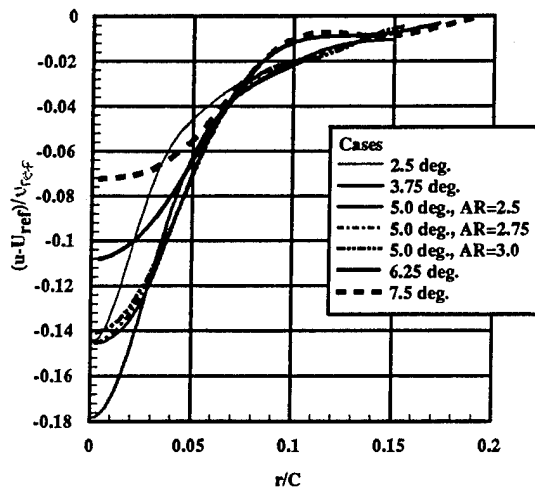


a. Wandering Data

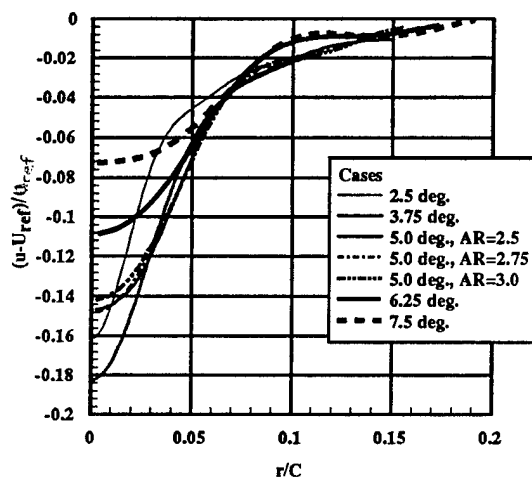


b. Unwandered Data

Figure 99. Curve Fits to Measured Data and Data Corrected for Wandering.
 Tangential Velocity.
 $X/C=10$, Aspect Ratio=2.5, Angle of Attack=5.0°, $Re_c=330000$



a. Wandered Axial Velocity Data



a. Unwandered Axial Velocity Data

Figure 100. Curve Fits to Measured Data and Data Corrected for Wandering. Axial Velocity.
 $X/C=10$, Aspect Ratio=2.5, Angle of Attack= 5.0° , $Re_c=330000$

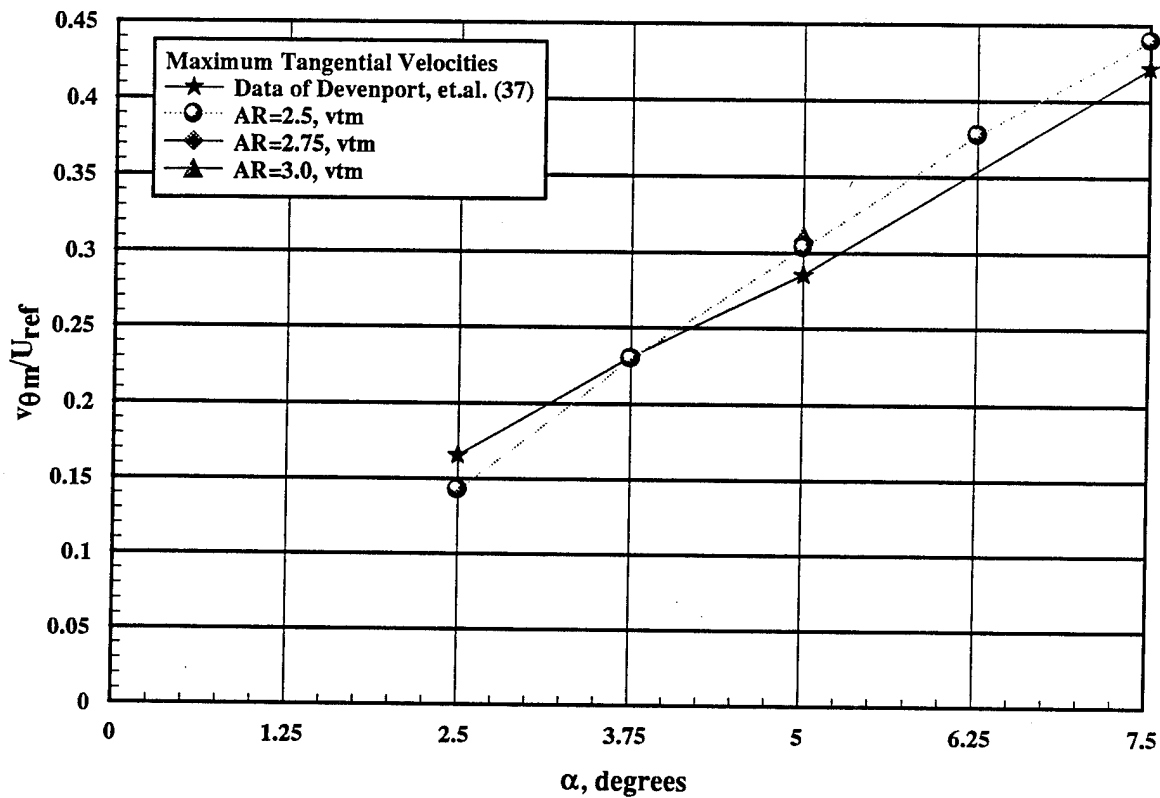


Figure 101. Maximum Tangential Velocity as a Function of Angle of Attack for the Current Data Set and that of Devenport, et.al.³⁷
 $X/C=10$, $Re_c=330000$

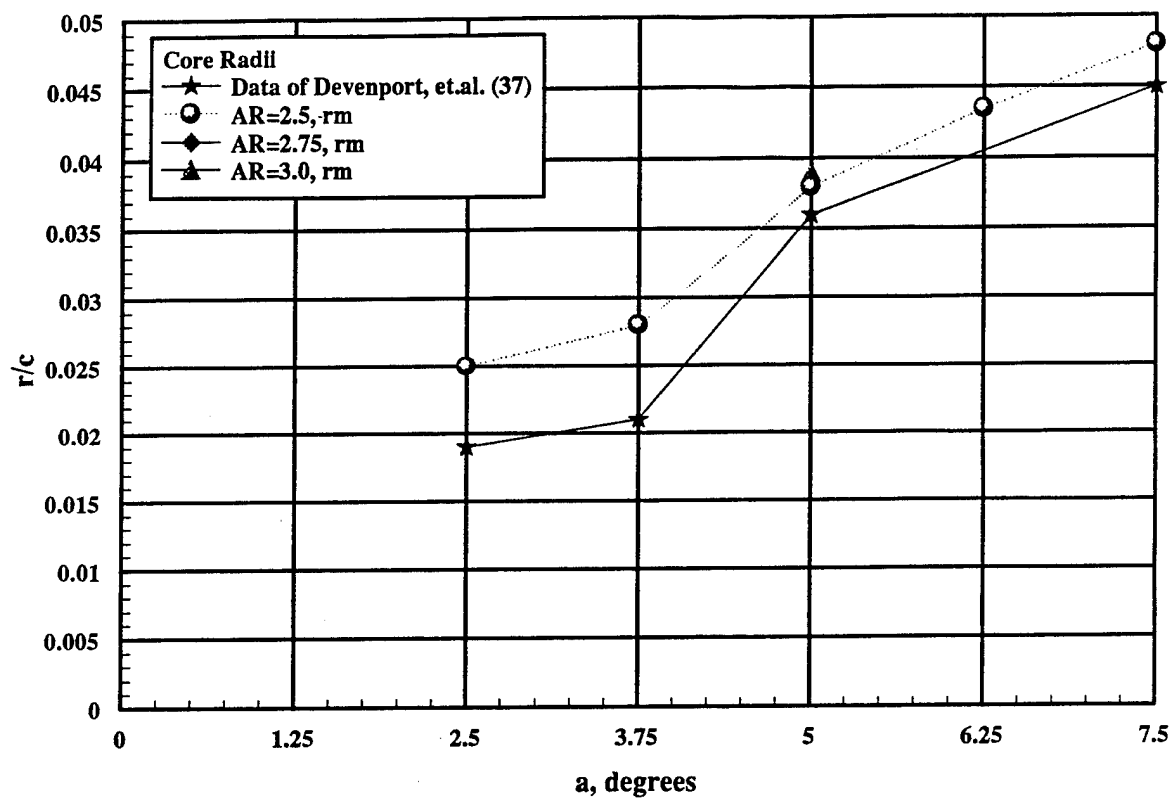


Figure 102. Core Radius as a Function of Angle of Attack for the Current Data Set and that of Devenport, et.al.³⁷
 $X/C=10$ $Re_c=330000$

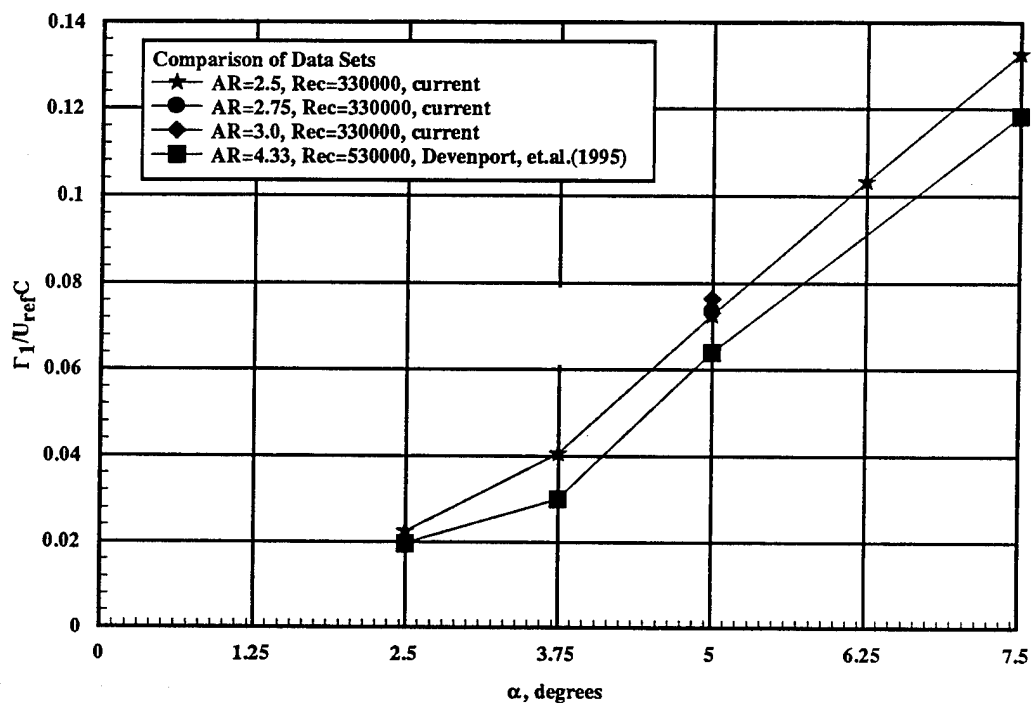


Figure 103. Normalized Core Circulation as a Function of Angle of Attack for the Current Data Set and that of Devenport, et.al.³⁷
 $X/C=10$, $Re_c=330000$

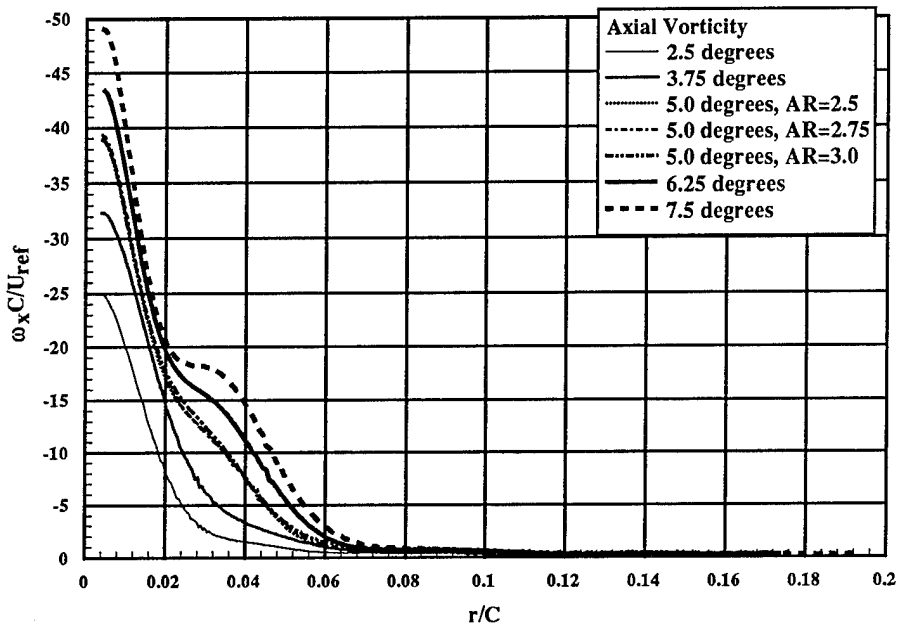


Figure 104. $\frac{\omega_x C}{U_{ref}}$ Profiles
 $X/C=10$, $Re_c=330000$

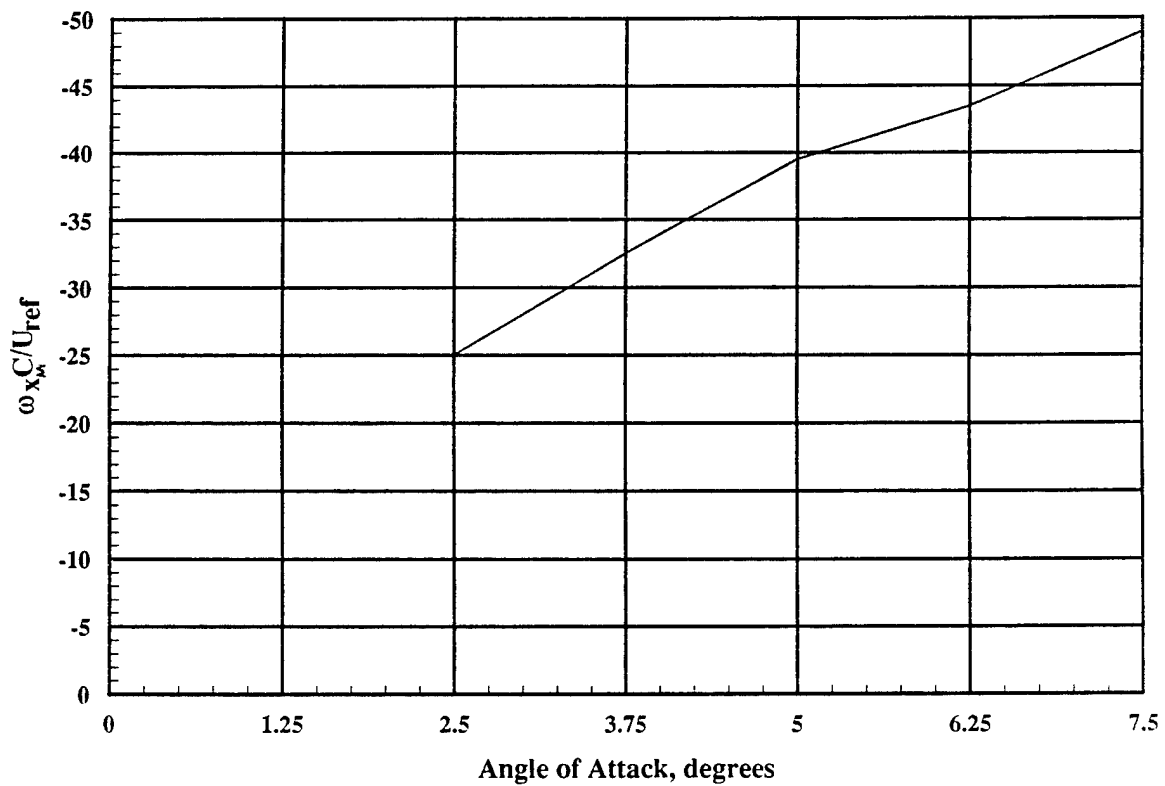
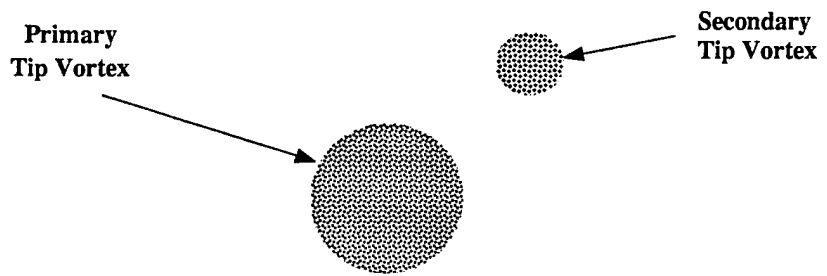
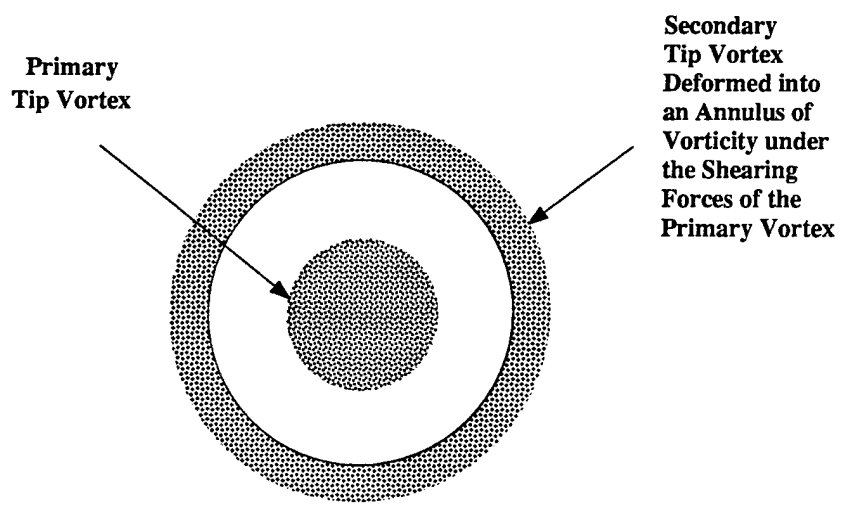


Figure 105. $\frac{\omega_{xm}C}{U_{ref}}$ as a Function of Angle of Attack
 $X/C=10$, $Re_c=330000$



a. Individual Vortices Photographed at the Wingtip



b. Differentiated Core Regions Measured at $X/C=10$

Figure 106. A Possible Model for the Cause of the Differentiated Core Regions

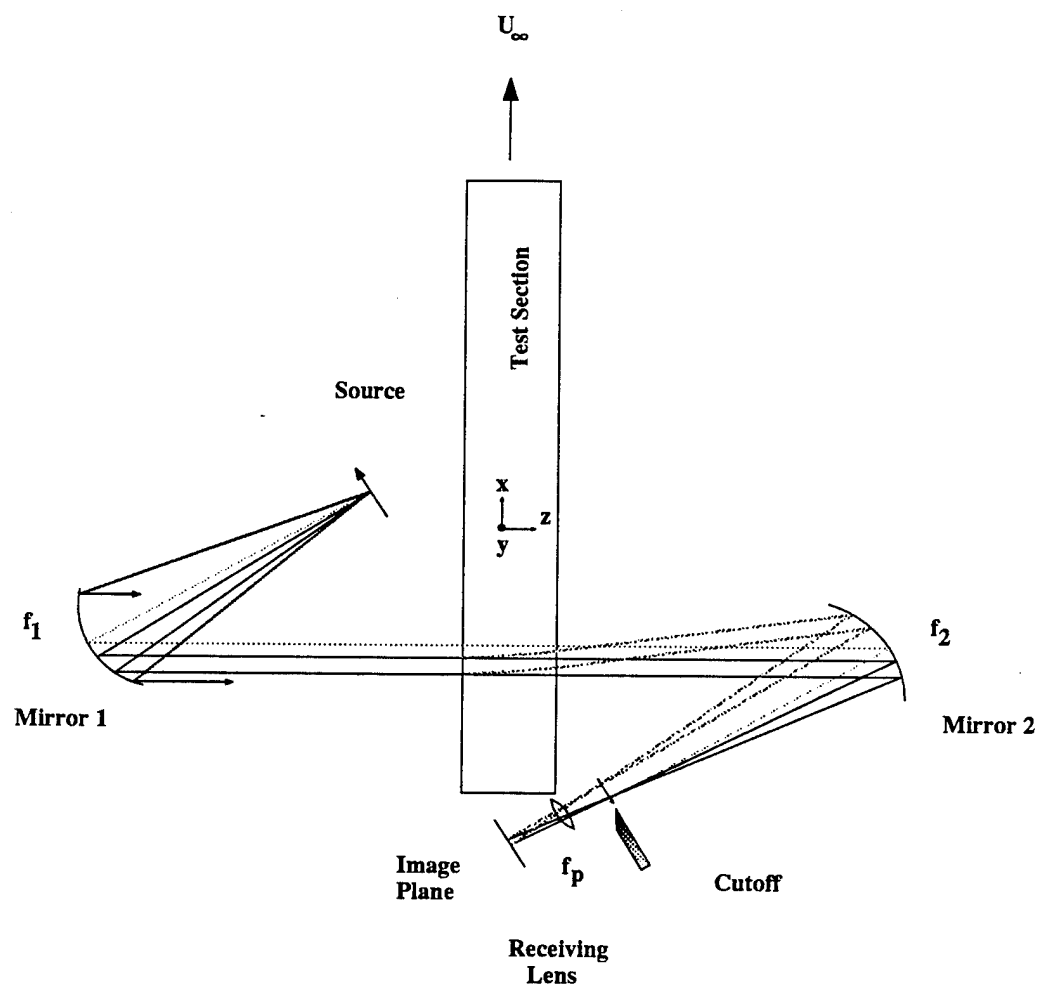


Figure 107. A Typical Toepler Schlieren System

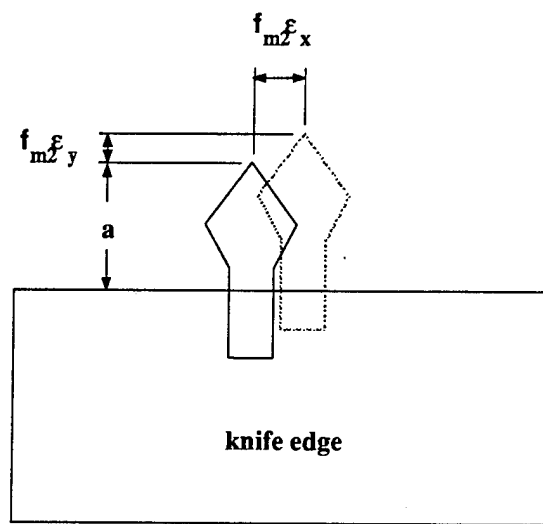


Figure 108. A Toepler Schlieren Knife Edge

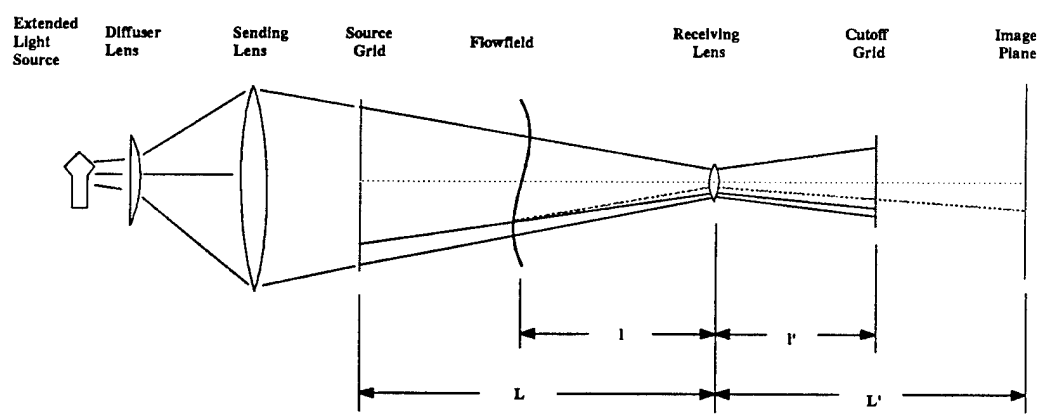


Figure 109. A Focusing Schlieren System

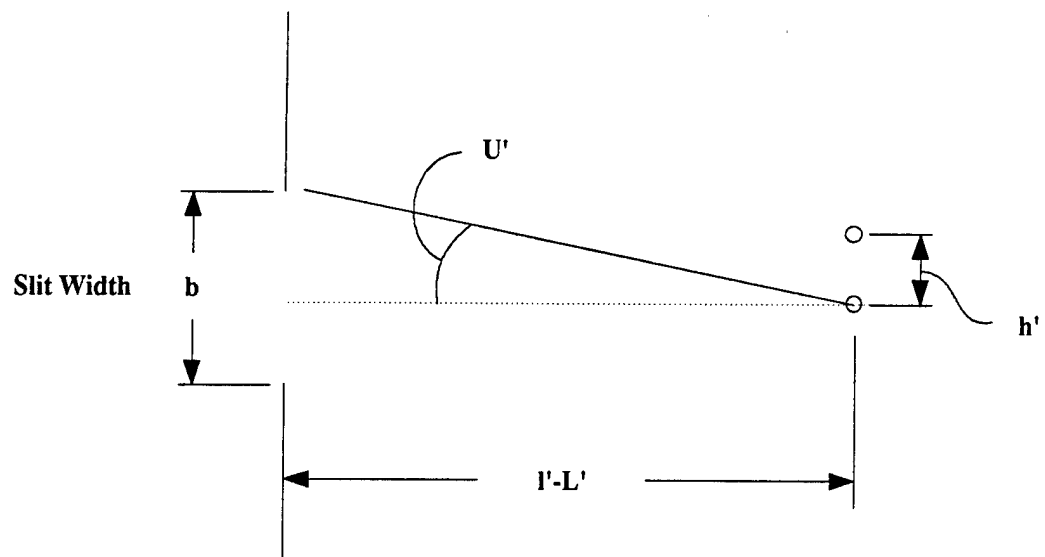
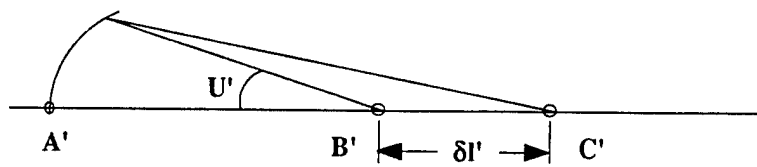
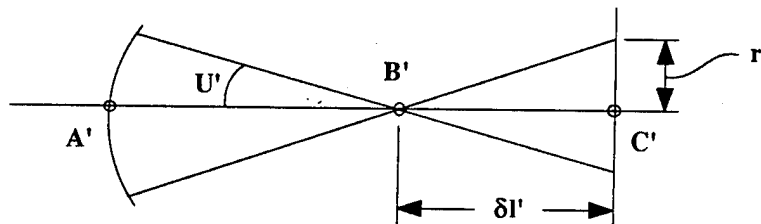


Figure 110. Geometric Image Separation at the Image Plane

(n')



a. Strict Definition of Depth of Focus



b. Less Strict Definition of Depth of Focus

Figure 111. Definitions of Depth of Focus

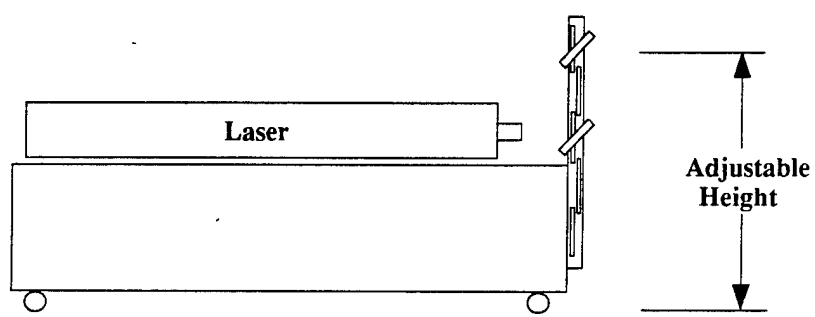


Figure 112. The Laser Table with Adjustable Beam Height

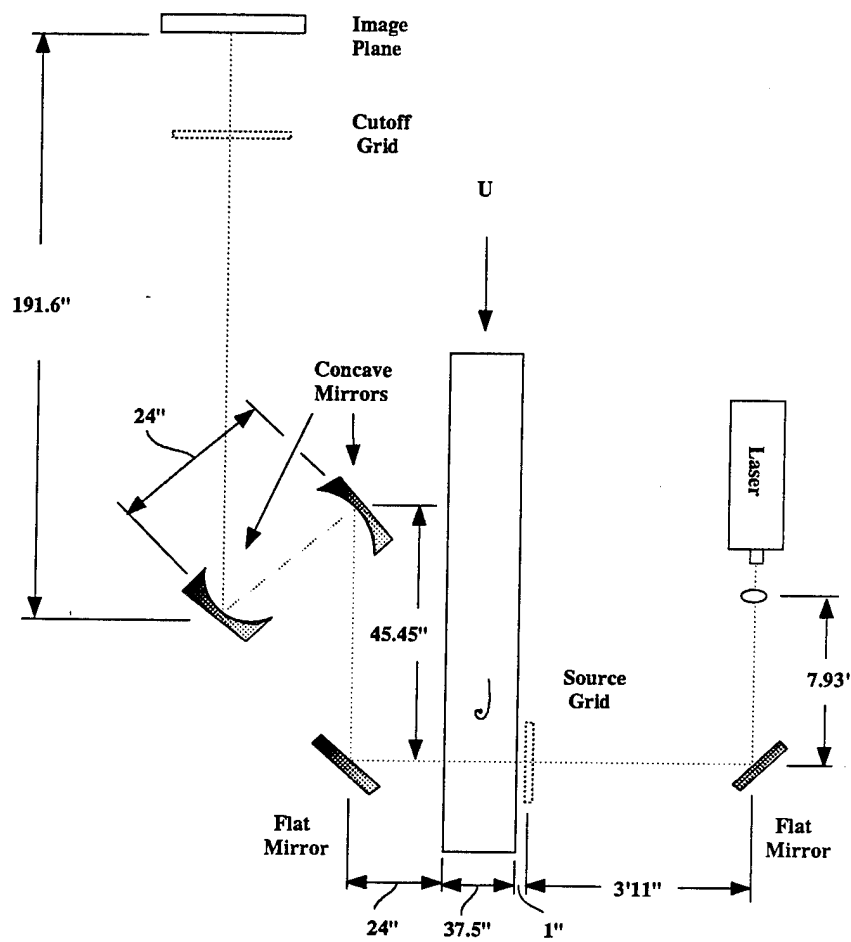


Figure 113. The Initial Focusing Schlieren Optical Layout

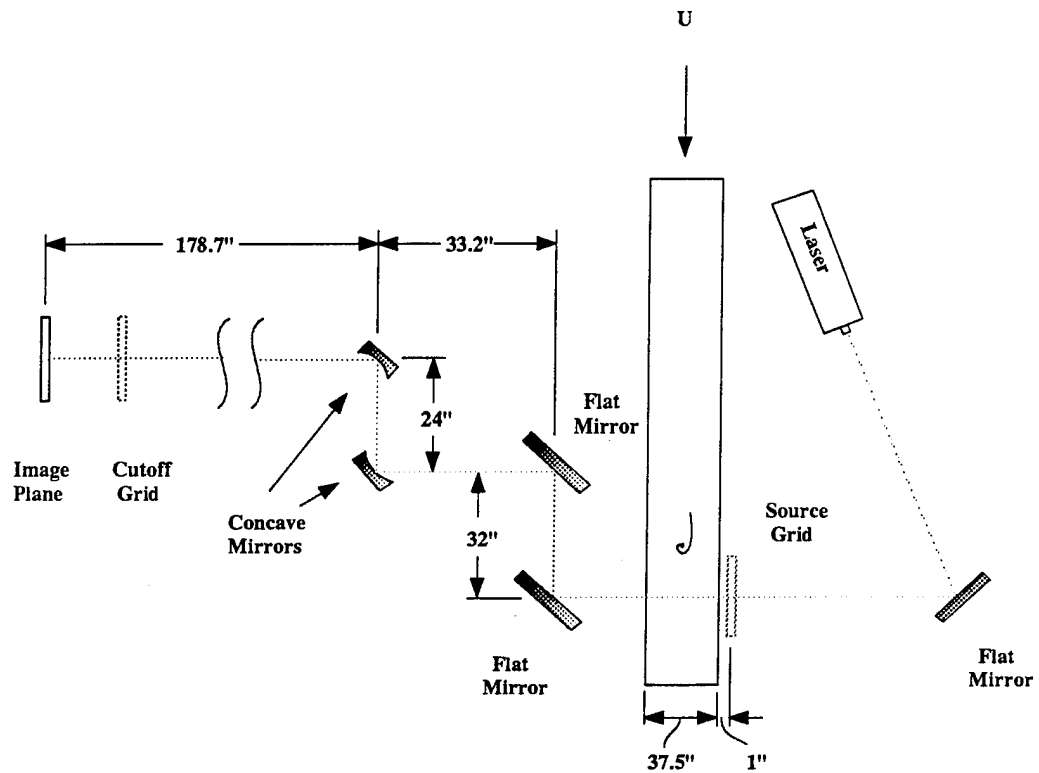


Figure 114. The Second Focusing Schlieren Optical Layout

RUN 1

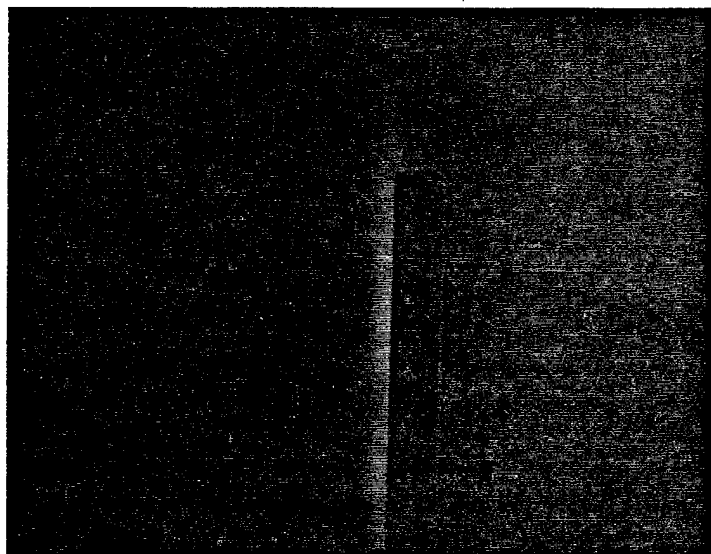


Figure 115. Heater Element in the Optical Path of a Focusing Schlieren System

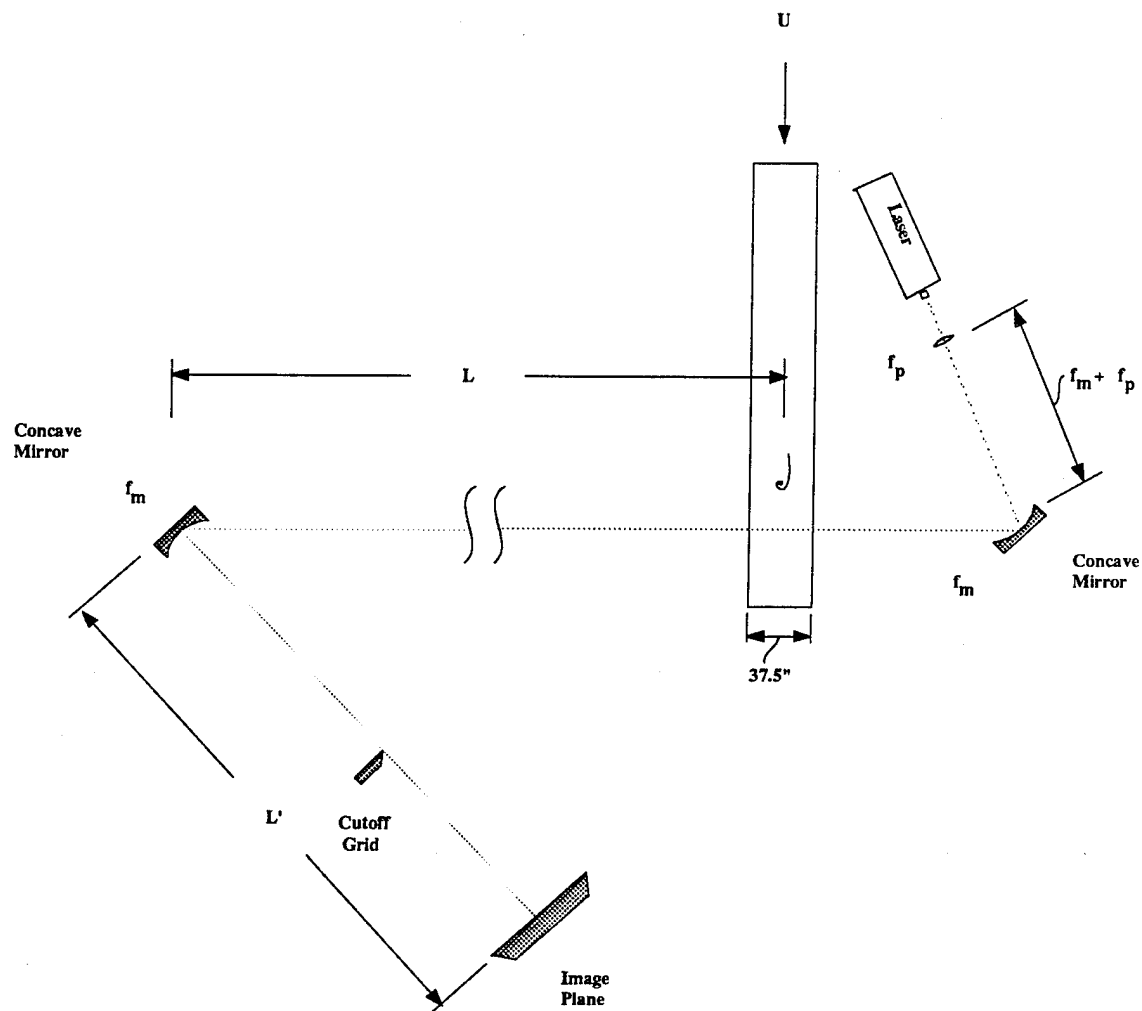


Figure 116. The Toepler Schlieren Optical Layout